In presenting this dissertation as a partial fulfillment of the requirements for an advanced degree from Emory University, I agree that the Library of the University shall make it available for inspection and circulation in accordance with its regulations, governing materials of this type. I agree that permission to copy from, or to publish, this dissertation may be granted by the professor under whose direction it was written, or, in his absence, by the Dean of the Graduate School when such copying or publication is solely for scholarly purposes and does not involve potential financial gain. It is understood that any copying from, or publication of, this dissertation which involves potential financial gain will not be allowed without written permission.

_____

Zhi Wang

Quantum Mechnical Study of Molecular Processes: From Gas Phase to Nano Phase

By

Zhi Wang
Doctor of Philosophy

Department of Chemistry

Dr. Keiji Morokuma
Advisor

Dr. Joel M. Bowman
Committee Member

Dr. James T. Kindt
Committee Member

Accepted:

Dean of the Graduate School

Date

Quantum Mechnical Study of Molecular Processes: From Gas Phase to Nano Phase

By

Zhi Wang

B.S. University of Science and Technology of China, 2004

Advisor: Keiji Morokuma, Ph.D.

An Abstract of
A dissertation submitted to the Faculty of the Graduate
School of Emroy University in partial fulfillment
of the requirements for the degree of
Doctor of Philosophy

Department of Chemistry

2008

Abstract

This thesis consists of theoretical studies of molecular processes in the scale from gas phase to nano phase.

The first part of the thesis includes theoretical studies of gas phase molecules. In chapter 2, high level ab initio methods combined with direct quasi-classsical molecular dynamics simulation have been used to study the potential energy surfaces in the photodissociation of HN_3 with particular interest on the ring closure process in the formation of cyclic-N_3. In chapter 3, low-lying potential energy states of N_3 are studied theoretically with focus on their electronic nature, and possible pathways of production of cyclic-N_3 through photoexcitation of linear-N_3 and/or suitable -N_3 precursors are suggested. Finally in chapter 4, we extend this study and construct the potential energy surfaces for 5 low-lying states of N_3.

The second part of the thesis is mainly about the study of carbon nanotubes. The density functional tight binding (DFTB) method is used throughout all the calculations. In chapter 6 and 7, the origin of the linear relationship between CH2/NH/O-SWNT reaction energies and sidewall curvature is investigated for armchair nanotubes and chiral nanotubes, respectively. Then in chapter 8, 9 and 10, high-temperature quantum chemical molecular dynamics simulations have been performed on model systems of thin SiC crystal surfaces to understand the nanotube formation process. Chapter 8 and 10 focus on the initio nanocap formation stage while chapter 9 focus on the later growth process.

Quantum Mechnical Study of Molecular Processes: From Gas Phase to Nano Phase

By

Zhi Wang

B.S. University of Science and Technology of China, 2004

Advisor: Keiji Morokuma, Ph.D.

A dissertation submitted to the Faculty of the Graduate
School of Emroy University in partial fulfillment
of the requirements for the degree of
Doctor of Philosophy

Department of Chemistry

2008

Acknowledgments

This dissertation arose in the course of my graduate study at Emory Univeristy, during which time a great number of people kindly helped me in various ways. The research done in my doctoral work would not have been possible without the support from these people. It is a pleasure to convey my sincere gratitude to them all in my acknowledgment.

In the first place, I would like to express my gratitude to my advisor, Dr. Keiji Morokuma, for all his patient guidence and constant support over the past four years. His truly scientist intuition and passion inspired my growth as a graudate student, his broad knowledge encouraged me to explore various fields in science, and his persistent training stimulated my analytical thinking that is essential as an independent researcher.

I am also very grateful to my other two committee members, Dr. Joel M. Bowman and Dr. James T. Kindt, for their tutelage and supervision. Their comments and suggestions are always beneficial to my works.

Many thanks go to Dr. Ioannis Kerkines and Dr. Peng Zhang, who helped me significantly throughout my gas phase research. Also special thanks go to Dr. Bastiaan J. Braams and Dr. Zhen Xie, who taught me the method for the construction of potential energy surface, which was used in one of my gas phase projects.

I would also like to express my appreciation to Dr. Stephan Irle and Dr. Guishan Zheng in the instruction of my nano research. Their advices were really valuable in my graduate works.

I would also like to give my thanks to the past and present members of Morokuma's group. It has been a great pleasure to work with these excellent researches. I really learned a lot from them.

Moreover, I thank Dr. Djamaladdin G. Musaev and Dr. Alex Kaledin for the mainteniance of Emerson Center computers that are critical to my research.

I should also acknoledge Ms. Jianli Zhao and Ms. Ann Dasher, who have kindly helped me in many administrative issues during my stay at Emory over years. Special thanks should also go to all nice people in ISSP at Emory University.

In addition, I want to thank all my friends in Emerson Center and at Emory University, who have made my life in Atlant enjoyable and memorable.

I thank Emerson center, PNNL, ORNL, and IMS for providing powerful computational resources over the years in conducting my research, and I thank AFOSR grant, Mitsubishi Chemical Corporation, American Chemical Society Petroleum research funds for the financial support of my prjects.

At last but not least, I owe all to my parents for their love and unconditional support in whatever I have strived to achieve. This dissertation is dedicated to my mother and father.

Contents

List of Tables

List of Figures

Introduction

With the fast development of theories and computer power, theoretical chemistry has more and more applications in understanding molecular reactions and chemical processes.[1,2] Its results no longer only serve as the complement for the information obtained by chemical experiments, but also can in many cases predict hitherto unobserved chemical phenomena and guide the design of new drugs and materials. Starting from Hartree-Fock method with Born-Oppenheimer approximation, various quantum mechanics methods with improved accuracy or efficiency have been developed in studying different systems. In the ab initio post Hartree-Fock methods, such as multireference configuartion interaction (MRCI),[3,4,5] coupled cluster (CC),[6] Møller-Plesset perturbation theory (MP2, MP3, MP4, etc.),[7,8] and quantum chemistry composite methods (G2, G3, CBS, etc.),[9,10] electron correlation is included in a more accurate way and high accuracy is expected. While these traditional electronic structure theories are based on the complicated many-electron wavefunction, the density functional theory (DFT) employs electronic density as the basic quantity. It is now among the most popular and versatile methods to study relative small or medium size molecules as well as condensed phases and gives quite satisfactory results at relatively low computational costs compared to other ways of solving the quantum mechanical many-body problem. Moreover, with the multi-configurational self-consistent field (MCSCF) method and time-dependent density functional theory (TDDFT), the theoretical study can be extended from the electronic ground states to the excited states. Not only the geometries and energies on potential energy surfaces can be determined accurately, many other important properties, such as electronic charge distributions, dipoles and higher multipole moments, vibrational frequencies, reactivity or spectroscopic quantities, can also be calculated with satisfactory preci-

son, thus providing us more insights into chemical systems. As the computation cost increases rapidly with the number of electrons, these ab initio methods are only suitable for simple chemical systems. For large molecules, such as nano phase systems, empirical or semi-empirical quantum methods is preferred to improve the computational efficiency while maintaining the theoretical accuracy. The two electron part of the Hamiltonian is not explicitly considered in general in these empirical methods. The Hückel method[11] for π-electron systems and extended Hückel method[12] for all valence electron systems were proposed for this purpose. Recently, the density functional based tight binding (DFTB) method is also developed and has been successfully applied to various problems in different systems and materials, covering carbon, silicon, and germanium structures, etc.[13,14,15,16,17]

In order to have a more detailed understanding of chemical process, the molecular dynamics simulation is an indispensable tool. With the aid of fast computer, it is possible to perform the quasi-classical molecular dynamics simulation in a direct manner, where the potential energy and its gradient are calculated on the fly.[18] The limitation is that one can hardly run a large number of trajectories to obtain statistical evaluations of physical observable, so instead one may run a few trajectories with representative initial conditions to obtain some qualitative or semi-quantitative understanding of the kinetics and dynamics process. The alternative to this direct dynamics is to construct potential energy surfaces first by fitting many ab initio calculations to some analytical functions, then running quasi-classical dynamics simulation based on these PESs. The quality of these surfaces may largely depend on the ab initio method used for the fitting, and the fitting process could be a tremendous and tedious work. However, once the potential energy surfaces are obtained, in principle unlimited number of trajectories can be simulated. As the internal degree of freedom of a moleucle increase rapidly with the number of atoms, this approach can only applied to small molecules, and reduced dimensionality theories[19,20] on PES should be

used for larger systems.

This dissertation is a summary of my graudate resarch work carried out in Professor Morokuma's group at Emory University from 2004 to 2008. It contains two parts: (1) ab initio studies on gas phase HN_3 and N_3 molecules; and (2) theoretical investigations on nano phase reactions with carbon nanotubes.

The first part of the thesis consists of our theoretical studies on gas phase molecules, with particular interest on N_3 and its possible precurssor HN_3. As one of the "high energy and density materials", the intriguing molecule N_3, especially its cyclic isomer, has been the focus of many studies.[21] It is considered for the production of new "clean" propellents since its only dissociation product is enviromental friendly nitrogen. Because the relavent system are rather small containing only 3 or 4 atoms, high level post Hartree-Fock methods such as complete active space SCF (CASSCF) and multireference configuration interaction with single and double excitations (MR-CISD)[3,4] are mainly used to determine the geometries and energies. Due to the complexity of the chemical process, multiple surfaces are investigated simutaneously and possible non-adiabatic porcess are studied. In chapter 1, essential techniques used in our gas phase study, such as an approximate diabatization scheme and the method to locate conical intersections are introduced. In chapter 2, high level ab initio methods combined with direct quasi-classsical molecular dynamics simulation have been used to study the potential energy surfaces in the photodissociation of HN_3. The possible cyclic N_3 formation mechanism has been proposed although no such process has been oberved in our limited number of trajectories, probably due to the extremely low cyclic N_3 formation possibility and insufficient sampling of the initial conditions. To further understand the ring closure process of N_3, low-lying doublet states of N_3 have been studied. In chapter 3, we located many critical structures such as stationary points and minimum on seam of crossings (MSXs) on N_3 low-lying potential energy surfaces. Their electronic nature are examined, and possible pathways of production

of cyclic-N_3 through photoexcitation of linear-N_3 and/or suitable -N_3 precursors are suggested. To faciliate molecular dynamics simulation on studying the cyclic N_3 formation process, we extend our study in chapter 4 and construct the potential energy surfaces for 5 low-lying states of N_3. These surfaces are compared with ab initio results and reasonable agreements are achieved.

The second part of the thesis is mainly about the nano phase studies involved with carbon nanotubes. As one of the most studied species nowadays, carbon nanotube features a wide range of electrical conductivity from semiconducting to metallic, depending on tube diameter and chirality[22,23,24] and functionalization.[25,26] Meanwhile, it has unique mechanical[27] and thermal properties.[28] These special properties make nanotubes excellent candidates in the applcation at nanoscale device designs. Considering that at least hundreds of atoms are usually presents in the nano phase model systems, the high accurate but extremely expensive post Hartree-Fock methods used in our gas phase studies would be formidable in such calculations; even the less expensive density functional theory would be unaffordable if larger number of calculations are needed. Therefore, to achieve the balance of accuracy and computational cost, a semi-emperical quantum mechanical method, density functional tight binding (DFTB) method is used throughout all the simulations. In chapter 6 and 7, the origin of the linear relationship between CH2/NH/O-SWNT reaction energies and sidewall curvature is investigated for armchair nanotubes and chiral nanotubes, respectively. Energy decomposition analysis is performed to help us to understand the interactions between carbon nanotubes and different functional groups. Then in chapter 8, 9 and 10, high-temperature quantum chemical molecular dynamics simulations have been performed on model systems of thin SiC crystal surfaces to understand the nanotube formation process. In chapter 8, we studied the model systems of thin SiC crystal surfaces with two graphene sheets placed on top of either C or Si face and found that C face-attached graphene layer warps readily to form nanocaps while Si face-attached

graphene sheet deoes not but keeps relative flat. Then in chapter 9, we managed to grow nanotubes on C face of SiC surface based on the previous nanocaps during the evaporation of Si atoms from the system, but we found Si-face appears not capable of nanocap formation and perpendicular tube growth. In chapter 10 we goes back to the initial nanocap formation process and found that incomplete nanocaps and entangled ring structure, as well as C chains perpendicular to the surface, tend to be formed on C face during the Si sublimation; whereas graphene layer or partial graphene layer like structure, with 5,6 and 7 rings, are preferable to be formed on Si face.

References

1. Atkins, P. W.; Friedman, R. S. *Molecular Quantum Mechanics*, 3rd ed.; Oxford University Press, 1999.

2. Szabo, A.; Ostlund, N. S. *Modern Quantum Chemistry*; Dover Publications, 1996.

3. WERNER, H.; KNOWLES, P. *JOURNAL OF CHEMICAL PHYSICS* **1988**, *89*, 5803–5814.

4. KNOWLES, P.; WERNER, H. *CHEMICAL PHYSICS LETTERS* **1988**, *145*, 514–522.

5. Knowles, P. J.; Handy, N. C. *Chem. Phys. Letters* **1984**, *111*, 315–321.

6. Knowles, P. J.; Hampel, C.; Werner, H.-J. *J. Chem. Phys.* **1993**, *99*, 5219–5227.

7. Amos, R. D.; Andrews, J. S.; Handy, N. C.; Knowles, P. J. *Chem. Phys. Letters* **1991**, *185*, 256–264.

8. Knowles, P. J.; Andrews, J. S.; Amos, R. D.; Handy, N. C.; Pople, J. A. *Chem. Phys. Letters* **1991**, *186*, 130–136.

9. Curtiss, L. A.; Redfern, P. C.; Raghavachari, K. *JOURNAL OF CHEMICAL PHYSICS* **2007**, *126*, 084108.

10. DeYonker, N.; Cundari, T.; Wilson, A. *JOURNAL OF CHEMICAL PHYSICS* **2006**, *124*, 114104.

11. Hückel, E. *Zeitschrift für Physik A Hadrons and Nuclei* **1931**, *70*, 204–286.

12. HOFFMANN, R. *JOURNAL OF CHEMICAL PHYSICS* **1963**, *39*, 1397– .

13. Elstner, M.; Cui, Q.; Munih, P.; Kaxiras, E.; Frauenheim, T.; Karplus, M. *JOURNAL OF COMPUTATIONAL CHEMISTRY* **2003**, *24*, 565–581.

14. Elstner, M.; Porezag, D.; Jungnickel, G.; Elsner, J.; Haugk, M.; Frauenheim, T.; Suhai, S.; Seifert, G. *PHYSICAL REVIEW B* **1998**, *58*, 7260–7268.

15. POREZAG, D.; FRAUENHEIM, T.; KOHLER, T.; SEIFERT, G.; KASCHNER, R. *PHYSICAL REVIEW B* **1995**, *51*, 12947–12957.

16. Frauenheim, T.; Seifert, G.; Elstner, M.; Hajnal, Z.; Jungnickel, G.; Porezag, D.; Suhai, S.; Scholz, R. *PHYSICA STATUS SOLIDI B-BASIC SOLID STATE PHYSICS* **2000**, *217*, 41–62.

17. Frauenheim, T.; Seifert, G.; Elstner, M.; Niehaus, T.; Kohler, C.; Amkreutz, M.; Sternberg, M.; Hajnal, Z.; Di Carlo, A.; Suhai, S. *JOURNAL OF PHYSICS-CONDENSED MATTER* **2002**, *14*, 3015–3047.

18. Gordon, M.; Chaban, G.; Taketsugu, T. *JOURNAL OF PHYSICAL CHEMISTRY* **1996**, *100*, 11512–11525.

19. BOWMAN, J. *JOURNAL OF PHYSICAL CHEMISTRY* **1991**, *95*, 4960–4968.

20. CLARY, D. *JOURNAL OF PHYSICAL CHEMISTRY* **1994**, *98*, 10678–10688.

21. Samartzis, P. C.; Wodtke, A. M. *INTERNATIONAL REVIEWS IN PHYSICAL CHEMISTRY* **2006**, *25*, 527–552.

22. White, C.; Mintmire, J. *JOURNAL OF PHYSICAL CHEMISTRY B* **2005**, *109*, 52–65.

23. Joselevich, E. *CHEMPHYSCHEM* **2004**, *5*, 619–624.

24. Anantram, M. *APPLIED PHYSICS LETTERS* **2001**, *78*, 2055–2057.

25. Collins, P.; Bradley, K.; Ishigami, M.; Zettl, A. *SCIENCE* **2000**, *287*, 1801–1804.

26. Kong, J.; Franklin, N.; Zhou, C.; Chapline, M.; Peng, S.; Cho, K.; Dai, H. *SCIENCE* **2000**, *287*, 622–625.

27. Wong, E.; Sheehan, P.; Lieber, C. *SCIENCE* **1997**, *277*, 1971–1975.

28. Hone, J.; Whitney, M.; Piskoti, C.; Zettl, A. *PHYSICAL REVIEW B* **1999**, *59*, R2514–R2516.

PART I.

Theoretical studies on gas phase molecules

Chapter 1. Introduction of techniques in studying non-adiabatic processes

In the first part of my thesis, the focus of study is on gas phase molecules. Our main interest is on the formation mechanism of cyclic N_3. Therefore, we performed extensive study on N_3 molecule, and its possible precussor HN_3. Due to the complexity of the chemical process, multiple surfaces of the target molecules should be investigated simutaneously and possible non-adiabatic porcess need to be studied. For this purpose, many essential techniques, such as locating the minimum on the seam of crossings (MSX), approximate diabatization, and constrained least square fitting, are needed in our studies. I will elaborate these techniques in details in this chapter.

1.1 Locating the Minimum on the Seam of Crossing (MSX)

Many molecular reactions involve non-adiabatic processes, which associate with crossing of multiple adiabatical potential energy surfaces. The electronic states and couplings around these crossing regions are essential in the non-adiabatic processes, therefore it is necessary to locate the conical regions where the surfaces of interest are degenerate.

Typically, for a n atoms molecule with $N = 3n - 6$ internal degree of freedom, the dimension of intersection hypersurface between two electronic states is either N-1 or N-2, depending on distinct or same space $\otimes$ spin symmetry of these two states. If there are additional M geometrical constraints, the dimension of this constrained hypersurface will be reduced to N-M-1 and N-M-2. The lowest energy point on this

hypersurface is often referred to as minimum on the seam-of-crossing (MSX), which represents a key bottleneck along the minimum energy path of an electronically non-adiabatic reaction. Therefore, it is desirable to locate these intersection points on the potential energy surfaces. A few different methods have been developed for this purpose. Morokuma and coworkers introduced the first approach by using Newton method with Lagrangian multipliers.[1] Other algorithms also emerged and involved the use of analytical gradients with evaluation of numerical Hessian.[2,3,4,5] A distinct efficient direct method without constraints was also innovated by Bearpark and currently used by Molpro package.[6] I will demenstrate both appoaches below.

1.1.1 Newton method with Lagrangian multiplier

Mathematically, this problem of locating the MSX is a constrined optimization:

$$\begin{cases} \min \quad f(x) &= \quad E_2(x) \\ \text{s.t.} \quad c(x) &= E_1 - E_2 \;=\; 0 \end{cases} \tag{1.1}$$

The Lagrangian thus can be constructed as:

$$L(x, \lambda) = f(x) + \lambda c(x) \tag{1.2}$$

At the solution, one will have

$$\begin{cases} \nabla f(x) \;+\; \lambda^T B(x) &= 0 \\ c(x) &= 0 \end{cases} \tag{1.3}$$

The Newton equality condition is defined as:

$$\begin{bmatrix} W(x,\lambda) & B(x)^T \\ B(x) & 0 \end{bmatrix} \begin{bmatrix} \delta x \\ \delta\lambda \end{bmatrix} = - \begin{bmatrix} \nabla f(x) + B(x)^T \lambda \\ c(x) \end{bmatrix} \tag{1.4}$$

where

$$W(x,\lambda) = \nabla^2 f + \frac{\partial}{\partial x}(B^T\lambda) \tag{1.5}$$

The solution satisfy:

$$\begin{array}{rcrcrcl} W_k\delta x & + & \nabla f_k & + & B_k\mu_k & = & 0 \\ & & B_k\delta x & + & c_k & = & 0 \end{array} \tag{1.6}$$

So we can updating x and λ with following equations in the optimzation:

$$\begin{array}{rcl} x_{k+1} & = & x_k + \delta x \\ \lambda_{k+1} & = & \mu_k \end{array} \tag{1.7}$$

This equation is iterally solved and the MSX can be determined.

1.1.2 Direct method without Hessian

In the direct method, the problem is slightly different defined as:

$$\begin{cases} \min & f(x) & = & E_2(x) \\ \text{s.t.} & c(x) & = & (E_1 - E_2)^2 & = & 0 \end{cases} \tag{1.8}$$

For a conical intersection, there are 2 directions that lift the energy degeneracy, the first one is the difference gradient vector, and defined as:

$$x_1 = \frac{\partial(E_1 - E_2)}{\partial q} = g_1 - g_2 \tag{1.9}$$

while the other one is called interstate coupling vector:

$$x_2 = < C_1^t(\frac{\partial H}{\partial q})C_2 > \tag{1.10}$$

which is 0 when two states are of different space $\otimes$ spin symmetry. The two states

energy are degenerate in the other n-2 dimensional space, which is the intersection hypersurface.

In order to locate the minimum on seam of crossing, one needs to minimize $E_1 - E_2$ based on the difference gradient x_1 in the x_1, x_2 plane:

$$\frac{\partial}{\partial q_\alpha}(E_2 - E1)^2 = 2(E_2 - E1)x_1 = 0 \tag{1.11}$$

the size of step depends on $E_1 - E_2$

$$g_{diff} = 2(E_2 - E1)\frac{x_1}{\sqrt{x_1 \cdot x_1}} \tag{1.12}$$

At the same time, one need to minimize E_2 based on the projection of gradient of E_2 onto the n-2 orthogonal complement to the plane $x_1 x_2$:

$$g_{proj} = Pg_2 \tag{1.13}$$

In the case of crossing with different symmetry states $x_2 = 0$. Therefore, one can determine the final gradient used in the optimization as:

$$g = g_{diff} + g_{proj} \tag{1.14}$$

By following this gradient step by step, the MSX would finally be located.

1.2 Approximate Diabatization Scheme by Analyzing CI Vectors

Another essential technique in the study of non-adiabatic process is to express the adiabatic states in terms of diabatic states, which exhibits simpler energy surfaces and less complex electronic structures regarding the dominant configurations. It is

highly preferrable to perform dynamic simulation in diabatic states around the region where two surfaces cross or barely avoid crossing. Under such conditions, the Born-Oppenheimer approximation breaks down and couplings between different adiabatic states must be taken into account. Since these couplings are embeding into nuclear derivative terms which become very large and difficult to evaluate, the construction of diabatic states is desired in order to avoid this numerical problems. Therefore, the diabatic state is defined by a unitary transformation from the adiabatic states satisfy the following condition:[7]

$$\langle \phi_i^d(r;R)|\frac{\partial}{\partial R_\alpha}\phi_j^d(r;R)\rangle = 0 \tag{1.15}$$

Although the numerical solution to 1.15 in one-dimensional case has been obtained easily,[8] it is well accepted that no rigorous solution to 1.15 exists in high dimension cases.[9] However, various techniques have been proposed to obtain the diabatic states in an approximate manner,[10,11,12,13,14,15] and we will introduce the one proposed by Ruedenberg and Atchity[10,11] by analyzing the CI coefficient in the following context.

Suppose one has two adiabatic states ψ_1 and ψ_2. At the CI region, there occurs a switch in the dominance of configurations between these two adiabatic states, which can be shown in the following scheme:

Dominant	Adiabatic States	
Configurations	Region I	Region II
$\chi_1 \cdots \chi_a$	dominant in ψ_1	dominant in ψ_2
$\chi_{a+1} \cdots \chi_{a+b}$	dominant in ψ_2	dominant in ψ_1

The two adiabatic states ψ_1 and ψ_2 can be constructed from two diabatic states ϕ_1 and ϕ_2 by a linear transformation T:

$$\begin{aligned} \psi_1 &= T_{11}\phi_1 - T_{12}\phi_2 \\ \psi_2 &= T_{21}\phi_1 + T_{22}\phi_2 \end{aligned} \tag{1.16}$$

Both adiabatic states and diabatic states are orthogonal, hence T is orthogonal

$$T^T T = T T^T = I \tag{1.17}$$

$$T = \begin{pmatrix} T_{11} & T_{12} \\ T_{21} & T_{22} \end{pmatrix} = \begin{pmatrix} cos\gamma & -sin\gamma \\ sin\gamma & cos\gamma \end{pmatrix} \tag{1.18}$$

Also, the diabatic states is dominated by the same set of configurations throughtout the CI region:

Dominant	Adiabatic States	
Configurations	Region I	Region II
$\chi_1 \cdots \chi_a$	dominant in ϕ_1	
$\chi_{a+1} \cdots \chi_{a+b}$	dominant in ϕ_2	

The adiabatic states are expressed in terms of a large number of given configurations $\chi_\alpha (\alpha = 1, 2, \ldots, A)$ spanning the configurational space:

$$\psi_n = \sum_{\alpha}^{A} \chi_\alpha C_{\alpha n}, \quad n = 1, 2. \tag{1.19}$$

Because of the orthogonalities

$$\langle \chi_\alpha | \chi_\beta \rangle = \delta_{\alpha\beta}, \quad \langle \psi_n | \psi_m \rangle = \delta_{nm} \tag{1.20}$$

One has

$$C^T C = \left[\sum_{\alpha} C_{\alpha n} C_{\alpha m} \right] = (\delta_{nm}) = I. \tag{1.21}$$

From the inverse transformation of equation (1.16), one has

$$\phi_i = \sum_{n=1}^{2} \psi_n T_{ni}, \quad i = 1, 2. \tag{1.22}$$

hence

$$\phi_i = \sum_{\alpha}^{A} \chi_\alpha F_{\alpha i}, \quad i = 1, 2. \tag{1.23}$$

where

$$F_{\alpha i} = \sum_{n}^{2} C_{\alpha n} T_{ni} = (CT)_{\alpha i} \tag{1.24}$$

Orthogonality yields

$$\begin{aligned} \langle \phi_i | \phi_j \rangle &= \langle \textstyle\sum_\alpha^A \chi_\alpha F_{\alpha i} | \sum_\beta^A \chi_\beta F_{\beta j} \rangle = \sum_{\alpha,\beta}^A \langle \chi_\alpha | \chi_\beta \rangle F_{\alpha i} F_{\beta j} = \sum_{\alpha,\beta}^A \delta_{\alpha\beta} F_{\alpha i} F_{\beta j} \\ &= \textstyle\sum_\alpha F_{\alpha i} F_{\alpha j} = (F^T F)_{ij} = (T^T C^T C T)_{ij} = (T^T T)_{ij} = \delta_{ij} \end{aligned} \tag{1.25}$$

Assume the dominant configurations are listed first, as $\chi_1 \chi_2 \cdots \chi_a \chi_{a+1} \cdots \chi_{a+b}$, and the remaining configurations follow as $\chi_{a+b+1} \cdots \chi_A$.Typically, $a + b$ is a relatively small number, whereas A, the dimension of the entire configuration space, is a large number.

The objective is to choose the 2×2 transformation T such that throught ϕ_1 is dominated by $\chi_1 \cdots \chi_a$ and ϕ_2 is dominated by $\chi_{a+1} \cdots \chi_{a+b}$, so it is demanded that T is to be determined by maximizeing the quantity:

$$F = F_a + F_b = \sum_{\alpha=1}^{a} F_{\alpha 1}^2 + \sum_{\beta=a+1}^{a+b} F_{\beta 2}^2. \tag{1.26}$$

From equation (1.24), one can obtain:

$$F_a = (T^T P T)_{11} \tag{1.27}$$

with

$$P_{nm} = \sum_{\alpha=1}^{a} C_{\alpha n} C_{\alpha m} = P_{mn}, \quad n, m = 1, 2 \tag{1.28}$$

and similarly

$$F_b = (T^T Q T)_{22} \tag{1.29}$$

with

$$Q_{nm} = \sum_{\beta=a+1}^{a+b} C_{\beta n} C_{\beta m} = Q_{mn}, \quad n, m = 1, 2 \tag{1.30}$$

Because of the property of the transformation matrix T,

$$\begin{aligned} T_{11} &= T_{22} \\ T_{12} &= -T_{21} \end{aligned} \tag{1.31}$$

one can rewrite F_b as

$$F_b = (T^T \widetilde{Q} T)_{11} \quad \text{with} \quad \widetilde{Q} = \begin{pmatrix} Q_{22} & -Q_{12} \\ -Q_{21} & Q_{22} \end{pmatrix}. \tag{1.32}$$

Combining equation (1.27) and (1.32), one can therefore obtain:

$$F = (T^T R T)_{11}, \tag{1.33}$$

where

$$\begin{aligned} R_{11} &= P_{11} + Q_{22} &&= \textstyle\sum_{\alpha=1}^{a} C_{\alpha 1}^2 + \sum_{\beta=a+1}^{a+b} C_{\beta 2}^2 \\ R_{22} &= P_{22} + Q_{11} &&= \textstyle\sum_{\alpha=1}^{a} C_{\alpha 2}^2 + \sum_{\beta=a+1}^{a+b} C_{\beta 1}^2 \\ R_{12} = R_{21} &= P_{12} - Q_{12} &&= \textstyle\sum_{\alpha=1}^{a} C_{\alpha 1} C_{\alpha 2} + \sum_{\beta=a+1}^{a+b} C_{\beta 1} C_{\beta 2} \end{aligned} \tag{1.34}$$

The maximization of F can be accomplished by diagonizing the matrix R. Meanwhile, the eigenvector with the larger eigenvalue yields (T_{11}, T_{21}) which determines ϕ_1, whereas the eigenvector with the smaller eigenvalue yields (T_{12}, T_{22}) which determines ϕ_2. The solution of this eigenvalue problem is:

$$\begin{aligned} \lambda_1 &= \overline{R} + \sqrt{(\Delta R)^2 + R_{12}^2} \\ \lambda_2 &= \overline{R} - \sqrt{(\Delta R)^2 + R_{12}^2} \end{aligned} \tag{1.35}$$

$$\begin{pmatrix} T_{11} & T_{12} \\ T_{21} & T_{22} \end{pmatrix} = \begin{pmatrix} cos\theta/2 & -sin\theta/2 \\ sin\theta/2 & cos\theta/2 \end{pmatrix} \tag{1.36}$$

where

$$\overline{R} = (R_{11} + R_{22})/2 \tag{1.37}$$

$$\Delta R = (R_{11} - R_{22})/2 \tag{1.38}$$

$$cos\theta = \Delta R/\sqrt{(\Delta R)^2 + R_{12}^2} \tag{1.39}$$

$$sin\theta = R_{12}/\sqrt{(\Delta R)^2 + R_{12}^2} \tag{1.40}$$

Denote

$$V_n = \langle\psi_n|H|\psi_n\rangle \quad n = 1, 2 \tag{1.41}$$

$$U_{ij} = \langle\phi_i|H|\phi_j\rangle \quad n = 1, 2 \tag{1.42}$$

one has

$$\begin{aligned} U_{ij} &= \langle\phi_i|H|\phi_j\rangle = \textstyle\sum_{n,m}\langle\psi_n|H|\psi_m\rangle T_{ni}T_{mj} \\ &= V_1T_{1i}T_{1j} + V_2T_{2i}T_{2j} \end{aligned} \tag{1.43}$$

Expressing V_1 and V_2 in terms of

$$\overline{V} = (V_{11} + V_{22})/2, \quad \Delta V = (V_{11} - V_{22})/2 \tag{1.44}$$

One obtains

$$U_{ij} = \overline{V}\delta_{ij} + \Delta V(T_{1i}T_{1j} - T_{2i}T_{2j}) \tag{1.45}$$

Which becomes

$$\begin{aligned} U_{11} &= \overline{V} + \Delta V cos\beta \\ U_{22} &= \overline{V} - \Delta V cos\beta \\ U_{12} &= -\Delta V sin\beta \end{aligned} \tag{1.46}$$

Insert the values obtained for $cos\beta$ and $sin\beta$ by the maximization procedure, one can finally obtain

$$\begin{aligned} U_{11} &= \overline{V} + \Delta V \cdot \Delta R / \sqrt{(\Delta R)^2 + R_{12}^2} \\ U_{22} &= \overline{V} - \Delta V \cdot \Delta R / \sqrt{(\Delta R)^2 + R_{12}^2} \\ U_{12} &= -\Delta V \cdot R_{12} / \sqrt{(\Delta R)^2 + R_{12}^2} \end{aligned} \tag{1.47}$$

This approximate diabatization scheme is employed to obtain the diabatic potential energy surface of N_3 at one conical intersection in chapter 4.

1.3 Constrained Least Square Fitting

In the construction of potential energy surfaces, the least square fitting method is usually employed in determining the coefficients of potential functions. In general the normal fitting would be enough for generating PESs, but in our special local fitting at conical intersection regions for N_3 molecule PESs, a constrained least square fitting is needed. It turns out this constrained fitting is not trivial; however, in mathematics it is a well defined problem with standard procedure for solution. We will introduce this standard solution taken from reference.[16]

Let E be an $m_2 \times n$ matrix, f an m_2-vector, G an $m \times n$ matrix, and h an m-vector. The least squares problem with linear inequality constraints will be stated as follows:

Problem 1.1 (LSI)**.** *Minimize* $\|Ex - f\|$ *subject to* $Gx \geq h$.

This is the general case for the constrained problem. There are also some important special cases, namely the NNLS (Nonnegative Least Squares) and the LDP (Least Distance Programming) problem, whose solution will finally lead to the solution of general LSI problem.

Problem 1.2 (NNLS)**.** *Minimize* $\|Ex - f\|$ *subject to* $x \geq 0$.

Problem 1.3 (LDP)**.** *Minimize* $\|x\|$ *subject to* $Gx \geq h$.

In order to better understand these problems, first we need to look at the conditions characterizing a solution for Problem LSI. Accordring to Lawson and Hanson,[16] it is subject to the Kuhn-Tucker theroem.

Theorem 1.1 (Kuhn-Tucker Conditions for Problem LSI)**.** *An n-vector $\hat{x}$ is a solution for Problem LSI if and only if there exists an m-vector $\hat{y}$ and a partitioning of the intergers 1 through m into subsets $\mathscr{E}$ and $\mathscr{S}$ such that*

$$G^T\hat{y} = E^T(E\hat{x} - f) \tag{1.48}$$

$$\hat{r}_i = 0 \quad for \quad i \in \mathscr{E}, \quad \hat{r} > 0 \quad for \quad i \in \mathscr{S} \tag{1.49}$$

$$\hat{y}_i \geq 0 \quad for \quad i \in \mathscr{E}, \quad \hat{y} = 0 \quad for \quad i \in \mathscr{S} \tag{1.50}$$

where

$$\hat{r} = G\hat{x} - h \tag{1.51}$$

The interpretation of this theorem is as follows. Denote g_i^T as the ith row vector of the matrix G. The ith constrint, $g_i^T x \geq h_i$, defines a feasible halfspace, $x : g_i^T x \geq h_i$. The vector g_i is orthogonal to the bounding hyperplane of this halfspace and is directed into the feasible halfspace. The point $\hat{x}$ is interior to the halfspaces indexed in $\mathscr{S}$ and on the boundary of the halfspaces indexed $\mathscr{E}$.

The vector $p = E^T(E\hat{x} - f)$ is the gradient vector of $\phi(x) = \|Ex - f\|^2/2$ at $x = \hat{x}$. Since $\hat{y}_i = 0$ for $i \notin \mathscr{E}$. Equation 1.48 can be written as

$$\sum_{i \in \mathscr{E}} \hat{y}_i(-g_i) = -p \tag{1.52}$$

which states that the negative gradient vector of ϕ at $\hat{x}$ is expressible as a nonnegative ($\hat{y}_i \geq 0$) linear combination of outward-pointing normals ($-g_i$) to the constraint hyperplanes on which $\hat{x}$ lies ($i \in \mathscr{E}$). Geometrically this means that the negative gradient vector $-p$ lies in the convex cone based at the point $\hat{x}$ and generated by the outward-pointing normals $-g_i$.

Any perturbation u of $\hat{x}$ such that $\hat{x} + u$ remains feasible must satisfy $u^T g_i \geq 0$ for all $i \in \mathscr{E}$. Multiplying both sides of equation 1.52 by such a vector u^T and using the fact that the $\hat{y}_i \geq 0$, it follows that u also satisfies $u^T p \geq 0$. From the identity $\phi(\hat{x} + u) = \phi(\hat{x}) + u^T p + \|Eu\|^2/2$, it follows that no feasible perturbation of $\hat{x}$ can reduce the value of ϕ. The vector $\hat{y}$ (or the negative of this vector) which occurs in the Kuhn-Tucker theorem is sometimes called the *dual* vector for the problem.

Second we will give the solution for Problem NNLS, the algorithm is as follows.[16]

Suppose we are initially given the $m_2 \times n$ matrix E, the itegers m_2 and n, and the m_2-vector f. The n-vector w and z porvide working space. Index sets $\mathscr{P}$ and $\mathscr{Z}$ will be defined and modified in the course of execution of the algorithm. Variables indexed in the set $\mathscr{Z}$ will be held at the value zero. Variables indexed in the set $\mathscr{P}$ will be free to take values different from zero. If usch a variable takes a nonpositive value, the algorithm will either move the varible to a positive value or else set the variable to zero and move its index from set $\mathscr{P}$ to set $\mathscr{Z}$. At the termination of the algorithm, x will be the solution vector and w will be the dual vector.

Algorithm 1.1 (NNLS$(E, m_2, n, f, x, w, z, \mathscr{P}, \mathscr{Z})$)**.**

Step	Description
1	Set $\mathscr{P}$:=NULL, $\mathscr{Z} := 1, 2, \ldots, n$, and x:=0.
2	Compute the n-vector $w := E^T(f - Ex)$.
3	If the set $\mathscr{Z}$ is empty or if $w_j \leq 0$ for all $j \in \mathscr{Z}$, go to Step 12.
4	Find an index $t \in \mathscr{Z}$ such that $w_t = max w_j : j \in \mathscr{Z}$.
5	Move the index t from set $\mathscr{Z}$ to $\mathscr{P}$.
6	Let $E_{\mathscr{P}}$ denote the $m_2 \times n$ matrix defined by Column j of $E_{\mathscr{P}} := \begin{cases} column j of E & if j \in \mathscr{P} \\ 0 & if j \in \mathscr{Z} \end{cases}$ Compute the n-vector z as a solution of the least squares problem $E_{\mathscr{P}} z \cong f$. Note that only the components $z_j, j \in \mathscr{P}$, are determined by this problem. Define $z_j := 0$ for $j \in \mathscr{Z}$.
7	If $z_j > 0$ for all $j \in \mathscr{P}$, set $x := z$ and go to Step 2.
8	Find an index $q \in \mathscr{P}$ such that $x_q/(x_q - z_q) = min x_j/(x_j - z_j) : z_j \leq 0, j \in \mathscr{P}$.
9	Set $\alpha := x_q/(x_q - z_q)$.
10	Set $x := x + \alpha(z - x)$.
11	Move from set $\mathscr{P}$ to set $\mathscr{Z}$ all indices $j \in \mathscr{P}$ for which $x_j = 0$. Go to Step 6.
12	The computation is completed.

On termination the solution vectro x satisfies

$$x_j > 0 \qquad j \in \mathscr{P} \tag{1.53}$$

$$x_j = 0 \qquad j \in \mathscr{Z} \tag{1.54}$$

and is a solution vector for the least squares problem

$$E_{\mathscr{P}} x \cong f \tag{1.55}$$

The dual vector w satisfies

$$w_j = 0 \qquad j \in \mathscr{P} \tag{1.56}$$

$$w_j \leq 0 \qquad j \in \mathscr{Z} \tag{1.57}$$

and

$$w = E^T(f - Ex) \tag{1.58}$$

Equation (1.53), (1.54), (1.56), (1.57), and (1.58) constitute the Kuhn-Tucker conditions characterizing a solution vector x for Problem NNLS. Equation 1.55 is a consequence of equation 1.54, 1.56, and 1.58.

This NNLS algorithm may be regarded as consisting of a main loop, Loop A, and an inner loop, Loop B. Loop B consists of Steps 6-11 and has a single entry point at Step 6 and a single exit point at Step 7. Loop A consists of Steps 2-5 and Loop B. Loop A begins at Step 2 and exits from Step 3.

At Step 2 of Loop A the set $\mathscr{P}$ identifies the components of the current vector x that are positive. The components of x indexed in $\mathscr{Z}$ are zero at this point. In Loop A the index t selected at Step 4 selects a coefficient not presently in set $\mathscr{P}$ that will be positive if introduced into the solution. This coefficient is brought into the tentative solution vector z at Step 6 in Loop B. If all other components of z indexed in set $\mathscr{P}$ remain positive, then at Step 7 the algorithm sets $x := z$ and returns to the beginning of Loop A. In this process set $\mathscr{P}$ is augmented and set $\mathscr{Z}$ is diminished by the transfer of the index t.

In many examples this sequence of events simply repeats with the addition of one more positive coefficient on each iteration of Loop A until the termination test at Step 3 is eventually satified. However, if some coefficient indexed in set $\mathscr{P}$ becomes zero or negative in the vector z at Step 6, then Step 7 causes the algorithm to remain in Loop B performing a move that replaces x by $x + \alpha(z - x), 0 < \alpha \leq 1$, where α

is chosen as large as possible subject to keeping the new x nonnegative. Loop B is repeated until it eventually exits successfully at Step 7.

Since all operations within Loop B are well defined, at least one more index, the index called q at that point, is removed from set $\mathscr{P}$ each time Step 11 is executed, while z_t is always positive. Thus exit from Loop B at Step 7 must occur after not more than $\pi - 1$ iterations within Loop B, where π denotes the number of indices in set $\mathscr{P}$ when Loop B was entered. In practice Loop B usually exits immediately on reaching Step 7 and does not reach Step 8-11 at all.

Also, note that the residual norm function

$$\rho(x) = \|f - Ex\| \tag{1.59}$$

has a strictly smaller value each time Step 2 is reached and thus that at Step 2 the vector x and its assoicated set $\mathscr{P} = i : x_i > 0$ are distinct from all previous instances of x and $\mathscr{P}$ at Step 2. Since $\mathscr{P}$ is a subset of the set $1, 2, \ldots, n$ and there are only a finite number of such subsets, Loop A must terminate after a finite number of iterations. Typically loop A required about $n/2$ iterations.

Now we will move to the problem LDP. The solution vector for Problem LDP can be obtained by an appropriate normalization of the residual vector in a related NNLS Problem. This method of solving Problem LDP and its verification was made by Alan Cline.[16]

Suppose we are given the $m \times n$ matrix G, the integers m and n, and the m-vector h. If the inequalities $Gx \geq h$ are compatible, then the algorithm will set logical variable $\phi = TRUE$ and compute the vector $\hat{x}$ of minimal norm satisfying these inequalities. If the inequalities are incompatible, the algorithm will set $\phi = FALSE$ and no value will be assigned to $\hat{x}$.

Algorithm 1.2 (LDP$(G, m, n, h, \hat{x}, \phi)$)**.**

Step	Description
1	Define the $(n+1) \times m$ matrix E and the $(n+1)$-vector f as $E := [G : h]^T$ and $f := [\overbrace{0, \ldots, 0}^{n}, 1]^T$. Use Algorithm NNLS to compute an m-vector $\hat{u}$ solving Problem NNLS: Minimize $\|Eu - f\|$ subject to $u \geq 0$.
2	Compute the $(n+1)$-vector $r := E\hat{u} - f$.
3	If $\|r\| = 0$, set $\phi := FALSE$ and go to Step 6.
4	Set $\phi := TRUE$.
5	For $j := 1, \ldots, n$, compute $\hat{x}_j := -r_j / r_{n+1}$.
6	The computation is completed.

The validity of Algorithm LDP can be shown as follows. First consider the Problem NNLS, which is solved in Step 1 of Algorithm LDP. The gradient vector for the objective function $\|Eu - f\|^2/2$ at the solution point $\hat{u}$ is

$$p = E^T r \tag{1.60}$$

From the Kuhn-Tucker conditions for this Problem NNLS there exist disjoint index sets $\mathscr{E}$ and $\mathscr{S}$ such that

$$\mathscr{E} \cup \mathscr{S} = 1, 2, \ldots, m \tag{1.61}$$

$$\hat{u}_i = 0 \,\text{for}\, i \in \mathscr{E}, \qquad \hat{u}_i > 0 \,\text{for}\, i \in \mathscr{S} \tag{1.62}$$

and

$$p_i \geq 0 \,\text{for}\, i \in \mathscr{E}, \qquad p_i = 0 \,\text{for}\, i \in \mathscr{S} \tag{1.63}$$

Using equation 1.60 to 1.63 we obtain

$$\begin{aligned} \|r\|^2 &= r^T r = r^T[E\hat{u} - f] \\ &= p^T\hat{u} - r_{n+1} = -r_{n+1} \end{aligned} \tag{1.64}$$

Consider the case in which $\|r\| > 0$ at Step 3. From equation 1.64 this implies that $r_{n+1} < 0$, so division by r_{n+1} at Step 5 is valid. Using equation 1.63 and the equations of Steps 2 and 5, we establish the feasibility of $\hat{x}$ as follows:

$$\begin{aligned} 0 \leq p &= E^T r \\ &= [G : h] \begin{bmatrix} \hat{x} \\ -1 \end{bmatrix} (-r_{n+1}) \\ &= (G\hat{x} - h)\|r\|^2 \end{aligned} \tag{1.65}$$

Therefore,

$$G\hat{x} \geq h \tag{1.66}$$

From equation 1.63 and 1.65 it follows that the rows of the system of inequalities of equation 1.66 indexed in set $\mathscr{S}$ are satisfied with equality. The gradient vector for the objective function $\|x\|\|^2/2$ of Problem LDP is simply x. The Kuhn-Tucker conditions for $\hat{x}$ to minimize $\|x\|^2/2$ subject to $Gx \geq h$ require that the gradient vector $\hat{x}$ must be representable as a nonnegative linear combination of the rows of G that are associated with equality conditions in equation 1.66, the rows of G indexed in set $\mathscr{S}$.

From Steps 2 and 5 and equaiton 1.64 we have

$$\hat{x} = \begin{bmatrix} r_1 \\ . \\ . \\ . \\ r_n \end{bmatrix} (-r_{n+1})^{-1} = G^T \hat{u}(-r_{n+1})^{-1} = G^T \hat{u} \|r\|^{-2} \tag{1.67}$$

Noting the sign coniditons on $\hat{u}$ given in equation 1.62 completes the proof that $\hat{x}$ is a solution of Problem LDP.

If $\tilde{x}$ is a different solution vector, then $\|\tilde{x}\| = \|\hat{x}\|$ and the vector $\bar{x} = (\tilde{x} + \hat{x})/2$ would be a feasible vector having a strictly smaller norm than $\hat{x}$, which contradicts the fact that $\hat{x}$ is a feasible vector of minimum norm. Thus, it is clearly the solutin vector is unique.

Now consider the case of $\|r\| = 0$ at Step 3. It can be shown that the inequalities $Gx \geq h$ are inconsistent. Assume the contrary, that there exists a vector $\tilde{x}$ satisfying $G\tilde{x} \geq h$. Define

$$q = G\tilde{x} - h = [G : h] \begin{bmatrix} \hat{x} \\ -1 \end{bmatrix} \geq 0 \tag{1.68}$$

Then

$$0 = [\tilde{x}^T : -1]r = [\tilde{x}^T : -1] \left\{ \begin{bmatrix} \hat{x} \\ -1 \end{bmatrix} \hat{u} - f \right\} = q^T \hat{u} + 1 \tag{1.69}$$

This last expression cannot be zero, however, because $q \geq 0$ and $\hat{u} \geq 0$. From this contradiction we conclude that the condition $\|r\| = 0$ implies the inconsistency of the system $Gx \geq h$. This completes the mathematical verification of Algorithm LDP.

At this point the two special cases of constrained fitting Problem NNLS and Problem LDP have been solved. This is essential since the general solution for Problem LSI can be achieved by converting the Problem LSI to Problem LDP.[16] Consider Problem

LSI with the $m_2 \times n$ matrix E being of rank n. In various ways, such as single value decomposition, one can obtain an orthogonal decomposition of the matrix E:

$$E = Q \begin{bmatrix} R & 0 \\ 0 & 0 \end{bmatrix} K^T \equiv [\underbrace{Q_1}_{n} : \underbrace{Q_2}_{m_2-n}] \begin{bmatrix} R \\ 0 \end{bmatrix} K^T \tag{1.70}$$

where Q is $m_2 \times m_2$ orthogonal, K is $n \times n$ orthogonal, and R is $n \times n$ nonsingular. Furthermore, the matrix R can be obtained in triangular or diagonal form. Then we have an orthogonal change of variables

$$x = Ky \tag{1.71}$$

The objective function to be minimized in Problem LSI can then be written as

$$\begin{aligned} \phi(x) = \|f - Ex\|^2 &= \| \begin{bmatrix} Q_1^T f \\ Q_2^T f \end{bmatrix} - \begin{bmatrix} Ry \\ 0 \end{bmatrix} \|^2 \\ &= \|\tilde{f}_1 - Ry\|^2 + \|\tilde{f}_2\|^2 \end{aligned} \tag{1.72}$$

where

$$\tilde{f}_i = Q_i^T f \qquad i = 1, 2 \tag{1.73}$$

With a further change of variables,

$$z = Ry - \tilde{f}_1 \tag{1.74}$$

we may write

$$\phi(x) = \|z\|^2 + \|\tilde{f}_2\|^2 \tag{1.75}$$

The original problem LSI of minimizing $\|f - Ex\|$ subject to $Gx \geq h$ is thus equivalent, except for the additive constant $\|\tilde{f}_2\|^2$ in the objective function, to the

following Problem LDP:

$$\text{Minimize} \quad \|z\| \quad \text{subject to} \quad GKR^{-1}z \geq h - GKR^{-1}\tilde{f}_1 \tag{1.76}$$

If a vector $\hat{z}$ is computed as a solution of this Problem LDP, then a solution vector $\hat{x}$ for the original Problem LSI can be computed from equation 1.74 and 1.71. The squared residual vector norm for the original problem can be computed from equation 1.75. This finalize the solution of general LSI Problem, and we will use this method in our constrained fitting in the construction of potential energy surfaces in chapter 4.

References

1. KOGA, N.; MOROKUMA, K. *CHEMICAL PHYSICS LETTERS* **1985**, *119*, 371–374.

2. MANAA, M.; YARKONY, D. *JOURNAL OF CHEMICAL PHYSICS* **1993**, *99*, 5251–5256.

3. YARKONY, D. *JOURNAL OF PHYSICAL CHEMISTRY* **1993**, *97*, 4407–4412.

4. RAGAZOS, I.; ROBB, M.; BERNARDI, F.; OLIVUCCI, M. *CHEMICAL PHYSICS LETTERS* **1992**, *197*, 217–223.

5. KUNTZ, P.; WHITTON, W. *JOURNAL OF CHEMICAL PHYSICS* **1991**, *95*, 5149–5158.

6. BEARPARK, M.; ROBB, M.; SCHLEGEL, H. *CHEMICAL PHYSICS LETTERS* **1994**, *223*, 269–274.

7. SMITH, F. *PHYSICAL REVIEW* **1969**, *179*, 111–&.

8. HAN, S.; HETTEMA, H.; YARKONY, D. *JOURNAL OF CHEMICAL PHYSICS* **1995**, *102*, 1955–1964.

9. MEAD, C.; TRUHLAR, D. *JOURNAL OF CHEMICAL PHYSICS* **1982**, *77*, 6090–6098.

10. RUEDENBERG, K.; ATCHITY, G. *JOURNAL OF CHEMICAL PHYSICS* **1993**, *99*, 3799–3803.

11. Atchity, G.; Ruedenberg, K. *THEORETICAL CHEMISTRY ACCOUNTS* **1997**, *97*, 47–58.

12. WERNER, H.; FOLLMEG, B.; ALEXANDER, M. *JOURNAL OF CHEMICAL PHYSICS* **1988**, *89*, 3139–3151.

13. PACHER, T.; CEDERBAUM, L.; KOPPEL, H. *JOURNAL OF CHEMICAL PHYSICS* **1988**, *89*, 7367–7381.

14. HIRSCH, G.; BUENKER, R.; PETRONGOLO, C. *MOLECULAR PHYSICS* **1990**, *70*, 835–848.

15. PACHER, T.; KOPPEL, H.; CEDERBAUM, L. *JOURNAL OF CHEMICAL PHYSICS* **1991**, *95*, 6668–6680.

16. Lawson, C. L.; Hanson, R. J. *Solving Least Squares Problems*; 1974.

Chapter 2. Ab initio study of the photodissociation of HN_3

2.1 Introduction

While an enormous number of all-nitrogen species have been predicted theoretically,[1,2,3,4] there are to date only five allotropes of Nitrogen that have been identified experimentally three of which are N_2, N_3 and N_3^-. One of the fundamental barriers to exploring the full diversity of all-nitrogen molecules is their near pathological resistance to ring formation. Experimental schemes that could demonstrate ring formation would provide new possibilities to the expansion of this intriguing field of chemistry. For some time, it has been proposed that cyclic N species might be produced from suitable photochemical precursors. Several recent experiments provide evidence that the UV photolysis of ClN_3 leads efficiently to the simplest cyclic all-nitrogen allotrope, cyclic-N_3.[5,6,7,8]

These results stand, however, in stark contrast to the paucity of theoretical studies on ClN_3 photochemistry and consequently, the photochemical mechanism remains unclear by which ClN_3 with a nearly linear-N_3 moiety may undergo ring-closure. In the hopes of perhaps finding another example of photochemical production of cyclic-N_3 and more importantly one where high-level quantum chemical methods could be used to guide our analysis of the microscopic reaction mechanism, we undertook the study of the photochemistry of hydrazoic acid, HN_3, the simplest member of the XN_3 family.

The UV photochemistry of HN_3 (especially in its first excited singlet state, S_1, possessing A'' symmetry) has attracted much attention; one might even refer to it as a benchmark system for the study of polyatomic ultraviolet photochemical dynamics.

All four of the products of HN_3 photolysis:

$$HN_3 \longrightarrow H + N_3 \qquad \text{Channel(1)}$$
$$HN_3 \longrightarrow NH(a^1\Delta) + N_2 \qquad \text{Channel(2)}$$

are suitable for efficient detection by optical means, thus the reaction has been studied with several quantum-state resolved methods.[9,10,11,12,13,14,15,16,17,18]

It is noteworthy that the possible formation of cyclic-N_3 in HN_3 photochemistry has never been the focus of any of these many high quality studies. Channel (2), which dominates at photolysis wavelengths where branching ratios have been measured,[15] has attracted much of the attention. Of those experiments focused on channel (1), most used photolysis wavelengths where cyclic-N_3 was not energetically accessible, $\lambda > 244$ nm, or employed methods that would not reveal the production of this molecule.

The H-atom Rydberg Time-of-Flight (HRTOF) method is one of the few possible means by which the formation of cyclic-N_3 in HN_3 photolysis might be observed and studied and it has already proven useful in understanding the dynamics of channel (1).[12,18] Cook et al. reported HRTOF results for photolysis wavelengths between 240 and 280 nm, providing comprehensive characterization of the energy release to photoproducts after excitation to the S_1 state.[12] Zhang et al. are the only to report HRTOF results on HN_3 at shorter photolysis wavelengths; they carried out photolysis experiments at 248 and 193 nm.[18] While these results do not reveal the full nature of the wavelength dependence of channel (1), photolysis at 193 nm clearly leads to more internally excited N_3 molecules than at 248 nm.

Theoretical investigations on HN_3, especially for its electronic excited states, are limited. To interpret the vacuum-ultraviolet (VUV) absorption spectrum, Schönnenbeck et al. calculated the vertical excitation energies for several valence and Rydberg excited states by means of the muliconfiguration coupled electron-pair approach (MC-

CEPA) with valence quadruple-zeta quality basis set.[17] Excellent agreement with experiment was achieved in their calculations. As for the dissociation dynamics, Alexander et al.[9,19] and Yarkony[20] performed MCSCF and MRCI calculations to study the spin-forbidden decomposition process on the ground state (S_0). The minima of seam-of-crossing between the S_0 and lowest triplet state (T_1) is located at ~47.2 kcal/mol[21] above the global minimum, and the spin-orbit coupling investigations combined with the one dimensional Landau-Zerner model indicated that the spin-forbidden process will be significant only near threshold.[20] Regarding the photodissociation on the first singlet excited state (S_1), Meier and Staemmler scanned the PESs of the low-lying excited states along N_2-N_3 coordinate as well as the product angular dependence[22] using CASSCF and valence CI (configuration interaction) methods. They concluded that the dissociation to NH($a^1\Delta$) is a barrierless process on the $1^2A''(S_1)$ state with much of the rotational excitation on the N_2 fragment. A more quantitative results was reported recently by Fang[23] with the CASSCF(8e/7o)/cc-pVDZ calculations, where a small barrier of 0.2 kcal/mol was characterized at CASPT2(8e/7o)/cc-pVTZ level of theory. Both of these results agreed well with the direct dissociation mechanism deduced from experiments by Chu et al.[11] and Hawley et al.[24] As for the decomposition into linear N_3 fragment, a high barrier of 41.3 kcal/mol was also reported in Fangs study.[23] Most recently, two-dimensional quantum mechanic wavepacket simulations of the $\tilde{A}$ state dissociation dynamics have been carried out on a couple of two-dimensional cuts through the full six-dimensional PES.[25] The fragmentation to the linear N_3 product was found in low bending vibrational states, which is in good accord with the H atom time-of-flight spectrum from the HN_3 photolysis.[12] This simulation was limited in the planar configuration, the out-of-plane motion during the fragmentation will, however, influence the bending vibrational state population of the linear N_3 product. In addition to the N_3 fragmentation dynamics, the competition channel leading to the NH($a^1\Delta$) product was also examined, and the excitation of the

N-H stretching motion will encourage the N-H bond fission.[12] This work produced no evidence of cyclic-N_3 formation despite the fact that some of the reported photolysis wavelengths surpassed its energetic formation threshold.

Most recently, Wodtke et al. have made a systematic and careful study of the wavelength dependence of the energy release dynamics in channel (1) using the HRTOF method, spanning the range of photolysis wavelengths between 280 and 188 nm in roughly 5 nm steps.[26] These results showed the onset of a low-translational-energy, H-atom producing channel that grows in importance above $\sim$5.6 eV. The translational energy release is consistent with known thermodynamics for formation of cyclic-N_3. No previous theoretical study has been reported on the possible ring closure pathway. In light of this very interesting experiment, we performed high level ab initio quantum calculations to study the ground and excited potential energy surfaces to try to gain deep insights into the interesting photochemical process.

2.2 Methodology

Geometries of potential energy minima and transition states were optimized using the analytical gradient at the state-specific (ss)-CASSCF (complete active space self-consistent field) level.[27] In ss-CASSCF calculations, the full valence active space, (16e/13o), consisting of 16 electrons in 13 molecular orbitals, was used with the cc-pVTZ (denoted as VTZ), Dunnings correlation consistent polarized valence triple-zeta basis set.[28] The Hessian matrix, vibrational frequencies and the zero point energy (ZPE) were calculated by numerical differentiation of the energy gradient at the same ss-CASSCF/VTZ level as in geometry optimization. Minima on the seam of crossing (MSX) were located also using the analytical gradient at both the same ss-CASSCF level and two state-averaged (with equal weight) sa(2)-CASSCF(16e/13o)/VTZ level.

At last, to obtain the better energetics, single point energy characterization was achieved using the internally contracted configuration interaction with single and

double excitations (MRCISD)[29,30] plus multireference version of Davidsons correction (Q)[31,32] with the Dunnings correlation consistent augmented polarized valence triple zeta basis (AVTZ),[28] where a predetermined CASSCF(16e/13o)/AVTZ wave function was selected as the corresponding reference configuration. In the MRCISD(Q) calculation, only the $1s$ orbitals of nitrogen atoms were kept doubly occupied in all configurations and remaining 16 electrons were correlated, denoted as MRCISD(Q)(16e/13o)/AVTZ.

The energies used in the following discussions are relative to the ground state global minimum at the MRCISD(Q)(16e/13o)/AVTZ level based on the ss-CASSCF (16e/13o)/VTZ optimized geometries, unless otherwise noted. We will consider two C_s symmetries; one called "C_s" is used for the structures in which all the atoms are coplanar, and the other called "C_s'" is for the non-planar structures in which the symmetry plane passes through NH bond and bisects the other NN bond. Two types of energy will appear in the discussion. The one in the parentheses is NOT ZPE corrected. ZPE correction has been applied on the other one outside the parentheses. None of the MSX is corrected for ZPE.

MOLPRO 2002.6 and 2006.1[33] was used for all the CASSCF and MRCISD calculations, except that CASSCF spin-orbit coupling calculations were performed by GAMESS-US 2004.[34] Our own SEAM program in conjunction with HONDO 8.5 was employed for the MSX search.[35,36]

2.3 Results and Discussion

The optimized stationary points on the ground and excited states are given in Figure 2.1 and their energies are listed in the Table 2.1. The corresponding potential energy profiles describing the associated transformation and dissociation are shown in Figures 2.2, 2.3 and 2.4 for S_0, S_1, and S_2 states, respectively.

2.3.1 Stationary points on the ground and excited states

(1) Stationary points on S_0 potential energy surface

The ground state global minimum of HN_3 was known from the microwave spectrum.[37] The optimized geometry using current ss-CASSCF method, S_0_C_s_LM1, agrees reasonably well with the experiment value. The largest deviations are from the H-N_3 and N_2-N_3 bond lengths, which are all about 0.01 Å longer than the experimental values. The NNN fragment is almost linear, 171.6°, which is only 0.3° larger than the experimental value. The migration of H atom between the two terminal N atoms will form a symmetric double well on the PES separated by a high energy, 86.59 (90.06) kcal/mol, migration transition state (TS), S_0_C_{2v}_TS1, located in the midpoint of this coordinate being of C_{2v} symmetry. Vibrational analysis shows that it has only one imaginary frequency ($461.4i$ cm^{-1}, b_2), which is clearly associated with the in-plane H migration motion. Intrinsic reaction coordinate (IRC) calculations verify this transformation.

Besides this global minimum, two other local minima are located on the S_0 state. One is of C_{2v} symmetry, S_0_C_{2v}_LM2, with the H atom attached to the middle N_3 atom. The energy of this species is very high, 82.62 (83.31) kcal/mol above the planar C_s global minimum. No transition state (TS) is found on this H migration process at CASSCF level, but discovered at CCSD(T)/cc-pVTZ level of theory, indicating the dynamic correlation is very crucial in this region. At CCSD(T) level, the TS is only slightly higher than S_0_C_{2v}_LM2. The other minimum, S_0_C_s'_LM3, is a non-planar C_s structure. In this structure, the three N atoms form a cyclic ring with H atom attached to the apex one and being almost perpendicular to the ring. Energetically, it is just 37.69 (38.34) kcal/mol above S_0_C_s_LM1. The existence of this low energy structure is quite interesting due to the possible cyclic N_3 fragmentation product. Therefore, the isomerization process to this local minimum is carefully examined. An isomerization TS, S_0_C_1_TS6, is identified and verified by the frequency and IRC

calculations. The activation energy is determined to be 64.92 (67.90) kcal/mol. This TS is of C_1 symmetry, and the only imaginary frequency (1500.7i cm^{-1}, a'') has mainly the NNN bending motion, which is the driving force to make S_0-C_s-LM1 reach this TS and eventually goes to S_0-C'_s-LM3. As for the S_0-C'_s-LM3 itself, there exists a TS, S_0-C_s-TS7, which connects two equivalent S_0-C'_s-LM3 images, where H atom is on different side of NNN plane in each structure. This TS is in C_s symmetry with energy determined to be 88.20 (90.54) kcal/mol and an imaginary frequency (1411.2i cm^{-1}, a'') corresponded to an out-of-plane motion. Besides these isomerization processes, the transformation between the C_{2v} and C'_s minima are found to go through a non-planar C_s TS, S_0-C'_s-TS5. Frequency calculation indicates it has only one imaginary vibration, 1471.1i cm^{-1} (a'), which is largely associated with the out-of-plane bending and NNN bending motions. The energy requirement for this transformation is fairly high, 61.58 (63.49) kcal/mol relative to the non-planar C_s minimum.

(2) Stationary points on S_1 potential energy surface

There is no experimental information of the S_1 state minimum. A planar C_s minimum with *trans* configuration was determined in previous study.23 Similar structure, S_1-C_s-LM1, is also found in our calculation but slightly different in geometry. The calculated adiabatic energy separation from the S_0 global minimum is 65.60 (67.44) kcal/mol, which is about 5.3 kcal/mol smaller than previous ZPE corrected CASPT2 value. Likely, this value is more accurate because of the better methodology. Besides this *trans* minimum, another planar C_s minimum, S_1-C_s-LM2 being of *cis* configuration, is located on the PES. Energetically, this *cis* minimum is just 1.56 (2.08) kcal/mol higher than the *trans* isomer, and geometrically, these two structures are very similar except the *trans* and *cis* configuration. The isomerization between these two minima is found to go through a planar C_s TS, S_1-C_s-TS2, which is located 34.90 (36.28) kcal/mol above the *trans* configuration. Again, both of the vibrational analysis and IRC calculations confirm this isomerization process. Comparing geome-

tries between this TS and those two minima, one can see that the NNN asymmetric stretching motion is also involved in the reaction coordinate, which is largely the NNN bending motion. In addition, the comparison with Franck-Condon structure indicates that this process could easily occur if the molecule is pumped into the Franck-Condon region on the S_1 state, because the energy separation between the Franck-Condon geometry and either of these two minima is higher than the isomerization barrier, and more importantly, this energy separation is largely accumulated in the isomerization coordinate, which is clearly illustrated by the geometrical difference between the Franck-Condon structure and S_1 state minima. Note that the *cis* minimum was not found in previous reduced CASSCF calculation,[23] implying that the structure on the excited state is very sensitive to the level of correlation.

Similar to the S_0 state, two other minima are found on the S_1 state. The one of C_{2v} symmetry, S_1_C_{2v}_LM3, is located at 51.29 (51.30) kcal/mol above the *trans* minimum, and the symmetry of the electronic wave function is B_1. This C_{2v} minimum is connected to the *trans* minimum through a planar C_s H migration TS, S_1_C_s_TS3, with an activation barrier of 70.91 (74.97) kcal/mol with respective to the *trans* minimum. The position of this TS on the reaction coordinate is more close to the C_{2v} well reflected by the geometrical difference as well as the energetics. Inspecting the IRC and vibrational analysis, one knows that at least three motions, NNN bending, HNN bending and NNN asymmetric stretching, involve in the reaction coordinate. Clearly, the absence of the HNN bending excitation from the Franck-Condon region will block the molecule to visit the C_{2v} minimum although the migration TS is energetically accessible upon the 220 nm excitation. The other minimum, S_1_C'_s_LM4, on the S_1 state is again a non-planar C_s configuration with H atom attached to a cyclic N_3 ring. Compared to its ground state analog, this structure has two shorter symmetric NN bonds, 1.397 vs 1.569 Å, and one longer N-N bond bisected by the symmetry plane, 1.431 vs 1.205 Å. These geometrical changes can be explained from the nature of electronic

excitation. S_1_C_s'_LM4 is formed by promoting an anti-bonding π^* electron, which is located between the apex N atom and two symmetry equivalent N atoms, to another anti-bonding π^* orbital mainly between the two symmetric equivalent N atoms. Energetically, this potential well is situated at 58.04 (57.50) kcal/mol above the *trans* minimum, and a TS, S_1_C_1_TS6, is identified to connect these two regions. Calculations show that this transformation features high activation energy, 66.41 (67.54) kcal/mol, from the *trans* minimum, but the reverse isomerization from the non-planar minimum only needs to surmount a small barrier of 8.89 (9.84) kcal/mol. The driving force for this process is basically the NNN bending motion combined with the HNNN torsion mode provided that the isomerization starts from the planar *trans* minimum. Upon the 220 nm excitation, the molecule would have enough internal energy to pass the S_1_C_1_TS6, and one knows that most of the energy is stored in the N-N stretching and NNN bending modes from previous analysis. Therefore, in principle, the molecule should be able to reach this TS. A similar TS, S_1_C_1_TS7 is also discovered and shown to connect the *cis* minimum and the same non-planar C_s minimum. Energetically, it is 0.83 kcal/mol above the S_1_C_1_TS6 before ZPE correction, and as ZPE correction applied, it becomes 0.07 kcal/mol lower in energy. Again, ring closure through this TS is also possible under 220 nm excitation.

The connection between the *trans* and C_{2v} minima is also examined. These two wells are separated by a planar H migration TS, S_1_C_s_TS3, located at 70.91 (74.97) kcal/mol above the *trans* minimum. Compared to the ring closure TSs, S_1_C_1_TS6 and S_1_C_1_TS7, this TS is only $\sim$4.5 kcal/mol higher in energy, which obviously forms a competitive pathway with ring closure process. However, substantially HNN bending excitation is necessary to push the molecule onto this reaction coordinate. The geometrical differences between Franck-Condon and the minima suggest the absence of the HNN bending excitation on the S_1 state.

(3) Stationary points on S_2 potential energy surface

As for the S_2 state equilibrium geometry, there is neither experimental nor theoretical study before. Similar to S_1 surface, one *trans* minimum, S_2-C_s-LM1, and one *cis* minimum, S_2-C_s-LM2, have been located on S_2 surface. However, unlike the S_1 surface, where *trans* minimum lies lower in energy than the *cis* minimum; the *trans* minimum S_2-C_s-LM1, has energy of 110.05 kcal/mol, which is higher than the *cis* minimum S_2-C_s-LM2 energy 101.01 kcal/mol. Compared to the *trans* and *cis* minimum on S_1 surface, these two minima have shorter middle NN bond but longer terminal NN bond. The middle and terminal NN bond distances of S_2-C_s-LM1 are 1.2944 Å and 1.2908 Å, compared to 1.4660 Å and 1.1881 Å of the *trans* minimum on S_1 surface. While for the *cis* minimum S_2-C_s-LM2, the middle and terminal NN bond distances are 1.3006 Å and 1.2450 Å, relative to 1.4684 Å and 1.1909 Å of the *cis* minimum on S_1 surface. The transition state connecting these two potential well is S_2-C_s-TS5, which is in C_s symmetry and has the energy of 146.4 kcal/mol. The NNN angle in this TS is 179.4, very close to linear, and the NNN in plane bending motion is the driving force for the change from *trans* configuration to *cis* configuration, with the imaginary frequency of $741.1i$ cm^{-1}.

Unlike S_0 and S_1 surface, we did not find a C_{2v} minimum on S_2 surfaces, but we did locate a non-planar C_s' minimum, S_2-C_s-LM3, which has a structure with hydrogen connected to a cyclic N_3 ring and similar to the non-planar C_s' minimum on S_0 and S_1 surface. Again, this non-planar C_s' minimum is very high in energy at 164.82 kcal/mol, about 60 kcal/mol higher than the *trans* and *cis* planar C_s minimum. Compared to its S_1 state analog, this structure has two shorter symmetric NN bonds, 1.368 vs 1.397 Å, and one longer N-N bond bisected by the symmetry plane, 1.621 vs 1.431 Å, and accordingly a larger NNN angle, 72.6° vs 61.6°. Due to the convergence problem and our less interest at high-energy states, we did not make strong effort to find all the stationary points on S_2 potential energy surface. Therefore, no transition states have been located between the two planar C_s minima and this nonplanar C_s'

minimum. However, we expect these TSs would be extremely high in energy and would play any important role in the photodissociation dynamics at excitation at 220 nm.

2.3.2 Adiabatic dissociation on S_0, S_1, and S_2 states

(1) Adiabatic dissociation on S_0 state

The dissociation on these electronic states can in principle produce N_2 + NH($^3\Sigma^-$), N_2 + NH($^1\Delta$), N_3($^2\Pi$) + H and cyclic N_3($^2B_1$) + H. The energetics of these asymptotes are given also in table I. As one see, the calculated singlet-triplet splitting of NH radical, namely 38.48 (38.39) kcal/mol, reasonably reproduces the experimental value from the stimulated emission pumping37 but slightly higher in energy, 2.20 kcal/mol. The calculated bond dissociation energy (BDE) for the ground state spin-forbidden dissociation process [$HN_3(\tilde{X}^1A') \rightarrow N_2(\tilde{X}^1\Sigma_g^+)$ + $NH(\tilde{X}^1\Sigma^-)$] is 10.61 (15.88) kcal/mol, which is in excellent accord with experiment value of 10.76 ± 1.43 kcal/mol.38 The other BDE for the ground state H decomposition [$HN_3(\tilde{X}^1A') \rightarrow$ H(^2S) + $N_3(\tilde{X}^2\Pi_g)$] is computed to be 86.47 (93.75) kcal/mol, which also agrees very well with experimental estimation of 88.3±1.1[14,15] and 91.78±5.02 kcal/mol.[38]

Adiabatically, HN_3 molecule on the S_0 state will correlate to $N_2(\tilde{X}^1\Sigma_g^+)$ + NH($\tilde{a}^1\Delta$) and H(^2S) + $N_3(\tilde{X}^2\Pi_g)$ products. Both of these processes have been well studied theoretically and experimentally. First, for the N-N bond breaking, the activation energies, relative to the dissociation product and determined by Alexander et al.,[19] were 4.15 and 5.00 kcal/mol using selected MRSDCI(Q) and MRACPF methods, respectively, which agreed well with the experimental finding of 4.97±1.43[39] and 3.43 kcal/mol.[40] The corresponding theoretical barriers relative to the S_0 HN_3 global minimum were 53.32 and 50.03 kcal/mol reported also by Alexander et al.[19] and again agreed well with experimental values of ≥50.61[41,42,43] and ≤53.62 kcal/mol.[40] Our calculated results are in general consistent with these findings. The dissociation process is determined to go through a TS, namely S_0_C_s_TS2, featuring the highly stretched

N_2-N_3 bond (2.243 Å) and being of C_s symmetry. S_0_C_s_TS2 is located 50.45 (54.14) kcal/mol from the S_0_C_s_LM1, which corresponds to a small recombination barrier of 1.36 (-0.13) kcal/mol. This small recombination barrier does not agree well with the values mentioned above but is more close to the estimated experimental result of 1.26±0.12 kcal/mol from the temperature dependence of the rate constant for quenching of NH($\tilde{a}^1\Delta$) by N_2.[44] Remember that there is a ∼2.20 kcal/mol overestimation in our calculated singlet-triplet splitting of NH and the BDE for the corresponding process agrees very well experiment. Therefore, it is likely that the recombination barrier is underestimated by that amount. Besides the S_0_C_s_LM1, the other minimum, namely S_0_C'_s_LM3, on the S_0 state can also adiabatically dissociate into the $N_2(\tilde{X}^1\Sigma_g^+)$ + NH($\tilde{a}^1\Delta$) product but with breaking two N-N bonds simultaneously. The corresponding dissociation TS, S_0_C_s_TS3, is identified in the non-planar C_s symmetry with two highly stretched N-N bonds of 2.068 Å. The energy of S_0_C_s_TS3 is just 3.84 (3.10) kcal/mol higher than the dissociation TS of S_0_C_s_TS2, which leads to a higher recombination barrier of 5.20 (2.98) kcal/mol. Note that the small difference in those two recombination reactions will complicate the quenching of NH($\tilde{a}^1\Delta$) by N_2 given that the system has initially higher kinetic energy. The activation barrier from the non-planar minimum S_0_C'_s_LM3 is on the other hand relatively low, 16.60 (18.90) kcal/mol.

The fission of N-H bond from the S_0 planar global minimum was also well understood previously. Our calculations indicate that it is a pure endothermic process, which is consistent with previous theoretical[21,23] and experimental results.[12,14,15] On the other hand, the H fission from the non-planar minimum, S_0_C'_s_LM3, will produce the cyclic N_3 radical. Previous theoretical studies have confirmed the existence of this species and showed that the ground state is B_1 symmetry and lays 30.28 kcal/mol above the linear isomer.[5,8] Our calculations show that this dissociation is also a pure endothermic process.

(2) Adiabatic dissociation on S_1 state

Similar to S_0 state, the adiabatic dissociations on the S_1 state can also occur from both of the planar and non-planar regions. At First, let us look at the dissociations from the planar minima. For the N-N bond breaking, S_1 state will also correlate to the $N_2(\tilde{X}^1\Sigma_g^+)$ + $NH(\tilde{a}^1\Delta)$ asymptote. Starting from the *trans* planar minimum, S_1-C_s-LM1, the decomposition goes through the dissociation TS of S_1-C_s-TS1 with a small barrier of 2.01 (3.42) kcal/mol, which can be expected from the electronic nature of S_1 state and agrees very well with previous studies.[11,23,24,45] Comparing the geometrical difference between S_1-C_s-TS1 and S_1-C_s-LM1, one can see that this is relatively an early TS with the breaking N-N bond stretched from 1.467 to 1.651 Å. In addition, the earlier analysis tells us that there is substantially amount of energy deposited in the N-N stretching mode after the excitation. Therefore, the short S_1 lifetime will be expected if the molecule is pumped into the *trans* minimum region. Similarly, an early TS being of *cis* configuration, S_1-C_s-TS10, is found between the *cis* minimum and the same dissociation product. The activation energy is found also to be small, 1.95 (3.36) kcal/mol, which also leads to the fast dissociation in this region.

The H atom dissociation from this side of PES is also correlated to $H(^2S)$ + $N_3(\tilde{X}^2\Pi_g)$ adiabatically. From the *trans* well, the dissociation is an endothermic process, and no TS is found on the dissociation pathway. On the contrary, a high energy TS is identified between the *cis* well and the asymptote, namely S_1-C_s-TS9. This TS features the highly stretched N-H bond of 1.470 Å, suggesting that it is a late TS. Previous study[23] also found this TS, but it was incorrectly connected to the *trans* minimum. To reach this TS, S_1-C_s-LM3 needs to accumulate 43.97 (48.07) kcal/mol energy in largely the N-H stretching mode; on the other hand, the recombination reaction only needs to prevail a barrier of 24.66 (23.84) kcal/mol. Upon 220 nm excitation or even lower energy at 248 nm, energetically the dissociation from either

of these two minima could occur, but *trans* dissociation would be preferred thanks to the less energy requirement. Comparing the N_3 fragment in the S_1 *trans* minimum, Franck- Condon structure and the linear N_3 dissociation product, one could expect that there would be NNN bending and NNN asymmetric stretching excitations in the product, as observed in the experiment.[14,18] Similarly, if decomposition occurs through S_1_C_s_TS9, the same excitations in the product will be anticipated, which are clearly illustrated by NNN angle (156.3°) and the length of the two N-N bonds (1.248 and 1.188 Å) in the structure of S_1_C_s_TS9.

Secondly, dissociation occurring from the non-planar minimum, S_1_C_s'_LM4, is also examined. For the H atom fission, S_1_C_s'_LM4 will correlate to the excited state ($2A_2$) of cyclic N_3, which is actually a transition state between two rotational equivalent ground state cyclic N_3 ($2B_1$). The dissociation TS, S_1_C_s'_TS12, is also located in the non-planar C_s symmetry with highly stretched dissociating NH bond of 1.337 Å. A barrier of 11.41 (15.4) kcal/mol prevent S_1_C_s'_LM4 from dissociation. Note that S_1_C_s'_TS12 is almost at the same energetic level as ring closure TSs, S_1_C_1_TS6 and S_1_C_1_TS7. Through this process, the cyclic N_3 product could be formed. The NH fission from the C_{2v} minimum is also studied. A planar TS, S_1_C_s_TS13, is found to separate the linear N_3 product from this minimum with a barrier height of 8.3 (12.98) kcal/mol relative to the C_{2v} minimum.

(3) Adiabatic dissociation on S_2 state

Because S_2 state is much higher in energy than S_0 and S_1 state, the adiabatic dissociation from S_2 state also lead to high-energy products. For the N-N bond breaking, S_2 state correlate to the $N_2(\tilde{X}^1\Sigma_g^+)$ + $NH(\tilde{b}^1\Sigma^+)$ asymptote. Unlike the dissociation on S_2 surface with low barriers and early dissociation, the barriers on S_2 are not small at all. The decomposition from the *trans* planar minimum, S_2_C_s_LM1, goes through the dissociation TS of S_2_C_s_TS2 with a barrier of 28.95 kcal/mol. Geometrically, the breaking N-N bond has to stretch from 1.294 Å in the minimum S_2_C_s_LM1 to 1.625

Å in order to reach the S_2_C_s_TS2. Similarly, a TS of *cis* configuration, S_2_C_s_TS4, is found between the *cis* minimum S_2_C_s_LM2 and the same dissociation products. The activation energy is found to be higher in this case, at 39.37 kcal/mol. Apart from the NN stretching mode, the HNN bending mode is also important in this dissociation, since the HNN angle is changed from 135.4° in the *cis* minimum to 98.2° in the *cis* dissociation TS. Compare the *trans* and *cis* minima to the Frank-Condon geometry, the middle NN bond stretching as well as the HNN bending motion are able to be excited. Energetically, those transition states are only a little bit higher in energy than the excitation at 220 nm but could be reached if Frank-Condon excitation to S_2 surface occurs. Therefore, these dissociation channels would play an important role on the S_2 surface photodissociation.

For the H atom dissociation on S_2 surface, the resulted dissociation products are H(^2S) and bended N_3. However, it is not clear at all which state the bended N_3 is in. According to the N_3 C_{2v} potential energy surfaces, the two A' states, A_1 and B_2 are very close in energy at the angle around 109.6°, where a minimum of seam of crossing between A_1 and B_2 is located. At the bended N_3 region with angle between 100 and 120°, there is only one minimum on N_3 A_1 surface but no minimum on N_3 B_2 surface. However, this N_3 ($2A_1$) minimum belongs to the first A' state instead of the second A' state, so it does not correlates to HN_3 S_2 surface adiabatically, which is the second A' state. Therefore, we assign the dissociation of HN_3 to form H and bended N_3 in MSX_A_1/B_2 state. A high energy TS, S_2_C_s_TS1 is identified between the *trans* minimum S_2_C_s_LM1 and the dissociation products. This TS has a strongly stretched N-H bond of 1.697 Å, which indicates that it is a very late TS. The barrier height is 45.58 kcal/mol from S_2_C_s_LM1 to this TS, while the recombination barrier is only about 5.52 kcal/mol. On the other hand, no TS is found on the dissociation pathway from the *trans* well to the dissociation asymptote, which is also an endothermic process. Because these states are very high in energy, they would not

be reachable at the excitation at 220 nm or even if we consider the Frank-Condon excitation to S_2 surface occurs, which requires energy at about 146 kcal/mol.

For the H dissociation from the non-planar C_s' minimum, S_2_C_s'_LM3, the correlation is different from the dissociation from the planar C_s minima. Again, after dissociation, N_3 with cyclic ring structure is formed at excited states. With the symmetry plane bisecting NNN angle, A' state in C_s symmetry corresponds to A_1 and B_1 states in C_{2v} symmetry. Similar to the planar minima dissociation to bended N_3, there is no minimum as second A' state on either N_3 A_1 or B_1 surface. Instead, A_1 and B_1 surfaces cross at the NNN angle of 78.5°, and it is not clear which surface N_3 goes after H fission. Therefore, we assign the dissociation from S_2_C_s'_LM3 to form H and cyclic N_3 in MSX_A_1/B_1 state. The TS for this dissociation pathway has been determined, namely S_2_C_s'_TS6. It is again a late TS, with highly stretched NH bond at the length of 1.639 A. The dissociation barrier is 21.79 kcal/mol while the recombination barrier is only 4.12 kcal/mol, which supports that it is a late TS. Although dissociation from this path will lead to cyclic N_3 MSX_A_1/B_1 state, which may finally goes down to the cyclic N_3 minimum, the S_2_C_s'_TS6 is extremely high in energy and impossible to reach at the experimental condition.

2.3.3 Internal conversion between S_0/S_1 states and S_1/S_2 states

(1) Internal conversion between S_0/S_1 states

The internal conversion between S_1 and S_0 states has been studied by Fang at CAS(8e/7o)/cc-pVDZ level. A minimum on the seam-of-crossing (MSX) being of *trans* configuration and C_s symmetry was located at 6.9 kcal/mol above the N_2-N_3 bond breaking TS. Similar structure, MSX_S_0S_1_1, is also found in our calculation but with slightly different geometry, the longer (∼0.04 Å) N_3-N4 bond length and smaller (∼5.0°) NNN angle. Comparing the geometry between MSX_S_0S_1_1 and S_1_C_s_TS1, one knows that this crossing is located somewhere before the dissociation TS because of the short N_2-N_3 bond, which is largely the dissociation reaction coordination.

However, the longer N_3-N4 bond in this MSX indicates that it stays off this reaction coordination. Therefore, extra energy has to be paid to reach this non-adiabatic interaction zone. The calculations show that it is lying 7.25 kcal/mol above S_1_C_s_TS1 at CASSCF level, and this value becomes 6.45 and 7.63 kcal/mol (for the S_0 and S_1 state, respectively) with the single point MRCISD(Q) calculations, suggesting that the MSX at this level of theory will be slightly different from CASSCF result and its energy will be about 7.0 kcal/mol above the dissociation TS of S_1_C_s_TS1.

Besides the *trans* MSX, another minimum on the seam-of-crossing, MSX_S_0S_1_2, is identified in the vicinity of the *cis* well, S_1_C_s_LM2. Similar to its *trans* analog, this MSX also has stretched N_2-N_3 (1.572 Å) and N_3-N4 (1.320 Å) bonds, indicating it is not located on the minimum energy pathway and the N_3-N4 stretching excitation is necessary to push the molecule to approach this region on the PES. Energetically, MSX_S_0S_1_2 is located 12.84 kcal/mol above the *cis* N_2-N_3 bond breaking TS, S_1_C_s_TS10, at CASSCF level without ZPE correction, and single point MRCISD(Q) computations change the value to 13.92 and 12.87 for the S_0 and S_1 state, respectively, implying that the MSX at this level of theory will be similar to the CASSCF result and energetically will be about 13 kcal/mol above S_1_C_s_TS10.

Energetically, both of these MSXs are accessible upon the excitation shorter than 355 nm wavelength. In addition, we know that NNN bending and N_2-N_3 stretching modes are excited due to the electronic nature of S_1 state and the geometrical difference between Franck-Condon and minima structures. Therefore, the N^3-N^4 stretching excitation will be responsible for the internal conversion (IC) process. Detailed experimental studies at 283 nm 11 and 266 nm47 found that N_2 fragment was formed in the vibrationally ground state with large rotational excitations, which partially suggested that dissociation on the S_0 state via IC is less important. Since in that case some N_2 vibrational excitations would be expected. Our quasi-classical direct dynamics simulations also indicate that the system has less chance to visit this part

of PES.

(2) Internal conversion between S_1/S_2 states

The internal conversion between S_1 and S_2 has also been investigated in this study. A MSX_S_0S_1_1 being of *trans* configuration and C_s symmetry was located. This MSX is very similar to the S_2 state *trans* minimum, S_2_C_s_LM1, with only slight difference in bond lengths and angles. Therefore, the possibility for the molecule to reach this MSX would be significant as HN_3 travels down on the potential energy surface to the *trans* minimum S_2_C_s_LM1 after Frank-Condon excitation. From this CI, HN_3 would be able to hop to S_1 surface if it is excited to S_2 surface. Comparing this MSX to the Frank-Condon geometry, the most interesting features are found to be the elongated terminal N_3N4 bond of 1.294 Å, and highly compressed NNN angle of 102.4°. Therefore, the molecule coming from the Franck-Condon region on the S_2 state will have substantial excitations in these two modes. After hopping from S_2 to S_1 surface, these modes may be crucial to the formation of H connected cyclic N_3 ring structure.

2.3.4 Possible dissociation pathways to the cyclic N_3 formation

The cyclic N_3 is formed only after H dissociated from the HN_3 molecule. In the S_0 state global minimum, N_3 is almost linear. Therefore, as for the formation of cyclic N_3, there should be two distinct pathways in principle. The first one involves an early dissociation of H atom, after which N_3 is at a near linear or bend structure close to the global minimum, and then the NNN bending vibration brings the N_3 to be cyclic. The second mechanism involves a late H dissociation, where a H connected cyclic N_3 ring structure is formed in advance, and the H fission will lead to cyclic N_3 directly. We will discuss both of these two pathways separately.

(1) Early H dissociation on S_2 state

We have to include the N_3 C_{2v} potential energy profile, which is shown in Figure 2.5, to better understand this dissociation pathway. As we can see from N_3 C_{2v} PES, there are 4 lower lying states, with each belongs to one different irrep of C_{2v} group. At the N_3 linear region, where NNN angle is around 180°, A_1 and B_1, A_2 and B_2 state are degenerate, with A_1, B_1 higher in energy than A_2, B_2. As the NNN angle becomes smaller and reaches the bended N_3 region, A_1 and B_1, as well as A_2 and B_2, lose their degeneracy. Meanwhile, the energy of A_1 and B_1 states goes down while the energy of A_2 and B_2 states goes up, so these four states are close in energy at the NNN angle around 110°, and several MSXs are found at this region. As the NNN angle becomes even smaller, these four states become separated in energy again. At the cyclic N_3 region, A_2 and B_1 states are low in energy while A_1 and B_2 states are high in energy. When NNN angle is 60°, A_2 and B_1, A_1 and B_2 are exactly the same in energy and CIs are located there.

Since linear N_3 has to overcome a high barrier to become cyclic N_3, the H dissociation on S_1 will only lead to linear N_3 but not cyclic N_3. Therefore, we assume the early H dissociation at S_2 surface. Previous experiments showed that the molecule begins to be excited to the S_2 ($2^1A'$) state with 220 nm excitation. In addition, the sign change (from negative to position) in the anisotropic parameter in Wodtkes experiment also suggested the perpendicular transition changed to the parallel transition. Theoretically, our calculation shows that Frank- Condon excitation to S_2 surface requires an energy about 146 kcal/mol, which is determined at the MRCISD(Q)/AVTZ level of theory without zero point vibration correction, and a little bit higher than the experimental excitation at 220 nm. However, if zero point vibration is considered, S2 surface could be accessible, thus our assumption of the excitation to S_2 surface should be valid. On the S_2 surface, HN_3 could dissociate to H plus a bended N_3 at MSX_A_1/B_2 as discussed in previous section. Since NNN is almost linear in ground state HN_3, NNN bending mode should be able to be excited after the dissociation

of H. If N_3 goes to A_1 surface, then it could go through a MSX_A_1/B_1, which is about 30 kcal/mol higher than the MSX_A_1/B_2 in energy, to cross to B_1 surface, and finally reaches the cyclic N_3 ground state as the NNN angle becomes smaller. The full picture of this dissociation pathway is shown in Figure 2.6. Of course, after the H dissociation and bended N_3 formation, N_3 may hop to A_2 surface as well, due to the existence of MSX_A_1/A_2 close to the MSX_A_1/B_2. On the A_2 surface, N_3 just need to pass a second order saddle point, which is only slightly higher in energy than MSX_A_1/B_2. This would lead to an even lower pathway for the formation of cyclic N_3 regarding the early H dissociation. This early H dissociation pathway is quite similar to the photodissociation mechanism of ClN_3 at the excitation at 193 nm,

Although this is a possible cyclic N_3 formation pathway, if we look at the energetics more closely, we would conclude that it is energetically unreachable at the photo excitation of 220 nm. First of all, the dissociation TS, S_2_C_s_TS1 is higher in energy than the Frank-Condon structure at S_2 state. Since the NH bond is stretched strongly in this transition state, it is impossible to gain enough energy to excite the NH stretching mode and reach this TS. Second, the dissociation TS is not the highest energy state in the formation pathway, the MSX_A_1/B_1 is about 25 kcal/mold higher in energy and definitely inaccessible. Even if a lower energy path through N_3 A_2 TS is possible, this TS is around the same energy as MSX_A_1/B_1 and would be inaccessible in experiment. Therefore, this possible cyclic N_3 formation pathway I through early H dissociation should be ruled out.

(2) Late H dissociation on S_1 state

As we have shown before, there exist H connected cyclic N_3 structure on all three surfaces. Most probably, the late dissociation would be happen on S_1 surface, which is closest to the experimental energy. However, our assumption is still that HN_3 is excited to S_2 surface at first. Then the molecule travels down from the S_2 potential energy surface and come across the CI between S_2 and S_1 with high

probability. HN_3 hops from S_2 surface to S_1 surface through this CI, with substantial excitations in the NNN bending modes and terminal NN stretching mode. Because these modes are excited, HN_3 may reach the TS S_1-C_1-TS6 from *trans* minimum, or reach S_1-C_1-TS7 from the *cis* minimum, and then come to form the non-planar C_s' minimum S_1-C_s'-LM4, where a H connected cyclic N_3 structure is formed. This minimum further overcomes the TS S_1-C_s'-TS12, and forms cyclic N_3 in the excited A_2 state. Our previous study showed that the cyclic N_3 ($2A_2$) minimum in C_{2v} symmetry is actually a transition state between two rotational equivalent ground state cyclic N_3 ($2B_1$), and there is a conical intersection ($2B_1/2A_2$) in the cyclic N_3 region, through which the excited state cyclic N_3 will quickly move back onto the ground state. Therefore, we can say ground state cyclic N_3 could be formed under this pathway. The full dissociation pathway is shown in Figure 2.7.

Unlike the possible pathway I with early H dissociation where energy is not sufficient for the reaction to occur, all the state in the pathway II with late H dissociation is energetically accessible. Also, after the hopping from S_2 surface to S_1 surface, all the bending modes necessary for the non-planar C_s' minimum S_1-C_s'-LM4 formation should be excited to some extent, that is why our assumption of excitation to S_2 state is crucial in this formation pathway. Although this pathway is energetically accessible, we also notice that the energy is barely enough for the reaction to occur, thus the probability of dissociation leading to cyclic N_3 would be substantially small if it can actually occur in reality.

2.3.5 Quasi-classical molecule dynamics simulation

Photodissociation is essentially a dynamics process. After knowing the static picture of each of the PESs, then the further understanding could be gained from the dynamical simulation of the molecular processes on those PESs, which could be achieved by either classical or quantum methods depending on the nature of the problem.

In the present study, we are interested in providing the photodissocation picture

in a qualitatively ways. We want to know how the photodissociation would occur, what the energy requirements are, and what will contribute in the dissociation as well as their relative importance. Therefore, the quasi-classical molecular dynamics will be enough to fulfill most of these purposes. In our simulations, Newton's equations of motion are integrated in the Cartesian coordinate by means of a second-order Taylor expansion with a step length of 0.15 fs determined from a few tests. The gradient of PES is evaluated on the fly using the state-averaged CASSCF methods (see details in the following discussion).

(1) Direct dynamics on S_1 state

First, let us look at the dissociation process on the S_1 state. At low photon excitation energy, the molecule will be populated in the vicinity of S_1 origin; the N-N bond breaking would be the only energetically accessible process. With the increase of excitation energy, both the N-H fission and non-adiabatic IC channels begin to contribute. Especially, the contribution from later pathways will lead the dissociation on the ground state. Experiments at 266 and 308 nm found that NH($\tilde{a}^1\Delta$) fragments are formed with near-equal populations in the A' and A'' -doublet states,13,47 and our ab initio calculations predict planar dissociation TSs on both of S_1 and S_0 states, which seem to suggest that IC channels have almost the equal contribution as the direct adiabatic processes. However, another experiment46 also showed the N-N-N out-of-plane bending mode is reflected in the NH($\tilde{a}^1\Delta$) fragment rotation, suggesting that dissociation could evolve only on the S_1 state but with a non-planar parent geometry. To answer this question, we simulate the dissociation on the S_1 state by assuming that the molecule is vertically excited to this state from the near-equilibrium geometry of the ground electronic state. Because the calculated vertical excitation energy, 114.9 kcal/mol, at two-state averaged (equal weight) full valence CASSCF(16e/13o)/cc-pVDZ level is comparable to 248 nm excitation, where the ground state global minimum is also re-optimized at that same level. The initial

structures and kinetic energies are sampled by normal mode sampling in the phase space at 0K with only zero point vibrations added under harmonic approximation. Due to the computational cost, we only run 6 trajectories, which in principle lack of the statistical meaning but are effective for the qualitative purpose. In all these trajectories, 5 of them quickly dissociate into NH($\tilde{a}^1\Delta$) within 25 fs, which agrees well the experimentally estimated upper limit of the dissociation time of 17 fs.[15] The other trajectory dissociate into linear N_3 product. The dissociation in this channel starts also early in the simulation, ∼8 fs. The product energy analysis indicates that most of the energy is released as kinetic energy, Etrans= ∼32 kcal/mol, and the internal energy of the N_3 fragment is about 8 kcal/mol. Clearly, these simulations indicate the small contributions from the internal conversion pathways. As for the competition between those two adiabatic dissociation channels, these results are not enough to provide a quantitative ratio albeit 83% of the trajectories lead to the NH($\tilde{a}^1\Delta$) product, which is happen to be consistent with experimental findings.14,15 As for the branching ratio change from 266 to 248 nm, more detailed dynamical simulations are required to answer it.

(2) Direct dynamics on S_2 state

Similar direct trajectory simulations were performed on the S_2. The trajectories started from the the Frank-Condon geometry on S_2 surface with S_0 ZPE added under harmonic approximation. Again, full CAS space, (16e,13o), was adopted, since N 2s orbital should be important in the correlation in the cyclic N_3 region. The trajectories were propagated on the S_2 state with the energy and energy gradient calculated from a three state-averaged CASSCF including S_0, S_1 and S_2. Due to the expensive computational cost, only 13 trajectories were run. If no crossing is allowed to occur, 10 of them dissociate to $N_2(\tilde{X}^1\Sigma_g^+)$ + NH($\tilde{b}^1\Sigma^+$), while the other 3 did not dissociate within 60 fs. Some of these trajectories may involve crossing between S_2 and S_1 surfaces, if we let the crossing occurs by restarting the trajectories following the S_1

state gradient at the crossing point, most of them lead to dissociation to $N_2(\tilde{X}^1\Sigma_g^+)$ + $NH(\tilde{a}^1\Delta)$ finally, with only one trajectory of particular interest dissociate to $H(^2S)$ + $N_3(\tilde{X}^2\Pi_g)$. Therefore, only this trajectory will be presented, shown in Figure 2.8. Since the trajectory was started from the Frank-Condon geometry, the energy goes down at first following the S_2 state gradient. It reaches a barrier at around 38 fs where S_0, S_1 and S_2 all come close in energy but not really cross. At about 56 fs, we can see there is a clear crossing between S_1 and S_2 surfaces. At this geometry, N_3 is a little bit bended. From this point, we propagate the trajectory with S_1 state gradient but keep the velocities of the molecule. Then H dissociates and linear N_3 is formed with some NNN bending motions. In other trajectories where crossing occur, $N_2(\tilde{X}^1\Sigma_g^+)$ + $NH(\tilde{a}^1\Delta)$ are formed finally. Although the NNN bending and terminal NN stretching modes are excited in these trajectories, the middle NN stretching mode is also present. Because on S_1 state, the NN bond breaking has a very early TS and very small barrier, it is not surprised the other trajectories dissociate to NH + N_2. This result implies that the initial conditions are very important for the cyclic N_3 formation. Only under extreme conditions where the excitation of vibrations are only in the middle NN stretching and NNN bending mode might the molecule be able to reach the ring closure TS after the internal conversion from S_2 to S_1, otherwise NH + N_2 will be formed. This again indicates that cyclic N_3 formation is very low in probability and may only be observed by substantial number of trajectories, which is too expensive for our direct dynamics study.

2.4 Summary and Conclusion

In the present study, high level ab initio molecular orbital methods combined with direct quasiclasssical molecular dynamics simulation have been used to study the potential energy surfaces in the photodissociation of HN_3 at 220 nm. Particularly, we paid much attention to the ring closure process in the N_3 fragment followed by the

formation of cyclic-N_3.

On both of the ground (S_0) and excited (S_1 and S_2) states, non-planar minima featured with cyclic N_3 fragment were identified. The ring closure TS on the S_1 state was calculated to be $\sim$ 130.2 kcal/mol above the ground state, which agrees with energy threshold ($\sim$5.6 eV) for the slow channel observed in the recent photodissociation experiment. The competitive H migration pathway is only 4.5 kcal/mol higher in energy, but the absence of the HNN bending excitation makes this pathway less important. The dissociation TS leading to the cyclic N_3 product was discovered and about $\sim$5 kcal/mol above the ring closure TS. Similar ring closure process on the ground state was also identified with a barrier of $\sim$65 kcal/mol.

Two possible cyclic N_3 formation pathways are proposed, namely the early H dissociation on S_2 surface and late H dissociation on S_1 surface. However, the first pathway with early H dissociation is ruled out due to insurfficient excitation energy. The second pathway is energetically accessible but would be still low in probability.

Quasiclassical molecular dynamics simulations on the S_1 state suggested that the fast adiabatic NN bond breaking is the dominant dissociation pathway. The dissociation on the S_0 state via internal conversion has limited contribution due to the lack of terminal NN excitation. The simulation also implied that the ring closure process on the S_1 state does not directly occur also due to the lack of terminal NN bond excitation.

The study of the S_2 state minimum and the molecular dynamics propagated on the S_2 state suggested the ring closure process on the S_1 state involves the initial population on the S_2 state followed by internal conversion to S_1 and finally the ring closure. However, no ring closure process or even the approaching of the ring closure TS was observed in our limited number of trajectories. The reason could be due to the extremely low cyclic N_3 formation probability and insufficient sampling of the initial condition.

References

1. Tobita, M.; Bartlett, R. *JOURNAL OF PHYSICAL CHEMISTRY A* **2001**, *105*, 4107–4113.

2. Bruney, L.; Bledson, T.; Strout, D. *INORGANIC CHEMISTRY* **2003**, *42*, 8117–8120.

3. Strout, D. *JOURNAL OF PHYSICAL CHEMISTRY A* **2004**, *108*, 10911–10916.

4. Wang, L.; Mezey, P. *JOURNAL OF PHYSICAL CHEMISTRY A* **2005**, *109*, 3241–3243.

5. Bittererova, M.; Ostmark, H.; Brinck, T. *JOURNAL OF CHEMICAL PHYSICS* **2002**, *116*, 9740–9748.

6. Babikov, D.; Zhang, P.; Morokuma, K. *JOURNAL OF CHEMICAL PHYSICS* **2004**, *121*, 6743–6749.

7. Babikov, D.; Kendrick, B.; Zhang, P.; Morokuma, K. *JOURNAL OF CHEMICAL PHYSICS* **2005**, *122*, 044315.

8. Zhang, P.; Morokuma, K.; Wodtke, A. *JOURNAL OF CHEMICAL PHYSICS* **2005**, *122*, 014106.

9. ALEXANDER, M.; WERNER, H.; DAGDIGIAN, P. *JOURNAL OF CHEMICAL PHYSICS* **1988**, *89*, 1388–1400.

10. Barnes, R.; Gross, A.; Lock, M.; Sinha, A. *JOURNAL OF PHYSICAL CHEMISTRY A* **1997**, *101*, 6133–6137.

11. CHU, J.; MARCUS, P.; DAGDIGIAN, P. *JOURNAL OF CHEMICAL PHYSICS* **1990**, *93*, 257–267.

12. Cook, P.; Langford, S.; Ashfold, M. *PHYSICAL CHEMISTRY CHEMICAL PHYSICS* **1999**, *1*, 45–55.

13. GERICKE, K.; LOCK, M.; FASOLD, R.; COMES, F. *JOURNAL OF CHEMICAL PHYSICS* **1992**, *96*, 422–432.

14. HAAS, T.; GERICKE, K.; MAUL, C.; COMES, F. *CHEMICAL PHYSICS LETTERS* **1993**, *202*, 108–114.

15. Lock, M.; Gericke, K.; Comes, F. *CHEMICAL PHYSICS* **1996**, *213*, 385–396.

16. ROHRER, F.; STUHL, F. *JOURNAL OF CHEMICAL PHYSICS* **1988**, *88*, 4788–4799.

17. Schonnenbeck, G.; Biehl, H.; Stuhl, F.; Meier, U.; Staemmler, V. *JOURNAL OF CHEMICAL PHYSICS* **1998**, *109*, 2210–2219.

18. Zhang, J.; Xu, K.; Amaral, G. *CHEMICAL PHYSICS LETTERS* **1999**, *299*, 285–290.

19. ALEXANDER, M.; WERNER, H.; HEMMER, T.; KNOWLES, P. *JOURNAL OF CHEMICAL PHYSICS* **1990**, *93*, 3307–3318.

20. YARKONY, D. *JOURNAL OF CHEMICAL PHYSICS* **1990**, *92*, 320–323.

21. ALEXANDER, M.; DAGDIGIAN, P.; WERNER, H. *FARADAY DISCUSSIONS* **1991**, 319–335.

22. MEIER, U.; STAEMMLER, V. *JOURNAL OF PHYSICAL CHEMISTRY* **1991**, *95*, 6111–6117.

23. Fang, W. *JOURNAL OF PHYSICAL CHEMISTRY A* **2000**, *104*, 4045–4050.

24. HAWLEY, M.; BARONAVSKI, A.; NELSON, H. *JOURNAL OF CHEMICAL PHYSICS* **1993**, *99*, 2638–2642.

25. Cook, P.; Jimeno, P.; Ashfold, M.; Balint-Kurti, G.; Dixon, R. *PHYSICAL CHEMISTRY CHEMICAL PHYSICS* **2002**, *4*, 1513–1521.

26. Zhang, J.; Zhang, P.; Chen, Y.; Yuan, K.; Harich, S.; Wang, X.; Wang, Z.; Yang, X.; Morokuma, K.; Wodtke, A. *PHYSICAL CHEMISTRY CHEMICAL PHYSICS* **2006**, *8*, 1690–1696.

27. WERNER, H.; KNOWLES, P. *JOURNAL OF CHEMICAL PHYSICS* **1985**, *82*, 5053–5063.

28. DUNNING, T. *JOURNAL OF CHEMICAL PHYSICS* **1989**, *90*, 1007–1023.

29. KNOWLES, P.; WERNER, H. *CHEMICAL PHYSICS LETTERS* **1988**, *145*, 514–522.

30. WERNER, H.; KNOWLES, P. *JOURNAL OF CHEMICAL PHYSICS* **1988**, *89*, 5803–5814.

31. LANGHOFF, S.; DAVIDSON, E. *INTERNATIONAL JOURNAL OF QUANTUM CHEMISTRY* **1974**, *8*, 61–72.

32. DAVIDSON, E. *JOURNAL OF COMPUTATIONAL PHYSICS* **1975**, *17*, 87–94.

33. Werner, H.-J.; Knowles, P. J.; Lindh, R.; Manby, F. R.; Schütz, M. et al. *MOLPRO, version 2006.1, a package of ab initio programs*, 2006, see http://www.molpro.net.

34. SCHMIDT, M.; BALDRIDGE, K.; BOATZ, J.; ELBERT, S.; GORDON, M.; JENSEN, J.; KOSEKI, S.; MATSUNAGA, N.; NGUYEN, K.; SU, S.; WINDUS, T.; DUPUIS, M.; MONTGOMERY, J. *JOURNAL OF COMPUTATIONAL CHEMISTRY* **1993**, *14*, 1347–1363.

35. Cui, Q.; Morokuma, K.; Stanton, J. *CHEMICAL PHYSICS LETTERS* **1996**, *263*, 46–53.

36. KOGA, N.; MOROKUMA, K. *CHEMICAL PHYSICS LETTERS* **1985**, *119*, 371–374.

37. WINNEWISSER, B. *JOURNAL OF MOLECULAR SPECTROSCOPY* **1980**, *82*, 220–223.

38. PELLERITE, M.; JACKSON, R.; BRAUMAN, J. *JOURNAL OF PHYSICAL CHEMISTRY* **1981**, *85*, 1624–1626.

39. STEPHENSON, J.; CASASSA, M.; KING, D. *JOURNAL OF CHEMICAL PHYSICS* **1988**, *89*, 1378–1387.

40. CASASSA, M.; FOY, B.; STEPHENSON, J.; KING, D. *JOURNAL OF CHEMICAL PHYSICS* **1991**, *94*, 250–261.

41. FOY, B.; CASASSA, M.; STEPHENSON, J.; KING, D. *JOURNAL OF CHEMICAL PHYSICS* **1988**, *89*, 608–609.

42. FOY, B.; CASASSA, M.; STEPHENSON, J.; KING, D. *JOURNAL OF CHEMICAL PHYSICS* **1989**, *90*, 7037–7045.

43. FOY, B.; CASASSA, M.; STEPHENSON, J.; KING, D. *JOURNAL OF CHEMICAL PHYSICS* **1990**, *92*, 2782–2789.

44. NELSON, H.; MCDONALD, J.; ALEXANDER, M. *JOURNAL OF PHYSICAL CHEMISTRY* **1990**, *94*, 3291–3294.

45. GERICKE, K.; HAAS, T.; LOCK, M.; THEINL, R.; COMES, F. *JOURNAL OF PHYSICAL CHEMISTRY* **1991**, *95*, 6104–6111.

Table 2.1: Energies (relative to the ground state planar C_s minimum) of various critical points on the ground state (S_0), first singlet (S_1) and second singlet (S_2) excited states of HN_3 molecule calculated with different ab initio methods.[a]

	Relative Energy (kcal/mol)			ZPE	Nimag;
	CASSCF	MRCISD(Q)	Other work	(kcal/mol)	Frequency ($cm^{-}1$)[b]
S_0_C_s_LM1	-164.1267342	-164.548469		13.11	0
S_0_C_{2v}_LM2	87.00	83.31		12.42	0
S_0_C'_s_LM3	39.27	38.34		12.46	0
S_0_C_{2v}_TS_1	96.10	90.06		9.63	461.4 (b2)
S_0_C_s_TS_2	44.79	54.14	52.5c	9.42	261.9 (a')
S_0_C'_s_TS3	52.92	57.24		10.16	383.8 (a')
S_0_C_s_TS5	110.28	101.83		10.55	1471.1 (a')
S_0_C_s_TS6	71.82	67.90		10.12	1500.7 (a)
S_0_C_s_TS7	97.60	90.54		10.76	1411.2 (a'')
S_1_C_s_LM1	72.53	67.44	71.9c	11.27	0
S_1_C_{2v}_LM2	129.86	118.74		11.26	0
S_1_C_s_LM3	73.79	69.51		10.76	0
S_1_C'_s_LM4	137.56	124.94		11.09	0

Table 2.1 continues

	Relative Energy (kcal/mol)			ZPE	Nimag;
	CASSCF	MRCISD(Q)	Other work	(kcal/mol)	Frequency (cm^-1)[b]
S_1-C_s-TS-1	73.92	70.84	72.1c	9.88	589.8
S_1-C_s-TS-2	109.51	103.71		9.20	905.2
S_1-C_s-TS3	150.80	142.41		7.21	1637.9
S_1-C_1-TS6	145.82	134.78		10.14	944.7
S_1-C_1-TS7	145.73	135.61		9.24	1194.5
S_1-C_1-TS8	137.70	125.26		10.49	656.9
S_1-C_s-TS9	105.53	117.59	113.2c	6.65	1748.4(a')
S_1-C_s-TS-10	75.43	72.87		9.35	661.4 (a')
S_1-C_s-TS-12	147.05	140.34		7.10	2167.5
S_1-C_s-TS-13	139.04	131.72		6.58	1675.2
S_2-C_s-LM1	117.25	103.39		15.83	0
S_2-C_s-LM2	108.21	95.47		15.11	0
S_2-C'_s-LM3	172.02			14.09	0
S_2-C_s-TS-1	162.83	159.95		6.10	1402.8
S_2-C_s-TS-2	146.20	133.89		9.18	3165.3

Table 2.1 continues

	Relative Energy (kcal/mol)			ZPE	Nimag;
	CASSCF	MRCISD(Q)	Other work	(kcal/mol)	Frequency ($cm^{-}1$)[b]
S_2_C_s_TS3	144.38	137.40		8.76	1754.5
S_2_C_s_TS4	147.58	138.88		9.64	1148.2
S_2_C_s_TS5	153.60	135.86		9.84	741.1,635.3
S_2_C'_s_TS6	193.81			7.13	1086.4
N2($\tilde{X}^1\Sigma_g^+$) + NH($\tilde{X}^3\Sigma^-$)	-3.03	15.88	13.4	7.84	0
N2($\tilde{X}^1\Sigma_g^+$) + NH($a^1\Delta$)	42.64	54.27	48.8	7.93	0
N3($\tilde{X}^2\Pi_g$) + H(^2S)	79.70	93.75	85.3	5.84	0
c-N3($^2B_1$) + H(^2S)	115.43	126.08	3.92	0	
HNN($\tilde{X}^2A'$) + N(^4S)	88.03	102.61		7.51	0

[a]The energy of the ground state global minimum is expressed in a.u. For all others, relative energy is measured from that without zero point energy (ZPE) correction.

[b]Zero-point energies and vibrational frequencies are calculated CASSCF(16e/13o)/cc-pVTZ level. Nimag refers to the number of imaginary frequency. When nimag1, it is omitted, and only imaginary frequencies and corresponding symmetries are given.

[c]CASPT2(8e/7o)/cc-pVTZ in Ref.[23]

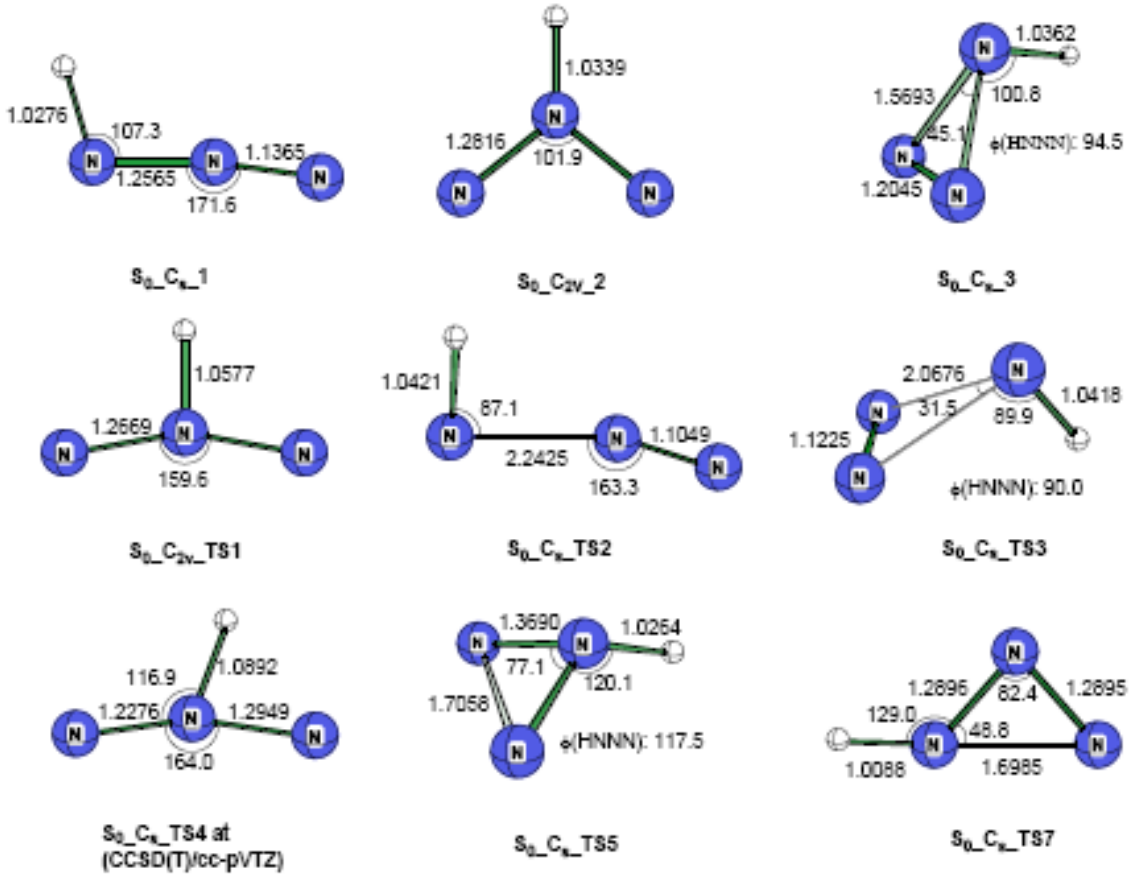

Figure 2.1: CASSCF optimized stationary structures on the S_0, S_1, and S_2 states. Numbers on the structures are bond lengths and bond angles (Å, and Degree).

Figure 1 continues

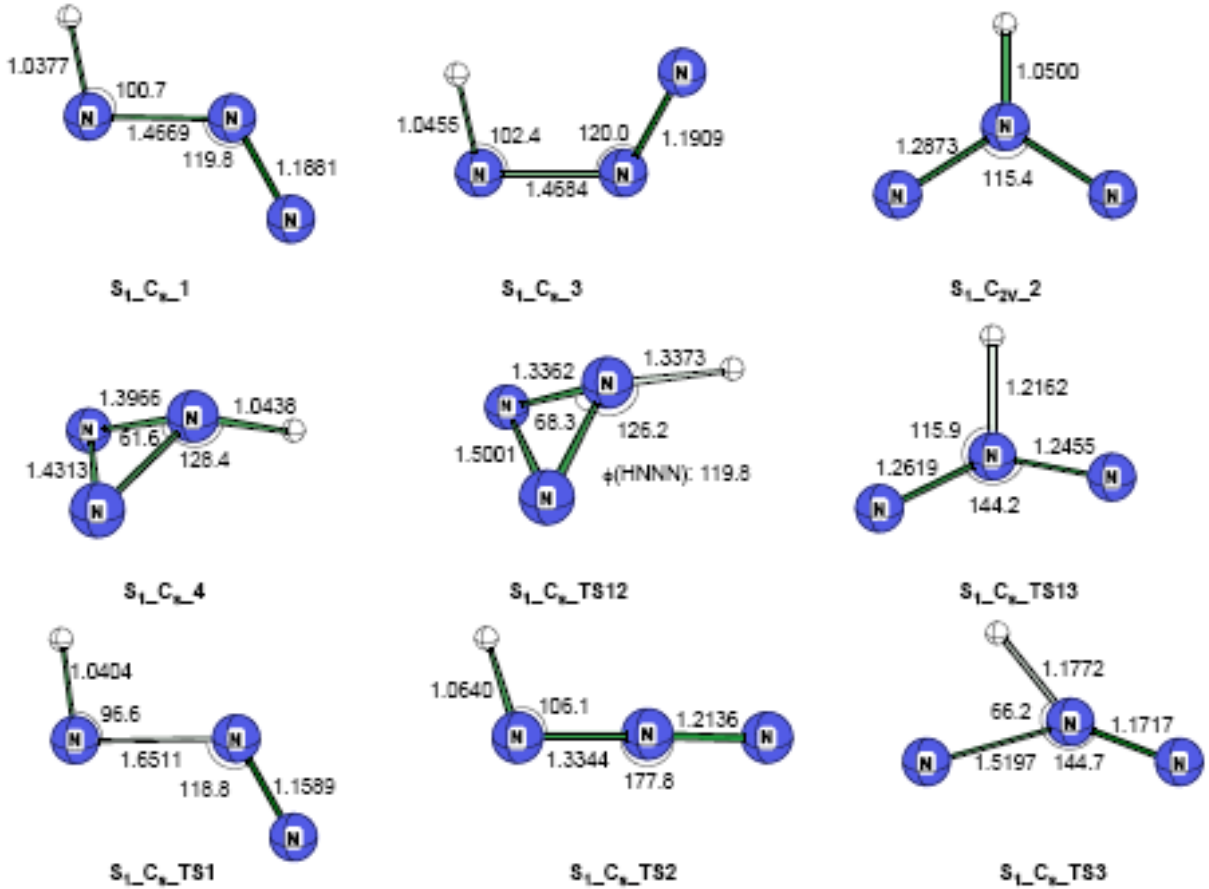

Figure 2.1 continues

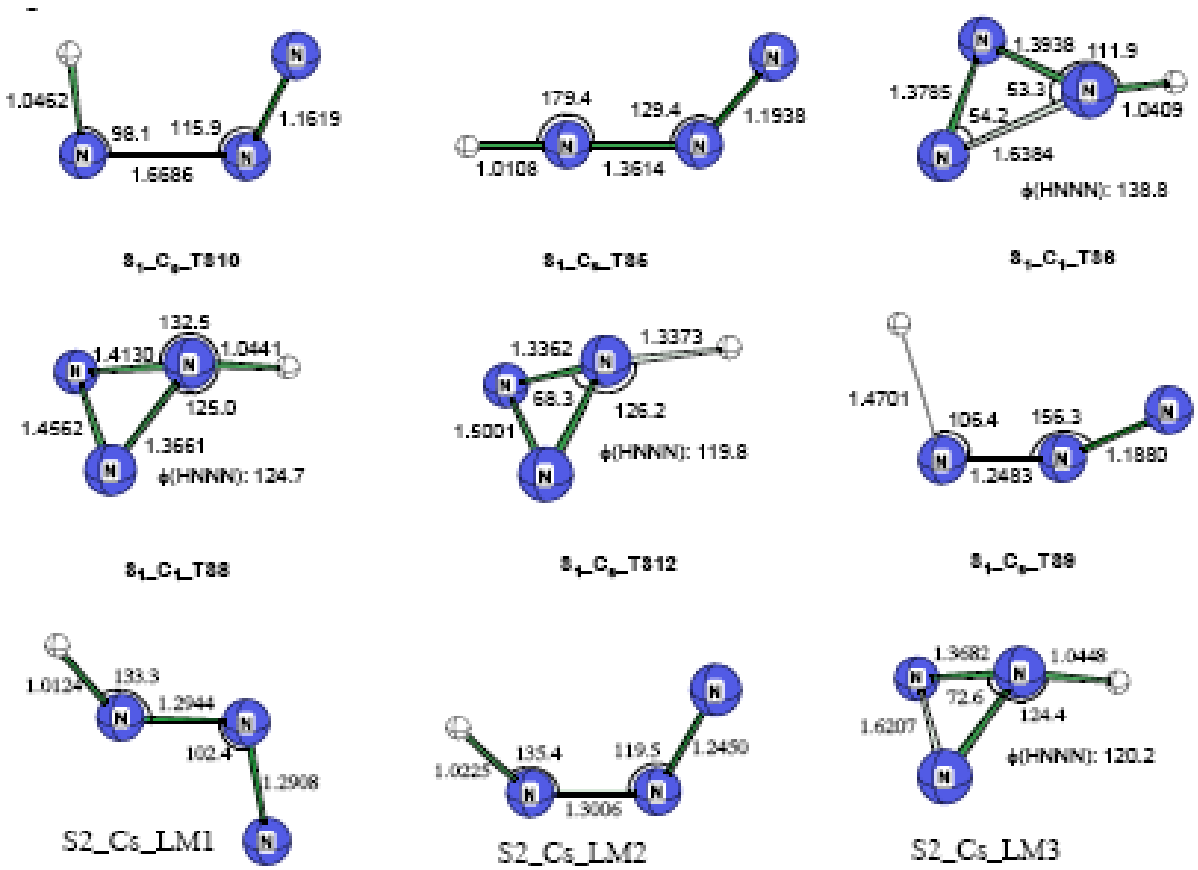

Figure 2.1 continues

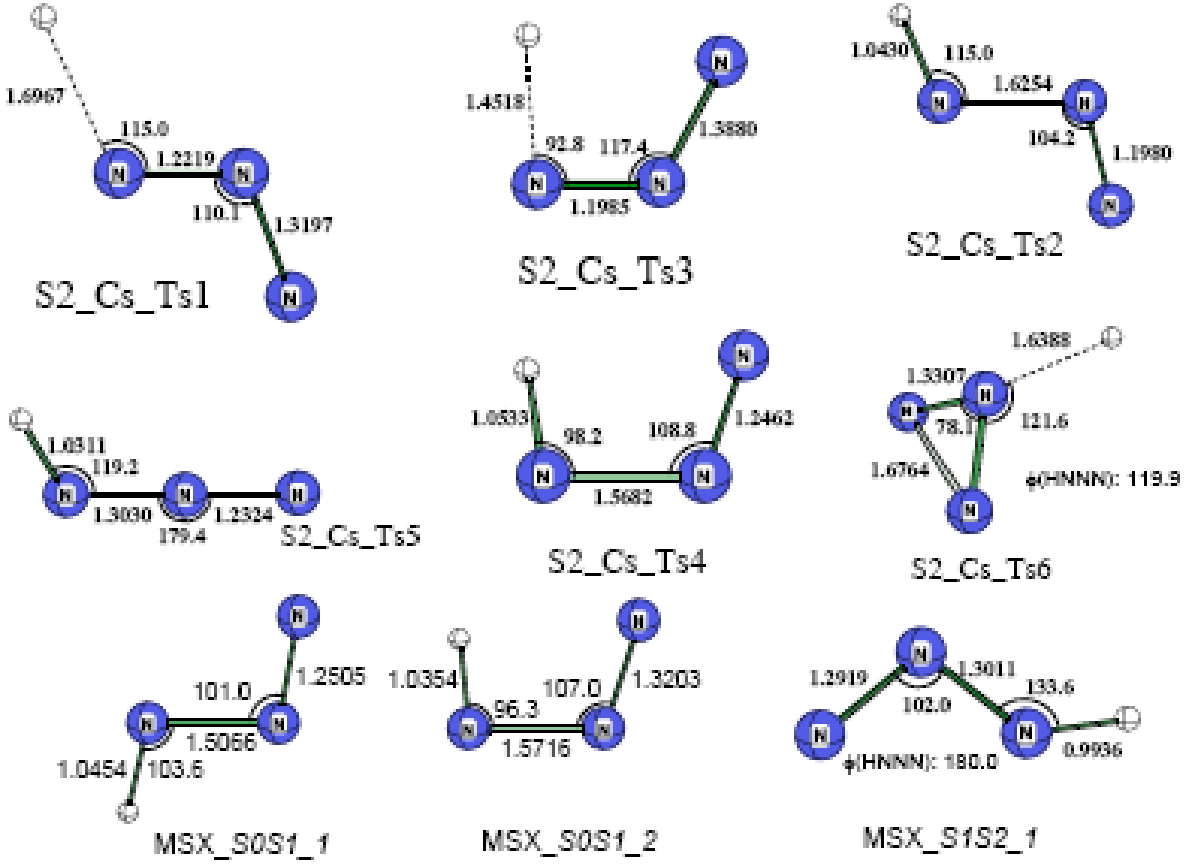

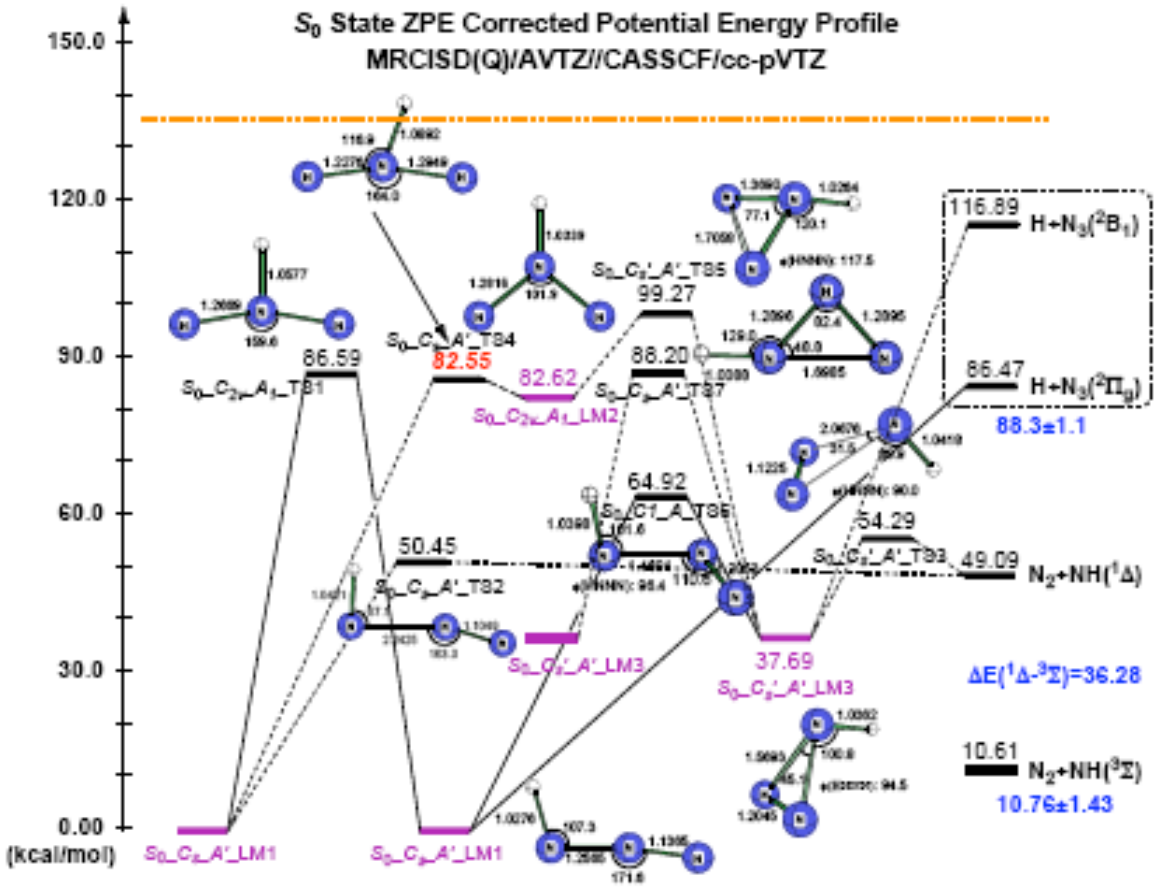

Figure 2.2: Schemetic representation of the potential energy profile of the ground state (S_0). Energies are calculated at MRCISD(Q)/aug-cc-pVTZ//CASSCF/cc-pVTZ level of theory. ZPE correction, calculated at CASSCF/cc-pVTZ level of theory, has been applied.

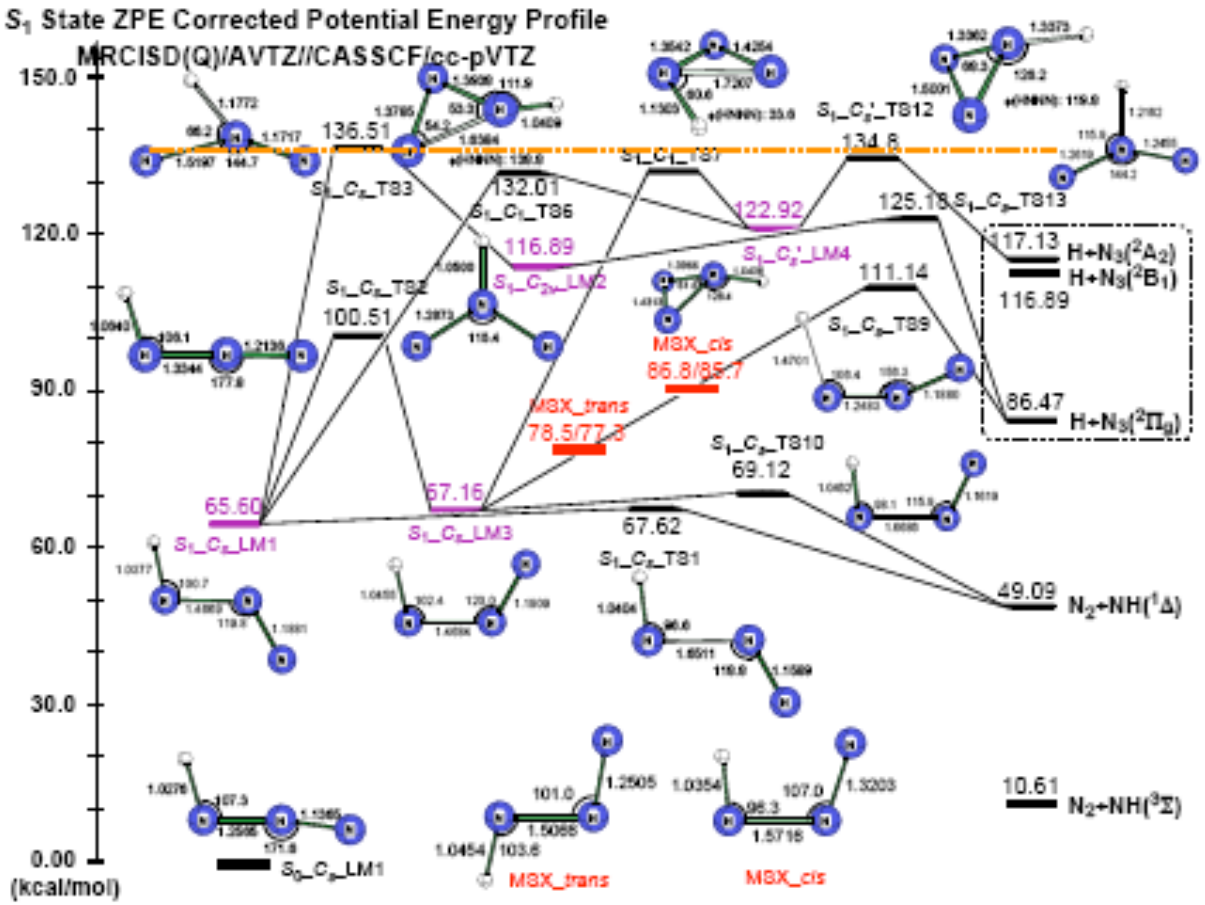

Figure 2.3: Schemetic representation of the potential energy profile of the first singlet excited state (S_1). Energies were calculated at MRCISD(Q)/aug-cc-pVTZ//CASSCF/cc-pVTZ level of theory. ZPE correction, calculated at CASSCF/cc-pVTZ level of theory, has been applied.

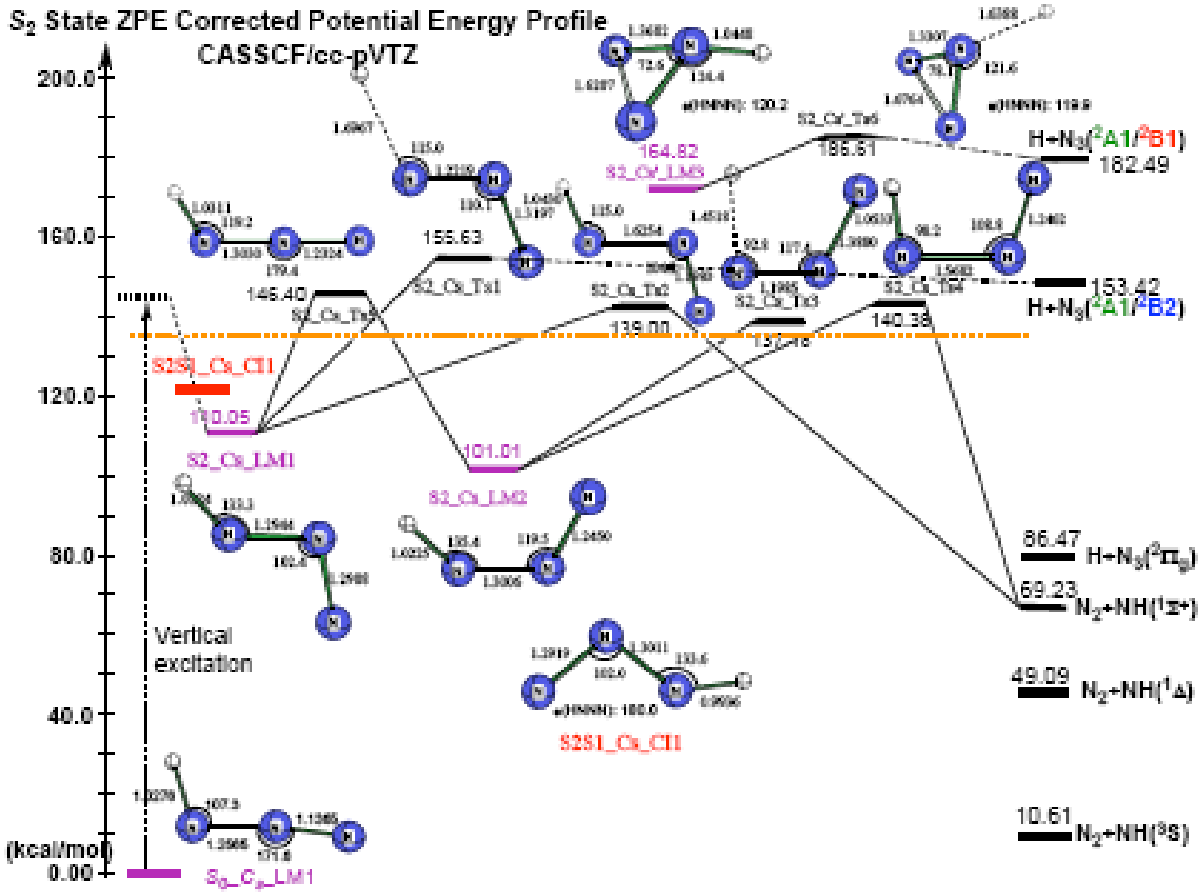

Figure 2.4: Schemetic representation of the potential energy profile of the lowest triplet excited state (S_2). Energies are calculated at calculated at CASSCF/cc-pVTZ level of theory, has been applied.

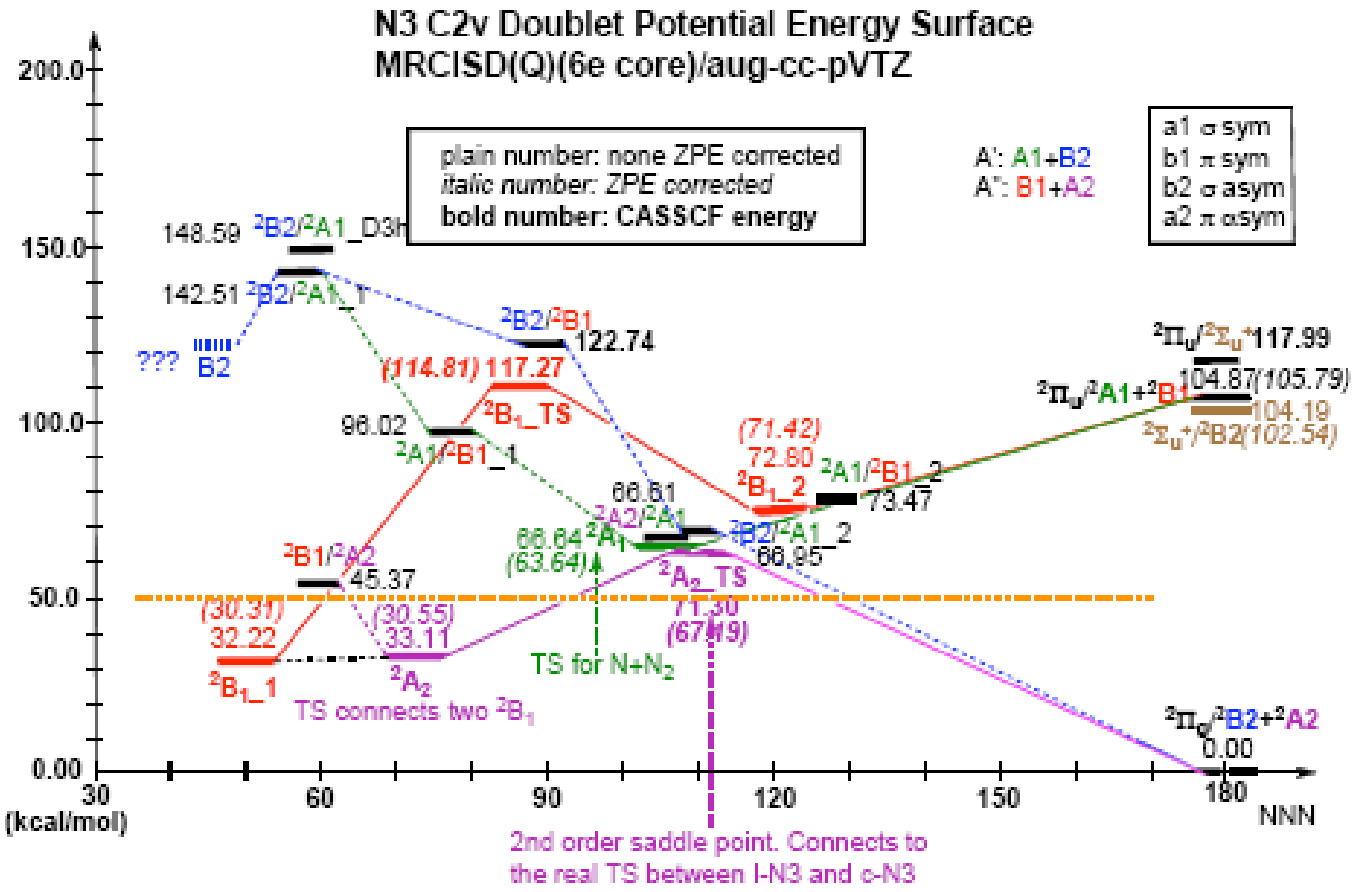

Figure 2.5: Schemetic representation of the C_{2v} potential energy profile of the four lowest doublet states of N_3.

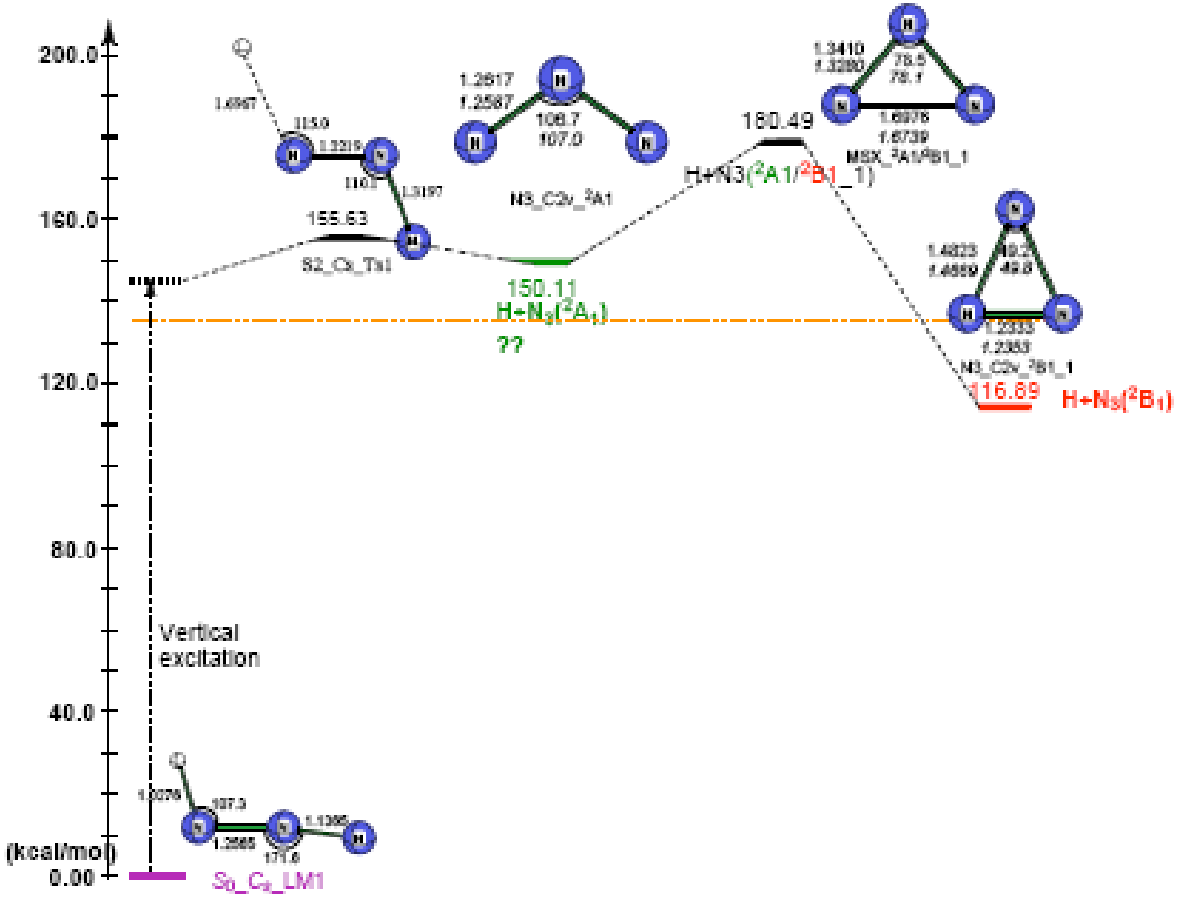

Figure 2.6: Schemetic representation of the possible cyclic N_3 formation pathway I with early H dissociation on S_2 state.

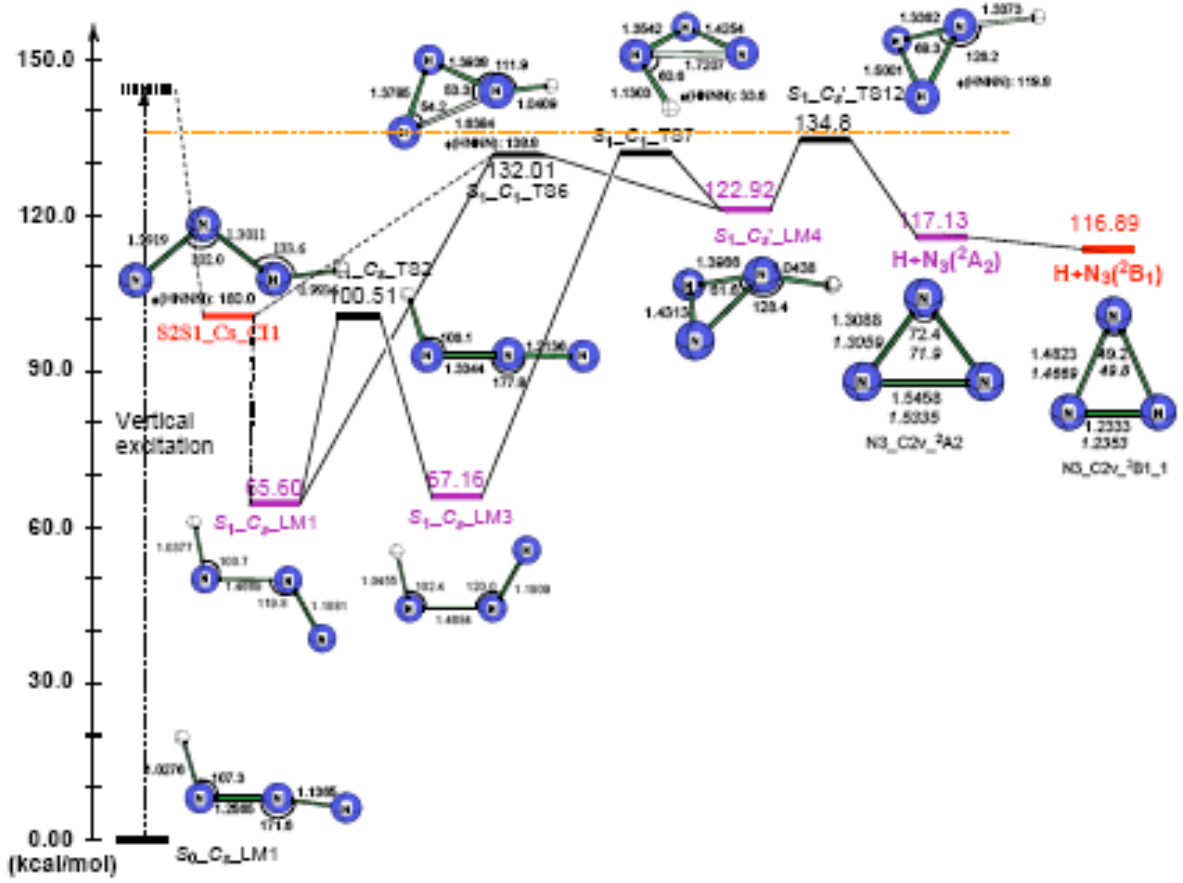

Figure 2.7: Schemetic representation of the possible cyclic N_3 formation pathway II with late H dissociation on S_1 state.

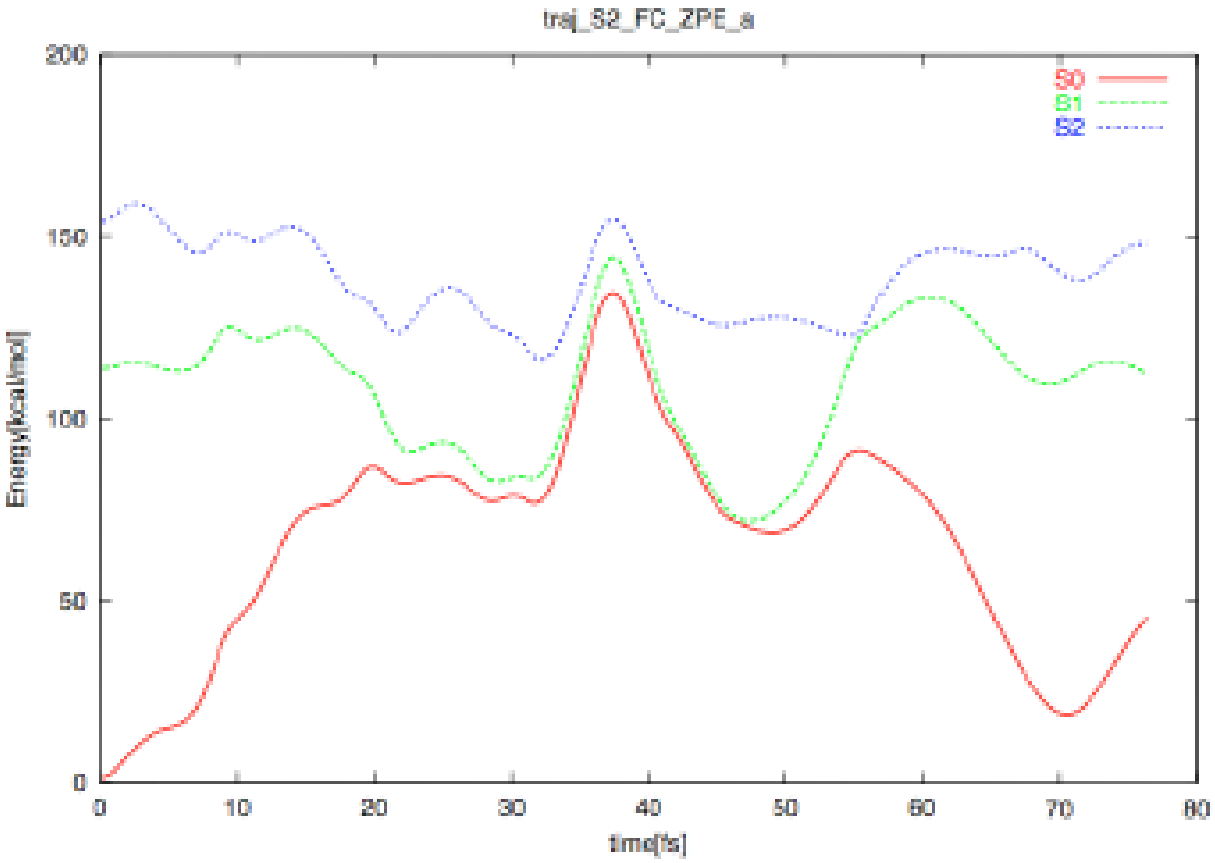

Figure 2.8: Potential energy changes along the trajectory propagated on the S_2 state from the Frank-Condon excitation.

Chapter 3. The low-lying doublet excited states of N_3

3.1 Introduction

Polynitrogen (N_x) compounds have recently been the focus of much theoretical and experimental work.[1] These compounds are generally predicted to be unstable with respect to dissociation to N_2 molecules, however, many of these dissociations are "protected" by barriers of several kcal/mol, rendering some of these species so-called "metastable". Theoretical studies have focused on understanding the factors which affect their stability as well as suggesting possible pathways of their formation.[1] If such compounds could be formed in the laboratory, this could possibly open the way for production of new "clean" fuels and propellants, as the N_2dissociation products are already present in Earths atmosphere.

The azide radical (N_3) is one of the smallest such compounds and its $^2\Pi_g$ linear ground state has been quite extensively studied either experimentally[2,3,4] or theoretically.[5,6,7,8,9,10,11,12,13,14] As evidenced by its spectroscopic designation, ground-state N_3 possesses $D_{\infty h}$ symmetry with an experimental r_0 bond length of 1.18115 Å.[4] A symmetry-broken $C_{\infty v}$ ground-state N_3 with two unequal bond lengths is found at the SCF level,[5,9,14] but the $D_{\infty h}$ point group is confirmed at higher levels of theory. Fairly recent calculations at the multireference configuration interaction singles and doubles plus the Davidson correction for quadruples (MRCISD+Q) level of theory predict a bond length of 1.1854 Å,[15] in agreement with the experimental value.[4]

Other stationary points also exist on the ground doublet hypersurface of N_3, the most remarkable being a "cyclic"-N_3 $^2B_1$ minimum 30.3 kcal/mol (corrected for zero-point energy difference) above the $\tilde{X}^2\Pi_g$ state, comprising an isosceles triangle with

the apex ∠NNN = 49.80° and the two equal N-N bond lengths being 1.4661 Å at the MRCISD/MRCISD+Q levels of theory.[15] This cyclic-N_3 isomer is a stable isomer needing 33.1 kcal/mol of energy in order to dissociate to $N(^2D) + N_2(X^1\Sigma_g^+)$, and 31.9 kcal/mol to overcome the C_s ($^2A''$) isomerization barrier to linear N_3.[15] Bittererova et al. have indicated that cyclic-N_3 could be used as a starting material in order to build larger "closed" polynitrogen structures, and have demonstrated this by calculating that tetraazatetrahedrane (N_4) could be formed in a barrierless exothermic manner by combining cyclic-N_3 with $N(^2D)$.[16] Therefore, it is of high interest to devise a way of formation of cyclic-N_3 in laboratory conditions and one way of achieving this would be via appropriate photoexcitation of the accessible linear N_3 isomer. Indeed, Wodtke and coworkers have very recently obtained indirect evidence of cyclic-N_3 formation in the gas-phase photodissociation of ClN_3 at 157 nm,[17,18] and theoretical calculations have shown that excited states of N_3 are crucial in understanding the mechanism of this formation.

For this reason, it is absolutely necessary to study in detail the excited state surfaces of N_3, especially as a function of ∠NNN. So far, interest on the excited N_3 states has been minor. To the best of our knowledge, other than the lowest $^2\Sigma_u^+$ linear excited state, there are not any other available experimental measurements for excited states either in the linear or the bent regions. Douglas and Jones[3] assigned the 270° Å bands observed in the flash photolysis of HN_3 by Thrush[2] to the $^2\Sigma_u^+ \leftarrow \tilde{X}^2\Pi_g$ transition of N_3. Their analysis indicated that the $^2\Sigma_u^+$ state lies 4.56 eV (105.04 kcal/mol) higher than the linear ground $\tilde{X}^2\Pi_g$ state,[3] and this value was also confirmed in subsequent Fourier transform spectroscopy experiments by Brazier et al.[4] Continetti et al. have studied the $^2\Sigma_u^+$ photodissociation dynamics to both spin-allowed $N(^2D) + N_2(X^1\Sigma_g^+)$ and spin-forbidden $N(^4S) + N_2$ products, and also measured the electron affinity of ground state N_3 to be 2.68 ± 0.01 eV.[19,20] Theoretically, Petrongolo was apparently the first to study in detail the low-lying excited spectrum of N_3, albeit in the linear re-

gion. By using configuration interaction (CI) and a rather small but acceptable basis set, he predicted the relative positions of several low-lying doublet and quartet states of linear N_3.[9] A year later, Martin et al. using unrestricted Hartree-Fock and Møller-Plesset perturbational theory (UHF and UMPx, respectively) were the first to point out the existence of several stationary bent structures on the ground doublet and quartet hypersurfaces.[10] In 1996, Wasilewski extended this work at the MRCI/TZP level employing a very minimal (5e/5o) reference space, and also discussed in terms of Walsh diagrams the nature of these states and their qualitative interaction along the ∠NNN coordinate.[14] Similar calculations were performed by Bittererova et al., with optimization of bent geometries at the full valence (15e/12o) CASSCF level, and single-point MRCI energies using the aug-cc-pVTZ basis set, and a calculation of two potential hypersurface "slices" of four low-lying bent states of N_3 along the ∠NNN coordinate.[16] Recently, Zhang et al. have pinpointed with much greater accuracy the stationary points on the ground doublet and lowest quartet hypersurfaces and have studied in more detail the unimolecular dissociation of linear and cyclic-N_3, as well as possible isomerization mechanisms including intersystem crossings between doublet and quartet surfaces.[15]

It is our purpose to extend our previous work and explore more accurately the low-lying excited doublet hypersurfaces of N_3 and to understand in detail how these surfaces interact with each other to give the unique and rather complicated excited energy profile of N_3, in particular as a function of the ∠NNN variation from linearity (180°) to the cyclic-N_3 vicinity (∼50°).

3.2 Technical Details

The geometrical structure of N_3 was optimized around several regions of its low-lying doublet potential energy hypersurfaces, employing both analytical and numerical energy gradients at the state specific complete active space SCF (ss-CASSCF) and MR-

CISD(Q) levels of theory. Harmonic vibrational frequencies at the stationary points were calculated at the CASSCF level. Minima on the crossing seams (MSX) between surfaces were located at the MRCISD(Q) level using numerical techniques. Furthermore, and in order to better understand the shape and interaction of these excited hypersurfaces, a three-dimensional geometry scan was also performed under C_{2v} symmetry restrictions along the N-N (1.0...2.0 Å) and ∠NNN (40°...180°) coordinates at the state averaged (sa) CASSCF of theory. The augmented correlation-consistent basis sets of Dunning of triple and quadruple zeta quality (aug-cc-pVTZ, aug-cc-pVQZ)[21,22] were used throughout all our calculations, with the latter numbering 240 generally contracted spherical Gaussian one-electron functions.

The CASSCF reference space employed in this work comprises the 12 orbital functions which correlate asymptotically to the $2s + 2p$ valence spaces of the three N atoms. Considering the $1s^2$ electrons of each N as 'core' (inactive), the CASSCF reference space is defined by distributing 15 electrons among the 12 valence orbitals, and denoted as CASSCF(15e/12o). Under C_{2v} symmetry restrictions, this reference space is formed by ∼47 000 CFs (configuration functions). The largest MRCI expansion contains $\sim 6.1 \times 10^9$ CFs and is very efficiently reduced to $\sim 2.6 \times 10^7$ through the internal contraction technique.[23,24] Calculations were performed with the molpro 2006.1 software package.[25] Our own seam code was used for MSX searches.[26]

3.3 Results and Discussion

As reported in our preceding work,[15] two low-lying stationary points ($^2\Sigma_u^+$, $^2\Pi_u$) are found at linearity (∠NNN = 180°) above the $\tilde{X}^2\Pi_g$ state. In the literature, the $^2\Sigma_u^+$ state is designated both as first ($\tilde{A}$) or second ($\tilde{B}$) doublet excited state of linear N_3. It is interesting to mention that Herzbergs compilation of polyatomic molecule data gives the $^2\Sigma_u^+$ state as "$\tilde{B}$", and there is no mention of an "$\tilde{A}$" state. However, our previous theoretical calculations have indicated that the $^2\Sigma_u^+$ and $^2\Pi_u$ stationary

points are practically degenerate;[15] CASPT2 (MRCISD(Q)) values using the aug-cc-pVTZ basis set predict the adiabatic energy separation from the ground state to be 99.94 (105.86) and 100.15 (102.25) kcal/mol, respectively, so it is quite probable that $^2\Pi_u$ could actually be the first excited state of N_3 at linearity.[15]

What is the nature of these two states? In a one-electron picture, they can be considered as originating from the $\tilde{X}^2\Pi_g \ldots (3\sigma_g)^2(4\sigma_g)^2(2\sigma_u)^2(3\sigma_u)^2(1\pi_u)^4(1\pi_g)^3$ electronic configuration after the $1\pi_g \leftarrow 3\sigma_u$ ($^2\Sigma_u^+$) and $1\pi_g \leftarrow 1\pi_u$ ($^2\Pi_u$) excitations. Asymptotically, they both correlate to the excited $N(2s^22p^3;^2P_u)$ + $N_2(X^1\Sigma_g^+)$ dissociation channel which lies 82.46 kcal/mol above the ground $N(^4S_u)$ + $N_2(X^1\Sigma_g^+)$ dissociation limit. The $N(^2D_u)$ + $N_2(X^1\Sigma_g^+)$ channel which lies only 54.98 kcal/mol above the ground state products can only give *gerade* doublet states. Therefore, both $^2\Sigma_u^+$ and $^2\Pi_u$ are unstable (higher in energy) with respect to both doublet dissociation channels.

Frequency calculations at the CASSCF/aug-cc-pVTZ level (Table 3.1) indicate that while the $^2\Sigma_u^+$ stationary point is a true minimum on this excited doublet hypersurface, the $^2\Pi_u$ stationary point has two imaginary degenerate ($342.95i$) bending modes, and is therefore subject to Renner-Teller deformation. Upon bending of the NNN skeleton on the yz plane and reduction of the point group from $D_{\infty h}$ to C_{2v} (with a consequent exchange between the z and y axes), the $^2\Pi_u$ state splits in two stabilized components of $^2A_1$ and $^2B_1$ symmetry, respectively. On the other hand, similar bending of the$^2\Sigma_u^+$ state leads to a single B_2 state, which is actually the second of B_2 symmetry in energy ordering, the first one coming from the C_{2v} splitting to $^2B_2$ + $^2A_2$ components.

The complexity evoked by the interactions among the total of these five C_{2v} components is pictorially shown in Figure 3.1, with a three-dimensional scan along different geometrical configurations of N_3 as a function of $\angle$NNN and R(N-N) under C_{2v} symmetry restrictions at the CASSCF/aug-cc-pVTZ level of theory. A variety of low-

lying stationary points and MSXs have been found and refined at the MRCISD(Q) levels and is presented in Table 3.1, and Figures 3.2, 3.3, and 3.4.

3.3.1 $^2B_2$ surfaces

Bending of the N_3 skeleton from linearity to a C_{2v} structure causes splitting of the $\tilde{X}^2\Pi_g$ state to its $^2B_2$ + $^2A_2$ components. As ∠NNN gets smaller than 180°, the $^2B_2$ state which is described by the electron configuration $\ldots(1b_1)^2(1a_2)^2(4b_2)^1$ becomes lower in energy than the $^2A_2$ state (Fig. 3.1), whose leading configuration is $\ldots(1b_1)^2(1a_2)^1(4b_2)^2$. As mentioned before, a second $^2B_2$ state (designated henceforth as 2^2B_2) with the electron configuration $\ldots(1b_1)^2(3b_2)^1(1a_2)^2(4b_2)^2$ is produced upon bending of the excited$^2\Sigma_u^+$ state. The surface of 2^2B_2 is highly complex (Fig. 3.1). Close to 140°, it crosses with the incoming (not calculated) 3^2B_2, changing the character of the former to $\ldots(1b_1)^2(6a_1)^2(4b_2)^1$. In the meantime, the 1^2B_2 state increases in energy rapidly as ∠NNN gets smaller and cuts successively the $^2A_1$ (MSX_C_{2v}_$^2B_2/^2A_1$_1) and $^2B_1$ (MSX_C_{2v}_$^2B_2/^2B_1$) surfaces (Fig. 3.1). These MSXs are found at angles of 110.3° and 87.8° and energies of 67.0 and 109.8 kcal/mol higher than the ground state, respectively (Table 3.1).

Next, the 1^2B_2 state meets the incoming 2^2B_2 state close to ∼100°. Due to the rapid energy decrease of the $6a_1$ orbital, the $\ldots(1b_1)^2(6a_1)^2(4b_2)^1$ configuration becomes the leading one in 1^2B_2. The two $^2B_2$ states will cross again twice, once close to ∼70° and once close to ∼65°, and finally the "new" 1^2B_2 state will then go through the nearby equilateral trianglar N_3 (∠NNN = 60°) N_3 MSX_D_{3h}_$^2B_2/^2A_1$ (Fig. 3.4) structure of $^2E'$ symmetry, lying 149.0 kcal/mol higher than the linear $\tilde{X}^2\Pi_g$ (Table 3.1). Even though this MSX could be termed as "conical intersection", in fact it is the doubly degenerate $^2E'$ state which is subject to Renner-Teller distortion to $^2B_2$ and $^2A_1$ components. Going to further smaller NNN angles, the $^2B_2$ states meet once again at 55.9°, the relevant structure being MSX_C_{2v}_$^2B_2/^2A_1$_2.

3.3.2 $^2A_2$ surface

As discussed previously,[15] the $^2A_2$ surface comprises a significant part of the ground state potential energy surface of N_3 (Fig. 3.1). It is the second C_{2v} component of $\tilde{X}^2\Pi_g$, and initially has a leading configuration of $\ldots(1b_1)^2(1a_2)^1(4b_2)^2$. As previously mentioned,[14,15] an incoming $^2A_2$ state close to $\angle$NNN = 110° changes the character of the lowest $^2A_2$ due to a double $(4b_2)^2 \rightarrow (6a_1)^2$ excitation. The relevant transition state structure has $\angle$NNN = 108.9° and has been calculated to be a second-order saddle point with two imaginary frequencies of a_1 and b_2 symmetry.[15] This saddle point is an artifact of C_{2v} symmetry constraints, and reduces to a C_s transition structure which connects the linear and cyclic N_3 and therefore describes the isomerization between each other isomers.

Very close to this point (NNN = 106.4°), the $^2A_2$ hypersurface cuts the $^2A_1$ one, and the energy minimum on this crossing seam lies 66.6 kcal/mol higher than the ground state and is shown in Figure 3.4 (MSX_C_{2v}_$^2A_2/^2A_1$).

The stationary $^2A_2$ structure which is close to $\angle$NNN = 72° (Fig. 3.2) has a $\ldots(1b_1)^2(1a_2)^1(6a_1)^2$ dominant electron configuration, and has an imaginary b_2 frequency which connects two equivalent D_0_C_{2v}_$^2B_1$ cyclic N_3's which differ from each other through a pseudorotation operator. By bending further, the equilateral ($\angle$NNN = 60°) N_3 geometry is reached, where the $^2A_2$ state will meet with the "cyclic" $^2B_1$ state through a D_{3h} conical intersection (or more formally, the doubly degenerate $^2E''$ structure of D_{3h}-N_3) in a "Mexican-hat-type" fashion.[27] This MSX_D_{3h}_$^2B_1/^2A_2$ $^2E''$ structure lies 45.4 kcal/mol higher with respect to $\tilde{X}^2\Pi_g$ (Table 3.1).

3.3.3 $^2A_1$ surface

The $^2A_1$ state is a C_{2v} component of the excited $^2\Pi_u$ state of N_3. It can also be viewed as the Jahn-Teller stabilized component of the $^2E'$ state of equilateral N_3. As the geometrical structure starts deviating from linearity, the $^2A_1$ component is

described by the $\ldots(3b_2)^2(1b_1)^2(5a_1)^2(1a_2)^2(6a_1)^1$ leading configuration. The shape of the surface is rather smooth and a stationary point $D_0\_C_{2v}\_^2A_1$ is found 67.2 (64.2, after ZPE correction) kcal/mol higher than the ground state, with R(N-N) = 1.2545 Å and ∠NNN = 107.0°, in qualitative agreement with previous CASCI calculations (71.5 kcal/mol, 1.242 Å, 112°).[14] CASSCF frequencies reveal that this structure has a rather strong ($1932i$) imaginary frequency of b_2 symmetry (Table 3.1).

The $^2A_1$ state is cut twice by $^2B_1$ (Fig. 3.1), with the corresponding crossing seams having minima at 125.8° and 78.1°, respectively. The structures obtained by MSX search are MSX_$C_{2v}_^2A_1/^2B_1_1$ and MSX_$C_{2v}_^2A_1/^2B_1_2$ and are depicted in Figure 3.4. These crossing seams were shown to play an important role in understanding the formation of cyclic-N_3 in relevant photodissociation experiments on ClN_3.[18] The dissociated "hot" N_3 can find its way to the cyclic-N_3 minimum by moving on the $^2A_1$ surface and crossing with the $^2B_1$ surface close to 80° (vide infra).

3.3.4 $^2B_1$ surface

The seconnd C_{2v} component of the excited $^2\Pi_u$ state of N_3 is of $^2B_1$ symmetry. A small (∼10°) departure from the linear structure reveals a highly multireference wavefunction, possibly due to interaction with a close-by higher $^2\Pi_u$ state.[9] Even somewhat far from linearity (∠NNN ≈ 140°), the $^2B_1$ and $^2A_1$ surfaces are practically degenerate and start separating noticeably from each other around ∠NNN ≈ 120°. This is the angle where the $^2B_1$ surface has a stable minimum structure $D_3\_C_{2v}\_^2B_1\_2$ (Fig. 3.3). The structure lies 73.6 (72.2 with inclusion of ZPE) kcal/mol higher than the linear N_3 ground state and is characterized by R(N-N) = 1.2614 Å and ∠NNN = 120.6°, calculated at the MRCISD(Q)/aug-cc-pVQZ level of theory (Table 3.1).

Its CASSCF electronic configuration reveals that it is has a highly multireference wavefunction, but it's best described as having three unpaired electrons coupled into a doublet: $\ldots(1a_2)^1(4b_2)^1(6a_1)^1$. This "open" $^2B_1$ isomer is a different minimum on the $^2B_1$ PES than the known cyclic $D_0\_C_{2v}\_^2B_1$ isomer (32.9 kcal/mol, 1.4593 Å,

49.9°). It needs 36.6 kcal/mol (ZPE included) to climb to D_2_C_{2v}_$^2B_1$_TS transition state connecting the open and the cyclic-N_3 minima. This transition state structure is calculated to have an angle of 86.1°, bond length of 1.3623 Å.

It is noted that the $^2B_1$ PES provides another candidate photoexcitation pathway for production of cyclic-N_3 from linear-N_3 or -N_3 containing precursors after the molecule is brought to the $^2\Pi_u$ state, according to the following scheme: $^2\Pi_u \rightarrow$ bending due to Renner-Teller stabilization $\rightarrow$ $^2B_1$ open minimum (D_3_C_{2v}_$^2B_1$_2) $\rightarrow$ $^2B_1$ TS (D_2_C_{2v}_$^2B_1$_TS) $\rightarrow$ $^2B_1$ cyclic-N_3 (D_0_C_{2v}_$^2B_1$).

3.4 Summary

The low-lying potential energy states of N_3 were studied theoretically with focus on their electronic nature, as well as on the interactions among them, especially as a function of the NNN bending coordinate. The morphology of their PESs is complex, leading to many surface crossings, conical intersections, and stationary points. Many of these critical points on their surfaces were characterized employing highly correlated ab initio methods. These are crucial in order to understand the course of events during photodissociation experiments involving azides, especially those which lead to important structures like cyclic-N_3. In particular, two possible pathways of production of cyclic-N_3 through photoexcitation of linear-N_3 and/or suitable -N_3 precursors were suggested. Our next step is to carry out a full multidimensional and simultaneous analytical potential energy surface fit to all these low-lying hypersurfaces, in hope of performing accurate quantum dynamics calculations on N_3.

References

1. Samartzis, P. C.; Wodtke, A. M. *INTERNATIONAL REVIEWS IN PHYSICAL CHEMISTRY* **2006**, *25*, 527–552.

2. THRUSH, B. *PROCEEDINGS OF THE ROYAL SOCIETY OF LONDON SERIES A-MATHEMATICAL AND PHYSICAL SCIENCES* **1956**, *235*, 143–&.

3. DOUGLAS, A.; JONES, W. *CANADIAN JOURNAL OF PHYSICS* **1965**, *43*, 2216–&.

4. BRAZIER, C.; BERNATH, P.; BURKHOLDER, J.; HOWARD, C. *JOURNAL OF CHEMICAL PHYSICS* **1988**, *89*, 1762–1767.

5. ARCHIBAL.TW,; SABIN, J. *JOURNAL OF CHEMICAL PHYSICS* **1971**, *55*, 1821–&.

6. DYKE, J.; JONATHAN, N.; LEWIS, A.; MORRIS, A. *MOLECULAR PHYSICS* **1982**, *47*, 1231–1240.

7. MURRELL, J.; NOVARO, O.; CASTILLO, S.; SAUNDERS, V. *CHEMICAL PHYSICS LETTERS* **1982**, *90*, 421–424.

8. BYUN, Y.; SAEBO, S.; PITTMAN, C. *JOURNAL OF THE AMERICAN CHEMICAL SOCIETY* **1991**, *113*, 3689–3696.

9. PETRONGOLO, C. *JOURNAL OF MOLECULAR STRUCTURE* **1988**, *175*, 215–220.

10. MARTIN, J.; FRANCOIS, J.; GIJBELS, R. *JOURNAL OF CHEMICAL PHYSICS* **1989**, *90*, 6469–6485.

11. YU, D.; RAUK, A.; ARMSTRONG, D. *JOURNAL OF PHYSICAL CHEMISTRY* **1992**, *96*, 6031–6038.

12. ZIEGLER, T.; GUTSEV, G. *JOURNAL OF COMPUTATIONAL CHEMISTRY* **1992**, *13*, 70–75.

13. SLUPSKI, R.; WASILEWSKI, J. *INTERNATIONAL JOURNAL OF QUANTUM CHEMISTRY* **1995**, *56*, 655–661.

14. Wasilewski, J. *JOURNAL OF CHEMICAL PHYSICS* **1996**, *105*, 10969–10982.

15. Zhang, P.; Morokuma, K.; Wodtke, A. *JOURNAL OF CHEMICAL PHYSICS* **2005**, *122*, 014106.

16. Bittererova, M.; Ostmark, H.; Brinck, T. *JOURNAL OF CHEMICAL PHYSICS* **2002**, *116*, 9740–9748.

17. Hansen, N.; Wodtke, A. *JOURNAL OF PHYSICAL CHEMISTRY A* **2003**, *107*, 10608–10614.

18. Samartzis, P. C.; Lin, J. J.-M.; Ching, T.-T.; Chaudhuri, C.; Lee, S.-H.; Wodtke, A. M. *JOURNAL OF CHEMICAL PHYSICS* **2007**, *126*, 041101.

19. CONTINETTI, R.; CYR, D.; METZ, R.; NEUMARK, D. *CHEMICAL PHYSICS LETTERS* **1991**, *182*, 406–411.

20. CONTINETTI, R.; CYR, D.; OSBORN, D.; LEAHY, D.; NEUMARK, D. *JOURNAL OF CHEMICAL PHYSICS* **1993**, *99*, 2616–2631.

21. DUNNING, T. *JOURNAL OF CHEMICAL PHYSICS* **1989**, *90*, 1007–1023.

22. KENDALL, R.; DUNNING, T.; HARRISON, R. *JOURNAL OF CHEMICAL PHYSICS* **1992**, *96*, 6796–6806.

23. WERNER, H.; KNOWLES, P. *JOURNAL OF CHEMICAL PHYSICS* **1988**, *89*, 5803–5814.

24. KNOWLES, P.; WERNER, H. *CHEMICAL PHYSICS LETTERS* **1988**, *145*, 514–522.

25. Werner, H.-J.; Knowles, P. J.; Lindh, R.; Manby, F. R.; Schütz, M. et al. *MOLPRO, version 2006.1, a package of ab initio programs*, 2006, see http://www.molpro.net.

26. KOGA, N.; MOROKUMA, K. *CHEMICAL PHYSICS LETTERS* **1985**, *119*, 371–374.

27. Babikov, D.; Zhang, P.; Morokuma, K. *JOURNAL OF CHEMICAL PHYSICS* **2004**, *121*, 6743–6749.

Table 3.1: Geometries and adiabatic transition energies relative to the $\tilde{X}^2\Pi_g$ ground state of various critical points on the low-lying doublet states of N_3 at the MRCISD(Q)/aug-cc-pVTZ and MRCISD(Q)/aug-cc-pVQZ (in parentheses) levels of theory. Harmonic frequencies and zero-point corrections (ZPE) calculated at the CASSCF/aug-cc-pVTZ level.

	ΔE(kcal/mol)	R_{N-N}(Å)	∠NNN(°)	ZPE(kcal/mol)	Nimag; frequency (cm^{-1})
$\tilde{X}^2\Pi_g$	0[a]	1.1857 (1.1820)	180.0 (180.0)	5.8	0
$^2\Pi_u$	104.2 (105.8)	1.2759 (1.2714)	180.0 (180.0)	4.2	2; 342.95i, 342.95i
$^2\Sigma_u^+$	104.9 (104.8)	1.1845 (1.1807)	180.0 (180.0)	6.7	0
D_0-C_{2v}-$^2A_1$	66.6 (67.2)	1.2587 (1.2545)	107.0 (107.0)	2.8	1; 1932i
D_0-C_{2v}-$^2B_1$	32.2 (32.9)	1.4669 (1.4593)	49.8 (49.9)	3.9	0
D_3-C_{2v}-$^2B_1$-2	72.8 (73.6)	1.2656 (1.2614)	120.5 (120.6)	4.4	0
D_2-C_{2v}-$^2B_1$-TS	109.1 (111.2)	1.3623 (1.3566)	86.1 (86.1)	3.4	1; 1967.96i
MSX-C_{2v}-$^2A_2/^2A_1$	66.6	1.2607	106.4		
MSX-C_{2v}-$^2B_2/^2B_1$	109.8	1.3118	87.8		
MSX-C_{2v}-$^2B_2/^2A_1$-1	67.0	1.2572	110.3		
MSX-C_{2v}-$^2B_2/^2A_1$-2	142.5	1.4578	55.9		
MSX-D_{3h}-$^2B_1/^2A_2$	45.4	1.3693	60.0		
MSX-D_{3h}-$^2B_2/^2A_1$	149.0	1.4408	60.0		
MSX-C_{2v}-$^2A_1/^2B_1$-1	73.5	1.2672	125.8		
MSX-C_{2v}-$^2A_1/^2B_1$-2	96.0	1.3280	78.1		

[a] MRCISD(Q)/aVTZ: E = -163.899228 E_h; MRCISD(Q)/aVQZ: E= -164.03432 E_h

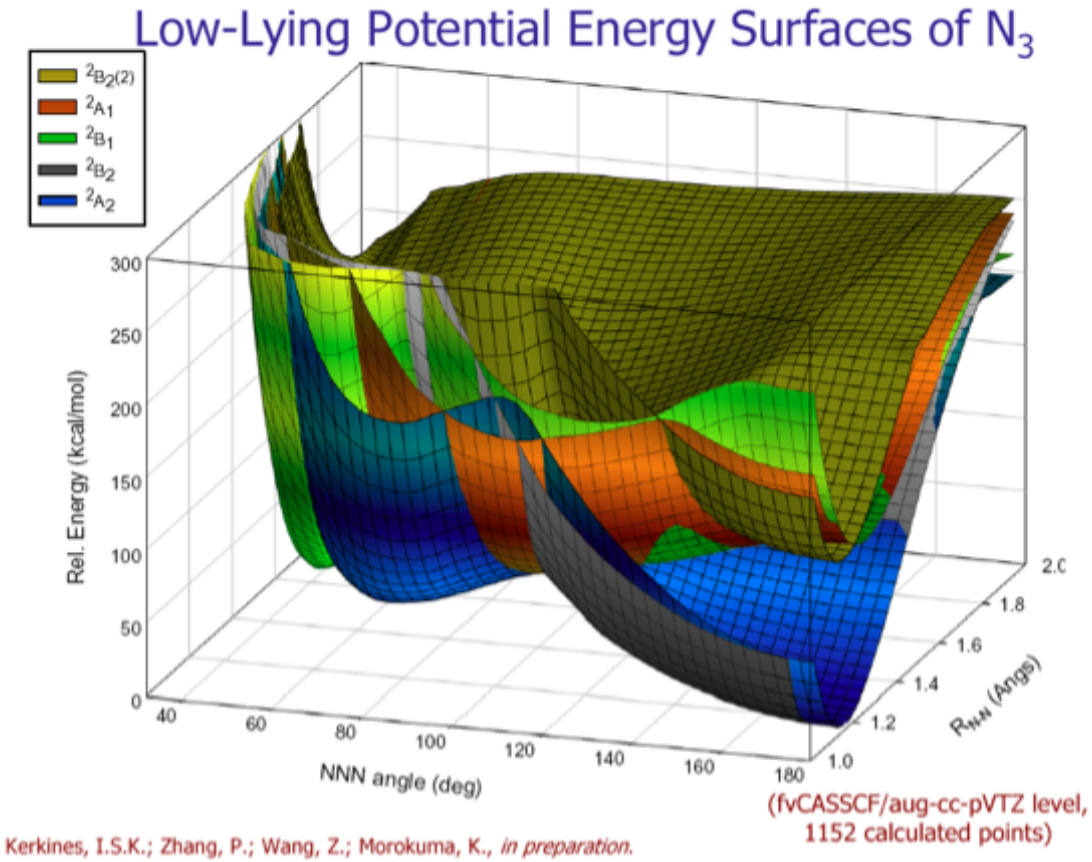

Figure 3.1: Potential hypersurface scan of ground and low-lying states of N_3 as a function of $\angle NNN$ and R_{N-N} in C_{2v} symmetry (CASSCF/aug-cc-pVTZ level of theory).

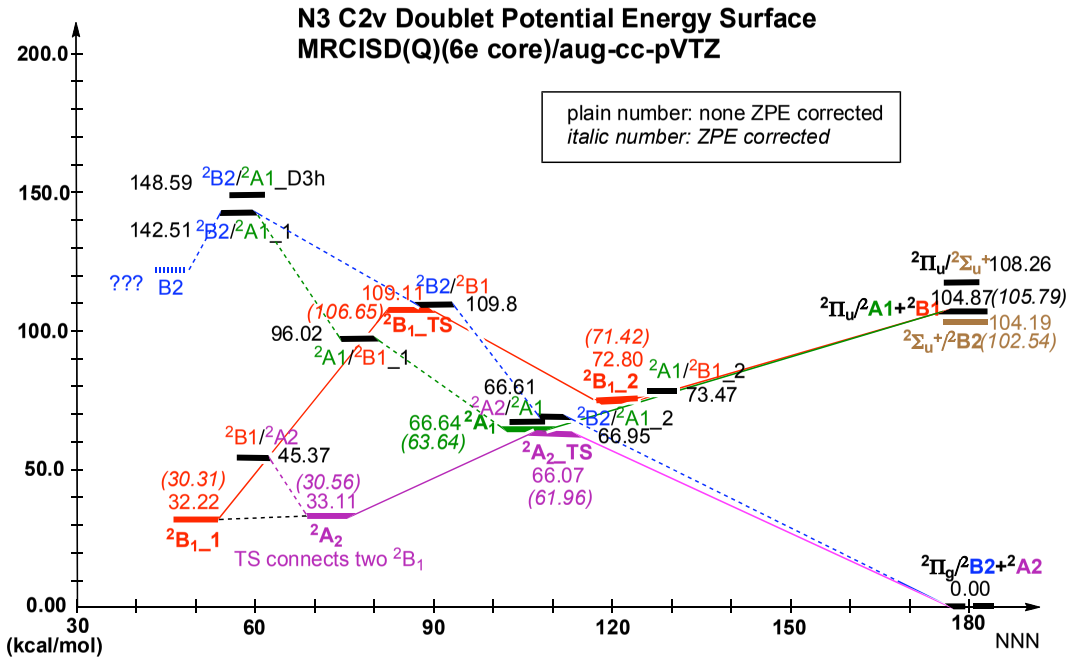

Figure 3.2: Stationary points on the low-lying states of N_3 as a function of $\angle NNN$ at the MRCISD(Q)/aug-cc-pVTZ level of theory. Results in parentheses indicate zero-point corrected relative energies.

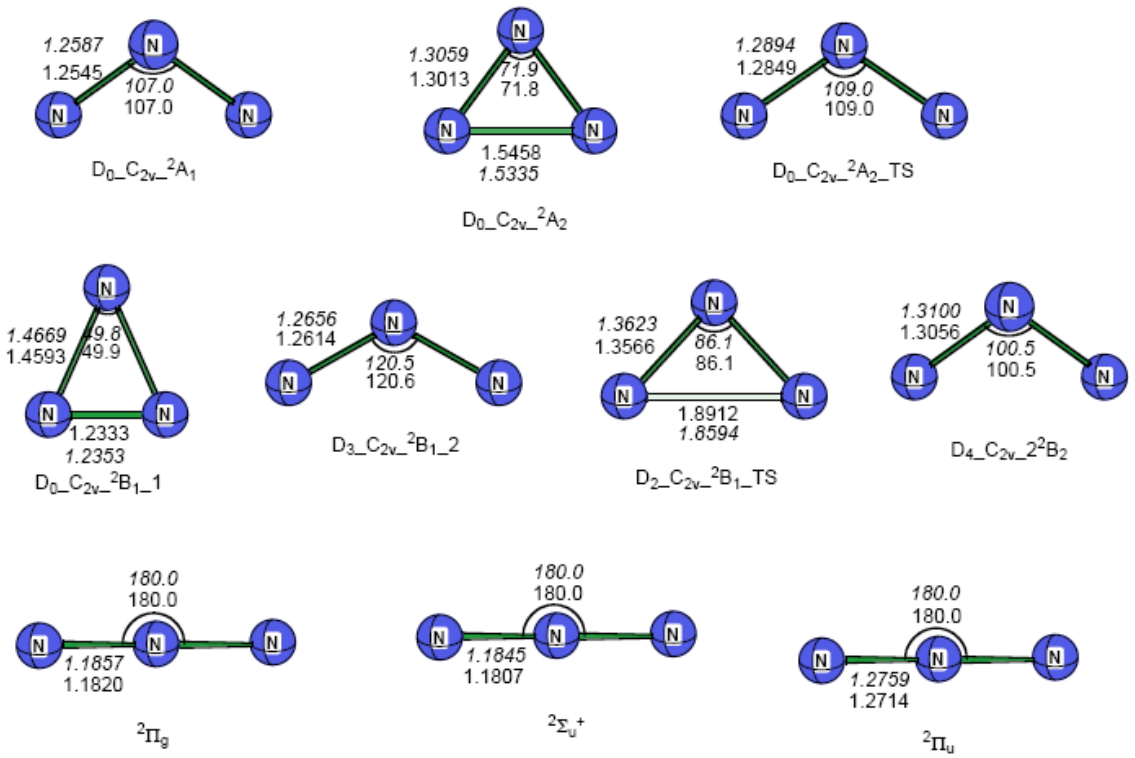

Figure 3.3: Stationary point structures on the low-lying excited doublet hypersurfaces of N_3 at the MRCISD(Q)/aug-cc-pVTZ (italic number) and MRCISD(Q)/aug-cc-pVQZ (plain number) level of theory.

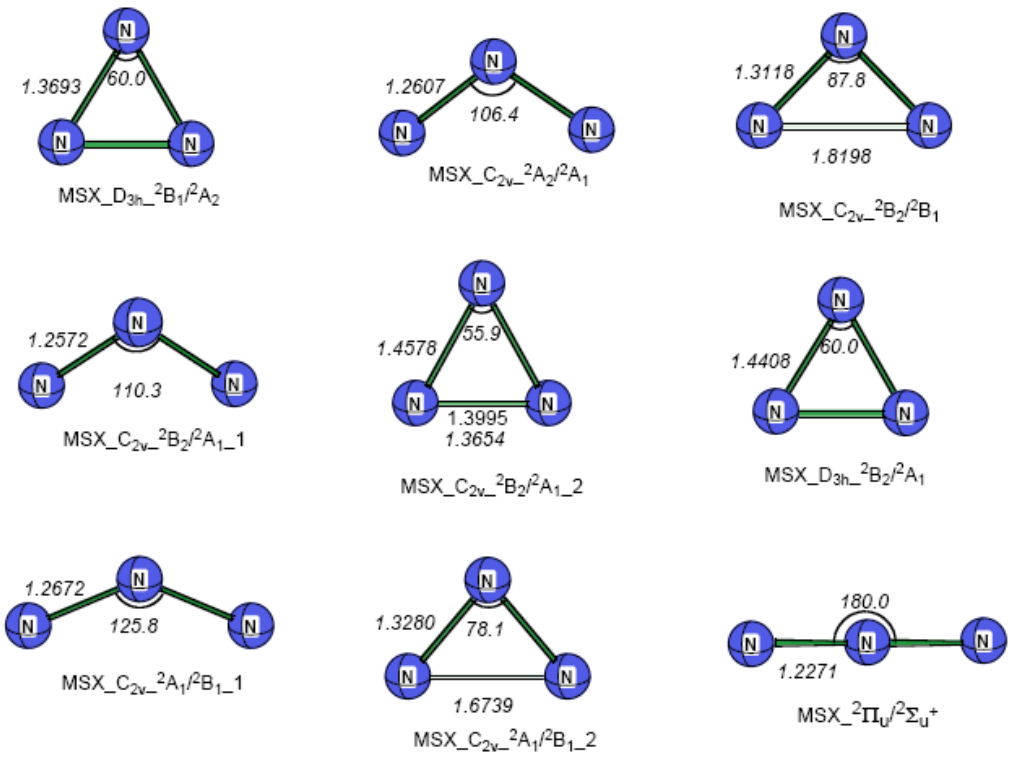

Figure 3.4: Structures of the minima on the seam of crossing (MSX) among the low-lying excited hypersurfaces of N_3 at the MRCISD(Q)/aug-cc-pVTZ level of theory.

Chapter 4. Ab initio potential energy surfaces for N_3 low-lying doublet states

4.1 Introduction

Due to their capability to store large amount of energy in minimal volumes, the "high energy and density materials" polynitrogen (N_x) compounds have been the focus of much theoretical and experimental work.[1] Since the dissociation products of these all-nitrogen species are simply the extremely stable N2 molecules, they not only provide significant amount of energy but also in an enviromental friendly way, hence are considered for the production of new "clean" fuels and propellants.

As the samllest compound in polynitrogen family, the azide radical, N_3, has been the interest of study for long times. Extensive experimental[2,3,4] and theoretical[5,6,7,8,9,10,11,12,13,14] investigation has been made on its $^2\Pi_g$ ground state, which is a linear structure in $D_{\infty h}$ symmetry. Its bond length is predicted theoretically at MRCISD(Q) level of theory at 1.1854 Å,[15] in very good agreement with experimental value of 1.18115 Å.[4] Other stationary points also exist on the ground doublet hypersurface of N_3, with the most remarkable one being a "cyclic"-N_3 $^2B_1$ minimum. MRCISD(Q) calculations suggest that it is 30.3 kcal/mol (with zero-point energy correction) above the $\tilde{X}^2\Pi_g$ state, comprising an isosceles triangle with the apex $\angle$NNN = 49.80° and the two equal N-N bond lengths being 1.4661 Å.[15] This cyclic-N_3 isomer stable as it needs 33.1 kcal/mol of energy in order to dissociate to N(^2D) + $N_2(X^1\Sigma_g^+)$, and 31.9 kcal/mol to overcome the C_s ($^2A''$) isomerization barrier to linear N_3.[15] Theoretical calulations have shown that this cyclic $^2B_1$ minimum could undergo a barrierless exothermic recombination with N(^{2}D) and form tetraazatetrahedrane (N_4).[16] Therefore this cyclic-N_3 could be used as the bulding blocks for

producing larger "closed" polynitrogen structures. Recent gas-phase photodissociation experiments of ClN_3 at 157 nm by Wodtke and coworkers have obtained indirect evidence of cyclic-N_3 formation,[17,18] while theoretical calculations have shown that excited states of N_3 are crucial in understanding the mechanism of this formation.

In order to understand this cyclization process of N_3, it is definitely necessary to study the excited states of N_3 in details. However, such studies are not many. For this reason, we have carried out accurate ab initio calculations on the low-lying excited doublet hypersurfaces of N_3 and managed to understand in detail how these surfaces interact with each other. Also, two possible pathways of production of cyclic-N_3 through photoexcitation of linear-N_3 and/or suitable -N_3 precursors were suggested, as demenstrated in the previous chapter. To further extend this study, and better understand the cyclization process of N_3, the construction of the full dimenstional potential energy surfaces for N_3 low-lying states and subsequent dynamic simulations on these surfaces would be desirable.

Regarding the construction potential energy surfaces, there are various ways. As for N_3 molecule, Babikov et al[19] has constructed its ground doublet electronic state surface by a 3D spline fit using adiabatically adjusting principal-axes hyperspherical (APH) coordinates, but only at the cyclic region. For a similar Ozone molecule, Leforestier et al[20] constructed its surfaces by fitting a standard Murrel-Sorbie function with many body expansion. A more sophisticated method, which is based on the computational invariant theory by Derksen and Kemper,[21] for fitting potential energy surface has recently been developed by Braams and Bowman. They have succefully applied this technique to H5O2+,[22] CH5+,[23,24] H3O2-[25] and other molecular systems. One distinguished feature for the potential energy surfaces built up in this way is that these PESe are invariant with respect to any permutation of like nuclei. Therefore, we decide to use this powerful method and construct N_3 PESs for low-lying doublet states.

In this paper, we first demenstrate the procedure for fitting 5 low-lying N_3 doublet states PESs with permutation symmetry based on thoudsands of points ab initio calculations. Then we perform a special local fit at the cyclic, bend, and linear N_3 conical intersection region to improve the quality of these surfaces. Moreover, approximate diabatization is done at the bend CI3 conical intersection region. The property of these surfaces is examined by comparing stationary points and minimum on seam of crosssings (MSXs) with ab initio results.

4.2 Ab initio Calculations

In order to have accurate description of the 5 lowest states of N_3 potential energy surfaces (PES), we performed the calculations using internally contracted configuration interaction with single and double excitations (MRCISD)[26,27] plus multireference version of Davidson's correction (Q)[28] with Dunning's correlation consistent augmented polarized valence triple zeta basis set,[29] aug-cc-pVTZ (abbreviated as AVTZ). A predetermined 5 states averaged (3 $^2A'$ and 2 $^2A''$ states) sa-CASSCF(15e/12o)/AVTZ wave function was selected as the corresponding reference configuration. In the MRCISD(Q) calculation, only $1s$ orbitals of nitrogen atoms were kept doubly occupied in all configurations and the remaining 15 electrons were correlated, denoted as MRCISD(Q)(15e/12o)/AVTZ.

As the whole N_3 PES consists of linear, bend and cyclic N_3 region, efficient sampling of the N_3 configuration spaces would be important to construct the full potential energy surfaces. This is relative easy for a small system with only 3 degree of freedom. Since our interest is mainly on the bounded N_3 region, we first generate a set of grid points, scanning the two short bond length r_1 and r_2 from 1.0 Å to 2.5 Å, with grid increment to be 0.1 Å for bond length shorter than 1.5 Å and 0.2 Åfor longer bond length. When both r_1 and r_2 become large, convergence problem may occur, we check all the calculations and make sure only converged results are included in

the dataset. In this way about 478 points are collected. Then another set of points are generated by randomly choose about 1000 configurations from trajectories based on a preliminary surface. These supplementary data points fill the vacancies in the grid and helps to have a better sampling of the configurational space. Finally, we exclude those configurations which has energy higher than 300 kcal/mol and obtain 1504 points for the fitting. It is noted that our scan of bond length up to 2.5 Å might not be enough to ensure a correct behavior of potential energy surfaces at long range. In principle a few points with much longer bond length should be included in the dataset in order to describe the dissociation limit of N_3, but our dataset should satisfy the purpose to investigate the cyclization process of N_3 at the bounded N_3 region. However, more calculations are expected to be performed at the dissociated N_3 region later as an improvement of our current surfaces.

Molpro 2006.1[30] was used for all the MRCISD(Q) calculations. As 5 states are evaluated simutaneously, these calculations are extremely heavy so that each configuration takes about 3 days for a single CPU. We have calculated in total around 1500 configurations, which sums up to about 4500 single CPU days, and takes about 3 months if 50 CPUs are working continuously.

4.3 Global Fit

The complete procedure for applying the computational invariant theory in building up PES is rather complicated for a molecule with several atoms. It may invovle constructing thousands of basis functions and evaluating tens of thousands configuration energies. However, for our N_3 molecule with degree of freedom only 3, the process is relatively easy. Therefore, we will demonstrate the procedure in details in the following context.

The primal variable for PES construction based on this method is internuclear distances. There are 3 internuclear distances for N_3 molecule, and we denote them as

$r_1, r_2, \text{and} r_3$, based on which we define the following auxillary variables x_i,

$$x_i = exp(-\gamma r_i) \tag{4.1}$$

Here γ is a constant number usually between 0 and 1, and might have different optimum numbers for various systems. In our N_3 PES fitting, we take it as 0.6. Then we construct the permutational invariant basis from these three auxillary variables:

$$p_1 = x_1 + x_2 + x_3 \tag{4.2}$$

$$p_2 = x_1^2 + x_2^2 + x_3^2 \tag{4.3}$$

$$p_3 = x_1^3 + x_2^3 + x_3^3 \tag{4.4}$$

It is easy to see that these basis are permutational invariant, that is, if we interchange two N atoms, thus switching x_i and $x_j, i \neq j$, the basis $p_i, i = 1, 2, 3$ are kept unchanged. Since the energy functions are simply polynomials of these permutational invariant basis, the PES constructed in this way satisfy the property of permutatioanl invariance. Note that for N_3 molecule, the number of internuclear distances is only 3, and equals the degree of freedom, thus no redundant coordinate is present. However, for a molecule with more than 5 atoms, the number of internuclear distances will be more than the degree of freedom, which significantly increase the number of basis functions, hence the complexity in constructing the PES. These three basis we obtained above are called *primary* invariants. In the computational invariant theory, the algebra of invariant polynomials are generated by both *primary* invariants and *secondary* invariants.[21] Usually for a system with heteronuclear atoms, the number of secondary invariants is much larger than the number of *primary* invariants, which is equal to the number of internuclear distances. However, as only N atoms are present in N_3 molecule, the only *secondary* invariant is 1, which again simplify the construction of potential energy surface. With these permutational invariant basis, the final

energy function is simply written down as following polynomials:

$$
\begin{aligned}
&\text{0th order term : } 1\\
&\text{1st order term : } p_1\\
&\text{2nd order term : } p_1^2, p_2\\
&\text{3rd order term : } p_1^3, p_1p_2, p_3\\
&\text{4th order term : } p_1^4, p_1^2p_2, p_1p_3, p_2^2\\
&\text{5th order term : } p_1^5, p_1^3p_2, p_1p_2^2, p_1^2p_3, p_2p_3\\
&\text{6th order term : } p_1^6, p_1^4p_2, p_1^2p_2^2, p_1^3p_3, p_1p_2p_3, p_2^3, p_3^2\\
&\text{7th order term : } p_1^7, p_1^5p_2, p_1^3p_2^2, p_1p_2^3, p_1^4p_3, p_1p_3^2, p_1^2p_2p_3, p_2^2p_3\\
&\text{8th order term : } p_1^8, p_1^6p_2, p_1^4p_2^2, p_1^2p_2^3, p_2^4, p_1^5p_3, p_1^2p_3^2, p_1^3p_2p_3, p_1p_2^2p_3, p_2p_3^2\\
&\text{9th order term : } p_1^9, p_1^7p_2, p_1^5p_2^2, p_1^3p_2^3, p_1p_2^4, p_1^6p_3, p_1^3p_3^2, p_3^3, p_1^4p_2p_3, p_1^2p_2^2p_3, p_1p_2p_3^2, p_2^3p_3
\end{aligned}
\tag{4.5}
$$

Typically, the fit with polynomial terms at low order degrees would be sufficient to describe the PES. Huang[22] polynomials up to 7 degree to construct H5O2+ surface, where redundant coordinates are present and thousands of polynomial terms are used. For our small N_3 system, it is relatively easy to include high order degree terms. We performed the fit with 7, 8, and 9 degree polynomials, while the largest number of coefficients to be determined for 9 degree polynomials is only 53.

To determine the coefficients for the energy functions, a weighted least square fit is employed. The problem size is well defined as $n \times m$, where n is the number of configurations in the dataset, and m is the number of polynomials terms in the energy functions. For our small system, the solution to this least square problem is trivially achieved by Matlab. The weight $\delta/[\delta + f(k) - f_{\min}]$ is given to the kth entry of the dataset with ab initio energy $f(k)$, where $f_{\min}$ is the N_3 linear ground doublet state potential energy obtained by ab initio calculation at MRCISD(Q)/AVTZ level and

the parameter δ is set to be 0.2 hartree.

4.4 Local Fit

As illustrated in previsou chapter, there are many conical intersections (CI) among these 5 low-lying states. We have located 9 minimum on seam of crossings (MSXs) in C_{2v} symmetry, and all of them cross between states with different symmetry. Now since we are constructing PESs under C_s point group, we have to correlate those states in a lower symmetry. Under C_s point group, 4 of these conical intersections are crossings between states within the same symmetry and the rest 5 are between states of different symmetry. We designate these 9 conical intersections from CI1 to CI9, and list the geometric parameters and energies of corresponding MSXs in Table 4.1. CI1 and CI2 are crossings at the equilateral triangle region, between two lowest A'' states (denoted as $1^2A''$ and $2^2A''$) and two lowest $^2A'$ states (denoted as $1^2A'$ and $2^2A'$), respectively; CI3 is the crossing between $1^2A'$ and $2^2A'$ at the bend N_3 region with $\angle NNN \approx 110°$; CI4 is the crossing between $2^2A'$ and $3^2A'$ (the third $^2A'$ state) at the linear region. According to the conical intersection theory, the dimension of the crossing hypersurfaces for these 4 CIs are $3 - 2 = 1$, which is a line for N_3 molecule. The other 5 CIs, from CI5 to CI9, are formed between $^2A'$ and A'' states. Most of them, CI5-CI8, are in the bend N_3 region, with $\angle NNN$ angle ranging from 78° to 126°. The CI9 is again in linear region, actually it is essentially the same one as CI4, as they are formed by $^2\Sigma_g^+$ and degenerate $^2\Pi_u$ states. Since these 5 CIs are formed with 2 different symmetry states, the condition $H_{12} = 0$ is automatically satisfied for a conical intersection, thus the dimenstion of the crossing hypersurfaces is $3 - 1 = 2$.

It is the first 4 conical intersections, CI1-CI4, that needs to be paid more attentions for of potential energy surfaces construction. Since the two invovled crossing states have same symmetry, the interactions between them are large when 2 states come close, and the adiabatical PESs will suffer drastic energy variations with respect to

the nuclear geometry. Therefore, although the fits for global PESs perform well in general, it is supposed to be bad in these CI regions, as the potential energy functions are only capable to describe smooth surfaces. If we look at the surfaces obtained by global fits at these CI regions, the two PESs are smoothed out but never cross.

4.4.1 Formulation of special local fit

In order to catch the correct feature of the adiabatic PES at CI region, we decide to do a local fit around these CI regions. Considering that the diabatic electronic wavefunctions reflect more clearly the physics of problem in concern and have more smooth potential energy curves, we chose to perform the local fit of adiabatic surfaces orginated from these diabatic states. We only consider the conical intersections involved with two states, and denote U_{11} and U_{22} as the energies in diabatic representation, U_{12} as the nonadiabatic coupling potential. Also we denote V_1 and V_2 as the adiabatic energy, which can be obtained by diagonalize the matrix in the diabatic representation:

$$\begin{bmatrix} U_{11} & U_{12} \\ U_{12} & U_{22} \end{bmatrix} \tag{4.6}$$

The solution is simple and well defined:

$$(U_{11} - V)(U_{22} - V) - U_{12}^2 = 0 \tag{4.7}$$

$$V^2 - (U_{11} + U_{22})V + (U_{11}U_{22} - U_{12}^2) = 0 \tag{4.8}$$

The adiabatic energy is related with diabatic energy and coupling potentials in the following formulae:

$$V_1 = \frac{1}{2}\left[(U_{11} + U_{22}) - \sqrt{(U_{11} - U_{22})^2 + 4U_{12}^2}\right] \tag{4.9}$$

$$V_2 = \frac{1}{2}\left[(U_{11} + U_{22}) + \sqrt{(U_{11} - U_{22})^2 + 4U_{12}^2}\right] \tag{4.10}$$

After a little transformation, we obtain:

$$V_1 + V_2 = U_{11} + U_{22} \tag{4.11}$$

$$(V_2 - V_1)^2 = (U_{11} - U_{22})^2 + 4U_{12}^2 \tag{4.12}$$

Ideally, at the CI region, U_{11}, U_{22}, and U_{12} should be linearly dependent on the CI coordinates. Therefore, instead of fitting the two adiabatic surface V_1 and V_2 sepearately, we can fit $V_1 + V_2$ and $V_2 - V_1$ with low degree polynomials.

$$V_1 + V_2 = g_1 \tag{4.13}$$

$$(V_2 - V_1)^2 = g_2 \tag{4.14}$$

Although this fit should in principle use CI coordinates as basis functions, to be consistent with our global fitting, we employ here the same permutational invariant basis for this special locat fit, which performs very well. For the relative small CI region, we only use polynomials up to 6 degree for this special fit instead of 9 degree in the global fitting.

To get the adiabatic energy of the two states, V_1 and V_2, we can simply transform back the functions g_1 and g_2:

$$V_1 = g_1 - \sqrt{g_2} \tag{4.15}$$

$$V_2 = g_1 + \sqrt{g_2} \tag{4.16}$$

In this way, the square root feature is built in for V_1 and V_2, thus catching correct behaviour of the adiabatic PES at CI region.

Another practical issue need to be considered for this special fitting is to ensure the nonnegativity of function g_2 throughout the CI region. By definition, the function g_2 is the square of the difference between the adiabatic energy of the two states. At the

conincal intersections, V_1 and V_2 come close and become degenerate, but there is no guarantee that nonnegativity of g_2 would be ensured with the standard least square fitting. To overcome this difficulty, a constrained least square fitting is employed here, which can be expressed as:

$$\begin{cases} \min & \|Ex - b\| \\ \text{s.t.} & Gx \geq 0 \end{cases} \tag{4.17}$$

The inequality constrained least square fitting has been well studied and the standard procedure to solve this problem exsist, and has been demonstrated in chapter 1 of this thesis as an essectial numerical technique used in our gas-phase study. To properly apply the constraint, we can simply choose the constrained matrix $G = E$ so that nonegativity of function g_2 is ensured at least for the input dataset for the fitting. However, to ensure the nonnegativity more strictly throughtout the CI region, a dense grid points along the CI line should be used to generating the constration matrix G.

4.4.2 Define the local CI region

As have been mentioned before, the dimension of crossing hypersurfaces for CI1 to CI4 is 1, which means the conical intersections is a line. When crossing occurs, two condtions $U_{11} = U_{22}$, and $U_{12} = 0$ should be satisfied simutaneously. Therefore, the crossing always happens when the two bond length $r_1 = r_2$, in which case N_3 moleucle has a higher C_{2v} point group symmetry, and the two invovled states become of different symmetry, thus the condition $U_{12} = 0$ is automatically satisfied. In order to define the CI region, we first find the crossing line with such geometric constrint, and then defined a column around this croosing line to be the CI region.

The CI1 crossing, which locates in the equilateral triangle region, has been well studied before.[19,15] Under C_s point group, it is between $1^2A''$ and $2^2A''$ states; while in C_{2v} point group, these two states are in $1A_2$ and $1B_1$ states. At the equilateral triangle geometry, the degneracy of $1A_2$ and $1B_1$ states is enforced automatically by symmetry. Thus, we define the crossing line is along the direction $(1, 1, \sqrt{2(1 - cos\theta)}$,

here $\theta = 60°$ for CI1. As plotted in Figure 4.1 (a), for any point A (r_1, r_2, r_3) close to CI1, the projection of A to this line is B $(u, u, u\sqrt{2(1-cos\theta)})$, where $u = (r_1 + r_2 + r_3)/(2 + \sqrt{2(1-cos\theta)})$. The distance between O and B is:

$$l = |OB| = u\sqrt{4 - 2cos\theta} \tag{4.18}$$

The distance between A and B is:

$$ad = |AB| = \sqrt{(r_1 - u)^2 + (r_2 - u)^2 + (r_3 - u)^2} \tag{4.19}$$

Define $\zeta = d/l$, and the CI region we choose here is $\zeta \leq 0.1$. By this choice, we let r_1, and r_2 to have larger deviations when the equilateral triangle is larger, but we keep the relative deviation the same. The choice of 0.1 is arbitrary, but numerical test suggested it is reasonable as the fit works well.

CI2 is the crossing between the two lowest $^2A'$ states instead of A'' states at equilateral triangle region. Under C_{2v} point group the two involved states are $1A_1$ and $1B_2$. A MSX exist at the exact equilateral triangle gemoetry for this conical intersection. However, as shown in previous chapter, a third $^2A'$ (or second $^2B_2$) state come close in energy at this region and another MSX is located in vicinity with $\angle NNN$ angle around 58°. This 3 three states crossing feature make the potential energy surfaces much more complicated hence beyond our two states local fitting scheme. Considering that this CI2 is very high in energy with MSX around 140 kcal/mol, it would not be very important in cyclization dyanmcis, we decide to ignore the local fit for this conical intersection.

Like CI2, CI3 crossing is also between $1^2A''$ and $2^2A''$ states under C_s point group, or $1A_2$ and $1B_1$ states under C_{2v} point group, but at the bend N_3 region, where $\angle NNN \approx 110$. The MSX occurs with $r_1 = r_2 = 1.257$ Å and $\angle NNN = 110.3°$. When r_1 and r_2 changes, the angle $\angle NNN$ which satisfy the degeneracy of these

two states also changes. However, this angle change is rather small, at about only 1 degree if the r changes from 1.0 Å to 1.7 Å. Since our goal is to define the CI region, it is not nessary to obtain the exact analytic function of this CI line. Therefore, as a good approximation, we simply define the CI3 crossing line similar to CI1, along the direction $(1, 1, \sqrt{2(1 - cos\theta)}$, but here $\theta = 110°$. Take the same procedure, for any point $A(r_1, r_2, r_3)$ close to CI3, we can obtain u, and thus d and l. Again, we will denote $\zeta = d/l$, and define the CI region as $\zeta \leq 0.1$.

The last conical intersection of interest, CI4, is the crossing between $2^2A'$ and $3^2A'$ states under C_s point group, or $1B_1$ and 2^2B_2 state under C_{2v} point group. The MSX of CI4 at $\angle NNN = 180°$ has bond length $r_1 = r_2 = 1.227$ Å. At this particular geometry, the molecule is in $D_{\infty h}$ point group and the symmetry of the two invovled states are Σ_u^+ and Π_u. Unlike the other three conical intersections, CI1 to CI3, where the $\angle NNN$ angle keeps almost constant with the change of bond length, for CI4, the bond length keeps almost constant at around 1.2 Å while the $\angle NNN$ angle deviates away from 180°. Since we are more interested in the linear region, we define the crossing region to be $160° \leq \angle NNN \leq 180°$. Again, like CI3, we did not obtain the exact function of CI line, but approximate it with the line $r_1 = r_2 = 1.2$ Å. As shown in Figure 4.1 (b), for any point $A(r_1, r_2, r_3)$ close to this line, the projection of A to this line is B $(1.2, 1.2, r_3)$. The distance between A and B is:

$$d = |AB| = \sqrt{(r_1 - 1.2)^2 + (r_2 - 1.2)^2} \tag{4.20}$$

The definition of l will not be very meaningful in this case, so we simply define $\zeta = d$, and then choose the CI region to be $\zeta \leq 0.15$ for CI4.

4.4.3 Connectting global surface and local surface

Another issue arised with this speical CI fit is how to connect the global PES and local CI PES smoothly. A switching function is used to get around this issue. The

final energy expression is in the following form:

$$V = V^L + S(\zeta)(V^G - V^L) \tag{4.21}$$

with switching functions taken from the reference[31]

$$S(\zeta) = \begin{cases} 1 & \zeta < \zeta_1 \\ 10\chi^3 - 15\chi^4 + 6\chi^5 & \zeta_1 \leq \zeta \leq \zeta_2 \\ 0 & \zeta > \zeta_2 \end{cases} \tag{4.22}$$

where

$$\chi = \frac{exp(\lambda(\zeta - \zeta_1)) - 1}{exp(\lambda(\zeta_2 - \zeta_1)) - 1} \tag{4.23}$$

It is easy to conform that with such choice of switching functions, both first derivative and second derivative are continuous at the boundary region.

4.5 Diabatization for CI3

The adiabatic surface fit is more or less done at this point. However, for the purpose of dynamic simulation with surface hopping, the diabatic states energies are preferred and the nonadiabatic coupling potentials are needed at the CI region. Therefore, the diabatization of conical intersetions is necessary. Since the ring clourse process, during which N_3 molecule transforms from linear to cyclic, is what we are most interested, we only diabatized CI3, which is in the bend N_3 region and could be important in this ring clousure process. Since CI1 and CI2 are already in cyclic region, while CI4 is in linear region, and also CI2 and CI4 have high energy, thus less important in the process, we neglect to do diabatization for these three CIs.

We choose to do an approximate diabatizaiton by analyzing CI vectors of the two states based on the method introduced in reference.[32,33] The idea for this diabatization scheme is to maximize the square of coefficients for the main configurations

of the two states. The detials of the diabatization process has been illustrated in chapter 1.

We randomly generated about 100 configuration around the CI3, and followed the diabatization processure describled above to obtain the diabatic energy U_{11}, U_{22} for the two states and the nonadiabatic matrix element U_{12}. Again, we want to fit these U_{11}, U_{22} and U_{12} with some analytical functions to obtain diabatic surfaces. Since U_{11} and U_{22} are smooth continuous functions and have the intrinsic property of invariance with respect to the permutation of like nuclei, we use permutational invariant basis in the fitting as in global and local fitting, with polynomial terms up to 6 degree. However, the nature of U_{12} is substantially different from U_{11}, U_{22}. Because of the CI phase effect, U_{12} is not permutational invariant. When passing through the conical intersections, the sign of U_{12} should change. Therefore, the coordinate (r_1, r_2, r_3) is not equivalent to (r_2, r_1, r_3) for U_{12} surface, U_{12} is asymmetric with respect to the coordinate $r_1 - r_2$. If U_{12} is fitted with permuational invariant basis, this phase effect will not be able to be distinguished. When the sign changes occur, the first derivative will not be continuous for such fitting. In addition, due to the small absolute value of U_{12}, over fitting might occur. Therefore, instead of using the permutational invariant basis, we use normal cordinate for the fitting. The basis functions that we used are $(r_1 + r_2)/2$, $(r_1 - r_2)/2$, and r_3. Polynomials up to 3rd degree are used in this fitting, with function form as follows:

$$\begin{aligned} U =& c_1 + c_2 p_1 + c_3 p_2 + c_4 p_3 + c_5 p_1^2 + c_6 p_2^2 + c_7 p_3^2 + c_8 p_1 p_2 + c_9 p_2 p_3 + c_{10} p_3 p_1 \\ &+ c_{11} p_1^3 + c_{12} p_2^3 + c_{13} p_3^3 + c_{14} p_1^2 p_2 + c_{15} p_1^2 p_3 + c_{16} p_2^2 p_3 + c_{17} p_2^2 p_1 \\ &+ c_{18} p_3^2 p_1 + c_{19} p_3^2 p_2 + c_{20} p_1 p_2 p_3 \end{aligned} \tag{4.24}$$

where

$$\begin{aligned} p_1 &= (r_1 + r_2)/2 \\ p_2 &= -(r_1 - r_2)/2 \\ p_3 &= r_3 \end{aligned} \tag{4.25}$$

Since the diabatic couplings U_{12} is asymmetric with respect to the asymmetric coordinate p_2, only odd terms of this coordinates are included in the fitting of U_{12}. The situation is opposite for U_{11} and U_{22}, thus only even p_2 terms were used in these two fittings with normal coordinates.

4.6 Results and Discussion

4.6.1 Fitting errors

A. Global fit

We performed the global fit for N_3 5 lowest states with polynomial degrees 7, 8, and 9, and summarized fitting errors in Table 4.2. The root mean square errors are about 2-3 kcal/mol for the 5 surfaces, while the maximum deviation could be rather large, about 10 kcal/mol for lower state and increase to about 20 kcal/mol for hige energy state. It is not surprised that states with higher energy always have larger fitting errors. Also, as the degree of polynomial terms increases, rms fitting errors decreases. For lower state $1^2A'$ and $1^2A''$, the rms errors are reduced from around 3 kcal/mol at 7 degree fit to less than 2 kcal/mol at 9 degree fit; for $2^2A'$ and $3^2A'$ states, rms errors are reduced about 0.5 kcal/mol; while for $2^2A''$ state, this improvement is about 2 kcal/mol. The improvement of maximum fitting errors is not very significant for $^2A'$ states when the higher order polynomial terms are used, but more significant effect are observed for the A'' states, in particular $2^2A''$ state, where e_{max} is reduced by half from about 26 kcal/mol to less than 13 kcal/mol. It is expected that the rms

error would be further reduced with even higher degree polynomials, but this decrease would not be significant so we stop at 9 degree. The reason that a higher order fit is necessary for the N_3 molecule is due to the high potential energies and complicated feature of the potential energy surfaces. As we have known from the previous chapter and other studies,[15] at the linear region, there exsist 2 excited stationary points, both of which are more than 100 kcal/mol in energy. At the bend region, all 5 states come close in energy and crossing occurs between the two lowest $^2A'$ surfaces. While at the cyclic region, although two stationary points in $^2A''$ symmetry has energy at around only 30 kcal/mol above the ground state minimum, a conical intersection is present. Also, unlike H5O2+ molecule, which has redundant independant variables with respect to its degree of freedom, N_3 primary invariants is equal to its number of freedom. This lack of redundancy may also require a higher order fit for a better description of potential energy surfaces.

B. Local fit

Because of the intrinsic problem for fitting PESs around the conical intersections formed by crossing between states with the same symmetry, we performed 3 additional constrained local fit for CI1, CI3 and CI4 conical intersection. The fitting errors for these local fits are listed in Table 4.3. From CI1 to CI4, the energy of these conical intersections increases, therefore the fitting errors increase accordingly. The CI1 local fit is apprantly the best fit in these 3, with rms error only 0.02 kcal/mol and maimum error 0.16 kcal/mol for both involved states. The magnitute of fitting errors increase an order for CI2 and CI3 concical intersections, and CI3 errors are about 2 times larger than the CI2 errors. To better understand the origin of these errors, we break down the fit and analyzed the fitting errors for function g_1 and g_2. It is found that the local fitting errors are mainly from g_2 fitting. As defined in previous section, g_1 is the sum of the adiabatical energy of two states, and should be linear around the CI region; while g_2 is the square of difference between two states adiabatic energy,

thus include second order terms and should have quadratic behaviour. Since we fit both function g_1 and g_2 with 6 degree polynomials, it is understandable that g_2 would have larger fitting errors. As the fitting errors are rather small, we are satisfied with these results. However, one can easily improve these local fits by increase the degree of polynomials for the g_2 function fit.

We plot the 2 dimensional potential energy surfaces around the regions where local fits are performed in Figure 4.2 4.3 4.4. Also, a few 1d-cut of potential energy surfaces at various bond angles and bond lengths are ploted in Figure 4.5 4.6 4.7 for CI1, CI3 and CI4, respectively. One can clearly see the improvements made by the local fit. For all 3 concial intersections, we only observe two surfaces come close at the CI region but no real crossings. However, two adiabatic surfaces do cross in our local fits. Also, in some cases stationary points might be in these CI region. The naive global fit may predict totally wrong geometries and energies for these important configurations on potential energy surfaces, like the $2^2A'$ minimum around CI3 region, or even miss some of these stationary points, like the case in CI4 region. Therefore, our special local fits are indispensable in describing these critical features on potential energy surfaces.

The final potential energy curves are in combination with the global fits and local fits. One can see in some cases the transitions from local fits to global fits do not look very natural. Although our switching functions ensure the continuity of derivatives of potential enrgy curves, small bumps might be present on the surfaces when the difference between global fits and local fits is large. In pincipal the transition would look more smoothly when the switching functions are applied at the places where global fits and local fits are close in energy, but this is rather hard to achieve. Therefore, we observe the little bumps for the upper $2^2A'$ state of CI3 at the region where $\angle NNN \leq 110^\circ$. We noticed that the $2^2A'$ enrgy from global fit is largely underestimated so that the crossing between the global surfaces are very close to the

CI3 crossing line at 110°, as shown in figure 4.6. If we made smooth transition by adjusting the swtiching functions, the final fit would not be good as the energies from global fits are bad here. Therefore there is a delima of whether to have a smooth transition or to reduce the fitting errors. In this case since the $2^2A'$ state are very high in energy at around 100 kcal/mol, we think the not so smooth trasistion, the bump, would not be a big issue.

4.6.2 Stationary points on adiabatical surfaces

As discussed in previous chapter, many stationary points have been located on these 5 low-lying potential energy surfaces. To check the quality of our surfaces, we examined our PESs in details and located the stationary points based on our PES as well. The structures and energies of these stationary points are compared with ab initio values at MRCISD(Q) level and shown in Table 4.4. We disucss them in the following context.

A. $^2A'$ surfaces

The $^2A'$ state in Cs point group may correlate to $^2A_1$ and $^2B_2$ states when N_3 has two equivalent bond length and in C_{2v} symmetry. Since $^2A_1$ and $^2B_2$ surfaces cross at around 110° and form CI3, in the region where $\angle NNN \leq 110°$, the $1^2A'$ surface will corresond to $^2A_1$ state, which is lower than $^2B_2$ state; while in the region where $\angle NNN \geq 110°$ and $^2B_2$ lower than $^2A_1$, $^2B_2$ will be $1^2A'$ adiabatical surface.

There are two stationary points on the $1^2A'$ surface, one is the doublet N_3 linear ground state $^2\Pi_g$, and the other is bend N_3 in the $^2A_1$ state. The linear ground state has been well studied before, with experimental bond length 1.181 Å[4] and theoretical value 1.185 Å at the MRCISD(Q)/AVTZ level.[15] The structure obtained from our $1^2A'$ surface has exactly the same bond length, 1.185 Å. Since we use the ab initio energy of N_3 ground state obtained from MRCISD(Q) calculation to be the reference point, the energy is not exactly 0 from our PES, but determined to be -0.94 kcal/mol. For the bend $^2A_1$ state, MRCISD(Q) calculation determines its bond length to be

1.259 Å and $\angle NNN$ angle 107.0°, with energy about 66.64 kcal/mol above the linear ground double state $^2\Pi_g$. We notice that this structure is very close to CI3 (see Table 4.1), the conical intersection between $1^2A'$ and 2A' surfaces around 110°. Without the special local fit at CI3, large devieation would be expected. However, from our PES, we obtain this geometry with bond length 1.257 Å very clsoe to the ab initio value, and $\angle NNN$ angle 108.7°, about 1.7° off from the ab initio value. In addition, our PES energy for this structure is 66.16 kcal/mol, again very close to the ab initio calculations.

For $2^2A'$ surface, in general it correlates to $^2B_2$ state in the region where $\angle NNN \leq 110°$ and $^2A_1$ state elsewhere. However, due to the exsistence of CI4, $2^2A'$ correlates to 2^2B_2 state when the bond length is smaller than 1.2 Å in the linear region. Therefore, two linear stationary points are there on $2^2A'$ surfaces, corresponding to N_3 excited states $\tilde{A}^2\Sigma_u^+$ (2^2B_2) and $\tilde{B}^2\Pi_u$ ($^2A_1$). Zhang determined the bond length of these two states to be 1.185 Å and 1.276 Å respectively at MRCISD(Q) level,[15] while our PESs predict them to be 1.184 Å and 1.273 Å, almost identical to ab initio values. The energy for these two state are very close, with 104.87 kcal/mol for $\tilde{A}^2\Sigma_u^+$ and 104.19 kcal/mol for $\tilde{B}^2\Pi_u$ from ab initio calculations. Our PESs give excellent agreement at the value 104.31 kcal/mol and 104.19 kcal/mol for each state. Again, since these two states are very close to CI4 conical intersection, our special local fit is very crucial here to obtain these two stationary points. The global fit will not be able to catch up the subtle change of the adiabatic $2^2A'$ potential energy surface at this linear region so that only one state could be obtained, which, of course, is expected to be farther away from either of the true states $\tilde{A}^2\Sigma_u^+$ and $\tilde{B}^2\Pi_u$. However, with our special local fit, both of these two states are predicted pretty accurately from our PES. As $\angle NNN$ decrease, the energy of $2^2A'$ state become smaller and reach the CI3 conincal intersection, then the energy climb up again and no other stationary point is found on the $2^2A'$ surface.

The $3^2A'$ surface should mainly correlate to 2^2B_2 state except in the linear region when bond length larger than 1.2 Å, where $^2A_1$ state is higher in energy. Only 1 stationary point is on this $3^2A'$ surface, locate at the bend region in 2^2B_2 state, with bond length 1.310 Å $\angle NNN$ angle 100.5°, and energy 112.02 kcal/mol at MR-CISD(Q) level. It seems that our PES for $3^2A'$ surface has some problem here at the bend region, we only locate a minimum with bond length 1.270 Å $\angle NNN$ angle 126.4°, and energy 106.69 kcal/mol. Both the structure and energy have large deviation from the ab initio calculations, indicating that our PES has some intrinsic problem at this region. It is possible that a second $^2A_1$ state may come close in energy at the bend region thus affect the $3^2A'$ surface, but it needs further check. Since $3^2A'$ surface is very high in enrgy and this 2^2B_2 minimum is not very important on the surface, we will ignore this issue and try to improve the surface later if needed.

B. $^2A''$ surfaces

Because of CI1 at equilateral triangle region, when $\angle NNN \leq 60°$, $1^2A''$ surface will correspond to 1^2B_1 state. Outside this small cyclic region, 1^2A_2 is lower in energy, and will correlate to the $1^2A''$ adiabatical surface. There are four stationary points on the adiabatical $1^2A''$ surafce, which are the linear ground doublet state $\tilde{X}^2\Pi_g$, bend state 1^2A_2 and 1^2A_2_TS, and the cyclic state 1^2B_1. Since the linear N_3 ground state $\tilde{X}^2\Pi_g$ is doubly degenerate, the linear minimum on $1^2A''$ surface should be essentially the same one one on $1^2A'$ surface. As $1^2A'$ and $1^2A''$ surface come from two seperate fit, these two states are not exactly the same from our PES. The linear minimum on our $1^2A''$ PES has bond length 1.186 Å and energy -0.71 kcal/mol, 0.001 Ålonger and 0.23 kcal/mol higher than the $1^2A'$ counterpart. This small difference and great agreement to ab initio values indicate nice fit for both surfaces at this linear region. As $\angle NNN$ angle decrease, the $1^2A''$ state rises up and reach the second order stationary point $^2A_2$_TS which has two imaginary frequencies in a_1 and b_2 symmetry.[15] We identify this $^2A_2$_TS from our PES with bond length 1.284 Åand $\angle NNN$ angle

106.7°, compared to 1.289 Åand 109.0° from ab initio MRCISD(Q) calculation. The 0.005 Å difference in bond length and 2.3° difference in angle are not very large; however, the PES energy for this $^2A_2$_TS is only 62.70 kcal/mol, 3.37 kcal/mol lower than the ab initio MRCISD(Q) value 66.07 kcal/mol. Moreover, if we follow the b_2 vibration, it should reach the real isomerization TS in Cs symmetry between the linear ground state ($\tilde{X}^2\Pi_g$) and the cyclic N_3 (1^2B_1). Nevertheless, we found that this $^2A_2$_TS is only a first order stationary point, and no such Cs transition state could be located from our surface. All these indicate that our $1^2A''$ PES is not very good at this bend region, probably due to the approaching of a second $^2A_2$ state, and need further improvement. While following the remaining a_1 vibration, another stationary point, 1^2A_2 is reached on $1^2A''$ surface. Previous study[15] shows that this state is actually a transition state between two equivalent cyclic N_3 (1^2B_1). We locate this 1^2A_2 state on our PES with bond length 1.305 Å and bond angle 72.0°, both are very close to the ab initio MRCISD(Q) values 1.306 Å and 71.1°. The energy is a little bit off, with PES value 35.57 kcal/mol, 2.46 kcal/mol higher compared to the ab initio value 33.11 kcal/mol. The last stationary point on $1^2A''$ surface, is the cyclic N_3 minimum 1^2B_1, which arise great interest in both theoretical and experimental studies due to its unique feature. Ab initio calculation at MRCISD(Q) level determines the bond length and bond angle of cyclic N_3 to be 1.467 Å and 49.8°, respectively. Also, its energy is calculated to be 32.22 kcal/mol above the linear ground state at the same level of theory. From our PES, we identify the cyclic N_3 on $1^2A''$ surface with bond lenth 1.511 Å and bond angle 47.0°. The 0.044 Å difference in bond length and 2.8° difference in bond angle is relative large for this important minimum. However, the PES energy is identified to be 32.35 kcal/mol, very close to the ab initio value. We notice that this 1^2B_1 cyclic N_3 structure is close to the CI1 conical intersection, and as bond angle decrease further, $1^2A''$ state energy will increase dramatically. These complicated feature of $1^2A''$ potential energy surface might be the reason for the flaw

of fit at this cyclic region.

The $2^2A''$ surface mainly correlate to $^2B_1$ state in C_{2v} symmetry, except for the cyclic region where $\angle NNN$ less than 60° and $^2A_2$ is higher in energy, yet no stationary point is located at this region. 3 stationary points are located on $2^2A''$ surfaces. Again, there is a linear structure, corresponding to the degenerated $\tilde{B}^2\Pi_u$ state. The geometry obtained from $2^2A''$ PES is exactly the same as the one obtained from $1^2A''$, with bond length 1.273 Å. Despite the degenerate geomerty for $\tilde{B}^2\Pi_u$ state from $2^2A'$ and $2^2A''$ surface, energy is not degenerated from our PES, with $2^2A''$ PES energy 106.62 kcal/mol, 2.46 kcal/mol above the $2^2A'$ PES energy. The better agreement in energy for $1^2A'$ linear minimum is due to the local fit, which is supposed to be more accurate then the $2^2A''$ PES energy obtained from global fit. As bond angle becomes smaller, energy decrease and another stationary point $^2B_1$_2 state is reached. We have discussed this state in previous chapter and the geometry parameter is determined to be $r_{NN} = 1.266$Å and $\angle NNN = 120.5°$ at the MRCISD(Q) level. Our PES gives fairly good agreement with bond length 1.253 Åand bond angle 123.6°. The PES energy is also about 2 kcal/mol off, at about 70.73 kcal/mol compared to ab initio value 72.80 kcal/mol. Then energy will rise again as bond angle $\angle NNN$ decreses more, and reach the $^2B_1$_TS transition state. The MRCISD(Q) calculation determines the structure of this state to be 1.362 Åin bond length and 86.1° in bond angle, with energy about 109.11 kcal/mol. From our PES, we locate this $^2B_1$ transition state with bond length 1.343 Å, bond angle 86.4°, and energy 103.83 kcal/mol. Although the geometry agrees fairly good, the energy is 5.28 kcal/mol off, indicating some difficulties in fitting at this region.

4.6.3 Conincal intersections

It is also important to check the conical intersections on our PESs. We have obtained the structures and energies of the MSXs for each conical intersections and compared them with ab initio values as shown in Table 4.4. Again, due to the complicated

feature of CI2 and its high eneregy, we will neglect this conical intersection and not discuss it in the following context.

A. CIs with same symmetry

The regions where two surfaces with the same symmetry cross are the most difficult part for fitting the adiabatic surfaces due to the drastic change of potential energies around the CI regions. This intrinsic problem initialize us to make the special local fit of the adiabatic surfaces. Following the procedure in section 4.4, these CIs are described in general very accurately.

CI1 is the crossing between 1^2A_2 and 1^2B_1 states, or $1^2A''$ and $2^2A''$ surfaces in our fit, at equilateral triangle region. Babikov has obtained an accurate fit for the ground state cyclic N_3 including this conical intersection.[19] The ab initio energy for the MSX_D_{3h}_$^2B_1/^2A_2$ at MRCISD(Q) level is 45.37 kcal/mol, and the three equivalent bond length is 1.369 Å. Our PES agree very well with these ab initio values, the energy is determined to be 45.01 kcal/mol while the bond length is exactly the same at 1.369 Å. Although our $1^2A''$ global surface does not perform well at the cyclic region, the local fit for CI1 is very precise. The next conical intersection CI3, is crossing between $^2B_2$ and $^2A_1$ states at the bend region, or adiabatically, the croosing between $1^2A'$ and $2^2A'$ surfaces. We have determined the MSX of this CI3 to have bond length 1.257 Å and bond angle 110.3°. Our PES predict very similar geomtrical parameteres, with $r_{NN} = 1.255$ Å and $\angle NNN = 111.4°$, and even better energy, 66.72 kcal/mol, compared to ab initio value 66.95 kcal/mol. Finally, the last crossing between same symmetry states, CI4 is the crossing between 1^A_1 and 2^2B_2 states, both are in $^2A'$ symmetry. Adiabaticall, it is the crossing between $2^2A'$ and $3^2A'$ adiabatic surfaces, thus relatively high in energy, with MSX calculated to be 108.26 kcal/mol at MRCISD(Q) level. Our PES predict the energy of this MSX to be 107.92 kcal/mol, a little bit lower. While the bond length from PES is 1.225 Å, very close to the ab initio value at 1.227 Å. In general, the local fit has relatively small errors compared

to global fit, as shown in Table 4.3. Therefore, these CIs from our PES are in great agreement with the results from ab initio calcutions.

B. CIs with different symmetry

The conical intersections caused by crosssing between surfaces with different symmetry do not interact with each other so that each can be fitted without problem and no special fit is needed. The accuracy of these CIs are mainly determined by the quality of PESs from global fit, thus may be less precise.

There are 5 such crossings, we label them from CI5 to CI9 with the increase of $\angle NNN$ angle as in table 4.1. CI5 is crossing between $^2A_1$ and $^2B_1$, or $1^2A'$ and $2^2A''$ adiabatically. The MSX is determined to be 96.02 kcal/mol above the ground state, with bond length 1.328 Åand bond angle 78.1°. The structure located on our PES are in fairly good agreement. The energy is slightly higher at 98.74 kcal/mol, the bond length is sligher longer at 1.332 Å, and the bond angle is slightly larger at 79.5°. As for CI6($1^2B_2/1^2B_1$), a crossing between $2^2A'$ and $2^2A''$ surface, the MSX is located by ab initio calculations with energy 109.84 kcal/mol, bond length 1.312 Å and bond angle 87.8°. The MSX found on our PES are quite off both in energy and geometry. The PES energy is 101.35 kcal/mol, more than 8 kcal/mol lower, while the bond length 1.325 Å and bond angle 91.9° are also kind of large deviations. We noticed that our global fit for the $2^2A'$ surface are not very good at this bend region, which is presumably the reason for this large deviations. As $\angle NNN$ angle becomes even larger, another crossing, CI7($^2A_1/^2A_2$) is present between $1^2A'$ and $1^2A''$ surfaces. The ab initio energy for this MSX is 66.61 kcal/mol, with $r_{NN} = 1.261$Å and $\angle NNN = 106.4°$. We have mentioned before that our $1^2A''$ PES is not very accurate at this bend region, therefore, our PES energy is about 3 kcal/mol higer than the MRCISD(Q) value at 69.24 kcal/mol. Also, although PES predict a similar bond angle at 107.0°, the bond length is off by about 0.05 Å at 1.215 Å. In order to get more accurate result of MSX for this CI7, a more accurate $1^2A''$ surface is defintely

indispensable. CI8($^2A_1/^2B_1$), like CI5, is again the crossing between $2^2A'$ and $2^2A''$ surfaces, but at the bend region with larger bond angle. We have located the MSX for this crossing with energy 73.47 Å, bond length 1.267 Å, and bond angle 125.8°. The prediction of our PES for this MSX is not excellent, with energy 70.78 kcal/mol, bond length 1.332 Å, and bond angle 122.5°, all of them are deviated from the ab initio values to some extent. The last crossing, CI9(Σ_u^+/Π_u), is of linear structure with $\angle NNN = 180°$. Ideally, the MSX of this crossing CI9 should be exactly the same one as CI4, due to the double degeneracy of Π_u state. Our local fit does a good job so that the MSX from PES for CI4 is in very good agreement to the true ab initio result, with energy 108.26 kcal/mol and bond length 1.227 Å. However, the MSX obtained from our PES for CI9 has larger deviations, with a slighly higher energy in 109.11 kcal/mol and a slightly longer bond length at 1.232 Å. The agreement is not perfect but fairly good, also it indicates that our $2^2A'$ ($^2A_1$) surface is not strictly degenerate from the $2^2A''$ ($^2B_1$) surface due to the fitting errors when N_3 is linear.

Diabatic surfaces for CI3

We have also fitted the diabatic potentials (U_{11} and U_{22}) and couplings (U_{12}) between $1^2A'$ and $2^2A'$ states at CI3 conical intersections. The fits are done with both permutational invariant basis and normal coordinates, and the fitting errors are shown in table 4.5. As we can see, for U_{11} and U_{22}, the fits with permutational invariant basis gave a much better results, with fitting errors around 0.1 kcal/mol, one order less than the fits with normal coordinates. However, the situation for U_{12} fits is reversed, the fits with normal coordinates generated one order smaller fitting errors compared with the other fits, since permutational invariant basis are intrinsically bad for U_{12} fits.

We presented the two diabatical potential energy surfaces, fitted with permutational invariant basis, and the diabatical coupling potentials, fitted with normal coordinates, in the Figure 4.8. As shown in Figure 4.8 (a), two diabatic surfaces cross

at around $\angle NNN \approx 110°$. Also, as $\angle NNN$ increases from 105° to 115°, two diabatic states swtich order. In figure 4.9, U_{12} surfaces are plotted. The absolute value of this coupling potential is close to 0 when $r_1 = r_2$. It scales linearly with respect to the asymmetric coordinates, and changes sing when passing through conical intersections. At last, the $U_{11} = U_{22}$ surface and $U_{12} = 0$ surface are plotted numerically in Figure 4.10, and the crossing line of these two surfaces indicates the seam of crossing for CI3 conical intersection.

4.7 Summary

In the present work, we have constructed permutional invariant potential energy surfaces for 5 lower lying N_3 states ($3\ ^2A'$ states and $2\ ^2A''$ states) based on 1504 single point calculations at MRCISD(Q) level with aug-cc-pVTZ basis set. The rms fitting errors from the global fits are around 2-3 kcal/mol for these five states. A special local fit was performed at the cyclic, bend, and linear N_3 conical intersection region to improve the quality of these surfaces. The final surfaces are the combinations of global surfaces and lcoal surfaces connected by swtich functions. Details of fitting strategies were presented. Several stationary points on the surfaces, as well as minimum on seam of crossings (MSXs) between these surfaces, were determined from the PESs and compared with available theoretical results. In most cases the agreements are very good, with a few exceptions at high energy configurations. In addition, we diabatized $1^2A'$ and $2^2A'$ states around CI3 conical intersections at the N_3 bend region by analyzing the CI coefficients. These two diabatical potentials are fitted at the same manner as the 5 adiabatical surfaces; while the diabatical couplings are fitted with some normal coordinates. We are going to use these potential energy surfaces to perform dynamic simulations and hopefully to understand N_3 cyclization process in a much better level.

References

1. Samartzis, P. C.; Wodtke, A. M. *INTERNATIONAL REVIEWS IN PHYSICAL CHEMISTRY* **2006**, *25*, 527–552.

2. THRUSH, B. *PROCEEDINGS OF THE ROYAL SOCIETY OF LONDON SERIES A-MATHEMATICAL AND PHYSICAL SCIENCES* **1956**, *235*, 143–&.

3. DOUGLAS, A.; JONES, W. *CANADIAN JOURNAL OF PHYSICS* **1965**, *43*, 2216–&.

4. BRAZIER, C.; BERNATH, P.; BURKHOLDER, J.; HOWARD, C. *JOURNAL OF CHEMICAL PHYSICS* **1988**, *89*, 1762–1767.

5. ARCHIBAL.TW,; SABIN, J. *JOURNAL OF CHEMICAL PHYSICS* **1971**, *55*, 1821–&.

6. DYKE, J.; JONATHAN, N.; LEWIS, A.; MORRIS, A. *MOLECULAR PHYSICS* **1982**, *47*, 1231–1240.

7. MURRELL, J.; NOVARO, O.; CASTILLO, S.; SAUNDERS, V. *CHEMICAL PHYSICS LETTERS* **1982**, *90*, 421–424.

8. BYUN, Y.; SAEBO, S.; PITTMAN, C. *JOURNAL OF THE AMERICAN CHEMICAL SOCIETY* **1991**, *113*, 3689–3696.

9. PETRONGOLO, C. *JOURNAL OF MOLECULAR STRUCTURE* **1988**, *175*, 215–220.

10. MARTIN, J.; FRANCOIS, J.; GIJBELS, R. *JOURNAL OF CHEMICAL PHYSICS* **1989**, *90*, 6469–6485.

11. YU, D.; RAUK, A.; ARMSTRONG, D. *JOURNAL OF PHYSICAL CHEMISTRY* **1992**, *96*, 6031–6038.

12. ZIEGLER, T.; GUTSEV, G. *JOURNAL OF COMPUTATIONAL CHEMISTRY* **1992**, *13*, 70–75.

13. SLUPSKI, R.; WASILEWSKI, J. *INTERNATIONAL JOURNAL OF QUANTUM CHEMISTRY* **1995**, *56*, 655–661.

14. Wasilewski, J. *JOURNAL OF CHEMICAL PHYSICS* **1996**, *105*, 10969–10982.

15. Zhang, P.; Morokuma, K.; Wodtke, A. *JOURNAL OF CHEMICAL PHYSICS* **2005**, *122*, 014106.

16. Bittererova, M.; Ostmark, H.; Brinck, T. *JOURNAL OF CHEMICAL PHYSICS* **2002**, *116*, 9740–9748.

17. Hansen, N.; Wodtke, A. *JOURNAL OF PHYSICAL CHEMISTRY A* **2003**, *107*, 10608–10614.

18. Samartzis, P. C.; Lin, J. J.-M.; Ching, T.-T.; Chaudhuri, C.; Lee, S.-H.; Wodtke, A. M. *JOURNAL OF CHEMICAL PHYSICS* **2007**, *126*, 041101.

19. Babikov, D.; Zhang, P.; Morokuma, K. *JOURNAL OF CHEMICAL PHYSICS* **2004**, *121*, 6743–6749.

20. LEFORESTIER, C.; LEQUERE, F.; YAMASHITA, K.; MOROKUMA, K. *JOURNAL OF CHEMICAL PHYSICS* **1994**, *101*, 3806–3818.

21. Derksen, H.; Kemper, G. *Computational Invariant Theory*, 1st ed.; Springer, 2002; Vol. 130.

22. Huang, X.; Braams, B.; Bowman, J. *JOURNAL OF CHEMICAL PHYSICS* **2005**, *122*, 044308.

23. Brown, A.; Braams, B.; Christoffel, K.; Jin, Z.; Bowman, J. *JOURNAL OF CHEMICAL PHYSICS* **2003**, *119*, 8790–8793.

24. McCoy, A.; Braams, B.; Brown, A.; Huang, X.; Jin, Z.; Bowman, J. *JOURNAL OF PHYSICAL CHEMISTRY A* **2004**, *108*, 4991–4994.

25. Huang, X.; Braams, B.; Carter, S.; Bowman, J. *JOURNAL OF THE AMERICAN CHEMICAL SOCIETY* **2004**, *126*, 5042–5043.

26. WERNER, H.; KNOWLES, P. *JOURNAL OF CHEMICAL PHYSICS* **1988**, *89*, 5803–5814.

27. KNOWLES, P.; WERNER, H. *CHEMICAL PHYSICS LETTERS* **1988**, *145*, 514–522.

28. DAVIDSON, E. *JOURNAL OF COMPUTATIONAL PHYSICS* **1975**, *17*, 87–94.

29. DUNNING, T. *JOURNAL OF CHEMICAL PHYSICS* **1989**, *90*, 1007–1023.

30. Werner, H.-J. et al. *MOLPRO, version 2006.1, a package of ab initio programs*, 2006, see http://www.molpro.net.

31. BOWMAN, J.; GAZDY, B.; SCHAFER, P.; HEAVEN, M. *JOURNAL OF PHYSICAL CHEMISTRY* **1990**, *94*, 2226–2229.

32. RUEDENBERG, K.; ATCHITY, G. *JOURNAL OF CHEMICAL PHYSICS* **1993**, *99*, 3799–3803.

33. Atchity, G.; Ruedenberg, K. *THEORETICAL CHEMISTRY ACCOUNTS* **1997**, *97*, 47–58.

Table 4.1: Conincal intersections of N_3 5 low-lying states

	label	states		geometry[a]		energy(kcal/mol)[a]
		Cs	C_{2v}	r(Å)	$\theta(^\circ)$	
same symmetry	CI1	$1^2A''/2^2A''$	MSX_$^2A_2/^2B_1$	1.3693	60.0	45.37
	CI2	$1^2A'/2^2A'$	MSX_$^2A_1/^2B_2$	1.4578	55.9	142.51
	CI3	$1^2A'/2^2A'$	MSX_$^2A_1/^2B_2$	1.2572	110.3	66.95
	CI4	$2^2A'/3^2A'$	MSX_$^2A_1/2B_2$	1.2271	180.0	108.26
different symmetry	CI5	$1^2A'/2^2A''$	MSX_$^2A_1/^2B_1$_1	1.3280	78.1	96.02
	CI6	$2^2A'/2^2A''$	MSX_$^2B_2/^2B_1$	1.3118	87.8	109.84
	CI7	$1^2A'/1^2A''$	MSX_$^2A_1/^2A_2$	1.2607	106.4	66.61
	CI8	$2^2A'/2^2A''$	MSX_$^2A_1/^2B_1$_2	1.2672	125.8	73.47
	CI9	$3^2A'/2^2A''$	MSX_$^2B_1/2B_2$	1.2271	180.0	108.26

[a] The geometry parameters and energies are determined at MRCISD(Q)/AVQZ level.

Table 4.2: Fitting errors for the 3 lowest $^2A'$ and 2 lowest $^2A''$ state of N_3 global potential energy surfaces. (Energy unit is kcal/mol.)

7 degree	$1^2A'$	$2^2A'$	$3^2A'$	$1^2A''$	$2^2A''$
s(kcal/mol)	2.95	3.12	3.41	2.85	4.23
e_{max}(kcal/mol)	12.13	18.88	18.54	11.51	26.08
8 degree	$1^2A'$	$2^2A'$	$3^2A'$	$1^2A''$	$2^2A''$
s(kcal/mol)	2.62	2.79	3.25	2.42	2.70
e_{max}(kcal/mol)	10.66	16.11	18.22	9.43	13.85
9 degree	$1^2A'$	$2^2A'$	$3^2A'$	$1^2A''$	$2^2A''$
s(kcal/mol)	1.85	2.62	2.80	1.70	2.33
e_{max}(kcal/mol)	11.60	14.83	18.87	8.42	12.51

Table 4.3: Local fitting errors for conical intersections CI1, CI3 and CI4. (Energy unit is kcal/mol.)

	$s(1^2A'')$	$e_{max}(1^2A'')$	$s(2A'')$	$e_{max}(2A'')$	$s(g_1)$	$e_{max}(g_1)$	$s(g_2)$	$e_{max}(g_2)$
CI1	0.02	0.16	0.02	0.16	0.02	0.08	0.04	0.32
	$s(1^2A')$	$e_{max}(1^2A')$	$s(2A')$	$e_{max}(2A')$	$s(g_1)$	$e_{max}(g_1)$	$s(g_2)$	$e_{max}(g_2)$
CI2	0.23	0.80	0.28	1.04	0.15	0.91	0.49	1.34
	$s(2^2A')$	$e_{max}(2^2A')$	$s(3^2A')$	$e_{max}(3^2A')$	$s(g_1)$	$e_{max}(g_1)$	$s(g_2)$	$e_{max}(g_2)$
CI3	0.39	1.90	0.48	2.07	0.23	1.12	0.85	3.80

Table 4.4: Geometries and adiabatic transition energies relative to the $\tilde{X}^2\Pi_g$ ground state of various critical points on the low-lying doublet states of N_3 obtained from the MRCISD(Q)/aug-cc-pVTZ calculation and our PESs (in parentheses)

	ΔE(kcal/mol)	r_{NN}(Å)	$\angle$NNN(°)
$1^2A'$_LM_1($^2\Pi_g$)	0.00 (-0.94)	1.1857 (1.1854)	180.00 (180.00)
$1^2A'$_LM_2($^2A_1$)	66.64 (66.16)	1.2587 (1.2570)	106.97 (108.65)
$2^2A'$_LM_1($^2\Sigma_u^+$)	104.87 (104.31)	1.1845 (1.1843)	180.00 (180.00)
$2^2A'$_LM_2($^2\Pi_u$)	104.19 (104.16)	1.2759 (1.2731)	180.00 (180.00)
$3^2A'$_LM_1(2^2B_2)	112.02 (106.69)	1.3100 (1.2696)	100.45 (126.40)
$1^2A''$_LM_1($^2\Pi_g$)	0.00 (-0.71)	1.1857 (1.1861)	180.00 (180.00)
$1^2A''$_TS_2($^2A_2$)	66.07 (62.70)	1.2894 (1.2838)	109.02 (106.07)
$1^2A''$_LM_3($^2A_2$)	33.11 (35.57)	1.3059 (1.3047)	71.91 (71.97)
$1^2A''$_LM_4($^2B_1$)	32.22 (32.35)	1.4669 (1.5107)	49.80 (47.01)
$2^2A''$_LM_1($^2\Pi_u$)	104.19 (106.6)	1.2759 (1.2727)	180.00 (180.00)
$2^2A''$_LM_2($^2B_1$)	72.80 (70.73)	1.2656 (1.2531)	120.49 (123.60)
$2^2A''$_TS_3($^2B_1$)	109.11 (103.83)	1.3623 (1.3433)	86.07 (86.45)
MSX_$1^2A''/2^2A''$ ($^2A_2/^2B_1$)	45.37 (45.01)	1.3693 (1.3693)	60.00 (60.00)
MSX_$1^2A'/2^2A'$ ($^2A_1/^2B_2$)	66.95 (66.72)	1.2572 (1.2550)	110.30 (111.39)
MSX_$2^2A'/3^2A'$ ($^2A_1/2^2B_2$)	108.26 (107.92)	1.2271 (1.2245)	180.00 (180.00)
MSX_$1^2A'/2^2A''$ ($^2A_1/^2B_1$)	96.02 (98.74)	1.3280 (1.3317)	78.14 (79.51)
MSX_$2^2A'/2^2A''$_1 ($^2B_2/^2B_1$)	109.84 (101.35)	1.3118 (1.3245)	87.84 (91.93)
MSX_$1^2A'/1^2A''$ ($^2A_1/^2A_2$)	66.61 (69.24)	1.2607 (1.2147)	106.37 (106.97)
MSX_$2^2A'/2^2A''$_2 ($^2A_1/^2B_1$)	73.47 (70.78)	1.2672 (1.2540)	125.77 (122.46)
MSX_$3^2A'/2^2A''$ ($^2B_1/2^2B_2$)	108.26 (109.11)	1.2271 (1.2321)	180.00 (180.00)

Table 4.5: Fitting errors for diabatical potentials and couplings of $1^2A'$ and $2^2A'$ states at CI3 conical intersection region.

degree	$s(U_{11})$	$e_{max}(U_{11})$	$s(U_{22})$	$e_{max}(U_{22})$	$s(U_{12})$	$e_{max}(U_{12})$
perm[a]	0.095	0.652	0.104	0.652	0.445	1.137
norm[b]	1.532	9.086	1.521	9.032	0.034	0.108

[a] "perm" stands for the fitting with permutational invariant basis.
[b] "norm" stands for the fitting with normal basis.

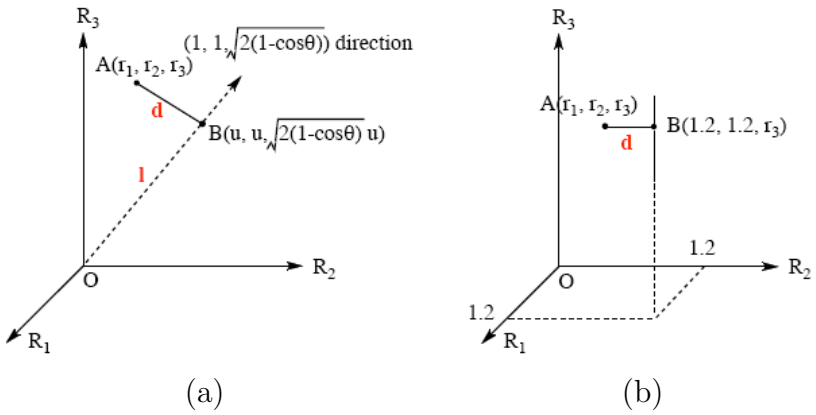

Figure 4.1: Scheme of defining the local CI region for (a) CI1 and CI3; (b) CI4.

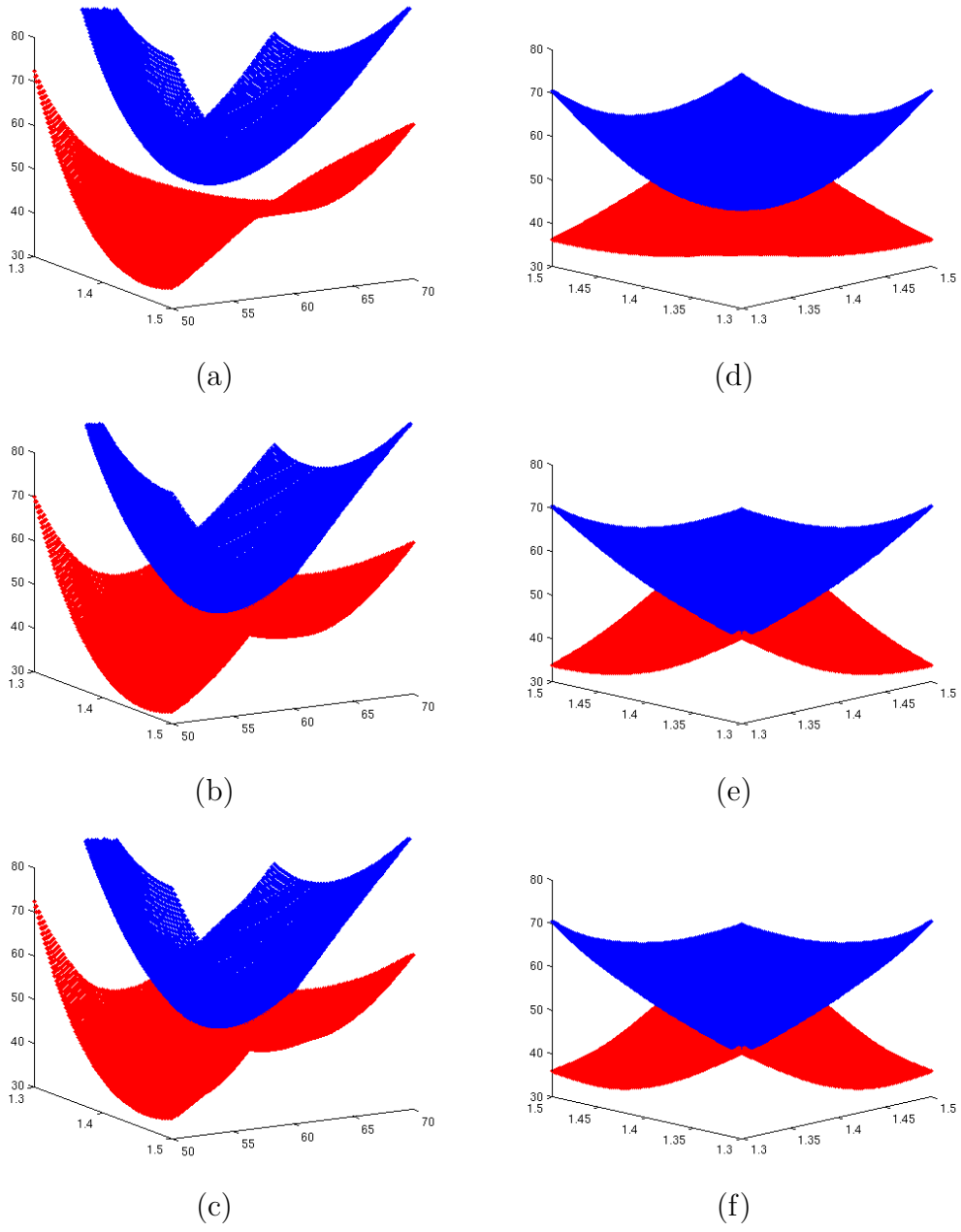

Figure 4.2: CI1 potential energy surfaces. (a), (d): Surface from global fit; (b), (e): surface from local fit; (c), (f): final surface. $r_1 = r_2$ Åfor (a), (b), (c); $\angle NNN = 60°$ for (d), (e), (f).

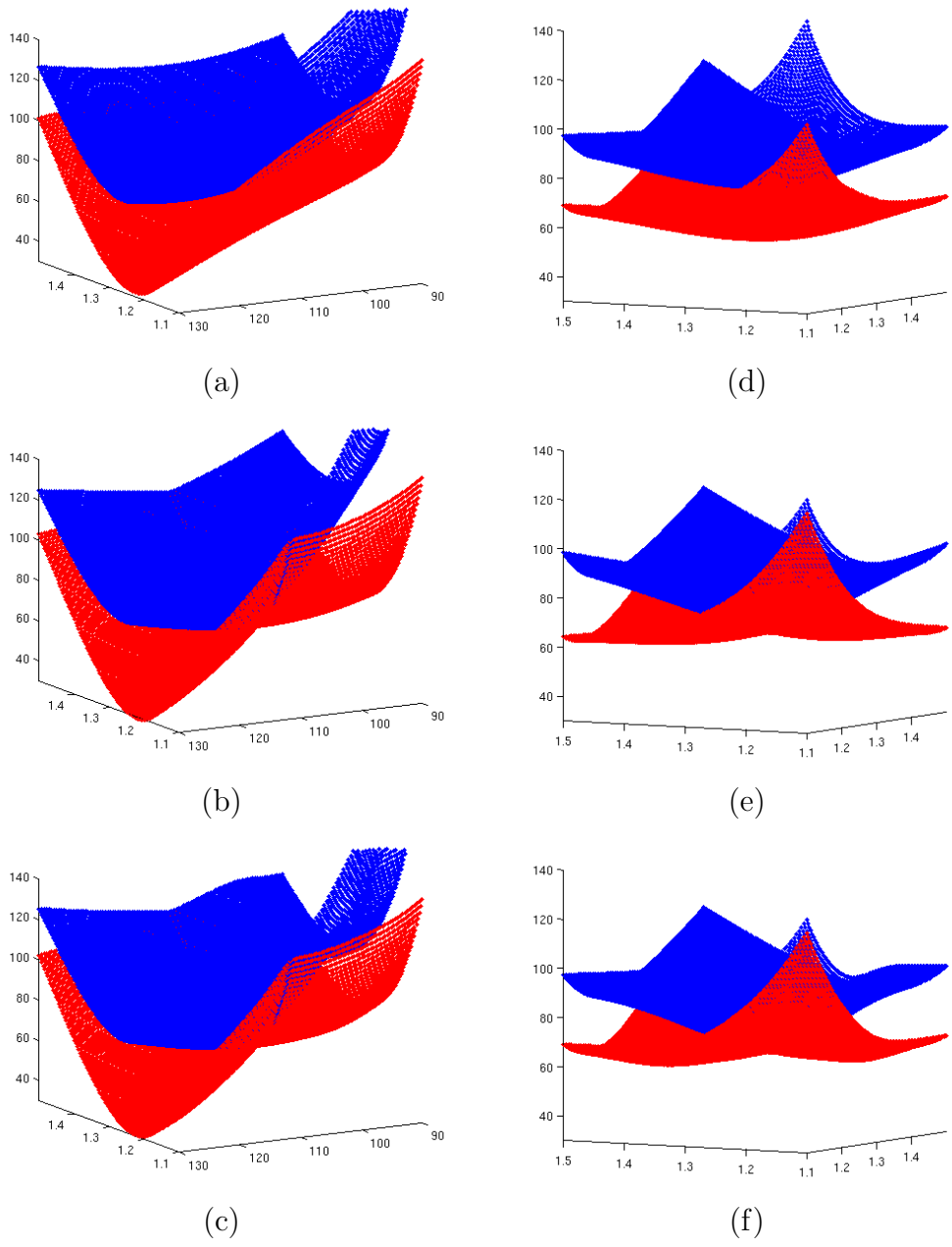

Figure 4.3: CI3 potential energy surfaces. (a), (d): Surface from global fit; (b), (e): surface from local fit; (c), (f): final surface. ($r_1 = r_2$ Åfor (a), (b), (c); $\angle NNN = 110°$ for (d), (e), (f).

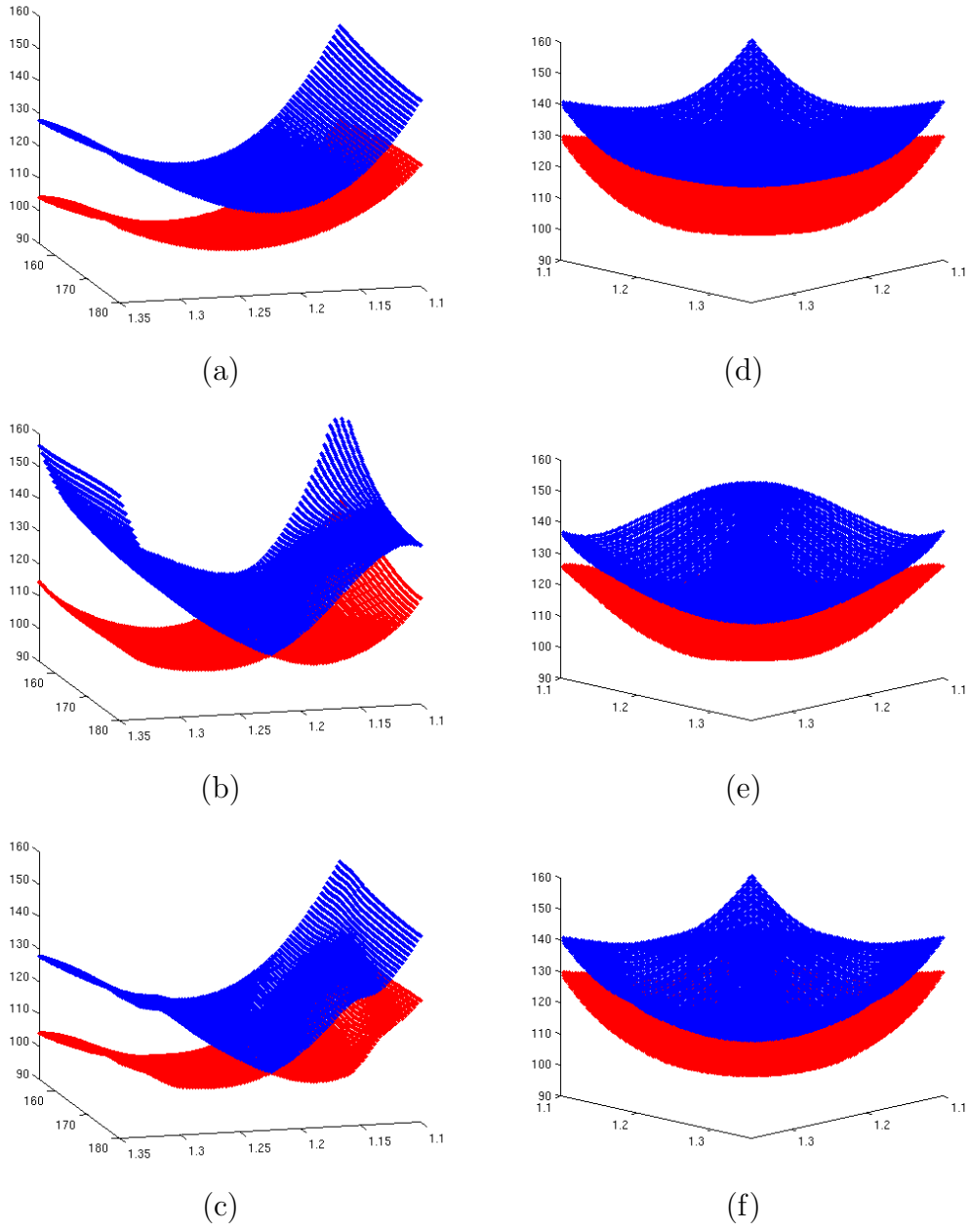

Figure 4.4: CI4 potential energy surfaces. (a), (d): Surface from global fit; (b), (e): surface from local fit; (c), (f): final surface. ($r_1 = r_2$ for (a), (b), (c); $\angle NNN = 180°$ for (d), (e), (f).

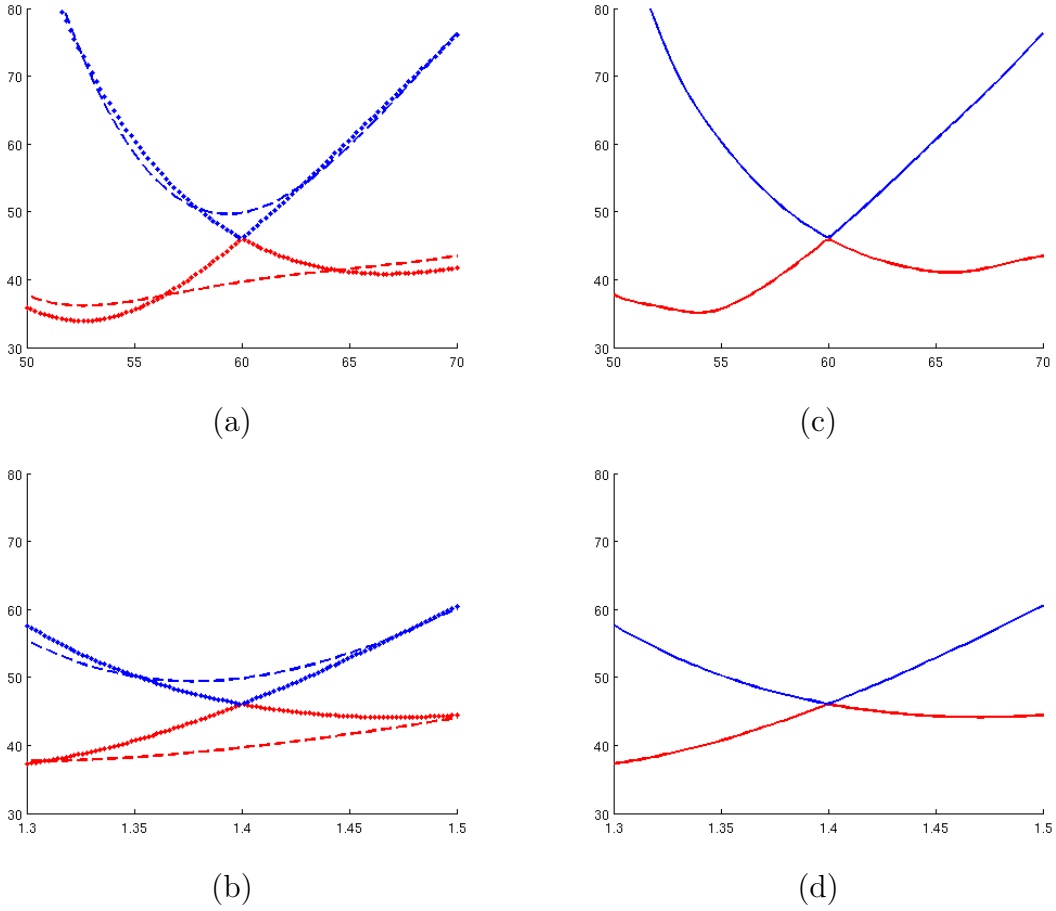

Figure 4.5: 1D cut of potential energy surfaces around CI1. (a), (d): Potential curve from global fit and local fit; (b), (d): final surface. $r_1 = r_2 = 1.40$ Åfor (a), (b); $r_1 = 1.40$ Å, $\angle NNN = 60°$ for (c), (d).

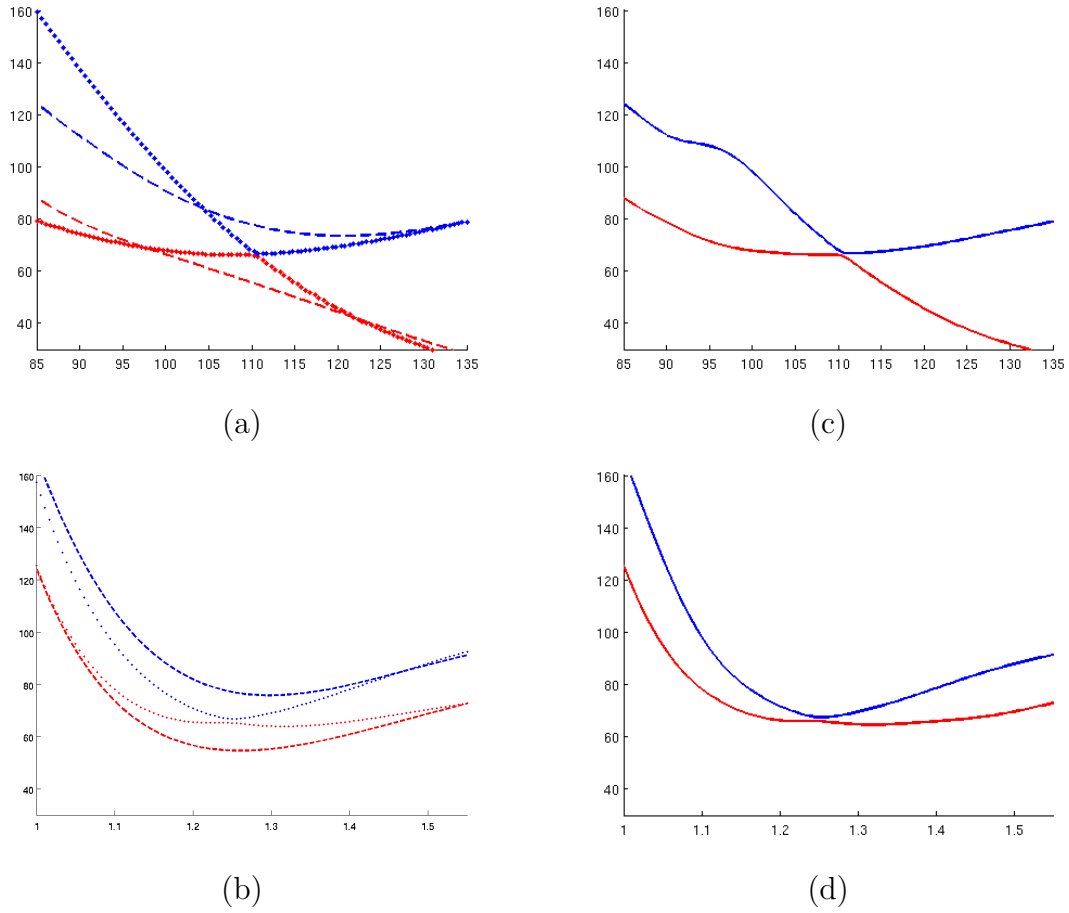

Figure 4.6: 1D cut of potential energy surfaces around CI3. (a), (b): Potential curve from global fit and local fit; (c), (d): final surface. $r_1 = r_2 = 1.25$ Åfor (a), (b); $r_1 = 1.25$ Å, $\angle NNN = 110°$ for (c), (d).

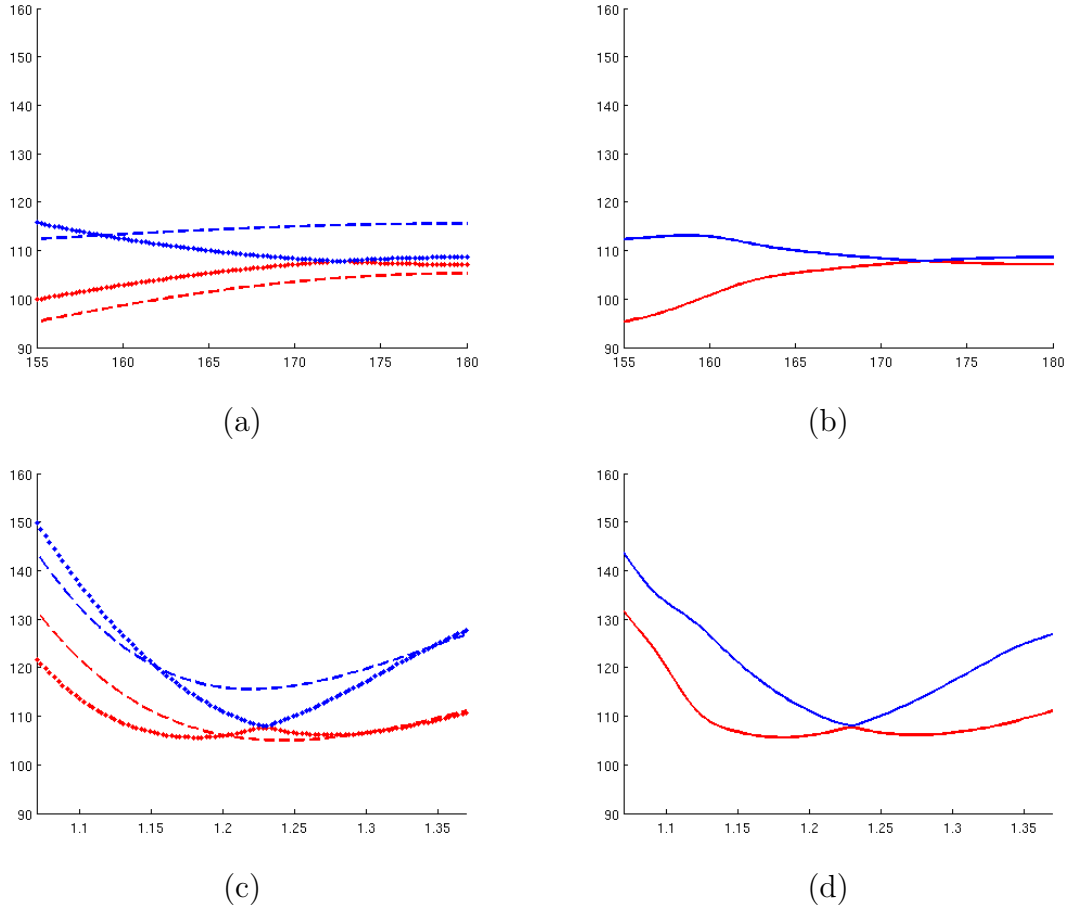

Figure 4.7: 1D cut of potential energy surfaces around CI4. (a), (d): Potential curve from global fit and local fit; (b), (d): final surface. $r_1 = r_2 = 1.22$ Åfor (a), (b); $r_1 = 1.22$ Å, $\angle NNN = 180°$ for (c), (d).

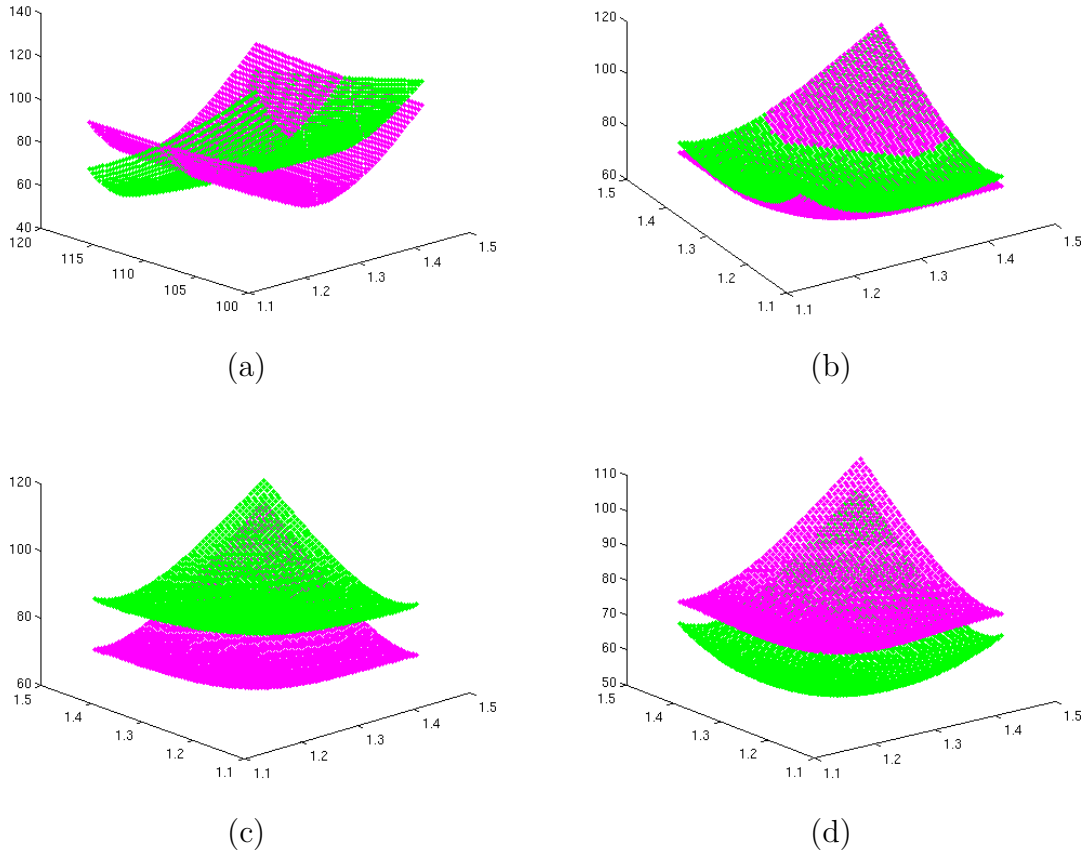

Figure 4.8: Diabatic potential energy surfaces U_{11} and U_{22} of CI3. (a)$r_1 = r_2$; (b)$\angle NNN = 110°$. (c)$\angle NNN = 105°$. (d)$\angle NNN = 115°$.

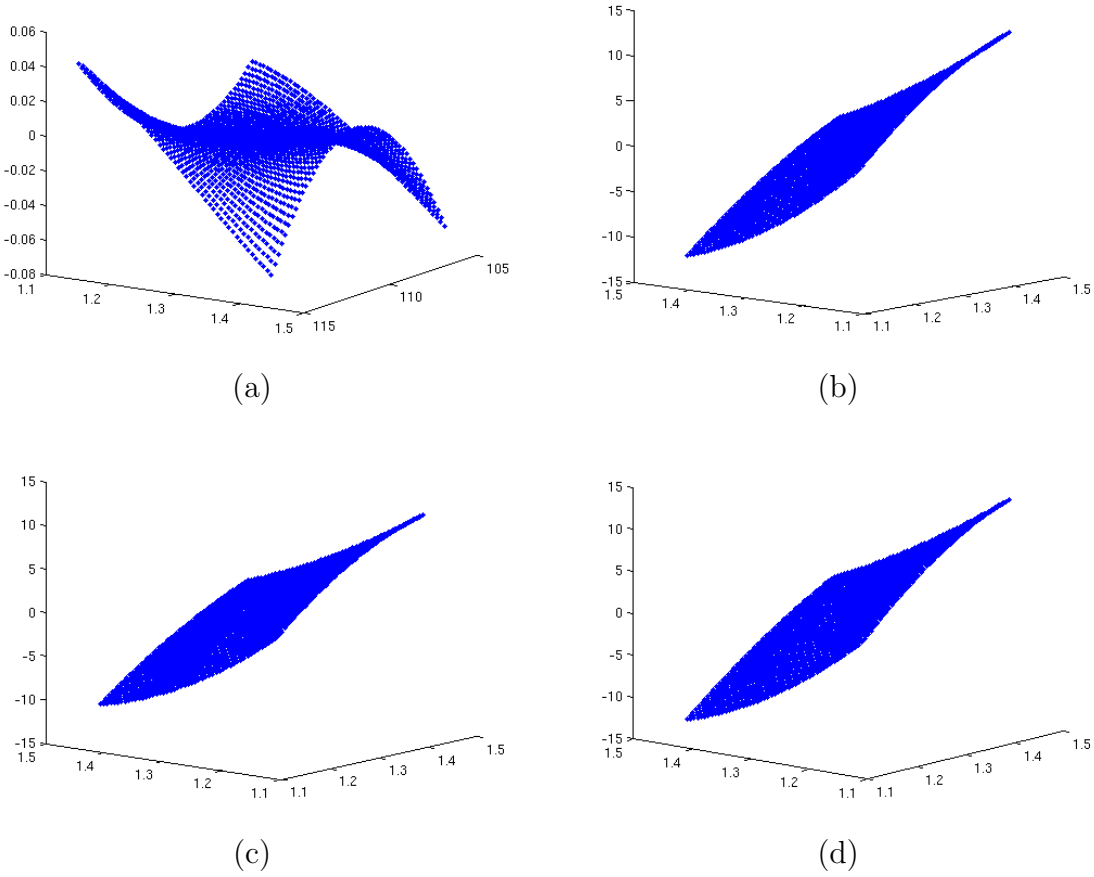

Figure 4.9: Diabatic coupling potential U_{12} of CI3. (a)$r_1 = r_2$; (b)$\angle NNN = 110°$. (c)$\angle NNN = 105°$. (d)$\angle NNN = 115°$.

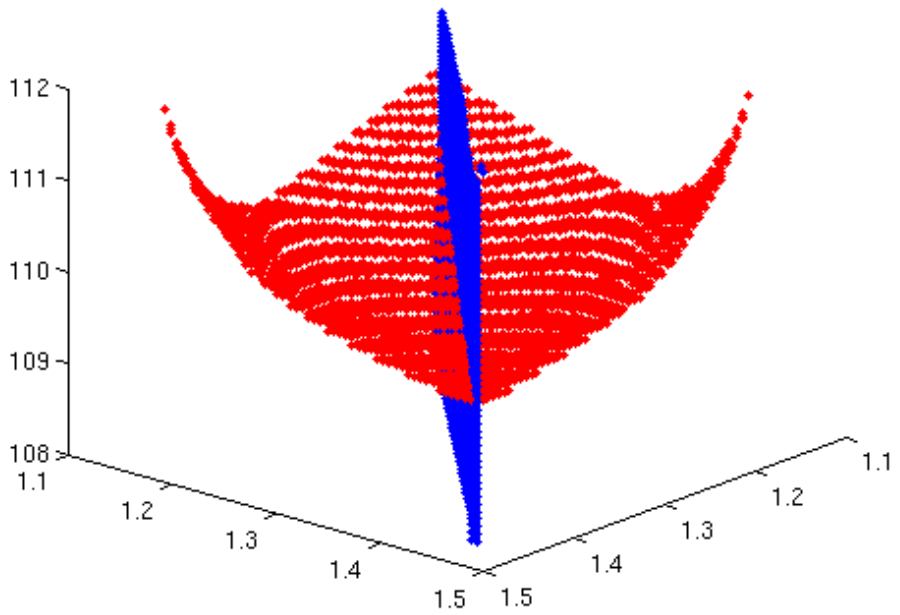

Figure 4.10: The crossing of diabatic $U_{11} = U_{22}$ surface (red) and $U_{12} = 0$ surface (blue) for CI3.

PART II.

Theoretical studies on nano phase reactions

Chapter 5. Introduction of DFTB method

In the second part of my thesis, we move our focus of study from small gas phase molecules to carbon nano tubes. The high accurate post Hartree-Fock method such as complete active space SCF (CASSCF) and multireference configuration interaction method would be computational prohibitive in this large system. Also, since the system contains large π-conjugation networks, a method which considers quantum effect would be desired to have accurate description of such problems. In order to increase the computational efficiency while maintaining the theoretical accuarcy at the same time, the density functional based tight binding (DFTB) method[1,2,3,4] is empolyed in our nano phase study.

The DFTB method is a semiempricial quantum mechanical method. It is similar to the traditional emperical tight-binding method but replaces the emperical fitting procedure for matrix elements by a well-defined integration procedure.[1] It originate from density functional theory (DFT) and takes advantage of the simplicity introduced by the traditional tight binding method to redcue the computational cost. We will introduce this DFTB method in the following sections.

The derivation starts from the Kohn-Sham total energy in density functional theory. For a system of M electrons in the field of N nuclei at positions $\vec{R}$, the total energy is written as a functional of a charge density $n(\vec{r})$ under DFT scheme:

$$E = \sum_{i}^{\text{occ}} \langle \Psi_i | -\frac{\Delta}{2} + V_{\text{ext}} + \frac{1}{2}\int \frac{n(\vec{r}\,')}{|\vec{r}-\vec{r}\,'|} d\vec{r}\,' | \Psi_i \rangle + E_{\text{XC}}[n(\vec{r})] + \frac{1}{2}\sum_{\alpha,\beta}^{N} \frac{Z_\alpha Z_\beta}{|\vec{R}_\alpha - \vec{R}_\beta|} \tag{5.1}$$

where the first term is the summation over occupied Kohn-Sham eigenstates Ψ_i, the second term E_{XC} counts for the exchange-correlation contribution, and the last term

covers the nuclear repulsion.

Following Foulkes and Haydock,[5] the total energy is rewritten to transform the leading matrix in equation 5.1 by the substitution of charge density $n(\vec{r})$ with a reference density $n_0 = n_0(\vec{r})$ plus a small fluctuation $\delta n = \delta n(\vec{r})$:

$$\begin{aligned} E = & \sum_{i}^{\text{occ}} \langle \Psi_i | -\frac{\Delta}{2} + V_{\text{ext}} + \int \frac{n_0'}{|\vec{r} - \vec{r}'|} d\vec{r}' + V_{\text{XC}}[n_0] | \Psi_i \rangle \\ & - \frac{1}{2} \iint \frac{n_0'(n_0 + \delta n)}{|\vec{r} - \vec{r}'|} d\vec{r} d\vec{r}' - \int V_{\text{XC}}[n_0](n_0 + \delta n) d\vec{r} \\ & + \frac{1}{2} \iint \frac{\delta n'(n_0 + \delta n)}{|\vec{r} - \vec{r}'|} d\vec{r} d\vec{r}' + E_{\text{XC}}[n_0 + \delta n] + \frac{1}{2} \sum_{\alpha,\beta}^{N} \frac{Z_\alpha Z_\beta}{|\vec{R}_\alpha - \vec{R}_\beta|} \end{aligned} \tag{5.2}$$

In this new equation, the second term and third term correct for the double counting of the new Hartree and new XC contribution in the leading matrix element respectively, and the fourth term is due to seperating the total Hartree energy in equation 5.1 into a part related to n_0 and to δn.

Expand the echange correlation energy E_{XC} at reference denisty to second order by Taylor series and substitute it in equation 5.2, also note that the terms linear in δn cancel each other at any arbitrary input density n_0, the final total energy can be expressed as:

$$\begin{aligned} E = & \sum_{i}^{\text{occ}} \langle \Psi_i | \hat{H}_0 | \Psi_i \rangle - \frac{1}{2} \iint \frac{n_0' n_0}{|\vec{r} - \vec{r}'|} d\vec{r} d\vec{r}' + E_{\text{XC}}[n_0] - \int V_{\text{XC}}[n_0] n_0 d\vec{r} \\ & + \frac{1}{2} \sum_{\alpha,\beta}^{N} \frac{Z_\alpha Z_\beta}{|\vec{R}_\alpha - \vec{R}_\beta|} + \frac{1}{2} \iint \left(\frac{1}{|\vec{r} - \vec{r}'|} + \left. \frac{\delta^2 E_{\text{XC}}}{\delta n \delta n'} \right|_{n_0} \right) \delta n \delta n' d\vec{r} d\vec{r}' \end{aligned} \tag{5.3}$$

here,

$$\hat{H}_0 = -\frac{\Delta}{2} + V_{\text{ext}} + \int \frac{n_0'}{|\vec{r} - \vec{r}'|} d\vec{r}' + V_{\text{XC}}[n_0] \tag{5.4}$$

In the traditional non-SCC tight binding approach, the Hamiltonian operator

$\hat{H}_0$ applies on the reference density n_0, while the last term in the final equation is ignored. To reduce computational cost, a frozen-core approximation is employed by considering only the valence orbitals. The Kohn- Sham equations are then solved non-self-consistently with the second order correction neglected. The contribution that depend only on the reference density n_0 and the core-core repulsion are taken to be a sum of one- and two-body potentials. The latter, denoted by E_{rep}, are strictly pairwise, repulsive, and short ranged. Thus, the total energy then reads:

$$E_0^{TB} = \sum_i^{\text{occ}} \langle \Psi_i | \hat{H}_0 | \Psi_i \rangle + E_{\text{rep}} \tag{5.5}$$

To solve Kohn-Sham equations, the wave functions Ψ_i are expanded by a suitable set of localized atomic orbitals φ_ν:

$$\Psi_i(\vec{r}) = \sum_\nu c_{\nu i}\, \varphi_\nu(\vec{r} - \vec{R}_\alpha) \tag{5.6}$$

These atomic orbitals are Slater-type orbitals which are determined by solving a modified Schrödinger equation for a free neutral pseudoatom with an additional confined potential within SCF-LDA calcaulations.

By applying the variational principal to the zeroth-order energy functional 5.5, the non-SCF Kohn-Sham equations are transformed to the following secular equations:[3]

$$\sum_\nu^M c_{\nu i}(H^0_{\mu\nu} - \varepsilon_i S_{\mu\nu}) = 0, \forall \mu, i \tag{5.7}$$

where,

$$H^0_{\mu\nu} = \langle \varphi_\mu | \hat{H}_0 | \varphi_\nu \rangle, S_{\mu\nu} = \langle \varphi_\mu | \varphi_\nu \rangle, \forall \mu \in \alpha, \nu \in \beta \tag{5.8}$$

The Hamiltonian matrix elements $H_{\mu\nu}$ are defined as:

$$H^0_{\mu\nu} = \begin{cases} \varepsilon_\mu^{\text{nertral free atom}} & \text{if} \quad \mu = \nu \\ \langle \varphi^\alpha_\mu | \hat{T} + V^\alpha_0 + V^\beta_0 | \varphi^\beta_\nu \rangle & \text{if} \quad \alpha \neq \beta \\ 0 & \text{otherwise} \end{cases} \tag{5.9}$$

α and β are the indices indicating the atoms on which the wave functions and potentials are centered. Only two-center Hamiltonian matrix elements, as well as the two-center overlap matrix elements, are treated and evaluated explicitly. The eigenvalues of the neutral free atom serve as diagonal elements of the Hamiltonian, which guarantees the correct limit for isolated atoms.

After solving the eigenvalue problem in 5.7, the first term in 5.5, which is a simple summation over all occupied Kohn-Sham orbitals ε_i, can be obtained. And the second term of 5.5, E_{rep}, can then be easily determined as a function of distance by taking the SCF-LDA cohesive and the corresponding TB band-structure energy for a suitable reference system:

$$E_{\text{rep}}(R) = \left\{ E^{\text{SCF}}_{\text{LDA}}(R) - \sum_i^{\text{occ}} n_i \varepsilon_i(R) \right\} \Bigg|_{\text{reference structure}} \tag{5.10}$$

For molecualr dynamics application, interatomic forces can also be easily derived from an explicit energy gradient calculation at the considered molecular structure:

$$\begin{aligned} M_\alpha \ddot{\vec{R}}_\alpha = -\frac{\partial E^{TB}_0}{\partial \vec{R}_\alpha} = &- \sum_i n_i \sum_{\mu\nu} c_{\mu i} c_{\nu i} \left[\frac{\partial H^0_{\mu\nu}}{\partial \vec{R}_\alpha} - \varepsilon_i \frac{\partial S_{\mu\nu}}{\partial \vec{R}_\alpha} \right] \\ &- \sum_{\beta \neq \alpha} \frac{\partial E_{\text{rep}}(|\vec{R}_\alpha - \vec{R}_\beta|)}{\partial \vec{R}_\alpha} \end{aligned} \tag{5.11}$$

This non-SCC DFTB approach has been successfully applied to various systems including carbon,[2] silicon,[6] and silicon carbide.[7] In general, this scheme performs well when electron density of the many-atom structure may be represented as a sum

of atomic like densities in good approximations, or equivalently, when there is no significant charge transfers in the system. Therefore, due to its good performance and relative inexpensive computational cost, we employ this non-SCC DFTB approach in our high temperature molecular dynamics study of carbon nanotube growth from SiC surface, the results are shown in chapter 8, 9 and 10.

Although non-SCC DFTB scheme is suitable for many systems, the uncertainties increase as the chemical bonding is controlled by a delicate charge balance between different atomic constituents, especially in heteronuclear molecules and in polar semiconductors. Therefore, the standard non-SCC approach has been extended to improve the total energy, forces, and transferability in the presence of long-range Coulomb interactions, by explicitly considering the second-order term in the density fluctuations in 5.3.

Elstner *et al* introduced the first approximation.[1] They decompose $\delta n_(\vec{r})$ into atomic centered contributions, which decay fast with increasing distance from the corresponding center. The second-order term then reads:

$$E_{2nd} = \frac{1}{2}\sum_{\alpha,\beta}^{N} \iint \Gamma[\vec{r},\vec{r}',n_0]\delta n_\alpha(\vec{r})\delta n_\beta(\vec{r}')d\vec{r}d\vec{r}' \tag{5.12}$$

where Γ is a functinal to denote the Hartree and XC coefficients. The δn_α may be expanded in a series or radial and angular functions:

$$\delta n_\alpha(\vec{r}) = \sum_{l,m} K_{ml}F^\alpha_{ml}(|\vec{r}-\vec{R}_\alpha|)Y_{lm}\left(\frac{\vec{r}-\vec{R}_\alpha}{|\vec{r}-\vec{R}_\alpha|}\right) \tag{5.13}$$

$$\approx \Delta q_\alpha F^\alpha_{00}(|\vec{r}-\vec{R}_\alpha|)Y_{00} \tag{5.14}$$

whre K_{ml} are the coefficients, F^α_{ml} denotes the normalized radial dependence of the density fluctuation on atom α for the corresponding angular momentum, Y_{lm} is the spherical harmonics function. Since the monopole term accounts for the most impor-

tant contributions of charge transfer, and since high-order interactions decay rapidly with increasing interatomic distance, multipole expansion terms are truncated. In this way, a substantial increase in the numerical complexity is avoided. Substitution of 5.14 into 5.12 yields the final expression for the second-order energy term:

$$E_{2nd} = \frac{1}{2}\sum_{\alpha,\beta}^{N} \Delta q_\alpha \gamma_{\alpha\beta} \Delta q_\beta \tag{5.15}$$

where

$$\gamma_{\alpha\beta} = \iint \Gamma[\vec{r}, \vec{r}', n_0] \frac{F_{00}^{\alpha}(|\vec{r} - \vec{R}_\alpha|) F_{00}^{\beta}(|\vec{r} - \vec{R}_\beta|)}{4\pi} d\vec{r} d\vec{r}' \tag{5.16}$$

In the limit of large interatomic distances, the XC contribution varnishes with LDA and E_{2nd} may be viewed as a pure Coulomb interaction between two point charges Δq_α and Δq_β. In the case where charges are located at one and the same atom, a regorous evaluation of $\gamma_{\alpha\alpha}$ would require the actual charge distribution and could be calculated by expanding the carge density into the basis set of localized orbitals. A simple approximation for $\gamma_{\alpha\alpha}$ that is widely used in semiemprical quantum chemistry based on Parisers observation is to take $\gamma_{\alpha\alpha}$ as the difference of the atomic ionization potential and electron affinity. This is related to the chemical hardness η_α, or the Hubbard parameter U_α:[8]

$$\gamma_{\alpha\alpha} \approx I_\alpha - A\alpha \approx 2\eta_\alpha \approx U_\alpha \tag{5.17}$$

Thus, $\gamma_{\alpha\beta}$ can be evaluated with the distance between the atoms α and β and the parameters U_α and U_β.

Practically, an analytical approach is made in order to obtain a well-defined expression of $\gamma_{\alpha\beta}$ for all scale system. The charge density is assumed to have an expontial

decay in accordance with the Slater-type orbitals:

$$n_\alpha(\vec{r}) = \frac{\tau_\alpha^3}{8\pi} e^{-\tau_\alpha|\vec{r}-\vec{R}_\alpha|} \tag{5.18}$$

Neglecting the second-order contribution of E_{XC}, one obtain:

$$\gamma_{\alpha\beta} = \iint \frac{1}{|\vec{r}-\vec{r}'|} \frac{\tau_\alpha^3}{8\pi} e^{-\tau_\alpha|\vec{r}'-\vec{R}_\alpha|} \frac{\tau_\beta^3}{8\pi} e^{-\tau_\beta|\vec{r}'-\vec{R}_\beta|} d\vec{r} d\vec{r}' \tag{5.19}$$

Integration over $\vec{r}'$ gives

$$\gamma_{\alpha\beta} = \int \left[\frac{1}{|\vec{r}-\vec{R}_\alpha|} - \left(\frac{\tau_\alpha}{2} + \frac{1}{|\vec{r}-\vec{R}_\alpha|} \right) e^{-\tau_\alpha|\vec{r}-\vec{R}_\alpha|} \right] \times \frac{\tau_\beta^3}{8\pi} e^{-\tau_\beta|\vec{r}-\vec{R}_\beta|} d\vec{r} \tag{5.20}$$

Set $R = |\vec{r} - \vec{R}|$ and transform to spheroidal coordinates, we get

$$\gamma_{\alpha\beta} = \frac{1}{R} - S(\tau_\alpha, \tau_\beta, R) \tag{5.21}$$

$$= \frac{1}{R} - \left[e^{-\tau_\alpha R} \left(\frac{\tau_\beta^4 \tau_\alpha}{2(\tau_\alpha^2 - \tau_\beta^2)^2} - \frac{\tau_\beta^6 - 3\tau_\beta^4 \tau_\alpha^2}{(\tau_\alpha^2 - \tau_\beta^2)^3 R} \right) \right. \tag{5.22}$$

$$\left. + e^{-\tau_\beta R} \left(\frac{\tau_\alpha^4 \tau_\beta}{2(\tau_\beta^2 - \tau_\alpha^2)^2} - \frac{\tau_\alpha^6 - 3\tau_\alpha^4 \tau_\beta^2}{(\tau_\beta^2 - \tau_\alpha^2)^3 R} \right) \right] \tag{5.23}$$

S is an exponentially decaying short-range function. Expanding the exponentials and we get the limit at $R = 0$ with

$$\lim_{R \to 0} S(\tau_\alpha, \tau_\alpha, R) = \frac{5}{16}\tau_\alpha + \frac{1}{R} \tag{5.24}$$

Assume at the limit of $R = 0$ the second order contribution can be expressed approximately via the so-called chemical hardness for a spin-unploarized atom or Hubbard parameter U_α, we obtain

$$\frac{1}{2}\Delta q_\alpha^2 \gamma_{\alpha\alpha} = \frac{1}{2}\Delta q_\alpha^2 U_\alpha \tag{5.25}$$

therefore,

$$\tau_\alpha = \frac{16}{5} U_\alpha \tag{5.26}$$

According to Janek theorem, the chemical hardness for a spin-unpolarized atom is the second derivative of the highest occupied atomic orbital with respect to the occupation number. Therefore, one can calculate chemical hardness or Hubbard values with a fully self-consistent *ab initio* method and include the include the influence of the second-ordercontribution of E_{XC} for small distances where it is imortant. In the limit of large interatomic distances, $\gamma_{\alpha\beta} \to 1/R$ and thus represents the coulomb interaction between two point charges Δq_α and Δq_β.

$$E_2^{TB} = \sum_i^{\mathrm{occ}} \langle \Psi_i | \hat{H}_0 | \Psi_i \rangle + \frac{1}{2} \sum_{\alpha,\beta}^{N} \Delta q_\alpha \gamma_{\alpha\beta} \Delta q_\beta + E_{\mathrm{rep}} \tag{5.27}$$

where $\gamma_{\alpha\beta} = \gamma_{\alpha\beta}(U_\alpha, U_\beta, |\vec{R}_\alpha - \vec{R}_\beta|)$. As in the non-SCC scheme, the contribution to $\hat{H}_0$ depends only on n_0. However, since the atomic charges depend on the one-particle wave function Ψ_i, a self-consistent procedure is required to find the minimum of 5.27.

Same as non-SCC approach, to solve Kohn-Sham equations, the wave functions Ψ_i are expanded by a suitable set of localized Slater-type atomic orbitals φ_ν, with expansion coefficient $c_{\nu i}$. Following the same procedure,and employing the Mulliken charge analysis for estimating charge fluctuations $\delta q_\alpha = q_\alpha - q_\alpha^0$,

$$q_\alpha = \frac{1}{2} \sum_i^{\mathrm{occ}} n_i \sum_{\mu \in \alpha} \sum_\nu^N (c_{\mu i}^* c_{\nu i} S_{\mu\nu} + c_{\nu i}^* c_{\nu i} S_{\nu\mu}) \tag{5.28}$$

one obtain those secular equations:

$$\sum_\nu^M c_{\nu i} (H_{\mu\nu}^0 - \varepsilon_i S_{\mu\nu}) = 0, \forall \mu, i \tag{5.29}$$

$$H^0_{\mu\nu} = \langle\varphi_\mu|\hat{H}_0|\varphi_\nu\rangle + \frac{1}{2}S_{\mu\nu}\sum_{\xi}^{N}(\gamma_{\alpha\xi} + \gamma_{\beta\xi})\Delta q_\xi = H^0_{\mu\nu} + H^1_{\mu\nu},$$

$$S_{\mu\nu} = \langle\varphi_\mu|\varphi_\nu\rangle, \forall\mu \in \alpha, \nu \in \beta \tag{5.30}$$

The overlap matrix elements generally extend over a few nearest-neighbor distances, thus introduce multiparticle interactions. The second-order correction due to charge fluctuation is now represented by the nondiagonal Mulliken charge depdendent contribution $H^1_{\mu\nu}$ to the matrix elements $H_{\mu\nu}$.

Consistent with non-SCC DFTB approach, the short-range repulsive pair potential E_{rep} are determined by taking the difference of the SCF-LDA cohesive energy and the corresponding SCC-DFTB electronic energy for a suitable reference structure. Because charge transfer effects are now considered explicitly, the transferability of E_{rep} is also improved compared to the non-SCC approach. Again, by taking the derivative of the final tight-binding energy in 5.27 with respect to the nuclear coordinates, a simple analytic expression for the interatomic forces is easily derived:

$$\begin{aligned}\vec{F}_\alpha = -\frac{\partial E_2^{TB}}{\partial \vec{R}_\alpha} = &-\sum_i n_i \sum_{\mu\nu} c_{\mu i}c_{\nu i}\left[\frac{\partial H^0_{\mu\nu}}{\partial \vec{R}_\alpha} - \left(\varepsilon_i - \frac{H^1_{\mu\nu}}{S_{\mu\nu}}\right)\frac{\partial S_{\mu\nu}}{\partial \vec{R}_\alpha}\right] \\ &- \Delta q_\alpha \sum_{\xi}^{N}\frac{\partial \gamma_{\alpha\xi}}{\partial \vec{R}_\alpha}\Delta q_\xi - \sum_{\beta\neq\alpha}\frac{\partial E_{\text{rep}}(|\vec{R}_\alpha - \vec{R}_\beta|)}{\partial \vec{R}_\alpha}\end{aligned} \tag{5.31}$$

In our curvature effects study of the reaction energy of SWNT with electrophilies, SCC-DFTB approach is employed due to the exsistence of polar atoms and thus significant charge transfer in the system. This SCC-DFTB approach is much cheaper than DFT calculations, which enables us to do a series of otherwise much more expensive calculations but achieve rather accurate results comparable to DFT calculations. We will illustrate the details of the results in chapter 6 and 7 in this thesis.

References

1. Elstner, M.; Porezag, D.; Jungnickel, G.; Elsner, J.; Haugk, M.; Frauenheim, T.; Suhai, S.; Seifert, G. *PHYSICAL REVIEW B* **1998**, *58*, 7260–7268.

2. POREZAG, D.; FRAUENHEIM, T.; KOHLER, T.; SEIFERT, G.; KASCHNER, R. *PHYSICAL REVIEW B* **1995**, *51*, 12947–12957.

3. Frauenheim, T.; Seifert, G.; Elstner, M.; Hajnal, Z.; Jungnickel, G.; Porezag, D.; Suhai, S.; Scholz, R. *PHYSICA STATUS SOLIDI B-BASIC SOLID STATE PHYSICS* **2000**, *217*, 41–62.

4. Frauenheim, T.; Seifert, G.; Elstner, M.; Niehaus, T.; Kohler, C.; Amkreutz, M.; Sternberg, M.; Hajnal, Z.; Di Carlo, A.; Suhai, S. *JOURNAL OF PHYSICS-CONDENSED MATTER* **2002**, *14*, 3015–3047.

5. MATTHEW, W.; FOULKES, C.; HAYDOCK, R. *PHYSICAL REVIEW B* **1989**, *39*, 12520–12536.

6. FRAUENHEIM, T.; WEICH, F.; KOHLER, T.; UHLMANN, S.; POREZAG, D.; SEIFERT, G. *PHYSICAL REVIEW B* **1995**, *52*, 11492–11501.

7. Gutierrez, R.; Frauenheim, T.; Kohler, T.; Seifert, G. *JOURNAL OF MATERIALS CHEMISTRY* **1996**, *6*, 1657–1663.

8. PARR, R.; PEARSON, R. *JOURNAL OF THE AMERICAN CHEMICAL SOCIETY* **1983**, *105*, 7512–7516.

Chapter 6. Origin of the Linear Relationship between CH_2/NH/O-SWNT Reaction Energies and Sidewall Curvature: Armchair Nanotubes

6.1 Introduction

The discovery of single-walled carbon nanotubes[1] (SWNTs) has spurred tremendous research activities on how to employ these nowadays cm-long[2] molecules in nanomaterials applications, from the investigation and optimization of various formation mechanisms over purification[3] and functionalization[4,5,6,7,8] techniques to SWNT-based molecular engineering. In particular, the electronic properties of these nanometer-size diameter tubes featuring a wide range of electrical conductivity (from semiconducting to metallic, dependent on tube diameter and chirality[9,10,11] and functionalization[12,13]), combined with unique mechanical and thermal properties (unusual strength,[14] high thermal conductivity[15]) make SWNTs excellent candidates to either replace conventional materials in a wide variety of electronic devices, or to allow the design of entirely new single-molecule based devices. On the other end of the length spectrum, armchair SWNTs have been seriously suggested as possible light-weight, cheap alternative for copper as material to construct continent-spanning power transmission lines from solar farms or nuclear fusion reactors.

Unfortunately, pure ("pristine") SWNTs usually form nanotube bundles due to their high polarizability causing poor solubility and dispersion,[6] which poses many difficulties for their manipulation and processing, and seriously limits their practical application. SWNT functionalization reactions of both covalent[4,5,6,7,16,17,18] (electronic structure and electrical conductivity modifying[4,12,19]) and π-stacking[20,21] (electronic structure preserving) type have become popular for improving SWNT solubility and

hence processability,[6] and may also become very important in tethering SWNTs to surfaces and nanostructures.[5] Moreover, it was discovered recently that metallic and semiconducting SWNTs give rise to different thermodynamic reactivity towards chemical addition reactions,[4,22] which allows to separate[5,23,24,25,26] and spectroscopically characterize[27,28,29] them.

Despite the obvious importance of covalent SWNT functionalization reactions, detailed atomic level understanding about the structural and electronic defects created by these reactions is still lacking. In particular, we do not know how exactly covalent functional groups are incorporated into the π-conjugated carbon network of the SWNT sidewalls, although it is clear that sp^3-hybridization, vacancy, and Stone-Wales type defects are most likely somehow involved in defect creation.[30] Experimentally, no method is capable to provide atomistically resolved structural data of functionalization defects, although it has recently become possible to quantify[31] and characterize sidewall attached functional groups themselves,[28,29,32,33] and it was also experimentally found that small diameter tubes (SDNTs) are more reactive towards oxidation than large diameter tubes.[34,35,36] Despite this progress, virtually nothing is known for certain about the molecular and electronic structures of functionalization induced defects created on the tube sidewall carbon network.

Theoretical exploration is a natural complimentary approach to such investigations, and exohedral SWNT functionalization has been widely studied using integrated ONIOM and QM/MM approaches[37,38,39] as well as pure density functional theory (DFT)[23,25,40,41,42,43,44,45,46,47,48,49,50,51,52] and density functional tight binding (DFTB) calculations.[50] A well defined problem easily accessible to theoretical investigations is the effect of curvature on the reactivity of the SWNTs, and it was found previously,[43,44,45,48,50,51,52] that the total reaction energy ΔE for the exohedral SWNT addition of addend X:

$$\Delta E(\text{X-SWNT}) = E(\text{X-SWNT}) - E(\text{X}) - E(\text{SWNT}) \tag{6.1}$$

shows a decreasing trend with increasing d. This behavior was explained by the larger pyramidalization angle[53] of SDNT carbon atoms, which are already more susceptible to adapt sp^3 configuration than those of large diameter tubes. In addition, a greater strain energy in the case of SDNTs is released by breaking the central C_a-C_a bond, stabilizing the reaction product.[54] In more quantitative studies, it was found that the total reaction energy $\Delta E$of exohedral addition products depends linearly on the reciprocal tube diameter d for X=H and Al atoms[42] and X=NH_2[47] according to

$$\Delta E = \Delta E_0 + C/d \tag{6.2}$$

based on generalized gradient approximation (GGA) DFT calculations with periodic boundaries. The binding energy BE these authors are referring to is simply defined as $-\Delta E$from equation 6.1. The Gülseren and Zhao groups suggested that ΔE_0 is a quantity related solely to the adatom/electrophilic agent and corresponds to its reaction (=negative binding) energy on a planar graphite surface ($1/d$=0 which is equivalent to $n = \infty$), and that C is a constant related to the tube itself according to Reference.[42] One of the factors determining C is apparently related to tube chirality: Gülseren *et al.* determined C to be -144.8 kcal·Å/mol for zigzag SWNTs independent from the electrophile, whereas Zhao *et al.* found C to be -114.2 kcal·Å/mol for a series of armchair SWNTs. While both groups noticed the linear relationship between $\Delta E$and $1/d$, they did not give a satisfactory quantitative explanation for this finding besides a general statement on *s*-*p* mixing.[42] Kudin *et al.* have investigated in detail the $1/d^2$-behavior of the sidewall deformation energy, and investigated fluorination energies and energy cancellation of the quadratic terms due to kink formation.[54] In a very recent paper, Li *et al.* have introduced the concept of chirality-independent "bond curvature" defined to be $1/d$-dependent to investigate the linear relationship between $\Delta E$and $1/d$ for exohedral additions with X=CH_2, NH, O, CCl_2, and SiH_2.[49]

As to the difference between reactivities of the inside and outside surfaces of the

SWNT sidewalls, ΔE for exohedral (outside, convex tube surface, positive curvature) and endohedral (inside, concave tube surface, negative curvature) functionalization of SWNTs was investigated regarding diameter dependence for the addition reactions of hydrogen and fluorine atoms, using calculations on finite model systems.[44,51] It was found that the convex surface (positive values of $1/d$) of carbon nanotubes is more reactive than the concave surface (negative values of $1/d$), which is the reason why the inside of a SWNT has also been characterized as a "chemical reactor" for instance for fullerene peapod to double-walled nanotube (DWNT) coalescence.[18] Theoretical studies also confirmed the experimental observation[34,35,36] that SDNTs are more reactive than larger diameter SWNTs. It was argued that the carbon pyramidalization angle is the origin of the differences in reactivity between convex and concave carbon surfaces.[50,51] Curiously, Lu *et al.* found in periodic boundary DFT calculations that two structurally distinct minima exist for [2+1] cycloaddition derivatives of (n, n) SWNTs with O and NH, namely an open structure with completely broken C-C bond > 2.0 Å for $n \leq 10$, and closed 3-membered ring (3MR) structures with C-C $<$ 1.7 Å for $n > 10.58$ In fact, Chen *et al.* reported the existence of almost isoenergetic minima for [2+1] cycloaddition products earlier,[51] but neither group elaborated further on this phenomenon. Li *et al.* have applied their "bond curvature" (K) concept to the problem and stated that, if K is large, the open structure is formed, and if K is small, the 3MR structure is favorable, with a threshold of roughly 1.5 nm^{-1} for a critical value of K *separating* both situations.[49] They however did not elaborate on the origin of the two isomers or their energetic relationship in dependence on $1/d$. In the following, we will distinguish exohedral 3MR isomers as exo(s) (s for "short" CC bond) and the exohedral open isomers as exo(l) (l for "long" CC bond).

In the present work, we will study the molecular structures and thermodynamic stabilities of [2+1] bridge-site cycloaddition reaction products of simple electrophilic agents, namely methylene CH_2, imine NH, and the oxygen atom, with hydrogen-

terminated 15 Å long (n, n) armchair SWNT models with varying diameters d from $n = 3$ to $n = 13$:

$$d = 3na_{C-C}/\pi \tag{6.3}$$

(a_{C-C} is the SWNT C-C bond distance and typically 1.44 Å). We have selected the bridge-site addition due to its popularity in the theoretical community, although [4+1] hole-site cycloaddition reactions are likely to yield more stable products, as we have shown before.[37] Results for bridge- site additions on tubes of different chirality type will be presented in a separate, forthcoming paper. Both DFT as well as the self-consistent charge density functional tight-binding (SCC-DFTB, denoted in short "DFTB" in the remainder of the text) methods have been employed in this study.

First of all, we present a careful comparison between these two theoretical methods in terms of geometries and energetics for CH_2/NH/O reaction systems. The DFTB method has already been exhaustively tested on a series of fullerene isomers and we found excellent agreement between DFTB and the computationally much more expensive ab initio B3LYP/6-31G(d) regarding optimized geometries and relative isomer energetics.[55] The low computational requirement of the DFTB method allows us to investigate complete series of all three armchair (n, n) SWNT-CH_2/NH/O reaction systems for diameters up to 1.79 nm ($d(n = 13)$ with a_{C-C} =1.44 Å). Exo(s)- and exo(l)- as well as endo-adducts are studied, and ΔE is analyzed by means of energy decomposition into deformation (DEF) and interaction (INT) energy terms. We will explore the origin for the barrier between the exo(l) and exo(s) isomers and investigate the positions of the corresponding minima and their separating transition states on the C-C potential energy surfaces in dependence on tube curvature. The linear relationship of equation 6.2 for reaction energies and individual energy decomposition analysis (EDA) contribution terms will then be discussed for the CH_2/NH/O adducts on convex and concave surfaces of different diameter armchair SWNTs, using frontier orbital principles applied to extended systems,[10,56] and the simple geometry-derived

pyramidalization angle concept[53] will be re-examined using selected Fock matrix elements in the fragment MO basis.

6.2 Computational Details

For DFT geometry optimizations on finite-size hydrogen-terminated SWNT models we selected the popular hybrid density functional theory B3LYP[57,58] with the polarized 6-31G(d) basis set as implemented in GAUSSIAN 03 Rev. D01+.[59] DFTB is an approximate density functional theory method based on the tight binding approach,[60,61,62,63,64] which utilizes an optimized minimal LCAO Slater-type all-valence basis set in combination with a two-center approximation for Hamiltonian matrix elements. In this study we selected the self-consistent charge formulism (SCC-DFTB), since we are dealing with the interaction of electronegative functional groups with SWNT sidewalls. The energy threshold for self-consistent charge SCF in DFTB was chosen as 10-9 hartree. DFTB geometry optimizations were carried out using the GAUSSIAN program by means of the "external" keyword, connecting the Gaussian geometry optimizer to a stand-alone DFTB program,[61] thus making use of the same geometry optimizer for both DFT and DFTB calculations. Default optimization criteria as implemented in GAUSSIAN were employed. Kitaura-Morokuma energy decomposition analysis (EDA)[65,66] was performed in the case of the X=CH_2 adduct using the implementation in GAMESS.

6.3 Results and Discussion

6.3.1 Comparison between B3LYP/6-31G(d) and DFTB energetics and geometries of exohedral CH_2/NH/O adducts of (n,n) SWNTs with $n = 3$ to 6

Since its first conception in 1995[60] and in particular through the introduction of an atomic self-consistent charge energy term,[61] the DFTB method has been proven successful during the last decade in a wide variety of areas.[63,64] Recently, we have tested the DFTB performance for geometries and energetics of different isomers of fullerenes,[55] and compared the results with B3LYP, AM1[67] and PM3[68] methods. DFTB performed remarkably better than AM1 and PM3 regarding geometries and energetics when compared to B3LYP/6-31G(d) results.[55] In this study, we first compare B3LYP/6-31G(d) optimized geometries as well as corresponding ΔE with those of DFTB for the exo(l)-addition products of CH_2, NH, and O to one of the n central C-C bonds of (n,n) armchair SWNTs with $n = 3-6$. As reference for the computation of the stabilization energy ΔE according to equation 6.1 we have employed closed shell B3LYP and DFTB wavefunctions of the pristine SWNTs, and open shell triplet UB3LYP and spin-polarized DFTB wavefunctions for the X=CH_2/NH/O addends. The respective B3LYP and DFTB ΔE values are plotted in Figure 6.3. The average ΔE difference between B3LYP/6-31G(d) and DFTB for CH_2 functionalized armchair SWNT is found to be 13.8 kcal/mol, for NH functionalization this difference is 17.0 kcal/mol, and for O functionalization the average ΔE difference is 8.8 kcal/mol. The relative order of exothermicities is the same in both levels of theories: CH_2 > O > NH. In all cases, DFTB is found to systematically overbind relative to the B3LYP/6-31G(d) results. Of course, this difference changes with the choice of the first principles density functional, as a recent comparison of DFTB with GGA DFT illustrates,[50] where larger discrepancies were found. Since B3LYP is used for the pa-

rameterization of the two-center repulsive DFTB energy terms, the hybrid functional is very suitable for energy comparisons. Moreover, the difference is nearly constant from (3,3) SWNTs to (6,6) SWNTs, indicating that the entire DFTB potential energy surface (PES) is shifted as a whole compared to the B3LYP/6-31G(d) PES to lower ΔE values, and we conclude therefore that the description of the carbon network is unaffected by this shift (meaning that ΔE_0 from equation 6.2 is affected but not the parameter C).

As to optimized geometries, the bond lengths of C_a-C_a (the attacked C-C bond), C_a-C_b (one of the four symmetry equivalent C-C bonds connected to the attacked carbon atoms) and C_a-X (X=C,N,O for CH_2, NH and O addends, respectively) predicted by DFTB are comparable with those of B3LYP/6-31G(d) as shown in Table 6.1, where also an atom labeling scheme can be found. The largest bond length deviations are observed for the SWNT C_a-C_a bonds, which is most problematic with a difference of 0.07 Å in the case of the O-(6,6) SWNT. This discrepancy however can be considered less critical since in the exo(l) isomers the bridge carbon atoms do not have a strong bonding interaction. The largest C_a-X bond deviation is found for the C_a-O bond of O-(5,5) SWNT with a 0.04 Å longer bond in case of the DFTB optimized geometry. Overall, these benchmark results show convincingly that the DFTB method can reasonably reproduce first principles B3LYP/6-31G(d) level geometries and energetics for SWNT and derivatives, and that in particular the features of the C_a-C_a PESs for the addition product bonds are adequately described by the DFTB method.

6.3.2 One or two local minima on the C_a-C_a PES of exo-addition products

While 3MR isomers corresponding to endohedral and exo(s) additions are characterized by C_a-C_a bridges with each carbon atom having four bond neighbors and

sp^3 hybridization, the bridge carbon atoms for opened exo(l) isomers retain partial sp^2 hybridization since they only have 3 direct bond neighbors, as the C_a-C_a bond is almost completely broken (see Figure 6.1). This situation can be compared to the closed and open isomers of the ozone molecule, which is isoelectronic with an extremely simplified CH_2-X-CH_2 model of the SWNT functionalized C_a-X-C_a area, where X=CH_2/NH/O. In the case of ozone, both isomers correspond to the minima of two different electronic singlet states of same symmetry,[69] which form a conical intersection.[70] The opened isomer is energetically very unfavorable for CH_2-X-CH_2 because its ground state corresponds to a diradical electronic state where both carbon atoms carry an unpaired electron. However, in the case of SWNT-X, the C_a-C_a bridge atoms are connected to C_b atoms, and because the C_a atomic p_z-orbitals can conjugate with the attached SWNT π-electron network, the diradical system can be stabilized as shown in Figure 6.1. This difference is the origin for the existence of opened (exo(l)) and closed (exo(s)) isomers in the case of exohedral addition products with large diameters as observed by Lu *et al.*,[52] Chen *et al.*,[51] and Li *et al.*,[49] and the barrier between them is a remnant of the conical intersection between the corresponding different electronic states. In the case of small diameter tubes, exo(l) becomes the only minimum on the C_a-C_a PES, and the 3MR minimum disappears completely. Table 6.2 lists optimized bond lengths C_a-C_a, C_a-C_b, and C_a-X (X=C,N,O) for exo(l)-, exo(s)-, and endohedral addition products of CH_2, NH, and O to (n, n) SWNTs, and the longer C_a-C_b bonds (sp^3 hybridization) with ∼1.46 Å for exo(s)- and endohedral addition products (both are 3MR isomers) compared to their values for exo(l) of about 1.42 Å (sp^2 hybridization) validate this simple valence bond picture.

The relative energy order of these exo(s) and exo(l) isomers is determined by four factors: (1) the presence of the C_a-C_a σbond, which favors the 3MR exo(s) structure, (2) the strain energy contained in the 3MR structures associated with the three-membered ring, favoring the exo(l) structure, (3) the strain energy release

of the SWNT bond network due to the breaking of the C_a-C_a bond also favoring the exo(l) structure, and (4) the perturbation of the SWNT π-electron conjugation network, which is larger in the case of the 3MR structures due to the sp^2 to sp^3 change in hybridization, and favors therefore also the exo(l) isomers. The delicate balance among these four energetic factors determines the depths of the associated opened and closed isomer minima on the C_a-C_a PES and the barrier separating them. Out of these four factors, only the SWNT strain energy release (factor 3) is significantly affected by a diameter change. Its dominance in the d-dependence of the relative positions of the isomer minima becomes apparent in the fact that the 3MR exo(s) minimum completely disappears for small d due to the extraordinary energetic lowering of the exo(l) minimum.

As depicted in Figure 6.1, the overall order of the reaction energies of the electrophiles with the SWNTs is a function of the σ-character contained in the C_a-X bond. While exo(l) features a clear σ bond, exo(s) and endo represent cases where X interacts with C_a only in a partial sp^3-hybridized state, and a significant fraction of the interaction stems from X-π overlap because of the large deviation of the 3MR bond angles from ideal tetrahedral sp^3 hybrid angles. We note that in the 3MR compounds the C_a bridge atoms arrange more favorable C_b-C_a-X bond angles by slightly lifting outside (exo(s)) or becoming sucked inside (endo) the tube perimeter (see Figure 6.1). A hypothetical endohedral structure with a broken C_a-C_a σbond (endo(l)) does not exist because the concave SWNT sidewall curvature allows geometrically only π-interaction with the addend, while the σ-type bond required by the hypothetical endo(l)-structure would require that the sp^2 bridgehead carbon acquires an almost 90° bond valence angle, which of course is impossible. The order of the reaction energies is therefore exo(l) > exo(s) > endo, which agrees perfectly with previous observations, in particular that endohedral interactions are very weak.[18]

In Figure 6.4, relaxed PES scans for the adducts of CH_2/NH/O addends with

(a) (6,6), (8,8), (10,10) SWNTs in exohedral configuration, and (b) (6,6) and (8,8) SWNTs in endohedral configuration are shown, together with similar scans for a CH_2/NH/O-graphite model system. These plots give an impression of how the opened and 3MR isomer minima behave with changing curvature. According to Hammond's theory, the barrier connecting two minima decreases as the energy difference between the two isomers increases, and consequently develops into a shoulder in most of the cases. In the case of convex curvature (group a), exo(l) minima are lower than exo(s) but disappearing as d approaches infinity (zero curvature), and for concave curvature only the 3MR minimum survives. Different X addends show slightly different PES and relative isomer minima, but the qualitative description is similar for all cases and generally applicable to SWNT functionalization.

6.3.3 Linear relationships between the stabilization energy (ΔE) and the inverse radius ($1/d$) of exo- and endohedral addition products of CH_2/NH/O to (n,n) SWNTs with n=4 to 13 and $n = \infty$

Regarding electronic properties, we note that the armchair series of SWNTs with increasing diameter is the only systematic series that can be easily constructed by systematically increasing tube chiral indices n and m while maintaining the main features of the electronic state such as electrical conductivity and HOMO-LUMO gap,[71,72,73] as well as aromatic character.[74] In the general case, one has to consider that series of tubes with similar electronic structures follow the $(n - m)$ mod 3 rule,[72,73,75] which has been derived using simple π-Hückel theory (which is very closely related to π-orbital only tight binding). We note, however, that although the HOMO-LUMO gap of an infinite armchair tube is exactly 0 in p-Hückel theory, finite size and *s-p* mixing provides for a de facto HOMO-LUMO gap in our model systems. Geometrically, for armchair tubes Li's "bond curvature" index is simply $K = 1/d$.

In Figure 6.5, we plot the DFTB ΔE for exo(s)-, exo(l)-, and endohedral CH_2/NH/O addition products to a central (n,n) SWNT C_a-C_a bond as a function of $1/d$ for $n = 4 - 13$. We are starting the series at $n = 4$ because $n < 4$ does not allow sterically the formation of endohedral addition products. In agreement with References,[42,47,49] and others who did not elaborate on the linear relationship between ΔE and $1/d$ but which is nevertheless present in their findings,[50,51,52] we observe a perfect linear relationship between ΔE and $1/d$ from (4,4) to (13,13) armchair SWNTs in all three CH_2/NH/O cases. Table 6.3 lists the values for ΔE_0 and C parameters from equation 6.2 as well as linear regression R^2 values, which are all almost identical to 1.0 for both endohedral and exohedral addition products.

In the case of exohedral products, we distinguish two series corresponding to (a) exo(s): closed 3-membered ring (3MR) isomers with C_a-C_a bonds shorter than 1.7 Å (these isomers were only found for large diameter tubes starting from $n =$ 8, 10, and 6 for X=CH_2, NH, and O, respectively), and (b) exo(l): open product isomers with C_a-C_a bonds larger than 2.0 Å. In general we note that the 3MR exo(s) isomers exhibit much smaller overall changes in the SWNT carbon bond network than the exo(l) isomers when evaluating the root mean square difference between pristine and functionalized SWNTs. C is negative for both series of exohedral addition products, with values between -201 kcal·Å/mol and -224 kcal·Å/mol for exo(s) and -317 kcal·Å/mol to -349 kcal·Å/mol for exo(l), depending on the addend. O seems to be associated with smaller slopes, and those for NH and CH_2 are larger in magnitude and rather similar. In comparison, Zhao's value for the addition of NH_2 to armchair SWNTs is much smaller with -114 kcal·Å/mol, which certainly is related to the weaker electrophilicity of the agent, as well as to the different level of theory (GGA instead of DFTB, parameterized to mimic hybrid B3LYP density functional PESs). Comparing our results to the findings by Li *et al.*[49] we note that a) instead of obeying their critical threshold for K of 1.5 nm, the exo(s) minima disappear for smaller values of

$1/d$ in dependence on X, from $n = 8$ and $K = 1.1$ nm^{-1} (CH_2), $n = 10$ and $K = 1.4$ nm^{-1} (NH), and $n = 6$ and $K = 0.8$ nm^{-1} (O), and that b) both opened and 3MR minima can co-exist at least up to $n = 13$ and $K = 1.7$ nm^{-1}, with exo(s) isomers higher in energy than exo(l) isomers.

In case of endohedral addition reactions we notice a reversed dependence of ΔE on $1/d$, namely slightly increased ΔE with larger diameters, with overall smaller reaction energies compared to their exohedral equivalents. C is correspondingly positive and very dependent on the reagent, with values of 161 kcal·Å/mol (CH_2), 118 kcal·Å/mol (NH), and 70 kcal·Å/mol (O). The O addend gives rise again to the smallest absolute slope value, but the slopes of ΔE corresponding to CH_2 and NH are now very different. The linear relationship between ΔE and $1/d$ holds also in this case, with values very close to 1.0.

As n increases, d approaches infinity, which represents a planar graphene sheet where endo- and exohedral addition products can no longer be distinguished. According to equation 6.2, in the large diameter limit, ΔE becomes identical to ΔE_0. This is more or less the case for X=CH_2 and X=O with extrapolated values for ΔE_0 of -53 kcal/mol and -42 kcal/mol ±1 kcal/mol for all three series (exo(s), exo(l), and endo), respectively. We have computed ΔE for a planar graphene model $C_2$96 in periodic boundary condition (PBC) representing the case for $n = \infty$for each reagent, and the values, -53.6 kcal/mol and -46.0 kcal/mol for X=CH_2 and X=O, respectively, agree well with E0 above; in the graphene model, only exo(s) isomers were found. In the case of NH, however, we find that the exo(l)- and endohedral addition curves do not intersect on the vertical axis (see Figure 6.5 and Table 6.3), but that the intersection points for exo(s) (-28.5 kcal/mol) and endohedral (-26.3 kcal/mol) curves match the same bonding mode (3MR) when approaching infinite diameter (-29.5 kcal/mol). It appears that the exo(l) series for X=NH with an extrapolated value of ΔE_0 and an R^2 value of 1.000 describes a somewhat different bonding situation, for which we have

no explanation at this moment.

In summary, we find that the linear relationship of ΔE with $1/d$ for both exo- and endohedral addition reaction products can be used to accurately predict ΔE for general armchair (n, n) SWNT addition reactions, provided ΔE_0 and the slope parameter C are known.

6.3.4 Energy decomposition analysis of ΔE and the origin of the $1/d$ dependency

In order to investigate the origin of the linear relationship of ΔE with $1/d$ in greater detail, we are decomposing ΔE for the reaction systems of Section C into various components of energy decomposition analysis (EDA) as functions of $1/d$. We focus only on the structures with short C_a-C_a bonds, namely exo(s) and endo, as exo(l) structures are quite different from the others and can therefore not be directly compared. In the EDA, the total reaction energy $\Delta E$is at first decomposed as:

$$\Delta E = \text{PROM(X)} + \text{DEF(SWNT)} + \text{DEF(X)} + \text{INT} \tag{6.4}$$

Here PROM(X) is the energy required to promote the species X=CH_2/NH/O from its ground state (in the present case from the triplet ground state in $(a_1)^1(b_1)^1$ active orbital occupancy assuming the C_{2v} geometry of the adduct) to the valence state (here a singlet state with $(b_1)^2$ occupancy), which correlates symmetrically to the ground state adduct. DEF(SWNT) and DEF(X) are the energies required to deform their respective equilibrium structures to the structures in the adduct, and INT is the interaction energy between deformed (or prepared) SWNT and X to form the adduct. DEF(X) and PROM are found to be nearly independent of $1/d$ for both exo and endo, and can be disregarded as factors determining the $1/d$ dependency.

We found and show in Figure 6.6(A) that both DEF(SWNT) (below simply denoted as DEF) and INT, as well as ΔE, calculated at the DFTB level can be expressed

well in quadratic forms as functions of $1/d$, with both exo(s) and endo structures placed on the same horizontal scale where positive values of $1/d$ correspond to exo(s) and negative values to endo (the value with $1/d = 0$ should represent the extrapolated value for graphene), ranging from $1/d = -0.18$ Å^{-1} corresponding to endo-(4,4) SWNT to 0.09 Å^{-1} corresponding to exo(s)-(8,8) SWNT. For instance for X=CH_2 (energies are in units of kcal/mol and d in Å):

$$\text{DEF} = 370.36(1/d^2) + 28.44(1/d) + 28.56 \qquad (R^2 = 0.9862) \tag{6.5}$$

$$\text{INT} = -479.37(1/d^2) - 213.26(1/d) - 84.75 \qquad (R^2 = 0.9989) \tag{6.6}$$

$$\Delta E = -93.56(1/d^2) - 183.08(1/d) - 53.95 \qquad (R^2 = 0.9994) \tag{6.7}$$

The fact that the ratio of the quadratic coefficient over the linear coefficient for ΔE is very small (0.51) indicates that ΔE is nearly perfectly linear with respect to $1/d$ from a negative (-0.18) to positive (0.09) values of $1/d$, as discussed in the preceding Section (R^2 for a purely linear regression of ΔE is 0.9981). On the other hand DEF is nearly completely quadratic with the quadratic/linear ratio of 13.4, while INT has a modest quadratic contributions of opposite sign, with the quadratic/linear ratio of 2.25. The important finding in this analysis that the nearly perfect linear $1/d$ dependency of ΔE is due to cancellation of quadratic contributions of DEF and INT, and that the dominant contributor to the linear term comes from INT.

DEF with small linear coefficient indicates that this term is heavily quadratic. DEF, which is related to mechanical properties of SWNTs, has been known a strong dependence on sidewall curvature, or equivalently, on the tube diameter.[76,77] While the tube's strain energy, defined as the difference of the energy per atom in the tube and that in the corresponding infinite flat sheet, has a characteristic dependence on $1/d^2$.[43,54,78] The energy increase of the tube due to partial loss of πconjugation and the local σbond distortion (for exo(s) and endo) or breaking (for exo(l)) should also

contribute to DEF.

INT is the energy gained by forming two C-X bonds between the prepared SWNT and X fragments, and is also a function of $1/d$. In order to clarify its $1/d$ dependency, we further decompose INT into the electrostatic interaction (ES), the exchange repulsion (EX) and the orbital contribution (ORB), which is defined as INT-(ES + EX):

$$\mathrm{INT} = \mathrm{ES} + \mathrm{EX} + \mathrm{ORB} \tag{6.8}$$

According to the Kitaura-Morokuma EDA, the orbital contribution ORB itself can be further decomposed into the charge transfer interaction (CT), polarization (PL), and a higher mixing term (MIX), or alternatively into the donative interaction (CTPLX(A→B)), back-donative interaction (CTPLX(B→A), and the remaining residue (RES).74 However, when the interaction is very strong, as in the present case, the coupling terms (MIX or RES) become large and the further decomposition of ORB loses its significance. Therefore we will not discuss the further decomposition of ORB. For EDA given in equation 6.8, the use of DFTB is not suitable since there is no exchange and the electrostatic term is only approximately evaluated. Since the EDA code available in GAMESS is limited to the Hartree-Fock (HF) method only, we decided to employ the minimum basis set HF/STO-3G method. The small basis set (STO-3G) will overemphasize the orbital interaction because of a large basis set superposition error (BSSE); however, we expect that this will reveal very qualitatively the nature of the interaction when used without further decomposition of ORB. We used a shorter (5 Å long) model of the SWNT consisting of only two six-membered armchair rings (2 layers) along the tube axis and terminated with hydrogen atoms. The geometries of the endo and exo(s) CH_2 adduct models (as well as SWNT and CH_2) were cut from the DFTB optimized structures, and the positions of the terminating hydrogens were optimized at this level to obtain consistent DEF and other energy components.

The results of the EDA analysis are shown in Figure 6.6(B), with the detailed results given in Table 6.4. We find the following polynomial fits (energies are in units of kcal/mol and d in Å):

$$\begin{aligned} \text{EX} &= 1260.00(1/d^2) + 203.59(1/d) + 302.14 && (6.9) \\ \text{ES} &= -810.80(1/d^2) - 196.40(1/d) - 126.28 && (6.10) \\ \text{ORB} &= -996.78(1/d^2) - 312.12(1/d) - 357.00 && (6.11) \\ \text{INT} &= -523.31(1/d^2) - 300.61(1/d) - 181.01 && (6.12) \end{aligned}$$

Although the INT coefficients in this analysis of the small model at the HF/STO-3G level are somewhat different from the INT coefficients in equation 6.7 obtained for the large model at the DFTB level, the qualitative feature of attractive and modestly quadratic interaction is the same and the qualitative argument can be made using equations 6.10-6.12. This analysis shows that ES, EX and ORB have substantial quadratic contributions with the quadratic/linear coefficient ratio of 6.2, 4.1, and 3.2, respectively. On the other hand this ratio is 1.7 for INT, indicating that cancellation of quadratic contributions between EX, ES and ORB makes INT substantially more linear in $1/d$ than their components.

The present analysis also shows that the largest linear $1/d$ contribution to INT and therefore to ΔE originates from the ORB term. Therefore the clarification of dominant linear terms in ORB should provide the origin of the linear $1/d$ dependence of ΔE. In order to further elucidate this point, we examined the Hartree-Fock and overlap matrix elements of the adducts in the basis of the MOs of deformed fragments and solved the partial general eigenvalue problems (see Table 6.5 for a few examples). We found two major contributors to ORB. One is in a_1 symmetry and is the donative interaction from the C=C πHOMO of SWNT to the CH_2 a_1 sp^2-type σ MO that is vacant in the $(b_1)^2$ reference electronic configuration (see above). The other is in

b_1 symmetry and is the back-donative interaction from the CH_2 $p\pi$MO to the C=C π^*LUMO of SWNT. Upon going from large to small concave curvature (small to large tube endo, or negative $1/d$) through zero curvature (graphene, $1/d = 0$) to small to large convex curvature (large to small tube exo(s), or positive $1/d$), the MO overlap (hence the magnitude of stabilization) due to this b_1 interaction increases steadily and thus is the most important factor for controlling the change of the entire interaction INT. On the other hand, the MO overlap due to the a_1 interaction decreases more slowly because of smaller angular dependence.

The qualitative picture of such changes can be illustrated in Figure 6.2. Going from planar graphene to nanotube of gradually smaller radius, the nature of the C=C π^*LUMO changes from a linear combination of pure p AOs to sp^n hybrid AOs, and they become more concentrated on the outside of the tube and also point more away from the vertical direction (see for instance Figure 6.5 in Reference[79]). Because s-p hybridization of the C=C π^*LUMO goes with $1/d^2$,[80] the overlap on the outside (exo) of the nanotube increases with $1/d^2$ while that on the inside (endo) decreases with $-1/d^2$. But even neglecting hybridization effects, the angle between the b_1 $p\pi$MO to the C=C π^*LUMO naturally changes with $1/d$ since the direction of the SWNT p orbitals deviate by $\theta/2$from a perpendicular direction to the surface linearly with $1/d$ (see right-hand side of Figure 6.2):

$$U = 2\pi r = \pi d = 3na_{C-C} \tag{6.13}$$

$$\theta = 2\pi/3n = 2\pi a_{C-C}/U = 2a_{C-C}/d \tag{6.14}$$

where U is the circumference, and we used equation 6.3. On the other hand, in the a_1 symmetry as shown in Figure 6.2, there is a substantial overlap between the C=C πHOMO of SWNT and the CH_2 sp^2-type σ MO that is placed inside the nanotube and the overlap decreases rather slowly going from inside to outside. *As a consequence, the $1/d$ dependence of the ORB term is dominated by the b_1 back-donative interaction,*

which increases steadily from large negative (concave, endo) curvature to large positive (convex, exo) curvature. The use of the pyramidalization angle concept previously put forth for a qualitative description of the curvature-dependence of the binding energy[48] or the "bond curvature" concept of Li *et al.*[49] is therefore only partially correct, as the donative SWNT→X interaction is clearly not so much affected by the pyramidalization angle, as inspection of the eigenvalues associated with the Fock matrix elements in the MO basis of the fragments shows (see Table 6.5). Instead, a delicate balance of individual energy contributions, including $1/d^2$-dependent *s*-*p* mixing, is responsible for the linear behavior of reaction energies.

Although the detailed EDA was performed only for X=CH_2 with a short SWNT model at the HF/STO-3G level, we fully expect that essentially the same picture governs the interaction of other addends and provides a guiding principle for further studies of SWNT functionalization.

6.4 Summary and Conclusions

We have carried out detailed and systematic theoretical studies on the curvature dependence of the interactions of electrophilic adducts X=CH_2/NH/O with armchair (n, n) SWNTs with $n = 3, 4, \ldots, 13$ using self-consistent charge DFTB, which was checked for accuracy against ab initio hybrid DFT in benchmark calculations. Both endo- and exohedral adducts were studied, representing interactions with the inside (concave) and outside (convex) curvature of the tube sidewalls. In agreement with previous computational studies and experimental observations, we find that small diameter tubes are more reactive than large diameter tubes, and that endohedral functionalization is energetically much less feasible than exohedral functionalization. In particular, a linear relationship between reaction energies E and the reciprocal tube diameter $1/d$ was found, as reported previously by Gülseren *et al.*,[42] Zhao *et al.*,[46,47] and Li *et al.*,[49] who had not provided a satisfactory explanation. Our findings

can be summarized as follows.

1. DFTB can reproduce B3LYP/6-31G(d) level results rather well in terms of geometry and energetics for the addition reactions of SWNT as discussed in Section 3.A. Absolute reaction energies are somewhat overestimated with 10-20 kcal/mol, but the trend is systematic and potential energy surfaces (PESs) are consistently shifted, therefore the curvature comparisons are unaffected by the DFTB overbinding.

2. We find two isomers in case of exohedral additions, one where the C-C bond is completely broken with a bond distance > 2.0 Å (exo(l)), and a 3-membered ring (3MR) isomer where the C-C bond distance is still smaller than 1.7 Å, indicating considerable carbon-carbon binding. The open isomer for the endohedral addition compounds is geometrically impossible and not associated with a minimum. We have examined the C-C PESs for all three X=CH_2/NH/O endo- and exohedral addition products and find a systematic variation of the minima, separated by a barrier which can be interpreted as conical intersection between two electronic states arising from two possible connectivity modes of the C-X-C moiety with the CNT: One where the bridgehead carbon atoms are still sp^2-hybridized, forming a σ-bond with X (exo(l)), and one where the bridgehead carbon atoms are almost completely sp^3-hybridized (the 3MR series endo and exo(s)).

3. Gülseren's and Zhao's C-term in the linear relationship $\Delta E = \Delta E_0 + C/d$ depend not only on the nature of the binding interaction, but also on the isomer type (exo(l), exo(s), and endo). Tube chirality is certainly another determining factor, which will be examined in a forthcoming paper. Based on the clear addend-dependence of C unveiled in our study, we judge that the finding by Gülseren *et al.*[42] of a very similar slope C for H and Al additions to $(n, 0)$

zigzag SWNTs is most likely accidental.

4. A nearly perfect linear relationship between $\Delta E$and$1/d$ all through exo- (positive curvature) and endohedral (negative curvature) additions is due to cancellation between the quadratic contributions of the SWNT deformation energy (DEF(SWNT)) and the interaction energy (INT) between the deformed SWNT and CH_2/NH/O. The energy decomposition analysis (EDA) shows that the quadratic contributions in electrostatic (ES), exchange (EX) and orbital (ORB) terms mostly cancel each other making INT weakly quadratic and that the linear $1/d$-dependence of INT, therefore of ΔE, is dominated by the back-donative orbital interaction of b_1 symmetry from the occupied CH_2/NH/O $p\pi$ orbital to the vacant C=C π^* LUMO of the SWNT.

References

1. IIJIMA, S.; ICHIHASHI, T. *NATURE* **1993**, *363*, 603–605.

2. Zheng, L.; O'Connell, M.; Doorn, S.; Liao, X.; Zhao, Y.; Akhadov, E.; Hoffbauer, M.; Roop, B.; Jia, Q.; Dye, R.; Peterson, D.; Huang, S.; Liu, J.; Zhu, Y. *NATURE MATERIALS* **2004**, *3*, 673–676.

3. Dailly, A.; Yim, J.; Ahn, C.; Miura, E.; Yazami, R.; Fultz, B. *APPLIED PHYSICS A-MATERIALS SCIENCE & PROCESSING* **2005**, *80*, 717–722.

4. Strano, M.; Dyke, C.; Usrey, M.; Barone, P.; Allen, M.; Shan, H.; Kittrell, C.; Hauge, R.; Tour, J.; Smalley, R. *SCIENCE* **2003**, *301*, 1519–1522.

5. Banerjee, S.; Hemraj-Benny, T.; Wong, S. *ADVANCED MATERIALS* **2005**, *17*, 17–29.

6. Dyke, C.; Tour, J. *JOURNAL OF PHYSICAL CHEMISTRY A* **2004**, *108*, 11151–11159.

7. Banerjee, S.; Wong, S. *JOURNAL OF PHYSICAL CHEMISTRY B* **2002**, *106*, 12144–12151.

8. Niyogi, S.; Hamon, M.; Hu, H.; Zhao, B.; Bhowmik, P.; Sen, R.; Itkis, M.; Haddon, R. *ACCOUNTS OF CHEMICAL RESEARCH* **2002**, *35*, 1105–1113.

9. White, C.; Mintmire, J. *JOURNAL OF PHYSICAL CHEMISTRY B* **2005**, *109*, 52–65.

10. Joselevich, E. *CHEMPHYSCHEM* **2004**, *5*, 619–624.

11. Anantram, M. *APPLIED PHYSICS LETTERS* **2001**, *78*, 2055–2057.

12. Collins, P.; Bradley, K.; Ishigami, M.; Zettl, A. *SCIENCE* **2000**, *287*, 1801–1804.

13. Kong, J.; Franklin, N.; Zhou, C.; Chapline, M.; Peng, S.; Cho, K.; Dai, H. *SCIENCE* **2000**, *287*, 622–625.

14. Wong, E.; Sheehan, P.; Lieber, C. *SCIENCE* **1997**, *277*, 1971–1975.

15. Hone, J.; Whitney, M.; Piskoti, C.; Zettl, A. *PHYSICAL REVIEW B* **1999**, *59*, R2514–R2516.

16. Mickelson, E.; Huffman, C.; Rinzler, A.; Smalley, R.; Hauge, R.; Margrave, J. *CHEMICAL PHYSICS LETTERS* **1998**, *296*, 188–194.

17. Kim, K.; Park, K.; Kim, H.; Bae, D.; Lim, S.; Lee, Y. *JOURNAL OF THE KOREAN PHYSICAL SOCIETY* **2003**, *42*, S137–S142.

18. Kuzmany, H.; Kukovecz, A.; Simon, F.; Holzweber, A.; Kramberger, C.; Pichler, T. *SYNTHETIC METALS* **2004**, *141*, 113–122.

19. Kudin, K.; Bettinger, H.; Scuseria, G. *PHYSICAL REVIEW B* **2001**, *63*, 045413.

20. Chen, R.; Zhang, Y.; Wang, D.; Dai, H. *JOURNAL OF THE AMERICAN CHEMICAL SOCIETY* **2001**, *123*, 3838–3839.

21. Chen, J.; Collier, C. *JOURNAL OF PHYSICAL CHEMISTRY B* **2005**, *109*, 7605–7609.

22. Miyata, Y.; Maniwa, Y.; Kataura, H. *JOURNAL OF PHYSICAL CHEMISTRY B* **2006**, *110*, 25–29.

23. Chen, Z.; Du, X.; Du, M.; Rancken, C.; Cheng, H.; Rinzler, A. *NANO LETTERS* **2003**, *3*, 1245–1249.

24. Chattopadhyay, D.; Galeska, L.; Papadimitrakopoulos, F. *JOURNAL OF THE AMERICAN CHEMICAL SOCIETY* **2003**, *125*, 3370–3375.

25. Maeda, Y. et al. *JOURNAL OF THE AMERICAN CHEMICAL SOCIETY* **2005**, *127*, 10287–10290.

26. Kim, S.; Luo, Z.; Papadimitrakopoulos, F. *NANO LETTERS* **2005**, *5*, 2500–2504.

27. Brar, V.; Samsonidze, G.; Santos, A.; Chou, S.; Chattopadhyay, D.; Kim, S.; Papadimitrakopoulos, F.; Zheng, M.; Jagota, A.; Onoa, G.; Swan, A.; Unlu, M.; Goldberg, B.; Dresselhaus, G.; Dresselhaus, M. *JOURNAL OF NANOSCIENCE AND NANOTECHNOLOGY* **2005**, *5*, 209–228.

28. Kim, U.; Liu, X.; Furtado, C.; Chen, G.; Saito, R.; Jiang, J.; Dresselhaus, M.; Eklund, P. *PHYSICAL REVIEW LETTERS* **2005**, *95*, 157402.

29. Kim, U.; Furtado, C.; Liu, X.; Chen, G.; Eklund, P. *JOURNAL OF THE AMERICAN CHEMICAL SOCIETY* **2005**, *127*, 15437–15445.

30. Hirsch, A. *ANGEWANDTE CHEMIE-INTERNATIONAL EDITION* **2002**, *41*, 1853–1859.

31. Kuznetsova, A.; Mawhinney, D.; Naumenko, V.; Yates, J.; Liu, J.; Smalley, R. *CHEMICAL PHYSICS LETTERS* **2000**, *321*, 292–296.

32. Feng, X.; Matranga, C.; Vidic, R.; Borguet, E. *JOURNAL OF PHYSICAL CHEMISTRY B* **2004**, *108*, 19949–19954.

33. Zhang, L.; Kiny, V.; Peng, H.; Zhu, J.; Lobo, R.; Margrave, J.; Khabashesku, V. *CHEMISTRY OF MATERIALS* **2004**, *16*, 2055–2061.

34. Zhou, W.; Ooi, Y.; Russo, R.; Papanek, P.; Luzzi, D.; Fischer, J.; Bronikowski, M.; Willis, P.; Smalley, R. *CHEMICAL PHYSICS LETTERS* **2001**, *350*, 6–14.

35. Yudasaka, M.; Zhang, M.; Iijima, S. *CHEMICAL PHYSICS LETTERS* **2003**, *374*, 132–136.

36. Simon, F.; Kukovecz, A.; Kramberger, C.; Pfeiffer, R.; Hasi, F.; Kuzmany, H.; Kataura, H. *PHYSICAL REVIEW B* **2005**, *71*, 165439.

37. Irle, S.; Mews, A.; Morokuma, K. *JOURNAL OF PHYSICAL CHEMISTRY A* **2002**, *106*, 11973–11980.

38. Kar, T.; Akdim, B.; Duan, X.; Pachter, R. *CHEMICAL PHYSICS LETTERS* **2004**, *392*, 176–180.

39. Lu, X.; Tian, F.; Xu, X.; Wang, N.; Zhang, Q. *JOURNAL OF THE AMERICAN CHEMICAL SOCIETY* **2003**, *125*, 10459–10464.

40. Sorescu, D.; Jordan, K.; Avouris, P. *JOURNAL OF PHYSICAL CHEMISTRY B* **2001**, *105*, 11227–11232.

41. Chen, Z.; Cioslowski, J.; Rao, N.; Moncrieff, D.; Buhl, M.; Hirsch, A.; Thiel, W. *THEORETICAL CHEMISTRY ACCOUNTS* **2001**, *106*, 364–368.

42. Gulseren, O.; Yildirim, T.; Ciraci, S. *PHYSICAL REVIEW LETTERS* **2001**, *8711*, 116802.

43. Gulseren, O.; Yildirim, T.; Ciraci, S. *PHYSICAL REVIEW B* **2002**, *65*, 153405.

44. Bettinger, H. *ORGANIC LETTERS* **2004**, *6*, 731–734.

45. Lu, X.; Chen, Z.; Schleyer, P. *JOURNAL OF THE AMERICAN CHEMICAL SOCIETY* **2005**, *127*, 20–21.

46. Zhao, J.; Park, H.; Han, J.; Lu, J. *JOURNAL OF PHYSICAL CHEMISTRY B* **2004**, *108*, 4227–4230.

47. Zhao, M.; Xia, Y.; Lewis, J.; Mei, L. *JOURNAL OF PHYSICAL CHEMISTRY B* **2004**, *108*, 9599–9603.

48. Lu, X.; Chen, Z. *CHEMICAL REVIEWS* **2005**, *105*, 3643–3696.

49. Li, J.; Jia, G.; Zhang, Y.; Chen, Y. *CHEMISTRY OF MATERIALS* **2006**, *18*, 3579–3584.

50. Seo, K.; Park, K.; Kim, C.; Han, S.; Kim, B.; Lee, Y. *JOURNAL OF THE AMERICAN CHEMICAL SOCIETY* **2005**, *127*, 15724–15729.

51. Chen, Z.; Nagase, S.; Hirsch, A.; Haddon, R.; Thiel, W.; Schleyer, P. *ANGEWANDTE CHEMIE-INTERNATIONAL EDITION* **2004**, *43*, 1552–1554.

52. Lu, J.; Nagase, S.; Zhang, X.; Maeda, Y.; Wakahara, T.; Nakahodo, T.; Tsuchiya, T.; Akasaka, T.; Yu, D.; Gao, Z.; Han, R.; Ye, H. *JOURNAL OF MOLECULAR STRUCTURE-THEOCHEM* **2005**, *725*, 255–257.

53. HADDON, R. *ACCOUNTS OF CHEMICAL RESEARCH* **1988**, *21*, 243–249.

54. Kudin, K.; Scuseria, G.; Yakobson, B. *PHYSICAL REVIEW B* **2001**, *64*, 235406.

55. Zheng, G.; Irle, S.; Morokuma, K. *CHEMICAL PHYSICS LETTERS* **2005**, *412*, 210–216.

56. HOFFMANN, R. *ANGEWANDTE CHEMIE-INTERNATIONAL EDITION IN ENGLISH* **1987**, *26*, 846–878.

57. BECKE, A. *JOURNAL OF CHEMICAL PHYSICS* **1993**, *98*, 5648–5652.

58. LEE, C.; YANG, W.; PARR, R. *PHYSICAL REVIEW B* **1988**, *37*, 785–789.

59. Frisch, M. J. et al. *Gaussian 03, Revision D.01+*, Gaussian, Inc., Wallingford, CT, 2004.

60. POREZAG, D.; FRAUENHEIM, T.; KOHLER, T.; SEIFERT, G.; KASCHNER, R. *PHYSICAL REVIEW B* **1995**, *51*, 12947–12957.

61. Elstner, M.; Porezag, D.; Jungnickel, G.; Elsner, J.; Haugk, M.; Frauenheim, T.; Suhai, S.; Seifert, G. *PHYSICAL REVIEW B* **1998**, *58*, 7260–7268.

62. Elstner, M.; Cui, Q.; Munih, P.; Kaxiras, E.; Frauenheim, T.; Karplus, M. *JOURNAL OF COMPUTATIONAL CHEMISTRY* **2003**, *24*, 565–581.

63. Frauenheim, T.; Seifert, G.; Elstner, M.; Hajnal, Z.; Jungnickel, G.; Porezag, D.; Suhai, S.; Scholz, R. *PHYSICA STATUS SOLIDI B-BASIC SOLID STATE PHYSICS* **2000**, *217*, 41–62.

64. Frauenheim, T.; Seifert, G.; Elstner, M.; Niehaus, T.; Kohler, C.; Amkreutz, M.; Sternberg, M.; Hajnal, Z.; Di Carlo, A.; Suhai, S. *JOURNAL OF PHYSICS-CONDENSED MATTER* **2002**, *14*, 3015–3047.

65. MOROKUMA, K. *JOURNAL OF CHEMICAL PHYSICS* **1971**, *55*, 1236–&.

66. KITAURA, K.; MOROKUMA, K. *INTERNATIONAL JOURNAL OF QUANTUM CHEMISTRY* **1976**, *10*, 325–340.

67. DEWAR, M.; ZOEBISCH, E.; HEALY, E.; STEWART, J. *JOURNAL OF THE AMERICAN CHEMICAL SOCIETY* **1985**, *107*, 3902–3909.

68. STEWART, J. *JOURNAL OF COMPUTATIONAL CHEMISTRY* **1989**, *10*, 209–220.

69. LUCCHESE, R.; SCHAEFER, H. *JOURNAL OF CHEMICAL PHYSICS* **1977**, *67*, 848–849.

70. HAY, P.; DUNNING, T.; GODDARD, W. *JOURNAL OF CHEMICAL PHYSICS* **1975**, *62*, 3912–3924.

71. MINTMIRE, J.; DUNLAP, B.; WHITE, C. *PHYSICAL REVIEW LETTERS* **1992**, *68*, 631–634.

72. HAMADA, N.; SAWADA, S.; OSHIYAMA, A. *PHYSICAL REVIEW LETTERS* **1992**, *68*, 1579–1581.

73. SAITO, R.; FUJITA, M.; DRESSELHAUS, G.; DRESSELHAUS, M. *APPLIED PHYSICS LETTERS* **1992**, *60*, 2204–2206.

74. AIHARA, J.; YAMABE, T.; HOSOYA, H. *SYNTHETIC METALS* **1994**, *64*, 309–313.

75. WHITE, C.; ROBERTSON, D.; MINTMIRE, J. *PHYSICAL REVIEW B* **1993**, *47*, 5485–5488.

76. Hernández, E.; Goze, C.; Bernier, P.; Rubio, A. *Phys. Rev. Lett.* **1998**, *80*, 4502–4505.

77. Seifert, G.; Köhler, T.; Urbassek, H. M.; Hernández, E.; Frauenheim, T. *Phys. Rev. B* **2001**, *63*, 193409.

78. ROBERTSON, D.; BRENNER, D.; MINTMIRE, J. *PHYSICAL REVIEW B* **1992**, *45*, 12592–12595.

79. BLASE, X.; BENEDICT, L.; SHIRLEY, E.; LOUIE, S. *PHYSICAL REVIEW LETTERS* **1994**, *72*, 1878–1881.

80. YORIKAWA, H.; MURAMATSU, S. *PHYSICAL REVIEW B* **1995**, *52*, 2723–2727.

Table 6.1: Optimized bond lengths in [Å] in exohedral CH_2/NH/O adducts on (n, n) SWNTs at DFT(B3LYP/6-31G(d)) and DFTB levels.

X	CH_2						NH						O					
n	C_a-C_a		C_a-C_b		C_a-X		C_a-C_a		C_a-C_b		C_a-X		C_a-C_a		C_a-C_b		C_a-X	
	DFTB	DFT	DFTB	DFT	DFTB	DFT	DFTB	DFT	DFTB	DFT	DFTB	DFT	DFTB	DFT	DFTB	DFT	DFTB	DFT
3	2.25	2.27	1.41	1.41	1.51	1.52	2.21	2.20	1.41	1.40	1.45	1.45	2.20	2.16	1.41	1.40	1.45	1.41
4	2.22	2.21	1.42	1.41	1.50	1.50	2.19	2.14	1.41	1.41	1.44	1.44	2.17	2.11	1.41	1.40	1.44	1.40
5	2.21	2.19	1.42	1.41	1.49	1.49	2.18	2.13	1.41	1.41	1.44	1.43	2.16	2.10	1.41	1.40	1.44	1.39
6	2.20	2.17	1.42	1.42	1.49	1.49	2.18	2.12	1.41	1.41	1.44	1.43	2.16	2.09	1.41	1.40	1.43	1.39

[a] The atomic labels are shown in the inset drawing.

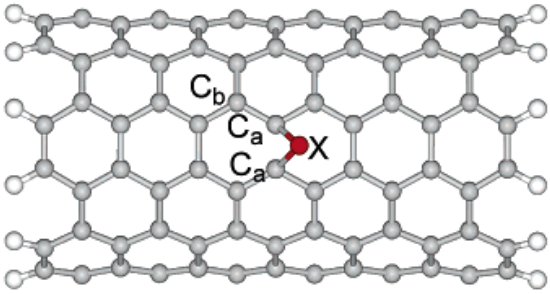

Table 6.2: Optimized C_a-C_a, C_a-Cb, and C_a-X bond distances (Å) for exo(l)- and exo(s)- addition products of (triplet) CH_2, (triplet) NH, and O(^{3}P) to 15 Å long (n,n) SWNTs for $n = 4-13$ at the DFTB level.

	X = CH_2						X = NH						X = O					
	C_a–C_a (Å)		C_a–C_b (Å)		C_a–X (Å)		C_a–C_a (Å)		C_a–C_b (Å)		C–X (Å)		C_a–C_a (Å)		C_a–C_b (Å)		C–X (Å)	
n	exo(l)	exo(s)	exo(l)	exo(s)	exo(l)	exo(s)	exo(l)	exo(s)	exo(l)	exo(s)	exo(l)	exo(s)	exo(l)	exo(s)	exo(l)	exo(s)	exo(l)	exo(s)
4	2.22		1.42		1.50		2.19		1.41		1.44		2.17		1.41		1.44	
5	2.21		1.42		1.49		2.18		1.41		1.44		2.16		1.41		1.44	
6	2.20		1.42		1.49		2.18		1.41		1.44		2.16	1.66	1.41	1.45	1.43	1.45
7	2.20		1.42		1.49		2.17		1.41		1.43		2.15	1.63	1.41	1.45	1.43	1.46
8	2.19	1.68	1.42	1.46	1.49	1.49	2.17		1.41		1.43		2.15	1.62	1.41	1.46	1.43	1.46
9	2.19	1.65	1.42	1.46	1.49	1.50	2.17		1.41		1.43		2.15	1.60	1.41	1.46	1.43	1.47
10	2.18	1.64	1.42	1.46	1.49	1.50	2.17	1.68	1.41	1.45	1.43	1.45	2.14	1.59	1.41	1.46	1.43	1.47
11	2.18	1.63	1.42	1.46	1.48	1.50	2.16	1.66	1.41	1.46	1.43	1.45	2.14	1.57	1.41	1.46	1.43	1.47
12	2.18	1.62	1.42	1.46	1.48	1.50	2.16	1.65	1.41	1.46	1.43	1.45	2.14	1.57	1.41	1.46	1.43	1.48
13	2.18	1.62	1.42	1.47	1.48	1.50	2.16	1.64	1.41	1.46	1.43	1.45	2.14	1.56	1.41	1.46	1.43	1.48

Table 6.3: Linear regression values for $\Delta E$for exo(l), exo(s) and endohedral addition products of (triplet) CH_2, (triplet) NH and O(^{3}P) to 15 Å long (n,n) SWNTs for $n = 4-13$ at the DFTB level[a].

		X = CH_2			X = NH			X = O		
		endo	exo(s)	exo(l)	endo	exo(s)	exo(l)	endo	exo(s)	exo(l)
	ΔE_0	−52.8	−52.1	−52.8	−26.3	−28.5	−32.9	−42.2	−44.4	−41.0
ΔE	C	160.7	−216.0	−349.0	117.6	−224.8	−328.0	69.6	−201.3	−317.0
	R^2	0.996	1.000	1.000	0.998	1.000	1.000	0.989	0.999	1.000
graphite		−53.6		−48.4	−29.5		−29.8	−46.0		−37.9

[a] $\Delta E$for PBC calculation of graphite is also shown. The case for graphite ($n = \infty$) is represented by an infinite graphite sheet in PBC calculations. The energy unit in kcal/mol and the unit for the slopes (C) is cal·Å/mol. See text for explanation of the symbols.

Table 6.4: The $1/d$ value (in Å^{-1}, with positive and negative values for exo and endohedral interactions) and the reaction energy ΔE and their EDA components (in kcal/mol, see text for individual terms) at HF/STO-3G level for the reaction of CH_2 on (n, n) armchair SWNT.

	Endo n=4	5	6	7	8	9	10	11	12	13	Exo(*s*) n=13	12	11	10	9	8
1/*d*	-0.1796	-0.1446	-0.1210	-0.1039	-0.0911	-0.0810	-0.0730	-0.0664	-0.0609	-0.0562	0.0562	0.0609	0.0664	0.0730	0.0810	0.0911
DEF(SWCNT)	62.0	53.5	41.9	45.6	43.4	43.5	41.1	40.3	40.7	40.1	42.3	42.6	42.6	42.8	45.0	45.2
DEF(CH_2)	47.3	46.6	47.2	46.1	46.1	46.0	46.0	45.9	45.9	46.0	47.2	47.3	47.4	47.5	47.7	48.0
INT	-142.0	-150.7	-153.5	-155.8	-157.9	-159.6	-161.3	-162.9	-164.3	-165.7	-199.8	-201.4	-203.2	-205.6	-206.3	-215.0
ES	-117.5	-114.4	-114.0	-114.7	-115.0	-115.6	-116.3	-116.9	-117.5	-118.1	-140.1	-141.4	-142.7	-144.3	-147.3	-151.4
EX	308.6	296.3	294.4	294.4	293.9	294.2	294.5	294.7	295.0	295.2	318.3	319.7	321.1	322.9	326.3	331.2
ORB	-333.0	-332.6	-333.8	-335.5	-336.8	-338.1	-339.5	-340.7	-341.8	-342.9	-377.9	-379.8	-381.7	-384.1	-388.5	-394.8

Table 6.5: Relevant Fock and overlap matrix elements and diagonalized eigenvalues in the fragment MO basis set for a_1 SWCNT$\rightarrow CH_2$ donation and b_1 CH_2*to*SWCNT backdonation processes in case of 5 Å/, 2-layer model compounds at the RHF/STO-3G level of theory for endo CH_2-(4,4) SWNT and exo(s) CH_2-(8,8) SWNT. Energy units are [ha].

endo CH2-(4,4) SWCNT

Fock matrix			Overlap matrix			eigenvalues
			b1 backdonation			
CH2 HOMO	CNT π*		CH2 HOMO	CNT π*		
-0.223546			1.000000			-0.248653
0.130813	0.183801		-0.107026	1.000000		0.236773
			a1 donation			
CH2 LUMO	CNT π	CNT π	CH2 LUMO	CNT π	CNT π	
-0.497616			1.000000			-0.567078
-0.251960	-0.280359		-0.220492	1.000000		-0.130320
-0.108687	-0.017053	-0.275073	-0.095369	0.000000	1.000000	-0.264093

exo (CH2)-(8,8) SWCNT

Fock matrix			Overlap matrix			eigenvalues
			b1 backdonation			
CH2 HOMO	CNT π*		CH2 HOMO	CNT π*		
-0.265653			1.000000			-0.350291
0.272295	0.064229		-0.242620	1.000000		0.276661
			a1 donation			
CH2 LUMO	CNT π	CNT π	CH2 LUMO	CNT π	CNT π	
-0.552495			1.000000			-0.583182
-0.179086	-0.287318		-0.159841	1.000000		-0.211427
-0.082506	-0.020946	-0.228496	-0.074528	0.000000	1.000000	-0.229057

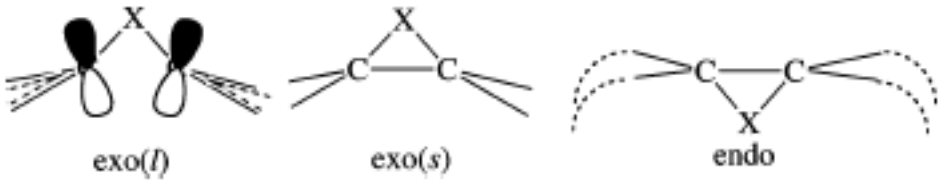

Figure 6.1: Schematic depiction of the different bonding types in exohedrally and endohedrally functionalized SWNTs.

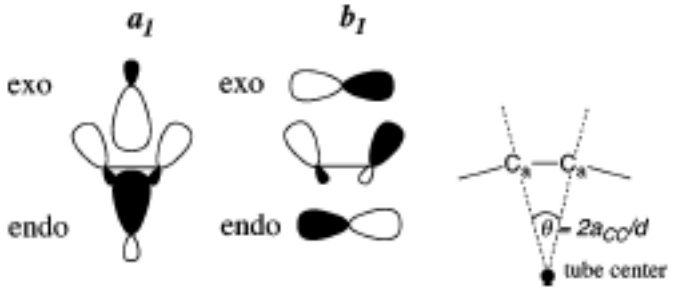

Figure 6.2: Schematic depiction of major $SWNTCH_2$ donative (a_1) and CH_2CNT back-donative (b_1) interactions for exohedral and endohedral reactions of SWNTs. The scheme on the right explains the relationship between the angle of C_a p-orbital deviation from a perpendicular direction to the SWNT surface and $1/d$.

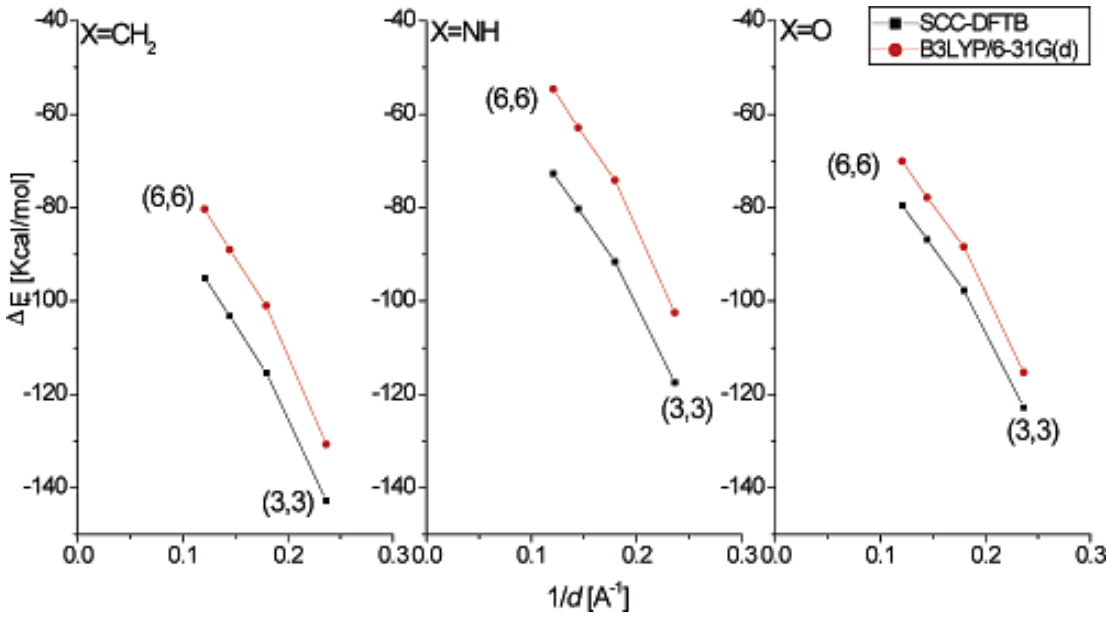

Figure 6.3: The diameter dependence of $\Delta E$for exohedral addition products (exo(l)) of X=CH_2, NH and O (^{3}P) to 15 Å (n, n) SWNTs at the B3LYP/6-31G(d) and DFTB levels of theory.

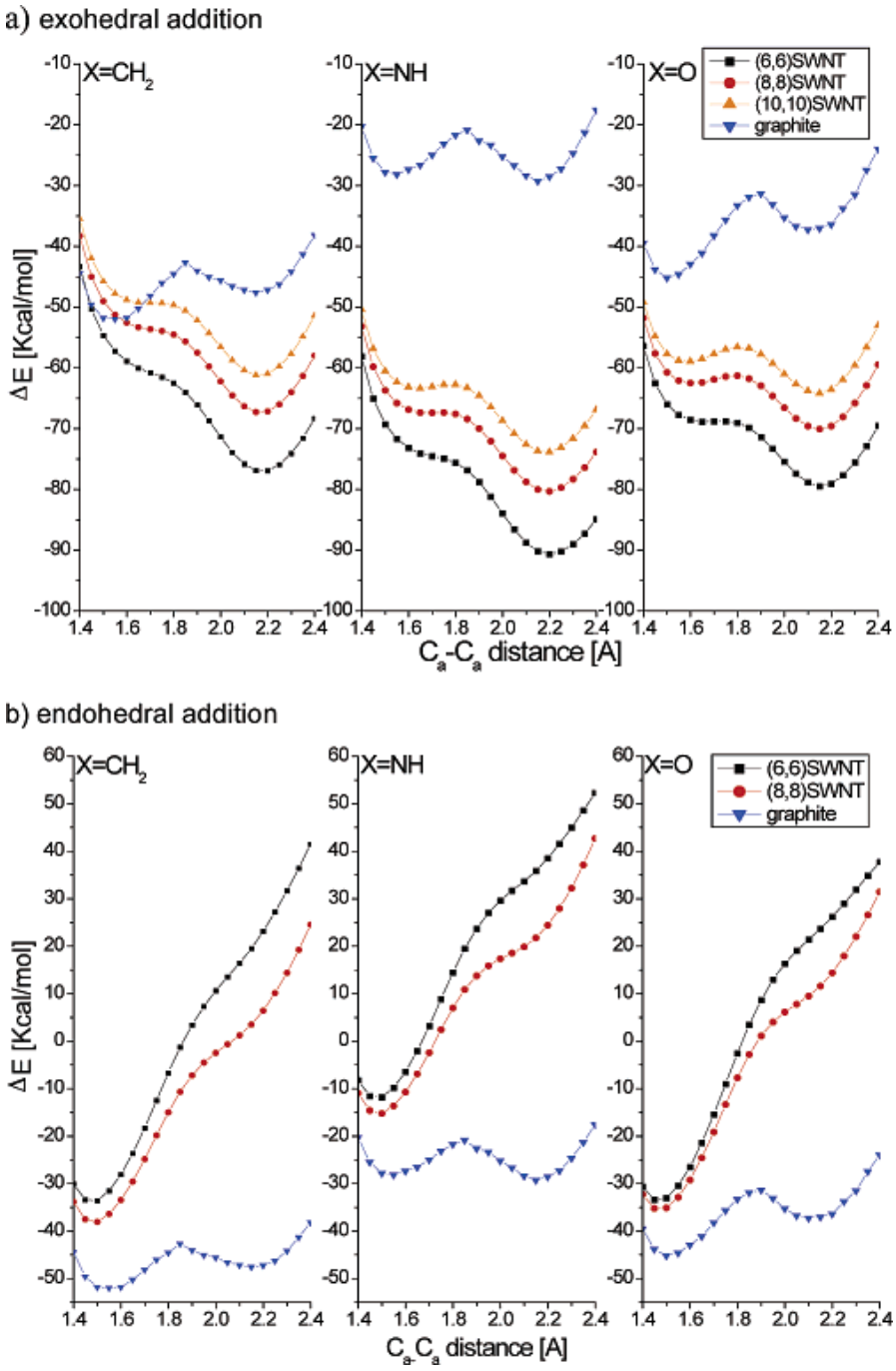

Figure 6.4: Relaxed PES scan as functions of the C_a-C_a distance that forms the C_aXC_a triangle with the addition of X = CH_2, NH and O on the convex (exohedral) and concave (endohedral) surface at the center of the 15 Å (n, n) SWNT as well as at the center of a periodic graphite model surface using the DFTB method.

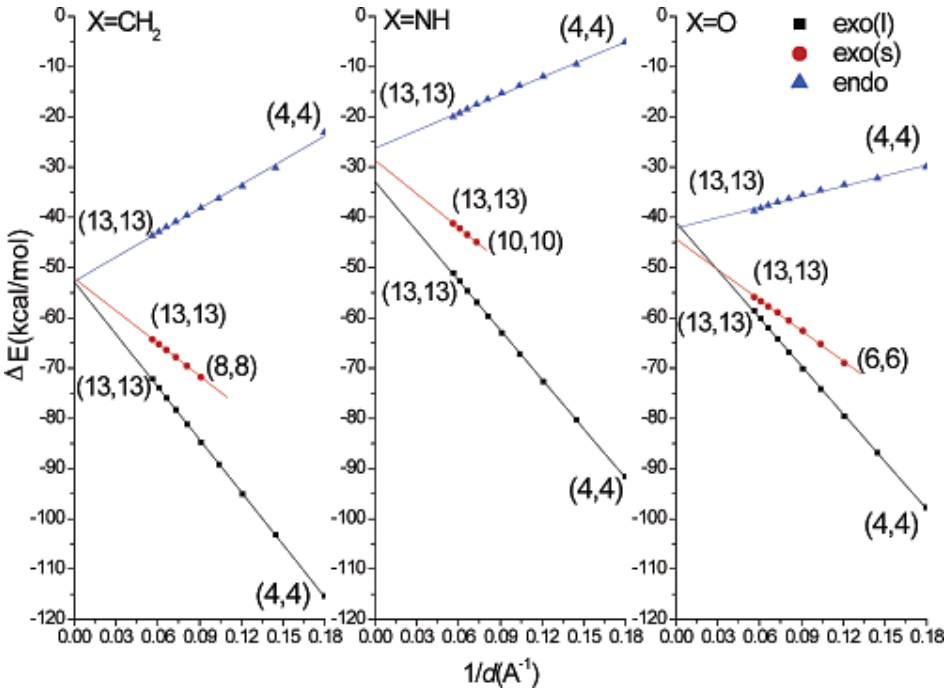

Figure 6.5: Linear regression plots for ΔEas a function of $1/d$ of exo- and endohedral addition products of X=CH_2, NH and O (^{3}P) with 15 Å (n, n) SWNTs at the DFTB level of theory. exo(l) and exo(s) denote opened and 3MR addition product isomers, respectively.

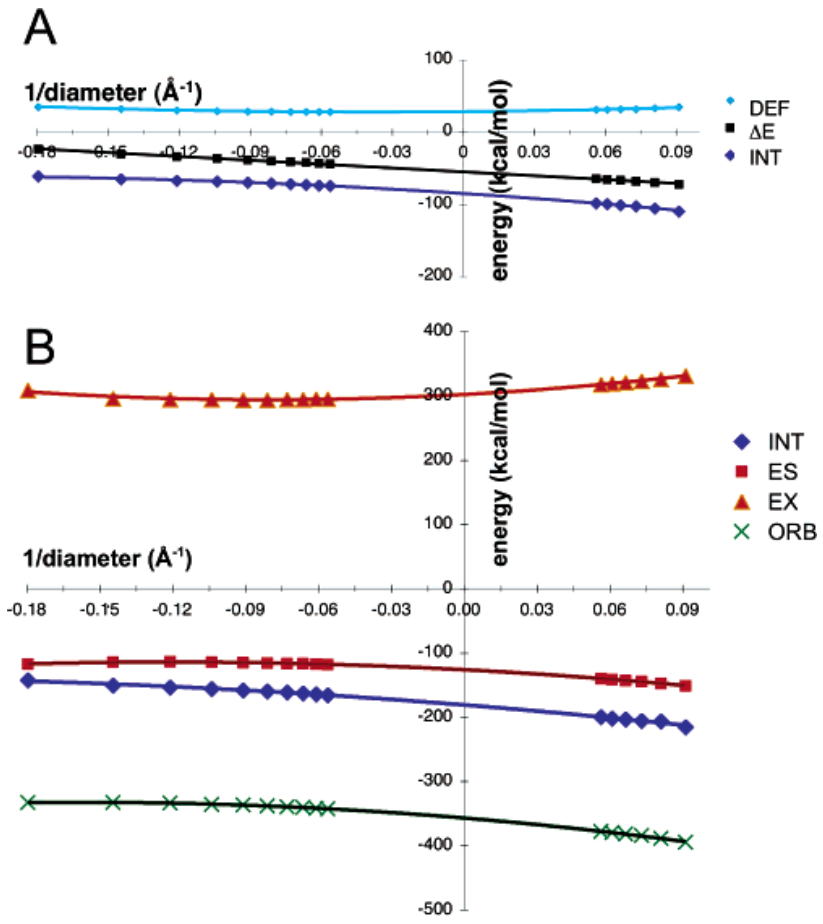

Figure 6.6: (A) The quadratic relationship between the stabilization energy ΔE, DEF(SWNT) and INT against $1/d$ for endo and exo(s) CH_2 adducts on the 15 Å SWNT at the DFTB level. (B) The quadratic relationship between INT and its EDA components ES, EX and ORB against $1/d$ for endo and exo(s) CH_2 adducts on the 5 Å SWNT at HF/STO-3G level.

Chapter 7. Analysis of the Relationship between Reaction Energies of Electrophilic SWNT Additions and Sidewall Curvature: Chiral Nanotubes

7.1 Introduction

Pristine single-walled carbon nanotubes (SWNTs) typically form bundles[1] and are difficult to manipulate and process due to their poor solubility and dispersion,[2] seriously limiting their practical application. Both covalent[2,3,4,5,6,7] and π-stacking[8,9] SWNT functionalizations have been employed to improve SWNT solubility and hence tube processability. Moreover, metallic and semiconducting SWNTs give rise to different thermodynamic reactivity towards chemical addition reactions,[10] which allows to separate[6,11,12,13] the different fractions. In this context, divalent addends such as CH_2, NH, and O do not significantly alter the tube band gap in low concentration,[14,15] and are therefore preferable for the separation process over monovalent addends such as F, H, OH, NH_2, which cause a localized impurity state close to the Fermi energy in the case of infinite tubes.[16] Knowledge about the factors governing reactivity of different bond types in SWNTs with divalent addends in dependence of the tube's main parameters, i) diameter d and ii) chirality (n,m), is therefore very valuable. We have previously investigated and analyzed the origin of the linear relationship between the total reaction energy ΔE (equivalent to the negative binding energy of the reactants):

$$\Delta E(\text{X-SWNT}) = E(\text{X-SWNT}) - E(\text{X}) - E(\text{SWNT}) \tag{7.1}$$

and the reciprocal SWNT diameter d for endo- and exohedral X=CH_2/NH/O [2+1] addition products with C-C bonds perpendicular to the tube axis on achiral armchair

(n,n) SWNTs.[17] Consistent with the calculations of other groups,[18,19,20] we found that ΔE can in this case be conveniently expressed as:

$$\Delta E = \Delta E_0 + C/d \tag{7.2}$$

In these density functional theory (DFT) and density functional tight binding (DFTB) based studies, we used finite-size, 15 Å long hydrogen- terminated (n,n) SWNT models with varying diameters $d = 3na_{C-C}/\pi$ and n ranging from n=3 to n=13, where a_{C-C} is the average of the nearest-neighbor C-C distance in the nanotube (expt: 1.421 Å in graphite; in our case, a changes slightly with the distance to the tube ends and due to slightly different bond length predictions at different levels of theory). Only a bond perpendicular to the tube axis at the tube center was used. In case of exohedral ("outside") additions, two isomers can exist depending on the tube diameter, which we denoted exo(s) (s for the "short" C-C bridgehead bond in a 3-membered ring (3MR) isomer) and exo(l) (l for "long" C-C bond $>$ 2 Å, essentially a broken C-C bond). Linear dependence of ΔE on $1/d$ was found for exo(s)- and endo-series, and separately with different values of ΔE_0 and C for the exo(l) series. In our analysis of the 3MR isomer exo(s)- and endo-series we made use of the fact that tube curvature $1/d$ can assume positive (convex curvature, exohedral addition) or negative (concave curvature, endohedral addition) values, and connected both branches in a linear fit. Straightforward frontier orbital and Kitaura-Morokuma energy decomposition analysis (EDA)[21] can be used to explain the origin of the linear relationship between ΔE and $1/d$ in the case of the 3MR isomers: It is a consequence of the curvature-dependent change in the SWNT C=C π^* "LUMO" back-donative interaction with the occupied (after promotion) CH_2/NH/O p_π MO; the angle between the atomic p_π orbitals in the antibonding π^* "LUMO" changes with $2a_{C-C}/d$ and the overlap of the π^* "LUMO" with the CH_2/NH/O pπ MO changes with it.[17]

Armchiral tubes have only two unique C-C bonds, and in the study mentioned

above we had chosen only the one exactly perpendicular to the tube direction (***p*** bond), for which the sidewall curvature effect is maximal. In the case of general chiral tubes, three non-equivalent C-C bond types ***t*** (bond most parallel to tube axis), ***d*** ("diagonal" bond, slightly skewed), and ***p*** (bond most perpendicular to tube axis) can be distinguished (see Figure 7.1). The three bonds form angles with the tube axis θ_x (x=***t,d,p***); the smallest such angle θ_t is identical with the chiral angle χ of the tube:

$$\theta_t = \chi = \arctan \sqrt{3m/(2n+m)} \tag{7.3}$$

and the two other angles are related to this angle by $\theta_x \pm 60°$. Interestingly, Gülseren *et al.* had deduced relationship (2) from the study of a series of (achiral) zigzag (n,0) SWNTs where $\chi = 0$, for both t and d types of bonds.[22] Recently, Li *et al.* have analyzed the energetics of [2+1] X-SWNT sidewall cycloaddition reactions with X=O at the B3LYP/6-31G(d) level of theory for several tubes of different diameters and chiralities and ***t/d/p*** bond types. They proposed a generalization of Equation 7.2:

$$\Delta E = \Delta E_0 + A \cdot K \tag{7.4}$$

where $K = 2\sin^2\theta/d$ is the average curvature of the corresponding arc of a C-C bond in the SWNT.[20] This "bond curvature" K is designed to account for sidewall curvature $1/d$, the bond orientation component relative to tube direction $\sin^2\theta$ and π-orbital misalignment effects,[23,24] all in one relationship. According to Equation 7.2 and Equation 7.4, $C = 2A\sin^2\theta$ which reduces to $C = 2A$ for bonds with $\theta = 90°$ for the ***p***-type C-C bonds in armchair tubes. Li *et al.* tested Equation 7.4 on a number of X=CH_2, NH, SiH_2, and CCl_2 compounds and found this linear relationship confirmed, using sometimes however only three different points. Nevertheless, they concluded that Equation 7.4 only holds for additions leading to exo(l) compounds, and that no simple linear relationship between ΔE and K exists for exo(s) type series. This

somewhat surprising result has to be viewed in the light that previously we did find a clear linear relationship for endo and exo(s) series of the ***p***-type bond in the case of the armchair tube. Therefore, the statement by Li *et al.* deserves clarification and we address this issue in the present work.

Here, we continue our systematic studies of the dependence of ΔE on $1/d$ for the three different bond types ***t/d/p*** in chiral (2n,n) SWNTs with constant chiral angle $\chi = \theta_t = 19.1°$, different from metallic armchair (n, n) where $\chi = 30°$. The relationship between ΔE and $1/d$ is investigated separately for each bond type ***t*** ($\theta_t = 19.1°$), ***d*** ($\theta_d = 40.9°$), and ***p*** ($\theta_p = 79.1°$), which have a constant bond orientation component $\sin^2\theta_x$ relative to the tube axis, and constant orbital misalignment (minimum for ***p***-type bonds, maximum for ***d***-type bonds). We show that, by separating bond orientation $\sin^2\theta_x$ and sidewall curvature $1/d$, a near-linear relationship between ΔE and $1/d$ can be recovered for 3MR series as well. As in our previous study, we will use X=CH_2, NH, O additions to finite-size, hydrogen-terminated, approximately 15 Å long SWNT model systems, this time for chiral $(2n, n)$ tubes with n ranging from 2 ((4,2)-chirality) to 8 ((16,8)-chirality), including all intermediate points of n in the investigation. In each case we investigate the reaction with the three different ***t/d/p*** C-C bond types of the chiral tubes, selecting a central carbon atom C_a in the center of the tube fragment. The tubes we investigated belong to the semi-conducting class of SWNTs with the exception of the (6,3) and (12,6) cases, which correspond formally to metallic SWNTs; however, a finite band gap remains also in these cases due to the finite SWNT length. As in our previous study, we first compare DFT energetics at the B3LYP/6-31G(d) level with DFTB results for exo-adducts of X=CH_2/NH/O to n=2-5 tubes to confirm that DFTB is capable of reproducing reliable energetics for the chiral $(2n, n)$ SWNT case as well. Using only DFTB, we then discuss the relationship between the two exohedral addition isomers (open exo(l) and 3MR exo(s)) for each ***t/d/p*** bond type in the case of X=O addition by investigating the behavior

of the associated minima on the C-C potential energy surfaces (PESs) with changing d. We will then present reaction energies for X=CH_2/NH/O for both series of exo- as well as endo-adducts, again separated for the three different ***t/d/p*** bond types, and analyze ΔE of 3MR series by means of simplified EDA as a composition of deformation energy (DEF) and interaction energy (INT) terms using quadratic fits to $1/d$. Finally, we briefly discuss the ΔE dependence of exo(l) adducts on $1/d$ in terms of the "bond curvature" quantity K of Li *et al.*[20]

7.2 Computational details

The DFTB[25,26,27,28,29] method is the central method employed in these studies. It is an approximate density functional theory based on the tight binding approach, utilizing an optimized minimal LCAO Slater-type all-valence basis set in combination with a two-center approximation for Hamiltonian and overlap matrix elements. We note that NDDO (neglect of differential diatomic overlap)-type methods such as AM1[30] or PM3[31] are inherently incapable reproducing the presented results, since the $1/d$ dependence of ΔE stems mainly from different orbital overlap for electron donation and back-donation, which is absent from NDDO by definition. Since our system includes functional groups with different electronegativities, we selected the self-consistent charge (SCC) formalism of DFTB. The energy threshold for SCC-SCF in DFTB was chosen to be 10^{-9} hartree. DFTB geometry optimizations were carried out using the GAUSSIAN 03 program[32] by means of the "external" keyword, which connects the Gaussian geometry optimizer to a standalone DFTB program. For benchmark DFT calculations, we chose the same hybrid functional B3LYP with the polarized 6-31G(d) basis set as in our previous armchair tube investigation, using its implementation in NWChem 4.6. Because of the generally excellent geometry agreement between B3LYP/6-31G(d) and DFTB,[17,33,34] in this paper, we did not perform B3LYP geometry optimizations for the present benchmark. Instead, in order

to check the validity of the DFTB method for the study of addition reactions on chiral SWNTs, single point energy calculations were carried out at the B3LYP/6-31G(d)//DFTB and DFTB levels of theory for the exo(l) CH_2, NH, and O addition products to the $(2n, n)$ SWNT with n ranging from 2 to 5.

7.3 Results and Discussion

7.3.1 Comparison between B3LYP/6-31G(d) and DFTB energetics of exo(l) X=CH_2/NH/O adducts to $(2n, n)$ SWNTs with n=2-5

We have employed closed shell singlet B3LYP and DFTB wavefunctions for the pristine SWNTs, and open shell triplet UB3LYP and spin-polarized DFTB wavefunctions for the CH_2/NH/O reactants. The respective B3LYP/6-31G(d)//DFTB and DFTB ΔE values for X=CH_2/NH/O adducts on the ***t/d/p*** bonds are plotted in Figure 7.2. The average ΔE differences between B3LYP/6-31G(d)//DFTB and DFTB for the ***t/d/p*** bonds are found to be 10.8, 8.0 and 7.4 kcal/mol (X=CH_2), 18.1, 16.3 and 15.1 kcal/mol (X=NH), and 10.7, 10.9 and 8.9 kcal/mol (X=O), respectively. As expected, DFTB exhibits the usual systematic overbinding tendency by nearly a constant amount for each X addend from the small-diameter (4,2) to the large-diameter (10,5) SWNT. This means that also in the case of $(2n, n)$ SWNTs, the PES derived from DFTB for the X-SWNT adducts is merely shifted by a near-constant amount, with NH showing the largest discrepancy as in our study of armchair tubes, and comparable to the PES obtained at the computationally much more expensive B3LYP/6-31G(d) level of theory.

7.3.2 Two local minima can exist on the C_a-C_x PESs of exo-addition products for X=O for the three *t/d/p* bond types

As pointed out before by others and us, there can exist two local minima termed exo(s) (3MR isomer) and exo(l) (opened isomer) on the C_a-$C_{a'}$ potential energy surface of the exo-addition products to armchair and chiral nanotubes. If it exists, the exo(s) isomer is energetically always less favorable than the exo(l) isomer, and its associated minimum does only exist for large tube diameters (see References[17] and[20] for details). A systematic variation of the relative exo(l) and exo(s) minima energies with tube diameter was found: both opened and 3MR minima are separated by a barrier that can be interpreted as avoided conical intersection between two electronic states arising from two possible connectivity modes of the C-X-C moiety with the CNT. In one configuration, the bridgehead carbon atoms are still sp^2-hybridized, forming a σ-bond with X (exo(l)), while in the other the bridgehead carbon atoms are almost completely sp^3- hybridized (the 3MR series endo and exo(s)). When d becomes smaller, the exo(s) minimum becomes gradually shallower and finally disappears, being reduced to a shoulder at small C_a-$C_{a'}$ distances.

In the case of chiral tubes, a similar behavior of the C_a-C_x PES for x=***t,d,p*** type bonds can be expected, and we present here a case study for X=O for endo- and exo-additions on (8,4) as well as for the exo- addition on (16,8), shown in Figure 7.3. Sidewall curvatures for these systems are -0.0595 $Å^{-1}$ for endo (8,4), 0.0350 $Å^{-1}$ for exo (16,8) and 0.0595 $Å^{-1}$ for exo (8,4). In case of the exothermic exo-additions, the exo(l) minima appear in the large C_a-C_x region around 2.2 Å in the case of all three ***t/d/p*** bond types, and the corresponding PESs for all three of them shift down in ΔE with increasing positive sidewall curvature. By inspection of Figure 7.3 one can see that reaction energies ΔE are more negative in the order ***p***<***d***<***t***

where absolute bond angles $|\theta|$ and bond-tube axis orientation component $\sin^2\theta$ of K follow the order $\boldsymbol{p}$>$\boldsymbol{d}$>$\boldsymbol{t}$. Clearly, the dependence of ΔE on $1/d$ for individual $\boldsymbol{t/d/p}$ bond type series is therefore in agreement with our previous observation that the exo-addition reaction to a particular bond type becomes more exothermic when the sidewall curvature $1/d$ becomes larger, even in case of the exo(s) systems where Li *et al.* did not observe linear dependence when the three bond type series are evaluated together in terms of bond curvature K.[20] We note that the $\boldsymbol{p}$-type bond tends to exhibit an exo(l) minimum with lower energy than the exo(s) minimum. On the contrary, the $\boldsymbol{t}$-type bond tends to exhibit an exo(s) minimum with lower energy than the exo(l) minimum. Obviously, the exo(l) minimum prefers a maximum overall bond curvature $K = 2sin^2\theta/d$, which is consistent with the findings by Li *et al.*[20]

In the case of negative curvature (endo addition), the addition reaction is endothermic. Here, the closed 3MR minimum is the only existing metastable minimum, with the exception of the endo- (8,4) SWNT adduct on the $\boldsymbol{t}$-type bond, which will be discussed later. The $\boldsymbol{p}$ bond addition is least endothermic. Since ΔE for endo-addition reactions becomes more endothermic with increasing concave curvature, ΔE PESs are energetically ordered following $\boldsymbol{t}$<$\boldsymbol{d}$<$\boldsymbol{p}$ in the case of endo-(8,4) SWNT adducts for R(C_a-C_x)¿1.8 Å. We even found a shallow endo(l) minimum for endo-(8,4) addition in t-position. However, a cross-over point exists when going to smaller R(C_a-C_x) distances < 1.7 Å, where the energy for the $\boldsymbol{p}$ endo(s) adduct becomes lower than that of $\boldsymbol{t}$ and $\boldsymbol{d}$, which are nearly isoenergetic in this region.

EDA has shown that the $1/d$ dependence of ΔE is determined mainly by DEF, and that INT is dominated by orbital interactions attributable to the leading back-donating interaction from the b_1 X pπ MO to the C=C π^*LUMO of SWNT, and that the donating interaction from the C=C π HOMO to the empty X σ acceptor MO of a_1 symmetry is not very important. It appears therefore that the angle of the b_1 X pπ MO (parallel or perpendicular to the direction of the sidewall curvature) is the most

important quantity, as is clearly visible in the results presented here, because this angle coincides with the ***t/d/p*** bond orientation angles towards tube axis, and the corresponding local bond curvatures $\sin^2\theta/d$. The endo(s) stability reversal in case of large C_a-C_x distances $>$ 1.8 Å to ***t***$<$***d***$<$***p*** order is consistent with the reduction of negative sidewall curvature by the local bond curvatures $\sin^2\theta/d$.

7.3.3 Linear relationship between the stabilization energy ΔE and the inverse radius $1/d$ of exo- and endohedral addition products of CH_2/NH/O to $(2n, n)$ SWNTs with n=3-8 and n=∞

In Figure 7.4, we plot ΔE obtained at the DFTB level for exo(s)-, exo(l)-, and endohedral CH_2/NH/O addition products to the three different ***t/d/p*** bonds of $(2n, n)$ SWNTs as a function of $1/d$ for n=3 to 8. We are starting the series from n equal 3 because tubes with n smaller than 3 do not allow the formation of endohedral addition products for steric reasons (lack of space, especially for the CH_2 addend). Moreover, (3,3) is probably the smallest SWNT that can by synthesized. To make discussions simpler, we introduce a new notation such as a exo(s)-p, combining type of addition product (here the 3MR exo-adduct) and the ***t/d/p*** type of bond (here ***p***-type) in one label.

Although the electronic properties, such as electrical conductivity and HOMO-LUMO gap, of the SWNTs in this series vary with the increasing diameter, we clearly observe for individual series of ***t/d/p*** bond types the linear relationship between ΔE and the inverse diameter that we had already reported in our study of the ***p***-type bond in armchair tubes. Table 7.1 lists our values for ΔE_0 and C parameters from Equation 7.1 as well as linear regression R^2 values, which are very close to 1.0 for both endohedral and exohedral addition products and all three ***t/d/p*** positions. The largest deviation from 1.0 is found for X=O, endo-***p*** with 0.977, followed by X=O,

exo(s)-***d*** with 0.978. All other regression coefficients are larger than 0.980.

Independent from the type of bond, the slope parameter C is always negative for both exo(s) and exo(l) additions. At first we discuss X=CH_2/NH/O adducts at the same time. The C values for the ***p***-type have very large absolute values for exohedral additions, which means that the change of ΔE with $1/d$ is very large. They range from -695 kcal·Å/mol to -474 kcal·Å/mol for exo(s)-***p*** and -746 kcal·Å/mol to -676 kcal·Å/mol for exo(l)-***p*** additions, depending on the addend. For ***d***-type bonds, the values are smaller in absolute magnitude, and range from -234 kcal·Å/mol to -186 kcal·Å/mol for exo(s)-***d*** and -381 kcal·Å/mol to -354 kcal·Å/mol for exo(l)-d. The C value is smallest in case of the ***t***-type bond, which ranges from -249 kcal·Å/mol to -199 kcal·Å/mol for exo(s)-***t*** and -210 kcal·Å/mol to -180 kcal·Å/mol for exo(l)-***t***, and we note that the exo(l)-***t*** minimum does not exist for O addition to the SWNTs in our series with n from 3 to 8. As for the different addends, the CH_2 group tends to have the largest absolute C values and O tends to have the smallest ones, with NH in between. In our previous study of ***p***-type bond additions to armchair tubes, we found a similar behavior of $|C|$, namely CH_2 >NH∼O. In terms of reaction energies ΔE, we find an order CH_2 <O<NH consistent with our previous armchair X-SWNT investigation.

Regarding endo additions, where the absolute value of negative curvature is taken into account, the slope parameter C is always positive. Here, the ***p***-type bond has the smallest C values and they increase via ***d***-type to the ***t***-type bond, but clearly the step between ***p*** and ***d*** is largest. It ranges from 191 kcal·Å/mol to 383 kcal·Å/mol for endo-***p***, while values for endo-***d*** range from 365 kcal·Å/mol to 603 kcal·Å/mol, and from 387 kcal ·Å/mol to 713 kcal·Å/mol for endo-***t***. We obviously have here a reversal of the order of absolute magnitude $|C|$ with respect to the ***t/d/p*** bond types, which is consistent with the fact that the ***t***-adducts in the case of endo- additions are the least endothermic products for a wide range of R(C_a-C_x). As for the different

addends, the CH_2 group tends again to have the largest absolute C values and O tends to have the smallest ones, with NH in between, which is the same behavior we observed for exo additions. This behavior seems to indicate that the X=CH_2 bond formation with the SWNT is most strongly dependent on the sidewall curvature and therefore direction of the resulting covalent bond, while the X=O bond formation has more polar character and is less dependent on the sidewall curvature.

As n increases, d approaches infinity, corresponding to a planar graphene sheet where exo- and endohedral addition products can no longer be distinguished. According to Equation 7.2, in the $d \to \infty$ limit, ΔE becomes identical to ΔE_0. Therefore, we can extrapolate ΔE and get the expectation value of graphite addition for all series. These ΔE_0 values are also listed in Table 7.1. The values are not very consistent at all as they differ considerably from each other for different series of the same X addend, with the largest difference of 20 kcal/mol for CH_2 addition series, 16 kcal/mol for NH addition series, and 15 kcal/mol for the O addition series. We explain this difference with the fact that we are using finite length model tubes where different series may have different edge effects. We have computed ΔE for a planar graphene model C_{296} in periodic boundary condition (PBC) 29.6Å×25.7Å representing the n=∞ case for each reagent (denoted ΔE_∞), and we obtained values for ΔE_∞ of 45.3 kcal/mol for CH_2, 26.5 kcal/mol for NH and 42.6 kcal/mol for O. As we can see, although the extrapolation of ΔE for all the series does not yield the same ΔE_0 values, the expectation values cluster around our calculated ΔE_∞, thus indicating that the linear extrapolations are reasonable.

In summary, we find that the linear relationship between ΔE and $1/d$ holds for both exo- and endo-additions separately for all three different ***t/d/p***-type bond positions and all three addends X=CH_2/NH,O. This information by itself can be used to predict ΔE for general $(2n, n)$ SWNT addition reactions, provided ΔE_0 and the slope parameters C are known for the respective combination of addend/tube type/bond

type parameters.

7.3.4 Energy decomposition analysis of ΔE

To investigate the origin of the linear relationships in detail, we performed a simplified version of the original energy decomposition analysis (EDA) of ΔE by Kitaura and Morokuma,[21] and studied the relationship between the energy decomposition terms and the inverse of the nanotube diameter.

In the simplified EDA, the total stabilization energy ΔE is decomposed as:

$$\Delta E = \mathrm{PROM(X)} + \mathrm{DEF(SWNT)} + \mathrm{DEF(X)} + \mathrm{INT} \tag{7.5}$$

which is only the first step in the original scheme. Here, PROM(X) is the energy required to promote the species X=CH_2/NH/O from its ground state (in the present case from the triplet ground state in the $(a_1)^1(b_1)^1$ active orbital occupancy in C_2v symmetry) to the valence state (here the $(b_1)^2$ singlet state), which correlates symmetrically to the ground-state singlet adduct. DEF are the energies required to deform their respective equilibrium structures to the structure in the addition complex, and INT is the interaction energy between deformed (or prepared) SWNT and X to form the adduct. PROM(X) and DEF(X) are nearly independent of $1/d$ and can be disregarded as factors determining the $1/d$ dependency.

Figure 7.5 depicts a plot of ΔE,DEF(SWNT) and INT with tube diameter d as abscissa separately for endo, exo(s) and exo(l) X=CH_2 additions to the SWNT ***d***-type bond. We include this direct comparison with the tube diameter in place of $1/d$ to emphasize more clearly the trend followed by ΔEas a function of d. For exo(s) and endo series, DEF(SWNT) seems little dependent on the tube diameter; its origin is the change of the C_a-C_d bond from π-conjugated in the pristine tube to single bond in the addend, associated with strain enforced on the remaining hexagon C-C framework. At the same time, INT for exo(s) and endo series originations from the formation of two

C-C bonds between the prepared SWNT and the X=CH_2 fragment. Qualitatively, by inspection of Figure 7.5 it becomes clear that ΔEfollows the same trend as INT as a function of d, since changes in INT are much larger than in DEF. Therefore, the curvature dependence of ΔE is actually dominated by the INT. The exo(l) series, on the other hand, displays strong dependence of DEF(SWNT) on d, much larger than in the case of endo and exo(s) series. In the exo(l) case, the bond strain imposed on the hexagon C-C framework while of the SWNT framework is more severe, as the gap created by the breaking of the C_a-C_x bond is much larger than in case of exo(s) or endo (about 0.5 Å). In addition, nearest neighbor carbon atoms to the bridgehead carbons are also strongly affected by the desire of bridgehead carbons to make up for the loss of C-C -bond by bonding more strongly to them, reflected in corresponding significant bond shortenings in this area that are not present in the exo(s) and endo species. On the other hand, local strain at the bridgehead carbon atoms is partially released due to the breaking of the C-C σ-bond. Altogether, DEF for exo(l) is nearly twice as large as in the case of the 3MR species. At the same time, INT for exo(l) originates from the formation of two C-X σ-bonds between SWNT and X and the hybridization of the bridgehead bonds has much larger sp^2 character than the clearly sp^3-hybridized defects in the 3MR exo(s) and endo compounds. As a consequence, INT for exo(l) is much more negative and less dependent on d. Therefore the INT for exo(l) series is again larger than endo and exo(s) series. As conclusion from this comparison we note that the d dependencies of INT and DEF for closed- and opened adduct isomers follow opposite trends: In case of 3MR isomers, d-dependence of DEF is small and INT is large, whereas in the case of exo(l) isomers, the d-dependence of DEF is large and INT is small. The origin of linear dependence of ΔE on $1/d$ therefore is different in the both cases.

Because of the intrinsic similarities of endo and exo(s) (both 3MR isomer) series, we analyze the curvature dependence of these two series together in the following

discussion. We had found earlier[17] that, if we consider a larger range of $1/d$, from -0.079 Å^{-1} corresponding to endo-(6,3) SWNT to +0.079 Å^{-1} corresponding to exo(s)-(6,3) X-SWNT, ΔE,DEF(SWNT) and INT can be expressed in quadratic forms of $1/d$:

$$\Delta E = E^{(0)} + E^{(1)} \cdot (1/d) + E^{(2)} \cdot (1/d^2) \quad (7.6)$$

$$\text{DEF} = D^{(0)} + D^{(1)} \cdot (1/d) + D^{(2)} \cdot (1/d^2) \quad (7.7)$$

$$\text{INT} = I^{(0)} + I^{(1)} \cdot (1/d) + I^{(2)} \cdot (1/d^2) \quad (7.8)$$

Therefore, in this study, we computed such quadratic fits for the CH_2, NH and O addends to different bond positions ***t/d/p*** and show them in Figure 7.6, while the fitted parameters E^i, D^i and I^i are listed in Table 7.2. The R^2 values in each case show that the quadratic dependence holds perfectly for all the separate cases in general. The quadratic relationship of DEF and $1/d$ originates from the fact that DEF, which is related to the mechanical properties of SWNTs, contains the change of local strain energy and the partial loss of π-conjugation, which is thought to have characteristic dependence on $1/d^2$.[35] INT is the energy gained by forming two C-X bonds between the prepared SWNT and X fragments, and can also be fitted more favorably as a function of $1/d^2$, as we have shown in our previous work.[17] In the case of armchair ***p***-type bond additions, we found near-perfect cancellation of the quadratic terms for DEF and INT that leave the linear term dominant and making ΔE appear linearly dependent on $1/d$ (that means, a linear fit gives nearly the same R^2 value as that of a quadratic fit). In the present case, we find that cancellation of the quadratic contributions from DEF and INT also occurs in case of chiral tubes for the three unique bond types, although with varying degrees between them dependent on the nature of the X addend, as will be explained in the next paragraph.

In the present study of chiral $(2n, n)$ SWNT electrophilic ***t/d/p***-type bond addi-

tions, we observe that for the X=NH additions, the ratio of the quadratic over the linear coefficient for the ΔE fit $E^{(2)}/E^{(1)}$ ranges below 0.1 (see Table 7.2), which indicates that ΔEcan not only be expressed as a function of $1/d$ for individual series of endo- and exo(s)-additions, but also for the complete series of 3MR structures in the full range from negative to positive sidewall curvature $1/d$. This is true for all three different bond types. Similarly, for the X=CH_2 and O additions, the ratio of the quadratic over the linear coefficient for the ΔE fit $E^{(2)}/E^{(1)}$ ranges below 0.2, with X=CH_2 being intermediate between the X=NH and X=O cases with values for $E^{(2)}/E^{(1)}$ around 0.15. We surmise that in these cases, a linear fit of ΔE for the full range from negative to positive sidewall curvature $1/d$ is therefore justified, in the case of X=NH more so than in the case of X=CH_2/O.No significant difference between bond types are seen, perhaps with the only exception of the X=O ***p***-type addition with a 0.15 ratio, coming closer to X=CH_2 values compared to the t- and ***p***-type O-additions. But visual inspection of Figure 7.6 suggests that in fact only the quadratic ΔE fit for the case of the X=CH_2 ***p***-type addition has a true linear appearance, and that other systems exhibit behavior of ΔEthat can be more fittingly described as quadratically dependent on $1/d$. In general, we find no intrinsic reason that the clearly quadratic contributions of DEF $D^{(2)}$ and INT $I^{(2)}$ should necessarily cancel each other, making ΔElinear in appearance, as we had discussed for the arm-chair ***p***-type bond addition for X=CH_2. We therefore conclude that the cancellation of quadratic terms $D^{(2)}$ and $I^{(2)}$, and hence the linear dependence on $1/d$ of ΔEover the entire range of negative and positive curvature is largely a matter of coincidence. More strictly, $\Delta E$for 3MR series is best described as quadratically dependent on $1/d$ when considering both endo and exo(s)-additions, in all three cases of addends when the three different bond types are considered individually. It is not possible to extract a meaningful relationship between ΔE and $1/d$ for 3MR series when all three different ***t/d/p***-type bonds are considered simultaneously in the same fit, as Li *et*

al. reported, even when their modified bond curvature K index from Equation 7.4 is used.[20]

As already mentioned above, the overall ΔEdependence on sidewall curvature $1/d$ in case of the exo(l) series is largely dominated by the large contribution from DEF. In this case, DEF mainly contains the C-C σ-bond breaking and reorganization energy, as well as the release of local strain at the bridgehead carbon atoms. Since the energy of a C-C σ-bond is very similar for all three bond types of a SWNT and independent of the tube diameter, the release of the local bond strain energy due to the breaking of the bond determines the $1/d$ dependence of DEF, and thus of ΔE. For each of the three addends, we confirm the linear dependence of ΔE with respect to Li *et al.*'s bond curvature K index reported by these authors[20] as shown in Figure 7.7; here, the three series for ***t/d/p***-type bonds for the exo(l) series are considered simultaneously in the same fit. In order to be compatible with their study, we computed ΔE at both the DFTB and the B3LYP/6-31G(d)//DFTB (DFT single point energy at the DFTB geometry) levels of theory and found that the linear relationship holds perfectly between stabilization energy $\Delta E$and bond curvature K, with R^2 values (see Table 7.3) almost identical to 1 for all the CH_2, NH and O addition at the two levels of theory.

7.4 Summary

Following up on our previous work on *armchair* single-walled carbon nanotubes (SWNT),[17] we have performed systematic quantum chemical studies on the single-walled carbon nanotube (SWNT) sidewall curvature $1/d$ dependence of the reaction energy ΔE of electrophilic adducts X=CH_2/NH/O in addition products of *chiral* $(2n, n)$ SWNTs (fixed chiral angle $\chi = 19.1°$),with n ranging from 2 to 8 at three different ***t/d/p***-type bonds in Figure 7.1. The three addition bond type sites are always oriented with the same angles θ_x (x=***t,d,p***) to the tube axis and are grouped in different series, to separate sidewall curvature $1/d$ and $\sin^2\theta_x$ bond orientation contri-

butions, the latter containing pπ-orbital misalignment and orientation. In case of exohedral ("outside") additions, two isomers can exist depending on the tube diameter, which we denote exo(s) (s for the "short" C-C bridgehead bond in a 3-membered ring (3MR) isomer) and exo(l) (l for "long" C-C bond). In our analysis of the 3MR isomer exo(s)- and endo-series we have made use of the fact that tube curvature $1/d$ can assume positive (convex curvature, exohedral addition) or negative (concave curvature, endohedral addition) values, and connected both branches in quadratic fits. We have applied a simplified energy decomposition analysis and decomposed ΔE into a deformation DEF and interaction INT energy term. We used B3LYP/6-31G(d) energy benchmark calculations and the computationally inexpensive self-consistent charge DFTB method for most of the calculations. We confirmed again that DFTB can describe the addition reaction of chiral SWNTs and electrophilic [2+1] addends very well compared with the B3LYP/6-31G(d) benchmark energetics. Our main findings are as follows:

1. Small diameter tubes are more reactive than large diameter tubes, and exohedral addition is far more favorable than endohedral addition.

2. Two possible minima for exohedral adducts can exist corresponding to C-C opened exo(l) and 3MR exo(s) isomers with a barrier separating them also in case of chiral tubes, and it is determined that their relative energies depend strongly on the ***t/d/p***-type of bond, as well as on the sidewall curvature $1/d$.

3. In both endo- and exo-cases, addition at the bond most perpendicular to the tube axis (***p***-type bond) leads to the energetically most favorable product, and addition at the bond most parallel to the tube axis (***t***-type bond) is least energetically favorable.

4. A linear relationship between reaction energies ΔE and the reciprocal tube diameter $1/d$ is found to be a valid description when endo, exo(s) and exo(l)

series are considered individually for three different ***t/d/p***-type bond series, for either negative (endo-addition) or positive (exo-addition) branches of $1/d$ separately.

5. Remarkably, if endo and exo(s) series are considered together, and thereby a larger range of $1/d$ is studied, ΔE, as well as DEF and INT, are better described as a quadratic function of $1/d$. The linear relationship of ΔE on $1/d$ however is still a reasonable approximation due to fortuitous cancellation of large, opposite quadratic contributions from DEF and INT. ΔE for endo and exo(s) appears the more linear, the stronger the covalent character of the bond, and the larger the curvature of the ***t/d/p***-type bonds is. A combined "bond curvature" K as proposed by Li *et al.* mixes effects of orbital misalignment and sidewall curvature, thus neglects the "chemistry" of the three different, symmetry-unique bonds in chiral tubes, and cannot be expected to work unless nanotubes were composed of homogenous, continuous matter instead of discrete carbon atom hexagon frameworks.

6. In case of exo(l) opened adducts, we find linear dependence of ΔE on $1/d$, which is largely dominated by a DEF contribution showing linear dependence on $1/d$ itself. The origin of linear relationship between 3MR series and opened exo(l) series is therefore of different nature.

We have shown that ΔE is very much determined by the local environment of the addition site, and that individual orbital interactions are very important to understand the energetic differences between different adducts. Simplified EDA into deformation and interaction energy components is sufficient to explain the delicate balance of quadratic and linear dependencies on $1/d$ of individual energy contributions in SWNT 3MR addition products.

References

1. Szabados, A.; Biro, L.; Surjan, P. *PHYSICAL REVIEW B* **2006**, *73*, 195404.

2. Dyke, C.; Tour, J. *JOURNAL OF PHYSICAL CHEMISTRY A* **2004**, *108*, 11151–11159.

3. Mickelson, E.; Huffman, C.; Rinzler, A.; Smalley, R.; Hauge, R.; Margrave, J. *CHEMICAL PHYSICS LETTERS* **1998**, *296*, 188–194.

4. Banerjee, S.; Wong, S. *JOURNAL OF PHYSICAL CHEMISTRY B* **2002**, *106*, 12144–12151.

5. Kim, K.; Park, K.; Kim, H.; Bae, D.; Lim, S.; Lee, Y. *JOURNAL OF THE KOREAN PHYSICAL SOCIETY* **2003**, *42*, S137–S142.

6. Banerjee, S.; Hemraj-Benny, T.; Wong, S. *ADVANCED MATERIALS* **2005**, *17*, 17–29.

7. Nair, N.; Kim, W.-J.; Usrey, M. L.; Strano, M. S. *JOURNAL OF THE AMERICAN CHEMICAL SOCIETY* **2007**, *129*, 3946–3954.

8. Chen, R.; Zhang, Y.; Wang, D.; Dai, H. *JOURNAL OF THE AMERICAN CHEMICAL SOCIETY* **2001**, *123*, 3838–3839.

9. Chen, J.; Collier, C. *JOURNAL OF PHYSICAL CHEMISTRY B* **2005**, *109*, 7605–7609.

10. Strano, M.; Dyke, C.; Usrey, M.; Barone, P.; Allen, M.; Shan, H.; Kittrell, C.; Hauge, R.; Tour, J.; Smalley, R. *SCIENCE* **2003**, *301*, 1519–1522.

11. Maeda, Y. et al. *JOURNAL OF THE AMERICAN CHEMICAL SOCIETY* **2005**, *127*, 10287–10290.

12. Kim, S.; Luo, Z.; Papadimitrakopoulos, F. *NANO LETTERS* **2005**, *5*, 2500–2504.

13. Menard-Moyon, C.; Izard, N.; Doris, E.; Mioskowski, C. *JOURNAL OF THE AMERICAN CHEMICAL SOCIETY* **2006**, *128*, 6552–6553.

14. Park, H.; Zhao, J.; Lu, J. *NANO LETTERS* **2006**, *6*, 916–919.

15. Lu, J.; Wang, D.; Nagase, S.; Ni, M.; Zhang, X.; Maeda, Y.; Wakahara, T.; Nakahodo, T.; Tsuchiya, T.; Akasaka, T.; Gao, Z.; Yu, D.; Ye, H.; Zhou, Y.; Meit, W. *JOURNAL OF PHYSICAL CHEMISTRY B* **2006**, *110*, 5655–5658.

16. Park, H.; Zhao, J.; Lu, J. *NANOTECHNOLOGY* **2005**, *16*, 635–638.

17. Zheng, G.; Wang, Z.; Irle, S.; Morokuma, K. *JOURNAL OF THE AMERICAN CHEMICAL SOCIETY* **2006**, *128*, 15117–15126.

18. Gulseren, O.; Yildirim, T.; Ciraci, S. *PHYSICAL REVIEW LETTERS* **2001**, *8711*, 116802.

19. Zhao, M.; Xia, Y.; Lewis, J.; Mei, L. *JOURNAL OF PHYSICAL CHEMISTRY B* **2004**, *108*, 9599–9603.

20. Li, J.; Jia, G.; Zhang, Y.; Chen, Y. *CHEMISTRY OF MATERIALS* **2006**, *18*, 3579–3584.

21. KITAURA, K.; MOROKUMA, K. *INTERNATIONAL JOURNAL OF QUANTUM CHEMISTRY* **1976**, *10*, 325–340.

22. Gulseren, O.; Yildirim, T.; Ciraci, S. *PHYSICAL REVIEW B* **2002**, *65*, 153405.

23. Weedon, B.; Haddon, R.; Spielmann, H.; Meier, M. *JOURNAL OF THE AMERICAN CHEMICAL SOCIETY* **1999**, *121*, 335–340.

24. Niyogi, S.; Hamon, M.; Hu, H.; Zhao, B.; Bhowmik, P.; Sen, R.; Itkis, M.; Haddon, R. *ACCOUNTS OF CHEMICAL RESEARCH* **2002**, *35*, 1105–1113.

25. Elstner, M.; Cui, Q.; Munih, P.; Kaxiras, E.; Frauenheim, T.; Karplus, M. *JOURNAL OF COMPUTATIONAL CHEMISTRY* **2003**, *24*, 565–581.

26. Elstner, M.; Porezag, D.; Jungnickel, G.; Elsner, J.; Haugk, M.; Frauenheim, T.; Suhai, S.; Seifert, G. *PHYSICAL REVIEW B* **1998**, *58*, 7260–7268.

27. POREZAG, D.; FRAUENHEIM, T.; KOHLER, T.; SEIFERT, G.; KASCHNER, R. *PHYSICAL REVIEW B* **1995**, *51*, 12947–12957.

28. Frauenheim, T.; Seifert, G.; Elstner, M.; Hajnal, Z.; Jungnickel, G.; Porezag, D.; Suhai, S.; Scholz, R. *PHYSICA STATUS SOLIDI B-BASIC SOLID STATE PHYSICS* **2000**, *217*, 41–62.

29. Frauenheim, T.; Seifert, G.; Elstner, M.; Niehaus, T.; Kohler, C.; Amkreutz, M.; Sternberg, M.; Hajnal, Z.; Di Carlo, A.; Suhai, S. *JOURNAL OF PHYSICS-CONDENSED MATTER* **2002**, *14*, 3015–3047.

30. DEWAR, M.; ZOEBISCH, E.; HEALY, E.; STEWART, J. *JOURNAL OF THE AMERICAN CHEMICAL SOCIETY* **1985**, *107*, 3902–3909.

31. STEWART, J. *JOURNAL OF COMPUTATIONAL CHEMISTRY* **1989**, *10*, 209–220.

32. Frisch, M. J. et al. *Gaussian 03, Revision D.01+*, Gaussian, Inc., Wallingford, CT, 2004.

33. Zheng, G.; Irle, S.; Elstner, M.; Morokuma, K. *JOURNAL OF PHYSICAL CHEMISTRY A* **2004**, *108*, 3182–3194.

34. Zheng, G.; Irle, S.; Morokuma, K. *CHEMICAL PHYSICS LETTERS* **2005**, *412*, 210–216.

35. Kudin, K.; Scuseria, G.; Yakobson, B. *PHYSICAL REVIEW B* **2001**, *64*, 235406.

Table 7.1: Linear regression values (Equations 7.2, 7.4, and 7.5) for ΔE as a function of $1/d$ for exo(l), exo(s) and endohedral addition products of CH_2, NH and O to 15 Å long $(2n, n)$ SWNTs for n from 3 to 8 at 3 different bond positions at the DFTB level.

	p-type bond			***d***-type bond			***t***-type bond		
X=CH_2	endo-***p***	exo(s)-***p***	exo(l)-***p***	endo-***d***	exo(s)-***d***	exo(l)-***d***	endo-***t***	exo(s)-***t***	exo(l)-***t***
ΔE_0	-54.27	-39.21	-48.37	-60.73	-51.27	-44.84	-62.09	-46.95	-41.15
C	382.79	-695.27	-746.40	603.19	-234.02	-380.83	713.44	-248.63	-210.42
R^2	0.994	0.991	0.992	0.995	0.982	0.997	0.995	0.988	0.999
X=NH	endo-***p***	exo(s)-***p***	exo(l)-***p***	endo-***d***	exo(s)-***d***	exo(l)-***d***	endo-***t***	exo(s)-***t***	exo(l)-***t***
ΔE_0	-27.70	-18.62	-29.12	-34.24	-28.02	-25.26	-34.45	-23.93	-22.12
C	299.46	-631.74	-699.32	501.09	-209.00	-361.73	556.81	-212.89	-197.14
R^2	0.987	1.000	0.991	0.992	0.984	0.997	0.996	0.988	0.995
X=O	endo-***p***	exo(s)-***p***	exo(l)-***p***	endo-***d***	exo(s)-***d***	exo(l)-***d***	endo-***t***	exo(s)-***t***	exo(l)-***t***
ΔE_0	-42.85	-38.86	-37.38	-48.33	-44.51	-33.64	-47.23	-40.31	-31.12
C	190.55	-474.06	-675.85	365.18	-186.06	-354.08	387.27	-199.18	-180.37
R^2	0.977	0.993	0.991	0.986	0.978	0.997	0.995	0.988	0.995

Table 7.2: Regression parameters from Equations 7.6 to 7.8 for quadratic fits of ΔE, DEF, and INT as a function of $1/d$ for endo- and exo(s)-addition products of X=CH_2, NH and O with 15 Å (n, n) SWNTs for three different bond types at the DFTB level of theory.

		CH_2			NH			O		
		p-type	***d***-type	***t***-type	***p***-type	***d***-type	***t***-type	***p***-type	***d***-type	***t***-type
ΔE	$E^{(0)}$	284.46	1585.03	2049.58	-399.14	1250.89	1513.9	-1080.52	758.8	832.76
	$E^{(1)}$	-343.24	-331.95	-342.45	-341.44	-298.11	-288.56	-291.78	-240.72	-229.93
	$E^{(2)}$	-53.05	-51.1	-48.5	-28.69	-27.24	-24.73	-44.85	-44.01	-41.34
	$R^2_{\Delta E}$	0.998	0.992	0.985	0.999	0.995	0.99	0.998	0.995	0.993
	$E^{(2)}/E^{(1)}$	0.15	0.15	0.14	0.08	0.09	0.09	0.15	0.18	0.18
DEF	$D^{(0)}$	1697.75	972.46	814.42	2158.74	847.89	474.67	1418.05	478.03	276.33
	$D^{(1)}$	49.75	-66.38	-94.17	130.23	-37.77	-74.23	52.8	-34.41	-33.63
	$D^{(2)}$	28.03	26.48	27.18	27.18	24.56	24.85	17.85	17.17	17.44
	R^2_{DEF}	0.995	0.952	0.963	0.969	0.87	0.961	0.948	0.883	0.925
INT	$I^{(0)}$	-1484.21	520.78	1126.68	-2572	397.79	1030.89	-2498.97	280.13	556.62
	$I^{(1)}$	-396.52	-266.57	-247.99	-471.56	-260.22	-214.19	-344.6	-206.32	-196.27
	$I^{(2)}$	-78.91	-75.35	-73.39	-56.03	-51.97	-49.74	-62.7	-61.18	-58.78
	R^2_{INT}	0.997	0.995	0.991	0.997	0.997	0.993	0.994	0.996	0.997

Table 7.3: Linear regression (Equations 7.2, 7.4, and 7.5) values for ΔE as a function of "bond curvature" K for exo(l), exo(s) and endohedral addition products of CH2, NH and O to 15 Å long $(2n, n)$ SWNTs for n from 2 to 5 at the DFTB and B3LYP/6-31G(d)//DFTB level of theory.

	CH_2		NH		O	
	DFTB	DFT//DFTB	DFTB	DFT//DFTB	DFTB	DFT//DFTB
ΔE_{0k}	-47.63	-379.40	-28.19	-8.56	-37.01	-26.81
C_k	-392.62	34.14	-370.28	-380.31	-354.10	350.23
R^2	0.992	0.992	0.988	0.990	0.984	0.979

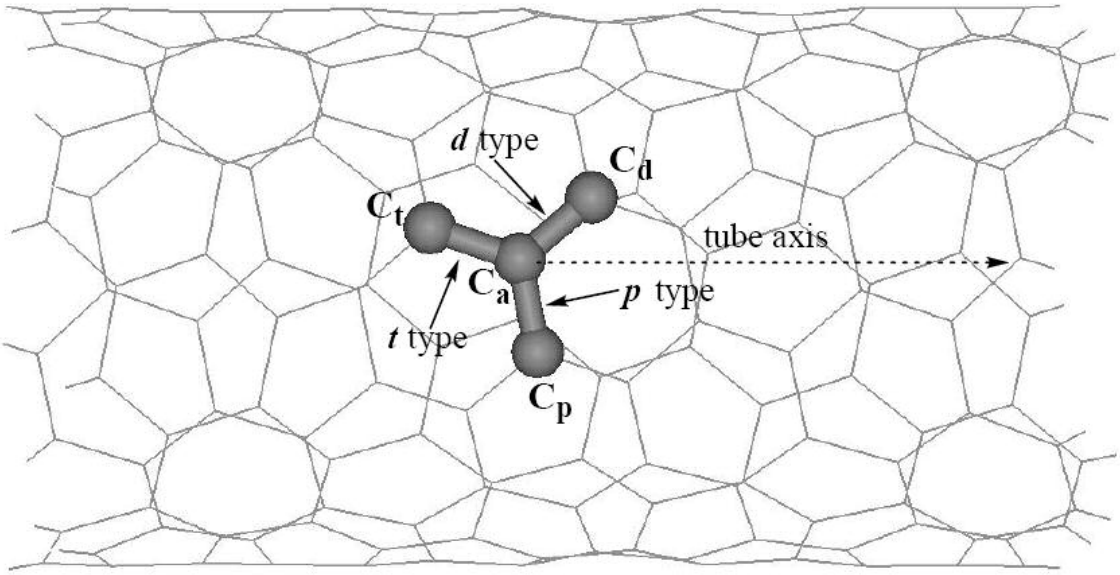

Figure 7.1: The atomic and bond labels for the three bonds in chiral SWNTs. "***t***" stands for "parallel to tube axis", "***d***" stands for "diagonal", and "***p***" stands for "perpendicular" with respect to the tube axis. The assignment of ***t/d/p*** bond types is always made such that the angles with the tube axis follow the relationship ***p***>***d***>***t***.

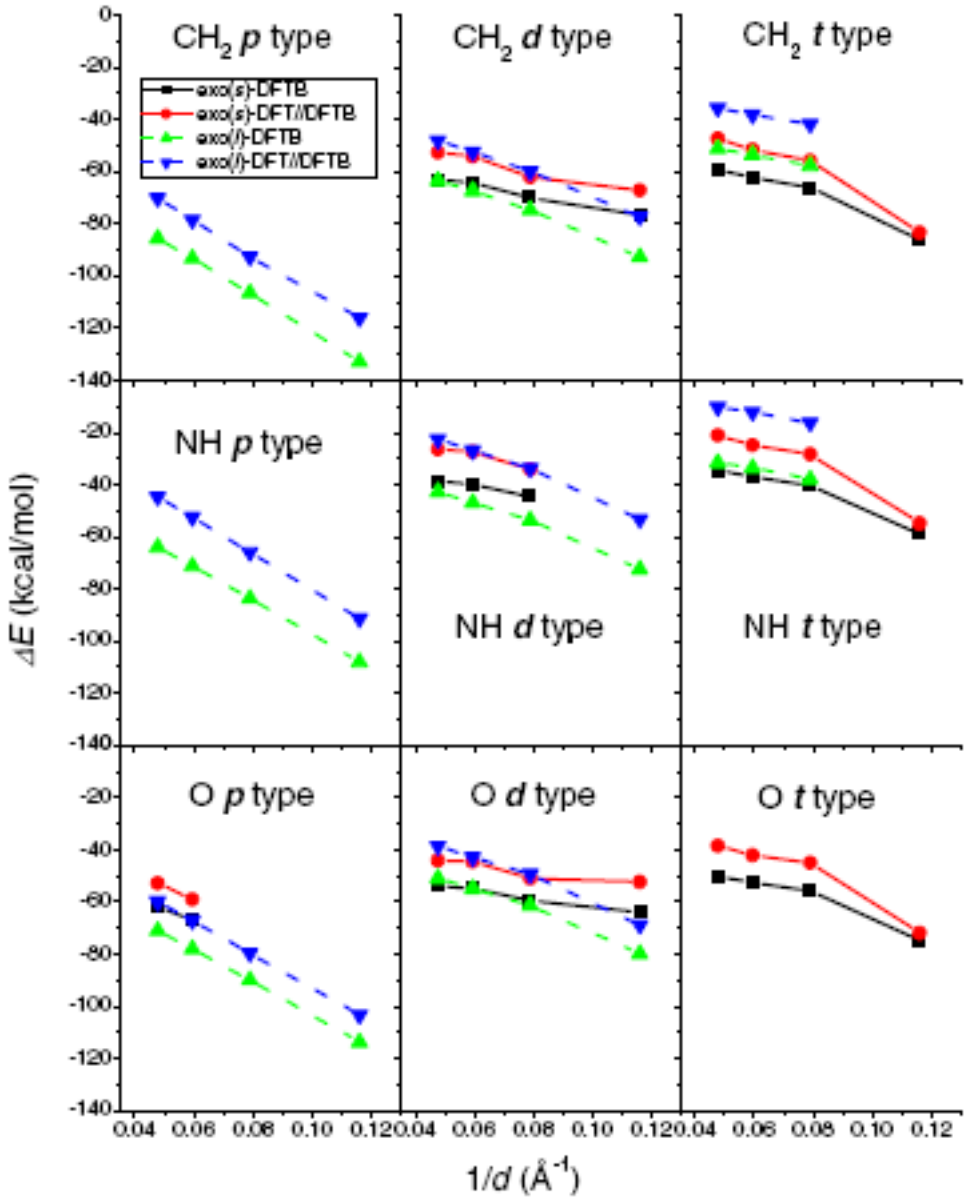

Figure 7.2: The diameter dependence of ΔE for exohedral addition products of X=CH_2, NH and O (^{3}P) to 15 Å $(2n, n)$ SWNTs at the DFTB and B3LYP/6-31G(d)//DFTB levels of theory.

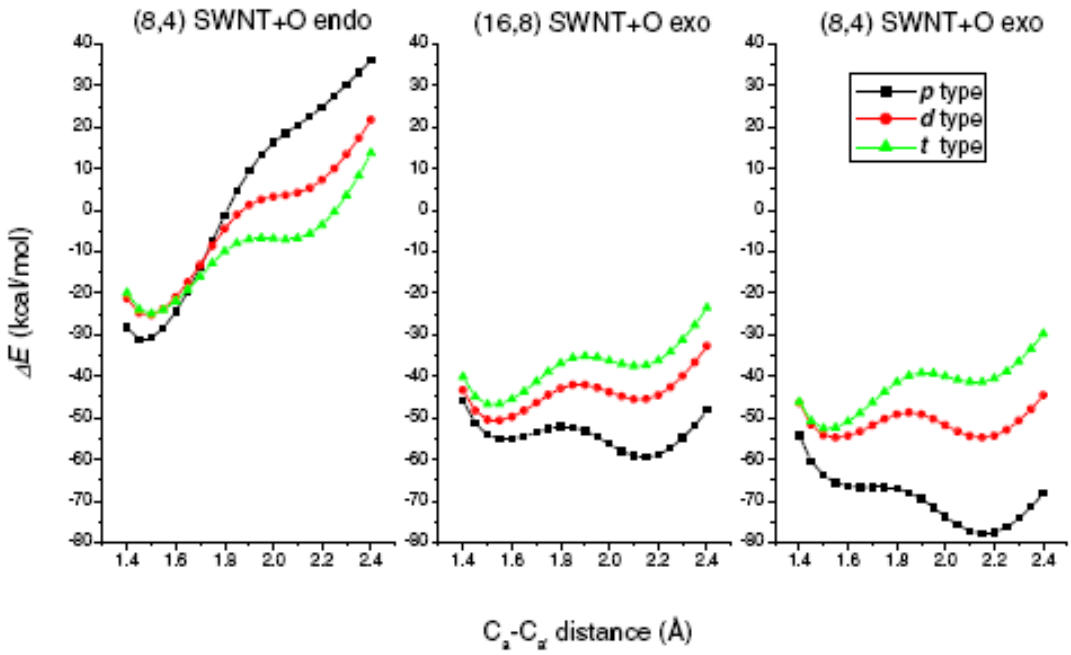

Figure 7.3: Relaxed DFTB PES scan of the C_a-C_x bond participating in the [2+1] addition reaction, with the addition of X = O on the concave (endohedral, $1/d$ curvature = -0.0595 Å^{-1}) and convex (exohedral, $1/d$ curvature = 0.0350 Å^{-1} for (16,8) and 0.0595 Å^{-1} for (8,4)) surface at three different x=***p,d,t*** bond types. In case of exo, a medium diameter tube (8,4) and a large diameter tube (16,8) are shown.

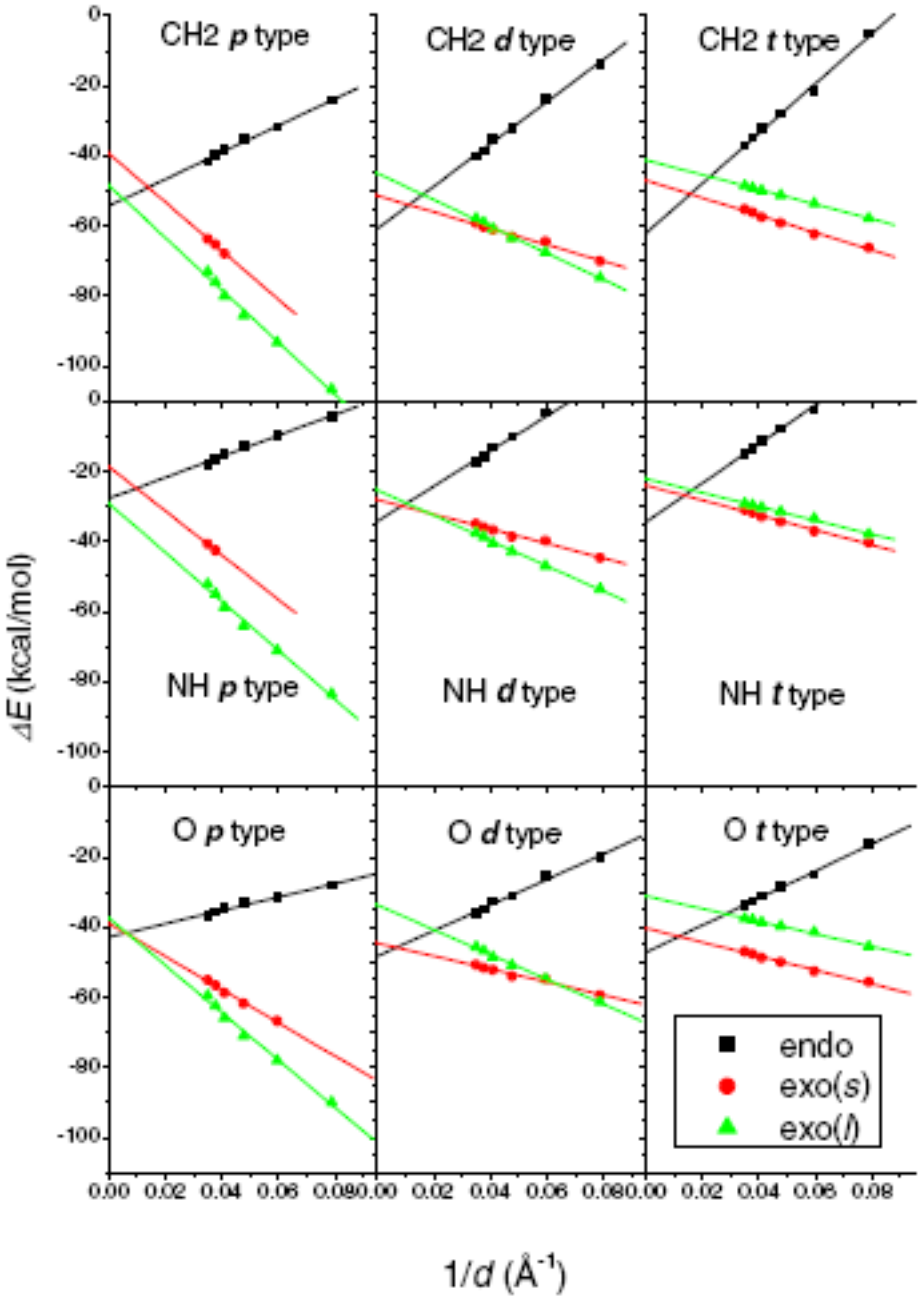

Figure 7.4: Linear regression plots for ΔE as a function of $1/d$ of exo- and endohedral addition products of X=CH_2, NH and O (^{3}P) with 15 Å (n, n) SWNTs at 3 different bond positions at the DFTB level of theory. exo(l) and exo(s) denote opened and 3MR addition product isomers, respectively.

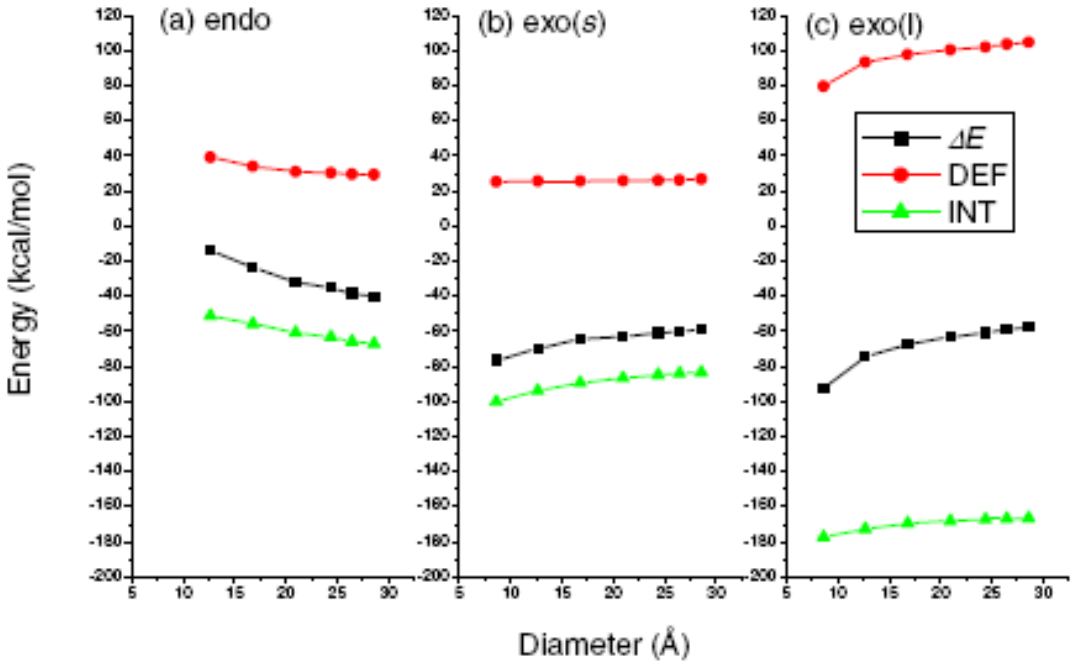

Figure 7.5: Energy decomposition of ΔE into DEF and INT terms as a function of tube diameter d for endo-, exo(s)- and exo(l)-addition products of CH_2 with 15 Å $(2n, n)$ SWNTs at the ***d***-type bond position at the DFTB level of theory.

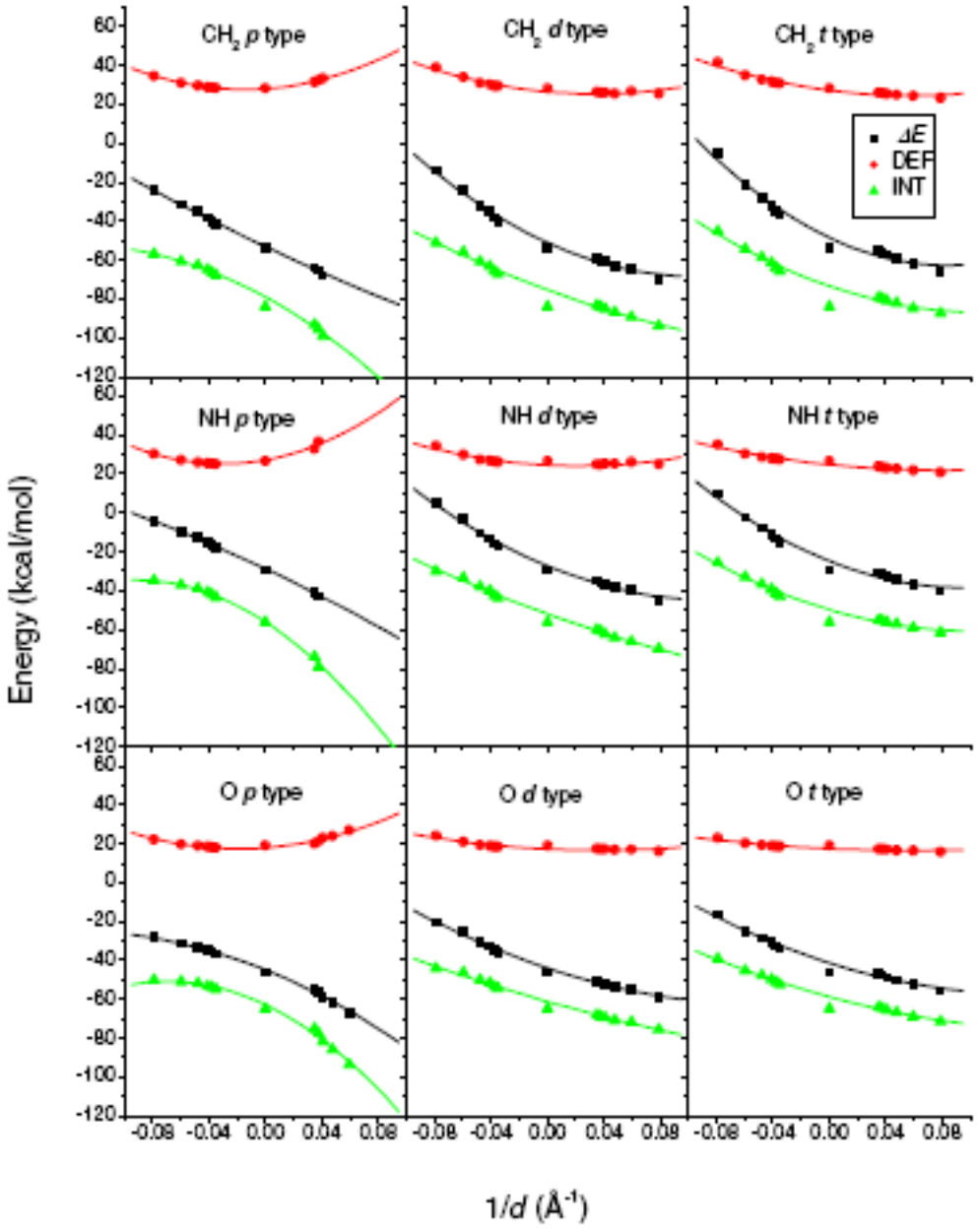

Figure 7.6: Quadratic fits for ΔE, DEF, and INT as a function of $1/d$ for endo- and exo(s)-addition products of X=CH_2/NH/O with 15 Å $(2n, n)$ SWNTs at the three different t/d/p-type bond positions at the DFTB level of theory. Only endo and exo(s) additions are used simultaneously in the fit: Endo-addition products correspond to points where $1/d < 0$, exo(s)-addition products correspond to points where $1/d > 0$. The points at $1/d = 0$ correspond to addition to planar graphite, where we used periodic boundary conditions and a C_{296} graphene model.

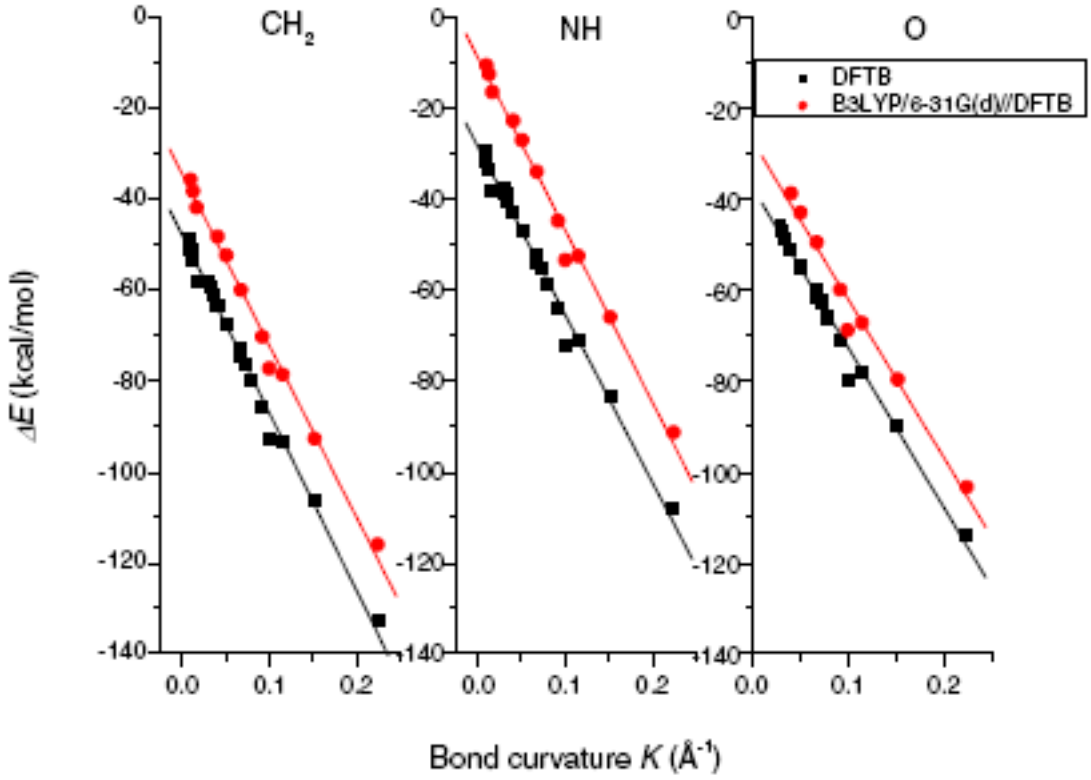

Figure 7.7: Linear regression plots for ΔE as a function of "bond curvature" K for exo(l)-hedral addition products of X=CH_2, NH and O (^{3}P) with 15 Å (n, n) SWNTs at the DFTB and B3LYP/6-31G(d)//DFTB level of theory.

Chapter 8. Theory and experiment agree: Single-walled carbon nanotube caps grow catalyst-free with chirality preference on a SiC surface

8.1 Introduction

The presence of a metal catalyst such as Fe, Co, Ni, Y, or Mo is very often thought to be indispensable in the synthesis of single-walled carbon nanotubes (SWNT) in either carbon arc or laser vaporization[1] processes, or in chemical vapor deposition (CVD) of carbon-rich gases.[2] Resulting SWNT yield, purity, and diameter distributions vary greatly with the metal catalyst, and different catalyst elements are performing differently under either arc/laser vaporization or CVD conditions.[3] However, metal catalyst-free SWNT synthesis has been reported in the exceptional case where SiC is used as base material and decomposed at temperatures around 1500 K, either in ambient conditions[4,5,6,7,8,9,10] or by means of laser vaporization.[11,12,13] Interestingly, Kusunoki *et al.* found SWNT and multi-walled carbon nanotubes (MWNT) nucleation preferentially occurring on the C face of crystalline SiC,[5,6,13] whereas Avouris *et al.*[7] reported SWNT growth and later Nagano *et al.* carbon nanotube (CNT) growth (both SWNT and MWNT) on the Si face.[10] In particular, tubes grown on the Si face have either parallel orientation to the crystal surface as a result of graphene rolling7 or very large caps which possibly stem from the formation of SiO2 bubbles during surface oxide decomposition,[10] while CNTs nucleating on the C face grow vertically aligned in dense forests perpendicular to the crystal surface.[4,5,6] Most notably, these CNTs have been shown to be predominantly of zigzag chirality type.[8,9] All three groups working in this field agree on the finding that thin layers of graphite readily develop on the decomposing SiC surface, and are obviously a prerequisite of nanotube

formation.

8.2 Computational Methodology

Kusunoki *et al.* stressed the importance of nanocap formation during the initial stage of the growth process by comparing the difference of the starting decomposition mechanisms between the Si and C faces of SiC (see Fig. 8.1).[6,10] To shed light on this initial growth process, we hav e performed 2D-periodic high-temperature quantum chemical molecular dynamics (QM/MD) simulations on two-layer $Si_{36}C_{36}$ model slabs with two rectangular p-stacked C_{72} graphene sheet fragments placed on top of either the Si or C face, using the respective van der Waals-radii of 1.70 Å (C) and 2.10 Å (Si) as interlayer distances (3.80 Å for Si-C and 3.40 Å for C-C) in initial geometries. To mimic defects in these graphite sheets, initial structures were chosen such that no connection between periodic images of the graphene sheets was assumed, and that the numbers of fully closed hexagons in each sheet were 20 (5x4, *a*-type) and 25 (5x5, *b*-type). This hexagon distribution leads in case of the *a*-type sheet to 2 C_2 units on opposite corners and 5 carbene C= units on each of its long sides, whereas the *b*-type sheet has less free-standing carbon atoms with only 2 C= units at the corners of one side. The Si (C-face) or C (Si-face) layer in bulk direction was passivated with hydrogen atoms and their positions kept frozen to simulate a rigid bulk environment. Fig. 8.2 displays initial and final structures of representative (a) Si and (b) C face simulations at 0 and 12 ps at 2000 K. These simulations are based on direct on-the-fly calculated density functional tight binding method[14] (DFTB) energies and gradients, and were performed at 2000 K and 3000 K with parameters adopted from Refs.[15,16] We have previously employed the same method successfully for the quantum chemical molecular dynamics simulation of the fullerene formation process and the discovery of the "shrinking hot giant" road of C_{60} buckminsterfullerene formation,[17,18] for the elucidation of SWNT self-capping mechanisms,[19,20] and for the investigation of Fe

catalyzed SWNT growth mechanisms.[21]

8.3 Results

We have carefully checked the accuracy of the DFTB parameters used in this study (both conventional and self-consistent charge (SCC) DFTB[22] with very little difference between them) employed against *ab initio* B3LYP/6-31G(d) calculations for binding energies and bond distances of ethane, methyl silane, and disilane (see Table 8.1). Consistent with our previous experience,[21] we find that geometry parameters are reproduced by DFTB in excellent agreement with the much more expensive B3LYP calculations, whereas DFTB tends to overestimate chemical bonding. We are content with the fact here that the order of binding energies is reproduced correctly and in appropriate proportionality, i.e. binding energies follow the order C-C > Si-C > Si-Si for both levels of theory, consistent with experiment, which means that DFTB and B3LYP potential energy surfaces are parallel and the dynamics on them should therefore be very similar.

We ran a total of 40 trajectories, 20 at 2000 K and 20 at 3000 K, with 10 trajectories of two series per Si and C face each, for about 12 ps simulation time. In series A, the C_2-containing *a*-type C_{72} fragment is placed on the surface in perfect AB p-stacking with the *b*-type sheet above, while in the B series, the *b*-type C_{72} fragment is placed next to the surface. The AB p-stacks are placed at an angle with respect to the SiC surface, which is changed from 0° (perfect edge alignment) to 4° (A/B1=0°, A/B2=+4°, A/B3=+2°, A/B4=-2°, and A/B5=-4°). In the following, we will describe in more detail A2 and B2 trajectories for 2000 K for the C and the Si face as representatives of the C/Si face A and B series. We used R(C-C)=1.80 Å and R(C-Si)=2.20 Å as thresholds for C-X bonding, corresponding to sums of covalent atomic radii12 multiplied by a factor of 1.17 to consider the effects of vibrational excitations. To determine the number of armchair versus zigzag type bond connections

between the sandwiched graphene sheet and the surface, we used the following counting algorithm: If a carbon atom on the cap bonding with any atom on the surface has at least one neighboring atom which also has bonds with the surface, it is counted as an "armchair" type atom; if its neighbors are not directly bound to the surface, it is supposed to have "zigzag" type connection with the substrate. Table 8.2 lists the number of developed pentagons in the sandwiched graphene sheet, the number of sheet-surface σ-bonds, the approximate radii of the developing nanocaps, and the numbers of armchair and zigzag type bonds after 12 ps simulation time for all 40 trajectories, separated in A and B series.

In the C face A2 trajectory at 2000 K, at first the sandwiched graphene layer starts to bend downward at one of its shorter (4 hexagons) side, the C_2 units at the open edges forming rapidly pentagons after only 0.2 ps. At the same time, two C_2 units catch edge carbons of the top layer, and a 3-dimensionally connected structure appears. Four surface C-graphene σ-bonds are formed at the corner of the bent graphene sheet, and at 0.25 ps their number increases to six, before the opposite side of the sandwiched layer starts forming C-C σ-bonds to the surface as well. Again, bonding between hexagons and surface C is preferred, which leads to armchair as well as zigzag type bonds at first. Regions where pentagons are connected to surface Cs appear more disordered, as their carbon densities is higher and more surface-graphene C-C bonds are promoted in their vicinity. At 0.34 ps, all four corners of the *a*-type sheet have been connected to the surface, while one C_2 unit was completely transferred to the upper *b*-type sheet, and a single C_2-bridge between the graphene layers remains. The newly formed dome-type shape of the freshly formed cap remains stable during the entire 12 ps simulation time, while the upper layer manages to connect to a surface C by means of the long polyyne chain that resulted from the previous C_2 transfer from the sandwiched layer. The ratio of armchair to zigzag connections is approximately 2:1 in the beginning of the simulation, but we notice that armchair type connections

are losing over time, as more stable zigzag bonds are made connecting the cap with the surface. The temperature averaged armchair:zigzag bond ratio for C face A series trajectories is 7.6:25.0, with higher temperatures favoring zigzag bonds.

In the C face B2 trajectory at 2000 K, where the C_2 unit-containing layer is on top, similar pentagon formation as in A2 is observed. Subsequently, an inter-graphene connection is made in one corner of the stack after 0.25 ps, while the sandwiched layer maintains a slight U shape bent towards the upper *a*-type sheet. However, surface-*b*-type sheet interaction begins from the center of the graphene sheet, and 7 surface C-graphene C σ-bonds are made after 0.30 ps. Again we note that both armchair and zigzag type configurations are formed, but during the course of the simulations, armchair configurations lose again over the zigzag configurations, and rapidly a nanocap is formed from almost the entire sandwiched graphene layer, which has a single connection with the upper layer after about 1.2 ps. Subsequently, more inter-graphene layer bonds are made, such that two adjacent edges are connected in the same "corners" of the surface, and this superstructure remains stable until the end of the simulation at 12 ps. The temperature averaged armchair:zigzag bond ratio for C face B series trajectories is even slightly lower than for the A series with 4.8:28.8, and higher temperatures favor similarly zigzag bonds.

In the Si face A2 trajectory at 2000 K, one of the corner C_2 units of the sandwiched *a*-type sheet rapidly grabs a surface-Si atom, tearing down this corner and increasing the number of Si-C σ-bonds to 5 in this region after 0.30 ps. Since the nonbonded Si-Si surface distances of the Si face are relatively shorter than the nonbonded C-C surface distances of the C face, we find that graphene C atoms make frequently two bonds instead of one, and change their bonding partner more frequently. This leads to a faster bond-alternation and shorter-lived graphene-surface connections, leaving the flat shape of the sandwiched graphene sheet more or less intact. In particular, we note that after one corner is connected, the entire sheet "lands" flat on the Si face,

forming 17 C-Si σ-bonds after only 0.60 ps. Since the C-Si σ-bond energy is smaller by about 16 kcal/mol than a C-C σ-bond, and because of the geometrical feature of the Si face, C-Si σ-bonds are fluctuating more and the π-conjugated graphene sheet remains flat over the course of the simulation. Consequently, no long-lasting connection is made with the top graphene layer either, which separates from the surface, displaying several long-lived C_2 units that emerged after Stone-Wales type edge transformations. The temperature averaged armchair:zigzag bond ratio for Si face A series trajectories is even noticeably higher than for the C face A series with 11.0:22.4, but higher temperatures favor zigzag bonds also in this case.

In the Si face B2 trajectory at 2000 K, the same rapid "flat landing" of the sandwiched graphene sheet is observed with 15 C-Si σ-bonds formed after 0.60 ps, but rapidly fluctuating. Again, the top layer remains detached from the surface system, which is a consequence of the "flatness" of the surface attached graphene layer (no point of attack is readily provided). The flat surface-attached graphene structure remains largely unchanged until the end of the simulation at 12 ps, and the top layer never attaches. The temperature averaged armchair:zigzag bond ratio for Si face B series trajectories is similarly higher than for the C face B series with 7.0:23.0, and higher temperatures favor zigzag bonds also in this case.

As a side note we would like to mention that, if only a single graphene layer is placed on either Si or C face of the SiC surfaces, the sheet experiences frequently a strong tendency to "lift off" from the surface without making strong surface-graphene connections. Apparently, the second top layer helps to prevent the surface-neighbored sheet to form quickly bonds with the surface, which is consistent with the fact that experimentally several graphite layers are observed in the HREM images (Fig. 8.3).

To summarize the main features from these trajectories: a) *a*-type graphene sheets transform their attached C_2 units rapidly into pentagons, introduce pentagons, and become therefore easier curved at the edges, bending easier down to form contacts

with the surface; b) C_2 units, in particular edge units, are frequently observed to make inter-sheet conections; c) surface-graphene C-C σ-bonds are long lived and do not change much; d) zizgag type bond formations are clearly favored over armchair type bonds, in particular over time, with higher temperatures, and for the more reactive A type series; e) surface-graphene Si-C σ-bonds are shorter lived and subject to greater fluctuation. Fig. 8.3 displays the change in the number of surface-C bonds for C and Si face systems at 2000 K and 3000 K, respectively. The number of Si-C σ-bonds clearly fluctuates more as a consequence of the flatness of the graphene sheet, which is itself a consequence of the less strong Si-C σ-bonds compared to the stronger C-C σ-bonds, and the closer Si-Si distances compared to the more isolated nonbonded C-C distances on the C face surface. These fluctuations increase with temperature, but again more so for the Si-C σ-bonds compared to the C-C σ-bonds. Clearly, in the case of the C face, the more defective *a*-type sheet leads to stronger structural deformation and more pronounced cap nucleation due to the ease of initial pentagon formation, whereas the Si face does not distinguish much between a- or *b*-type sheet-surface connections: the temperature averaged C face:Si face pentagon ratio is 4.0:2.6 for the A series, and 2.3:2.5 for the B series. Associated with the larger number of A-series C face pentagons are smaller cap diameters with a temperature averaged diameter of 5.64 Å, to be compared with 7.85 Å for A-series Si face and B-series C face and Si face values of 6.17 Å and 7.72 Å, respectively. Interestingly, higher temperature favors smaller diameters irrespective of sheet type but more so in the case of C face compared to Si face simulations, indicating stronger structural deformations. Cap nucleation is therefore prevalent in A-series C face simulations, but it clearly occurs also the case of the *b*-type sheet-C face interactions, but with about 0.5 Å larger cap diameter. Investigating the number of surface-C bonds, we see that the number of C face-sheet contacts is larger than the number of Si face-sheet contacts, and that higher temperature in fact increases the number of C-C bonds but

reduces the number of Si-C bonds. This is observed independent from the graphene sheet type in both A and B series. Concerning the ratio of armchair:zigzag bond connections to the surface, we observe that both C face series predominantly prefer zigzag type bonds with an approximate averaged ratio of 1:4, whereas the Si face series discriminate somewhat less, but still noticeably with an approximate averaged ratio of 1:2.5. Higher temperatures favor zigzag connections more than lower temperatures, indicating the importance of annealing processes towards more perfect zigzag type connections.

Considering these statistics, it becomes apparent that the more stable C-surface σ-bonds in case of the C face simulations forces the originally planar π-conjugated graphite fragment to stray in an arched conformation towards the surface, and more so in case of the A series where edge pentagons are readily formed, helping initial dome-shape formation. Consequently, in order to minimize the associated strain on the hexagon network, pentagons (including surface ones) are more frequently formed in case of the C face than for the Si face simulations where C-surface σ-bonds are less favored due to the lower thermodynamic stability of the Si-C σ-bond versus a C-C σ-bond. As a result of this, and because a ring-shaped arrangement of C-surface bonds minimizes the number of sp^3-hybridized atoms of the graphite sheet as opposed to, e.g. a quadratic shape, a characteristic dome with averagely 3-4 pentagons is emerging readily when the graphite sheet can interact with the C (000-1) surface of a SiC crystal, and remaining stable even at 3000 K temperature. The graphene sheet on the Si face remains largely flat, which is consistent with the experimental observation that either parallel graphene rolling7 or larger diameter caps9 are formed on this surface.

8.4 Summary

In summary, the cap formation mechanism on SiC crystal surfaces can be viewed as a result of balancing two opposing energy contributions: i) keeping graphene sheet π-conjugation intact as much as possible on one hand, and ii) forming surface-graphene σ-bonds as much as possible to saturate the dangling bonds of the SiC crystal, with Si-C σ-bonds being much more volatile than more stable C-C σ-bonds due to their energetically less favorable character as well as the shorter nonbonded Si-Si surface distances. The zigzag type chirality control of tubes grown on the C face of SiC (and much less pronounced on the Si face) is observed with a consequence of the 90° angle formed between the unfilled valence of the unsaturated sp^3 carbon atoms and the SiC crystal surface, which favors perpendicular C-C bonds, with a graphene sheet carbon atom connecting these perpendicular parallel C-C bonds, forming a C_5Si hexagon. The surface-sheet contacts are subject to relatively fast annealing processes within tens of picoseconds. It is generally accepted that cap chirality determines the diameter and chirality of the entire tube,[23,24] and we therefore feel strongly that the principal of chirality control achieved by the directionality of vacancy surface orbitals may be applied to other "matrix-type" catalyst surfaces as well in the future to allow the synthesis of SWNTs and MWNTs with specific chirality indices.

References

1. IIJIMA, S.; ICHIHASHI, T. *NATURE* **1993**, *363*, 603–605.

2. Li, W.; Xie, S.; Qian, L.; Chang, B.; Zou, B.; Zhou, W.; Zhao, R.; Wang, G. *SCIENCE* **1996**, *274*, 1701–1703.

3. Journet, C.; Bernier, P. *APPLIED PHYSICS A-MATERIALS SCIENCE & PROCESSING* **1998**, *67*, 1–9.

4. Kusunoki, M.; Rokkaku, M.; Suzuki, T. *APPLIED PHYSICS LETTERS* **1997**, *71*, 2620–2622.

5. Kusunoki, M.; Suzuki, T.; Kaneko, K.; Ito, M. *PHILOSOPHICAL MAGAZINE LETTERS* **1999**, *79*, 153–161.

6. Kusunoki, M.; Suzuki, T.; Hirayama, T.; Shibata, N.; Kaneko, K. *APPLIED PHYSICS LETTERS* **2000**, *77*, 531–533.

7. Derycke, V.; Martel, R.; Radosvljevic, M.; Ross, F.; Avouris, P. *NANO LETTERS* **2002**, *2*, 1043–1046.

8. Kusunoki, M.; Suzuki, T.; Honjo, C.; Hirayama, T.; Shibata, N. *CHEMICAL PHYSICS LETTERS* **2002**, *366*, 458–462.

9. Kusunoki, M.; Honjo, C.; Suzuki, T.; Hirayama, T. *APPLIED PHYSICS LETTERS* **2005**, *87*, 103105.

10. Nagano, T.; Ishikawa, Y.; Shibata, N. *JAPANESE JOURNAL OF APPLIED PHYSICS PART 1-REGULAR PAPERS SHORT NOTES & REVIEW PAPERS* **2003**, *42*, 1380–1385.

11. Botti, S.; Ciardi, R.; Terranova, M.; Piccirillo, S.; Sessa, V.; Rossi, M.; Vittori-Antisari, M. *APPLIED PHYSICS LETTERS* **2002**, *80*, 1441–1443.

12. Botti, S.; Asilyan, L.; Ciardi, R.; Fabbri, F.; Loreti, S.; Santoni, A.; Orlanducci, S. *CHEMICAL PHYSICS LETTERS* **2004**, *396*, 1–5.

13. Konishi, H.; Matsuoka, H.; Toyama, N.; Naitoh, M.; Nishigaki, S.; Kusunoki, M. *THIN SOLID FILMS* **2004**, *464-65*, 295–298.

14. POREZAG, D.; FRAUENHEIM, T.; KOHLER, T.; SEIFERT, G.; KASCHNER, R. *PHYSICAL REVIEW B* **1995**, *51*, 12947–12957.

15. FRAUENHEIM, T.; WEICH, F.; KOHLER, T.; UHLMANN, S.; POREZAG, D.; SEIFERT, G. *PHYSICAL REVIEW B* **1995**, *52*, 11492–11501.

16. Gutierrez, R.; Frauenheim, T.; Kohler, T.; Seifert, G. *JOURNAL OF MATERIALS CHEMISTRY* **1996**, *6*, 1657–1663.

17. Irle, S.; Zheng, G.; Elstner, M.; Morokuma, K. *NANO LETTERS* **2003**, *3*, 1657–1664.

18. Zheng, G.; Irle, S.; Morokuma, K. *JOURNAL OF CHEMICAL PHYSICS* **2005**, *122*, 014708.

19. Irle, S.; Zheng, G.; Elstner, M.; Morokuma, K. *NANO LETTERS* **2003**, *3*, 465–470.

20. Zheng, G.; Irle, S.; Elstner, M.; Morokuma, K. *JOURNAL OF PHYSICAL CHEMISTRY A* **2004**, *108*, 3182–3194.

21. Zheng, G.; Witek, H. A.; Bobadova-Parvanova, P.; Irle, S.; Musaev, D. G.; Prabhakar, R.; Morokuma, K. *JOURNAL OF CHEMICAL THEORY AND COMPUTATION* **2007**, *3*, 1349–1367.

22. Elstner, M.; Porezag, D.; Jungnickel, G.; Elsner, J.; Haugk, M.; Frauenheim, T.; Suhai, S.; Seifert, G. *PHYSICAL REVIEW B* **1998**, *58*, 7260–7268.

23. Kataura, H.; Kumazawa, Y.; Maniwa, Y.; Ohtsuka, Y.; Sen, R.; Suzuki, S.; Achiba, Y. *CARBON* **2000**, *38*, 1691–1697.

24. Reich, S.; Li, L.; Robertson, J. *PHYSICAL REVIEW B* **2005**, *72*, 165423.

Table 8.1: B3LYP, DFTB, and SCC-DFTB results for binding energies (BE) and bond distances R of ethane, methyl silane, and disilane, relative to methyl CH_3 and silane SiH_3 radicals.

	B3LYP/6-31G(*d*)		DFTB (SCC-DFTB)	
	BE (kcal/mol)	R (Å)	BE (kcal/mol)	R (Å)
$H_3Si-SiH_3$	74.1	2.35	96.8(96.0)	2.30(2.31)
H_3Si-CH_3	88.1	1.89	121.9(121.6)	1.87(1.86)
H_3C-CH_3	96.6	1.53	137.8(138.5)	1.50(1.50)

Table 8.2: Statistics at simulation end points 12 ps of DFTB-based QM/MD trajectories of $Si_{36}C_{36}H_{36}$ at 2000 and 3000 K with *a*- and *b*-type C_{72} graphic layers placed on top of Si or C faces, with HX bond lengths frozen during the MD. Detailed descriptions of structures and table contents are given in the main text.

	No. of Pentagons				No. of X–C *s* bonds				Cap radius (Å)				No. of armchair bonds				No. of zigzag bonds			
T	2000 K		3000 K		2000 K		3000 K		2000 K		3000 K		2000 K		3000 K		2000 K		3000 K	
Face	C	Si	C	Si	C	Si	C	Si	C	Si	C	Si	C	Si	C	Si	C	Si	C	Si
A1	5	3	3	2	16	23	24	18	5.14	7.20	5.26	7.04	6	10	5	2	9	10	14	13
A2	5	4	5	2	19	20	16	16	6.23	7.71	5.43	8.68	10	4	0	0	8	15	14	12
A3	3	2	6	3	18	19	24	20	5.62	8.87	5.00	8.05	4	4	2	0	12	13	9	8
A4	3	2	3	3	20	23	23	21	6.10	7.11	5.77	7.14	2	11	0	6	17	11	20	10
A5	3	3	4	2	19	19	25	23	5.68	9.59	6.20	7.02	5	6	4	12	13	12	9	8
Av.	3.8	2.8	4.2	2.4	18.4	20.8	22.4	19.6	5.75	8.10	5.53	7.59	5.4	7.0	2.2	4.0	11.8	12.2	13.2	10.2
B1	1	0	3	3	19	19	25	17	7.11	7.60	5.65	5.59	2	2	0	0	17	16	16	10
B2	1	3	3	4	19	17	25	15	6.99	9.40	4.90	9.03	3	4	0	4	14	12	13	10
B3	1	1	2	1	18	19	26	12	7.63	7.32	5.72	6.67	3	3	3	0	14	15	15	7
B4	3	5	5	4	18	20	25	17	6.06	7.49	4.90	6.73	4	10	2	4	14	9	13	11
B5	1	2	3	2	22	18	24	17	7.19	8.15	5.47	9.18	7	3	0	5	15	15	15	10
Av.	1.4	2.2	3.2	2.8	19.2	18.6	25.0	15.6	7.00	7.99	5.33	7.44	3.8	4.4	1.0	2.6	14.4	13.4	14.4	9.6

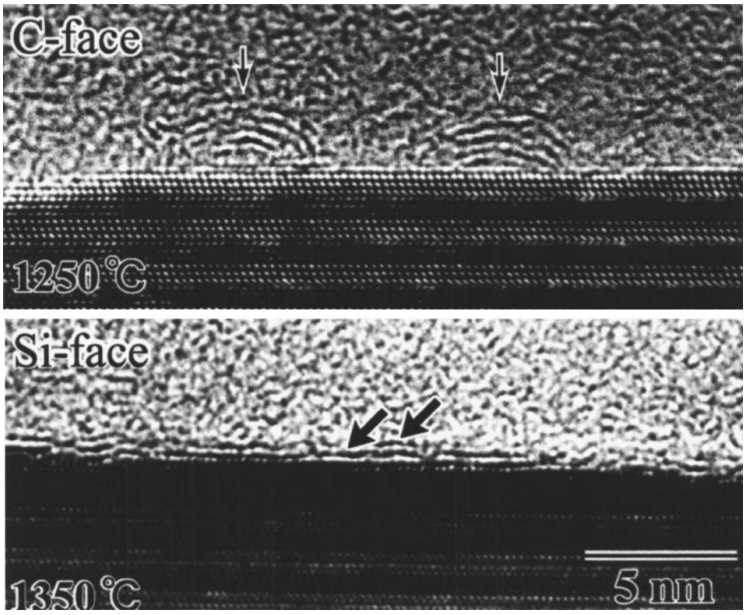

Figure 8.1: HREM images from Ref.[6] Growth of SWCNTs on C face and Si face of SiC. Outer carbon layers are indicated by arrows.

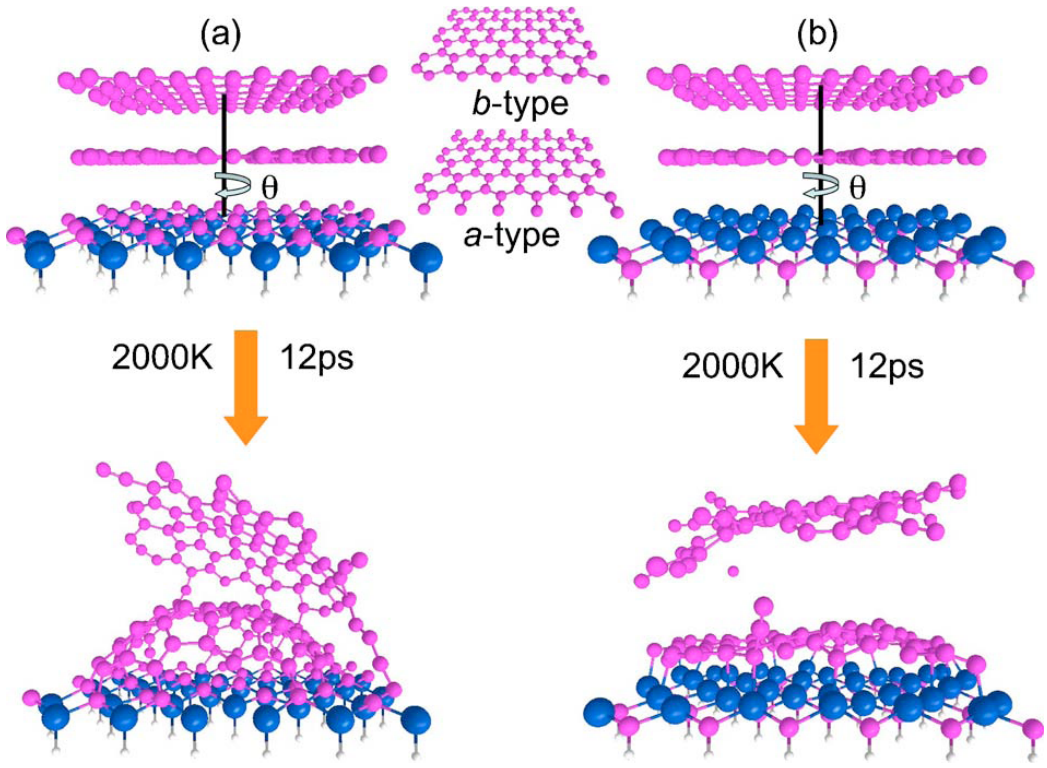

Figure 8.2: DFTB-based QM/MD simulation snapshot structures of $Si_{36}C_{36}H_{36}$ with two nonidentical C_{72} graphite layers at 2000 K after 12 ps. Carbon atoms are pink, silicon atoms blue, and hydrogen atoms white. (a) face of SiC and (b) Si face of SiC.

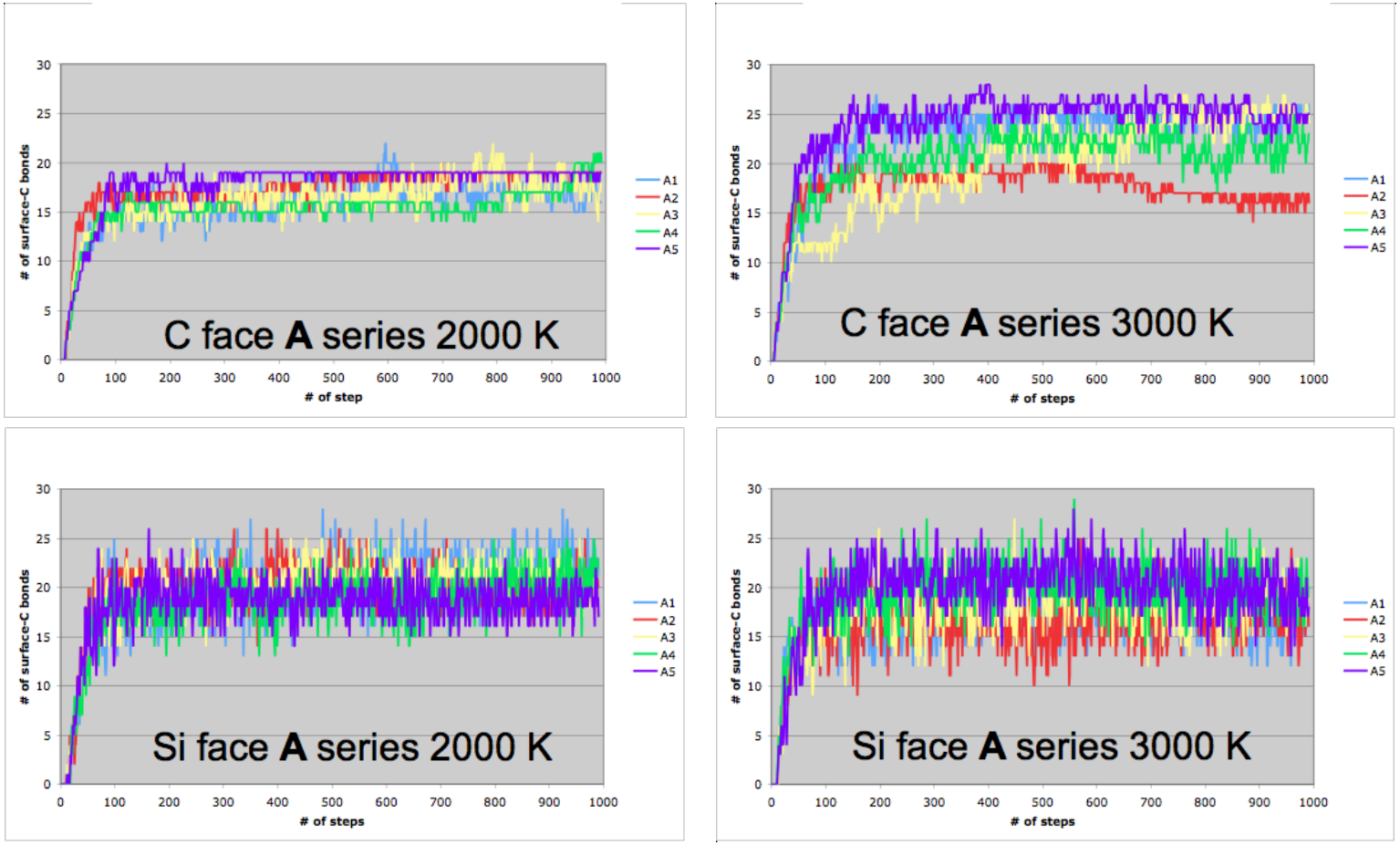

Figure 8.3: DFTB-based QM/MD simulation statistics on number of surface-graphene σ bonds during the simulation of C and Si faces at 2000 and 3000 K. Step size is 1.209 fs. Only A series results are shown for simplicity.

Chapter 9. Carbon Nanotubes Grow on the C Face of SiC $(000\bar{1})$ during Sublimation Decomposition: Quantum Chemical Molecular Dynamics Simulations

9.1 Introduction

Since the discovery of carbon nanotubes (CNTs) in the early 1990s,[1,2,3] scientists have made tremendous efforts on producing high quality nanotubes with various methods, such as arc-discharge,[1,2,3] laser vaporization,[4] pyrolysis,[5] and chemical vapor deposition (CVD).[6,7,8] While it is known that multi-walled carbon nanotubes (MWCNTs) can grow from pure graphite without addition of any catalyst under certain conditions,[1,9] the synthesis and production of single-walled carbon nanotubes (SWCNTs) has almost exclusively been achieved only in the presence of transition metal (TM) catalysts such as Fe, Co, Ni, Y, or Mo.[2,3,4,5,6,7,8,10,11] Nevertheless, MWCNT synthesis also benefits from the use of TM catalysts as their presence leads to higher quality[12] and narrower multi-walled tube diameters as well.[13] Unfortunately, the yield, purity, and diameter distributions of CNTs produced in this fashion generally vary with different metal catalysts and experimental conditions; moreover, for the use of CNTs in actual applications the TM catalyst needs to be removed from the nanotube material by purification treatments,[14] which often leads to the introduction of undesired tube defects.[15] Most severely, it is still impossible to synthesize tubes with specific chirality, which of course determines their electronic conductivity properties.[16,17]

TM catalyst-free CNT synthesis has been reported in the exceptional case where SiC is used as carbon source material and thermally decomposed in vacuum sublima-

tion at high temperatures, either by means of heating[18,19,20,21,22,23,24,25,26] or by laser vaporization.[27,28,29] This "carbide-derived-carbon" method produces typically MWCNTs with a very minor fraction of SWCNTs, but preferential SWCNT formation by the SiC decomposition method has also been claimed.[23] Interestingly, Kusunoki *et al.*[18,19,20,21,22,25,26] found that CNTs are preferentially grown in perpendicular direction on the C-face of the crystalline (000-1) SiC surface (see Figure 9.4) with 1-2 nm diameter of the inner tubes[22,25,26] and preference for zigzag chirality,[21] whereas Derycke *et al.*[23] claimed to have observed SWCNT growth on the Si-face parallel to the crystal surface with 1.2-1.6 nm diameter. Nagano *et al.*[24] observed CNT growth in perpendicular direction on the Si-face with larger CNT diameters and 65% shorter lengths than C-face grown tubes. We presume the latter growth is due to their surface treatment with HF before sublimation decomposition, thereby partially etching the top Si layer off and converting the former Si-face to a partial C-face. It is also clear that the degree of surface oxidation plays an important role for the ability of a surface to grow CNTs, for instance completely oxidized surfaces have been proven unusable while as-received surfaces typically show some degree of surface oxidation but nevertheless exhibit growth activity.[24] All experimental groups assume that Si atoms leave the surface in near-ultra-high vacuum conditions (10^{-8} to 10^{-9} Torr) by sublimation above ∼1470 K and that thin graphite layers readily develop on the remaining carbon-rich SiC surfaces,[30] perhaps even on the C-face of SiC(000-1).[31] However, nobody so far has given a satisfactory explanation of how exactly the Si atoms leave, although the working hypothesis of some groups is that gaseous SiO may play an important role in this process.[24] Thermal oxidation may originate from remaining atmospheric oxygen, oxygen-containing impurities on the furnace walls, or from the partially oxidized surfaces themselves.

The probably first atomistic simulations of carbon condensation on SiC surfaces was carried out by Gogotsi *et al.*, who used an empirical reactive molecular mechanics

force field for the study of diamond growth on the Si-face of the 6H-SiC (1000) surface.[32] In this pioneering study, individual carbon atoms were at first randomly placed on the top Si atom layer, and it was observed that carbon formed polyyne chains, similar to the ones we have reported in our QM/MD studies of fullerene formation from C_2 molecules at high-temperature.[33,34,35,36,37] Gogotsi subsequently added entire diamond layers on top of the SiC surface, but noticed that if only a single carbon layer was used, the sp^3-carbon atoms rearranged and formed a graphene sheet consisting of mostly sp^2-carbon atoms, in agreement with expectations raised from earliest SiC sublimation decomposition experiments,[30] but the question remains where such a thin diamond layer should come from in experiment under the low-pressure conditions. Moreover, our group has shown before in extensive comparisons between the reactive empirical bond order[38,39] (REBO) force field and density functional tight binding[40,41,42,43] (DFTB)-based molecular dynamics simulations of fullerene formation and self-capping of open-ended CNTs that the role of quantum mechanics for the description of π-conjugated carbon systems is crucial,[36,44] and that qualitatively very different trajectories are obtained concerning both chemical nature of events as well as their time scale for the same model systems. We have recently performed high- temperature quantum chemical molecular dynamics (QM/MD) simulations on model systems of thin SiC crystal surfaces with two graphene sheets placed on top of either C- or Si-face.[45] In agreement with experiment, we found that a) the C-face attached graphene layer warps readily to form small diameter, stable nanocaps, suitable to initiate further perpendicular growth of nanotubes, b) the Si-face attached graphene sheet does not readily warp and forms more volatile Si-graphene bonds, and c) C-face nanocaps appear to anneal to dome-shape short nanotube structures with tube-surface connectivity consistent with zigzag nanotube chirality. We did however not investigate how the growth of would proceed following the cap formation; this is the topic of the present study. Consequently, in the present investigation we start

our QM/MD simulations from a nanocap (C-face) or surface-attached graphene sheet (Si-face) "grown" in silico in a similar fashion as described previously,[45] and study the atomistic dynamics of continued CNT growth in simulations where Si atoms are successively removed. The removal of Si atoms is intended to simulate the experimental Si sublimation decomposition which occurs on the order of minutes, and is therefore too slow to be modeled straightforwardly. We will elaborate on two modes of Si atom removal, namely layer-wise and individual atom-wise, analyze tube lengths and their ring composition, and discuss the role of additional C_2 units placed near the growing tubes to simulate defect healing by excess carbon. We will conclude by comparing our results with experimental findings.

9.2 Computational Methods

The DFTB method[40,41,42,43] is employed as the quantum chemical potential in our molecular dynamics (MD) simulations, with the atomic and diatomic parameters adopted from References.[40,46,47] Energies and gradients are evaluated direct ("on the fly") during the dynamic simulation. We have previously compared the DFTB performance with *ab initio* DFT and semi- empirical AM1 and PM3 methods for energies and geometries of different fullerene isomers C_{28}-C_{86},[48] and showed that DFTB produces results comparable to B3LYP/6-31G(d) while performing substantially better than the other two semi-empirical methods. Regarding the use of DFTB for SiC we have already verified[45] its predicted geometries and energetics (both conventional and self-consistent charge (SCC)[41] variants with very little difference between them) against B3LYP/6-31G(d) calculations of small model compounds, and found that geometry parameters are reproduced by DFTB in excellent agreement with the much more expensive B3LYP calculations, whereas DFTB tends to systematically overestimate chemical bonding by about 30% while preserving the experimental and theoretical order of binding energies C-C > Si-C > Si-Si. This systematic overbind-

ing however only means that the potential energy surface (PES) is globally shifted towards lower energies, and that the landscape is similar in both DFTB- and DFT-based QM/MD simulations of SiC. As usual, we employed a velocity Verlet integrator with a time step of 1.209 fs (50 atomic units) to propagate the trajectories and used scaling of velocities with an overall probability of 20% to adjust the system temperature to the target temperature T_t. Although not ideal, such a simple approach to maintain target temperature is commonly employed, and in recent tests we did not find major differences in the dynamics obtained by using scaling of velocities versus Andersen or Nose-Hoover thermostats.

Regarding the employed model systems, periodic boundary conditions were employed with a unit cell size of 1000 Å in the direction perpendicular to the surface and 16.0 Å and 15.4 Å in the other two surface-directions to achieve two-dimensional slab periodicity. These dimensions are slightly smaller compared to our previous study;[45] we effectively re-performed the nanocap nucleation on C-face and graphene-attachment on Si-face by choosing a slightly smaller model to make the MD simulations more manageable on longer time scales. To mimic bulk effect in the direction away from the surface under investigation, the dangling bonds of the SiC layer farthest away are passivated with hydrogen atoms, and the movements of both hydrogen and hydrogen-connected atoms are frozen during the QM/MD simulations.

9.3 Results and Discussion

9.3.1 Cap nucleation and CNT growth initial structures

In our previous study[45] we investigated the nucleation of carbon nanocaps on SiC surfaces. Our 2D-periodic high-temperature QM/MD simulations were performed using two-layer $Si_{36}C_{36}$ model slabs for the SiC surface and two rectangular π-stacked C_{72} graphene sheet fragments placed on top of either the Si or C face, using the respective van der Waals-radii as interlayer distances in initial geometries at 2000 K

and 3000 K target temperatures. During all C-face simulations, spontaneous warping of the graphene layer closest to the surface containing dangling C-bonds was observed with pronounced dome-shape structures of nanocaps, while the graphene layers on the Si-face remained planar under otherwise same conditions. The reason for this astonishingly different behavior is that surface-graphene C-C σ-bonds are long lived and do not change much, allowing the formation of a stable curved structure, while surface-graphene Si-C σ-bonds are shorter lived and subject to greater fluctuation, with a flat graphene sheet loosely attached to the dangling Si surface atoms as a result. Curvature development in π-conjugated carbon systems is always reflected in the larger average number of pentagons in the graphene sheets attached to the C-face, which is a geometrical requirement for developing curvature in honeycomb lattices. Due to a high interconversion rate between five- and six-membered rings at 2000 K and 3000 K, it is difficult to discriminate whether pentagons induce sustained curvature or sustained curvature induces the occurrence of pentagons. We also found that zigzag type bonds are clearly favored over armchair type bonds from the onset of dome formation and this preference is enhanced as the time progresses during annealing of the dome-shaped structures. To illustrate the conditions leading to cap nucleation, we show in Figure 9.1 surface/graphene interactions leading to nanocap formation in a cut through the cap center (top panel), and along the border of the cap (bottom panel). The cap formation mechanism on SiC crystal surfaces can be viewed as the result of balancing two antagonistic forces: i) keeping the graphene π-conjugation intact as much as possible and the graphene sheet planar on one hand, and ii) forming as many as possible surface-graphene σ-bonds to saturate the dangling bonds of the SiC crystal. The weaker Si-C σ-bonds turn out to be much more volatile than more stable C-C σ-bonds due to their lower thermodynamic stability, and the planar graphene sheets therefore "win" on the Si-face. The zigzag type chirality of the dome on the C-face can be viewed as a consequence of the 90° angle formed between

the unfilled valence of the unsaturated sp^3 carbon atoms and the SiC crystal surface, effectively favoring the formation of C-C bonds perpendicular to the surface, and the formation of a C_5Si hexagon between two adjacent surface dangling bond sites.

In order to save computation time, a smaller cluster size was chosen for generating the initial nanocap (C-face)/surface-attached graphene sheet (S-face) compared to our initial work.46 This time, we chose two layers of $Si_{30}C_{30}$ instead of a single $Si_{36}C_{36}$ layer, terminated in bulk direction by hydrogen atoms, and added only one layer of a C_{60} graphene sheet on top of both surfaces, as the second layer used previously was demonstrated to act as a bystander after having performed the initial push-down of the surface-adjacent graphene layer. In order to achieve graphene-surface attachment in the present one-layer systems, the interlayer distance between SiC surface and graphene sheet was chosen to be 2.0 Å. For each face type of the SiC surface we ran one trajectory at the temperature of 2000 K, with the simulation time of 12 ps. Although the 2.0 Å distance is very short for the Si-C and even C-C systems, we do observe similar behavior with our previous two-graphene-layer models during the 12 ps simulations at 2000 K, namely on the C-face the graphene sheet warps to form a nanocap while on Si face the graphene sheet remains relatively flat. This capped structure on the C-face at 12ps is assumed to be the initial structure for the present CNT growth study and the simulation time clock was reset to 0 ps. An overview of trajectories run for this study is given in Table 1. We chose to name individual trajectories such as **Si_3000_R_0.12** which is a composed name consisting of the face type, target temperature, Si removal approach and Si removal time (the latter two quantities are explained later in the text). We have computed even more trajectories, but with less systematically, and they are therefore not list in Table 1. The Cartesian coordinates of the two initial model systems for C- and Si-face simulations are listed in the Supplementary Information.

9.3.2 CNT growth

A. Si removal and growth schemes

As of yet, it is not at all clear how Si atoms leave C atoms behind in high-temperature vacuum decomposition of SiC,24 although it is known that the higher vapor pressure of Si with respect to C is somehow related to the selective Si sublimation.[49,50] The fact that aligned CNTs can grow on the C-face in experiment[18,19,20,21,22,25,26] suggests that the Si removal follows an ordered evaporation layer by layer, otherwise perfect vertical tube alignment would not be possible. However, since nobody has analyzed the evaporated species immediately after leaving the surface, it is unknown in what chemical form the Si atoms are extracted from the SiC crystal. We found in simulations lasting several hundred picoseconds at 2000 K and 3000 K no evidence that Si atoms leave the surface by themselves or as Si_2 particles. We have also performed preliminary simulations using surface-attached oxygen atoms as well as added O_2 molecules above the SiC surfaces but could not find significant removal of Si in the form of SiO_x. Since the experiments are performed on the time scale of minutes, we decided to resort to an admittedly somewhat artificial "removal" of Si atoms to simulate sublimation, subsequently setting free carbon material required for continued tube growth. Kusunoki *et al.* have found that the height of the tip of the CNTs generated roughly corresponds to the height of the tip of the original SiC surface, and that the number of CNT sidewalls linearly corresponds to the CNT diameters.[22] Therefore they concluded that the C atoms on the surface mostly remain there instead of leaving as CO gas, and are almost exclusively used to construct the CNTs. We therefore argue that it is justified, at least in in zeroth order, to bremove Si atoms "manually" in studies of CNT growth on SiC surfaces for want of physically more realistic processes.

Figure 9.2 shows our scheme for the removal of Si atoms, which makes use of

the previously formed nanocaps on the C-face and annealed graphene layer on the Si-face, and can be summarized as two recursive steps: 1) Add one $Si_{30}C_{30}$ layer (except for the first cycle since 2 SiC layers are present in the initial structure) in bulk direction between the hydrogen-terminated "bottom" carbon or silicon layer of the SiC surface and the terminating hydrogen atoms themselves, using a distance of 1.887 Å for the new Si-C bulk bonds, followed by constant heating for 6 ps to allow for equilibration, and 2) subsequently, remove the 30 top layer Si atoms either suddenly all at once (we nickname this procedure "magic carpet" Si removal) or 30 times individually from random positions with Δt_g Si removal intervals ("random removal" of Si atoms). After the removal step the system is continuously heated for another 12 ps. In the case of "random removal", the Si removal proceeds for 30 times Δt_g, whereas in the case of "magic carpet" removal no simulation time is required for this step ($\Delta t_g = 0$ ps). Figure 9.2 displays 4 cycles but in case of "magic carpet" we have performed up to 6 removal cycles for a total simulation time of about 108 ps. Because the two "magic carpet" and "random removal" schemes of Si atom removal differ in the inclusion of annealing time during Si layer removal, we discuss the CNT growth mechanism separately for each case.

B. "Magic carpet" Si removal

If the top Si atom layer of the Si-face surface is removed at once, the original Si-face surface suddenly turns into a C-face surface, and we did observe cap nucleation in this case as described previously for the C-face.46 The fact that this would happen on what was originally a Si-face surface is obviously a consequence of the "magic carpet" removal in our simulations, but may actually occur during the surface etching employed by Nagano *et al.*[24] who actually observe CNT growth on the Si-face. Since "magic carpet" removal obviously does not allow discrimination between C-face and Si-face, we will here only describe events occurring for the C-face trajectory. The trajectory we discuss here is listed in Table 1 as **C_2000_C**. We have observed similar

events in similar magic carpet simulations but on different initial caps as well, but did not include them in Table 1 as the slab sizes and generation of the nanocaps differed slightly.

We performed the "magic carpet" CNT growth scheme at a target temperature of 2000 K for about 108 ps (6 layer addition/removal cycles including 18 ps annealing time for each), and the corresponding snapshot structures are shown in Figure 9.5. The starting structure (simulation "time clock" set to t=0) obtained above is shown as snapshot a. During the first 6 ps of the first cycle the structure displays very little structural change on the surface besides thermal vibrations, while the newly created interlayer Si-C distances equilibrate to about 1.895 Å. The cap remains stable and no significant bond changes or structural rearrangements are observable. As prescribed by the scheme explained above, at t=6 ps, we suddenly removed the top layer of 30 Si atoms (see snapshot b in Figure 9.5). This sudden removal leaves the cap and all surface carbon atoms "hanging" above the freshly exposed C-face of the SiC bulk layer. The sudden Si layer removal drives the system far from thermodynamic equilibrium, as the massive bond energy loss puts the system in a high potential energy state. We observed that some initial surface carbon atoms are lost as C_2 units, since they suddenly lost their Si bond partners. However, most unfilled valences of the two freshly cleaved surface atoms quickly combine into new bonds connecting both layers during the subsequent continued heating at 2000 K, in part facilitating short polyyne chains that are common during QM/MD simulations of high-energy forms of carbon,[33,34,35,36,37,44,51] and which are also found experimentally in high-energy-conditions derived carbon structures.[52,53,54,55,56] The cap re-attachment process actually occurs very fast; after 0.36 ps of the "magic carpet" removal, half of the cap border atoms are already connected to the freshly exposed C surface underneath. Since the cap region does not immediately attach to the SiC surface, the nanocap superstructure becomes visibly "loose" at its dangling side and starts to lose curvature due to the

tendency of the π-conjugated sheet towards planarity. The associated RMS curvature, which is the average curvature of the sp^2 hybridized atoms in the nancap as defined in Reference 38 changed from 0.188 Å^{-1} to 0.131 Å^{-1}. During the following time period, the carbon chains attached to the cap are "wobbling" at the opening of the curved superstructure, eventually creating σbonds with the unsaturated surface C atoms. The newly formed bi-connected chains form rings with the neighboring C atoms in the cap and thereby reduce the size of the defects. Such self-healing of a honeycomb graphene lattice via polyyne chains is very efficient to repair defects and has been observed in our simulations before.[33,34,35,36,37,44,51] At the end of the first cycle at t=18 ps the cap grew by almost the same distance as the removed Si layer occupied before, thereby extending the cap in vertical direction and giving the cap a more "rounder", semi-sphere appearance (see snapshot c in Figure 9.5). In this structure we find that the majority of C-Si bonds connecting the CNT to the Si layer are of zigzag type as in the initial structure.

Following the full first cycle of bulk layer addition, annealing, "magic carpet" removal, and repeated annealing described above, we added at t=18 ps a layer of SiC atoms in bulk direction following the afore-mentioned procedure, starting the second cycle. Similarly, in the first 6 ps, no major structural changes were occurring on the surface superstructure, indicating that the newly formed CNT C-C bonds perpendicular in surface direction were already in thermodynamic equilibrium after the preceding 12 ps and 6 ps continued heating steps that were interrupted only by bulk layer addition. After 6 ps (at t=24 ps), we removed for the second time all Si atoms of the top layer suddenly. As before, the dome attached partially to the SiC surface in less than 1 ps, as well as some of the C atoms that were previously part of the C-face surface atoms located inside the dome structure. Some of the former surface C atoms outside the CNT structure attached to the dome and assisted in connecting it with the atoms of the freshly exposed C-face SiC surface underneath.

As a consequence, the CNT again appeared to be stretched out at first. We noted that fresh polyyne chains formed on the ragged borders of the CNT "hovering" above the new surface, not immediately connecting to the surface and dangling above the surface. As before, several of them attached eventually to the SiC surface at the end of the 12 ps annealing period at t=36 ps, leading partially to the formation of more CNT hexagon rings by the self-healing ring-condensation mechanism described above. At the end of the second cycle (see snapshot d in Figure 9.5 at t=36 ps), still a few short polyyne chains in the dome are not attached to the surface and sidewall hexagon formation has not been completed. As a consequence, we observed several large defects at the surface/CNT interface with polyyne chains establishing surface connections rather than hexagons, thereby "dissolving" the zigzag chirality preference of the growing CNT carbon bond network around this time. We note that defect formation is not a consequence of a lack of carbon in the system, but is due to the low migration speed of freshly created C_2 molecules that are not capable to move to suitable positions along the CNT rim to assist in defect healing.

We repeated the same procedure in the following cycles a total of 5 times, and continued the simulation in this way up to 108 ps. The initial cap structure forms a clear tube structure, with length to diameter ratios progressing from 1.33 at 18 ps over 1.56 at 36 ps, 1.99 at 54 ps, 2.30 at 72 ps, 2.74 at 90 ps, to finally 3.17 at 108 ps. During each cycle, the system was observed to undergo similar patterns, as follows. During the first 6 ps after addition of the SiC bulk layer, we only observe bulk annealing with very little structural changes in the growing CNT on the "surface side". When Si atoms are then removed, freshly cleaved carbon atoms act to link to the newly exposed SiC surface or the CNT rim, which in turn assists in attaching the CNT fragment to link to the SiC surface. This linking process occurs very fast, on the order of less than 1 ps, with most covalent C-C bonds already established in this very short period. We note that this process resembles the polymerization

of C_2 molecules in high density carbon vapor,[33,34,35,36,37] where highly exothermic C-C bond formation occurs very rapidly on the order of 1 ps as well. The following approximately 11 ps simulation period constitutes mostly time to let the "wobbling" sp-carbon chains catch free C_2 molecules or attach to the CNT border, while the ends of the chains reach also the SiC surface in several cases.

We find that it is *this* stage which needs to be extended by far if one were to make a direct comparison between our "magic carpet" removal simulations and experiment, as the 12 ps time for continued heating does not seem quite long enough for defect healing. In other words, due to our very accelerated simulations, we find that the dome/tube structure only partially attaches to the surface, and that large sidewall defects are introduced because of the incomplete attachment process. After the second cycle in snapshot d (Figure 9.5, t=36 ps), there are already two rather large holes in the CNT sidewall close to the surface, which have become larger at the end of the third cycle (snapshot e, t=54 ps). In addition to this obvious defect, the CNT wall contains many 5- and 7-membered rings, which would anneal to hexagons if we were able to extend the time for annealing.38 The presence of such defects, together with the incorporation of pentagons and heptagons in the CNT sidewall, makes it impossible to distinguish whether the growing tube maintains the initial zigzag chirality of the nanocap or not.

Isolated C chains, as well as several free C_2 molecules, are seen formed during cleavage step of these high-temperature simulations, exhibiting long life-times without attaching to neither inside or outside of the tube. This observation is crucial for the CNT growth process in general. Even if temperature is very high, we find that polyyne chains are not prone to attach to the center of graphene sheets or the sidewalls of CNTs if they possess a sufficiently well-formed honeycomb lattice. The cost associated with loss of π-conjugation due to sp^3-defect formation seems too high in this case. We also note that not all "freed" surface carbon atoms are incorporated into the growing

CNT structure, and that in fact many of them become deposited to the SiC surface, which leads to a higher carbon density on the SiC surface inside the tube and becomes clearly visible after the fourth cycle. When the Si layer is then removed, these inside C atoms tend to connect to the CNT at its surface-joints, and in doing so making the diameter smaller, from 10.8 Å at the widest top position to 8.3 Å at the base, which will eventually lead to premature closure.

C. Random Si atom removal on the C-face

Although we were able to demonstrate substantial CNT growth by way of our "magic carpet" approach to Si atom removal, the rather artificial way of removing all Si atoms of the top surface layer at once ($\Delta t_g = 0$ ps) makes it hard to directly relate these simulations to experimentally observed CNT growth. Therefore, we used a second, more "gentle" removal approach, namely removing individual Si atoms of the top surface layer individually at randomly chosen positions with finite time intervals Δt_g between each removal, allowing some time for the individual defects to anneal instead of having all atoms removed instantaneously. After complete removal of the 30 surface Si atoms, we continue with 12 ps annealing as before. Although this approach is still somewhat artificial (in experiment, Si atom evaporation may only occur on a much longer time scale), it is somewhat more realistic as it avoids artificially created, very high- energetic structures with many broken bonds. One major difference of "random removal" from the "magic carpet" removal is that the C atoms inside the CNT cap are not able to move freely to the CNT rim to quickly connect and easily enlarge the surface.

The "random removal simulations" were performed using the same initial geometry as in the "magic carpet" approach, at 2000 K and 3000 K target temperatures with Δt_g of 0.024, 0.060, 0.120 and 0.240 ps, leading to a total of eight trajectories. Each removal-annealing cycle consists of the 6 ps pre-annealing before Si removal, followed by the removal time of $30\Delta t_g$ (removal of individual Si atom 30 times at

interval Δt_g) and then by the 12 ps post-annealing (see Figure 9.2); obviously simulation time of one removal cycle is $30\Delta t_g$ longer than the "magic carpet" case. We added one layer of SiC in bulk direction except for the first cycle (same as in "magic carpet" scheme), following the same afore-mentioned procedure for growth in bulk direction. Out of these eight trajectories, we will discuss as representative trajectory only events observed for **C_2000_R_0.24** with Si removal intervals Δt_g of 0.240 ps at 2000 K, and the corresponding snapshot structures from this trajectory are shown in Figure 9.6. Other trajectories follow overall similar behaviors, although some of them fail to maintain the tube structure as will be discussed below. This particular trajectory has the longest annealing time and the temperature of T_t=2000 K is closer to experiment than the T_t=3000 K simulations.

When a Si atom is removed, four carbon-silicon bonds are broken: three in the top layer, and one bond to a bulk carbon. It is common that the three adjacent top layer C atoms, having become more unstable with now two dangling bonds instead of one, move in bulk direction to attach to the unfilled valence of the carbon atom in the lower bulk SiC layer (see Figure 9.3 and an explanation further below). These inter-layer reorganization processes occur very fast ($\sim$0.2 ps). As in "magic carpet" removal it obviously sometimes happens that the removed Si atoms are important links between the cap and the SiC surface, and their removal can lead to the formation of polyyne chains instead of ring attachment to the cap sidewall. Sometimes these polyyne chains merge together to form rings during the following annealing time, but sometimes they leave defects in the cap sidewall. At the moment when all Si atoms of the top layer are finally removed, neither the shape nor the sidewall structure of the new caps are well established in any of the trajectories. In particular, the caps are not tightly connected to the SiC surface, often only on one side, and in this case as a result of the missing surface attachment, there were two large holes (see snapshot a in Figure 9.6, front and right side of the cap). During the first Si removal cycle of **C_2000_R_0.24**, we

noted that two small polyyne chains were located inside the cap, directly attached to the SiC surface. During the following 12 ps heating at 2000 K leading up to t=25.2 ps, we do not observe major restructuring: the inside carbon chains simply remained in their locations and seemed incapable to migrate further outside to heal the holes in the cap structure. This concluded the first full removal and annealing cycle.

Upon adding one layer of SiC in bulk direction at t=25.2 ps, and heated the system for 6 ps at 2000 K to continue annealing. As the cap grew longer to extend its shape and started to look closer to a nanotube, the inside chains also grew longer and started to become entangled, forming sp^2-carbon nuclei of small graphene patches. The second Si layer removal was finished at t=38.4 ps. During the following 12 ps annealing period after Si top layer removal, these chains could not migrate to the outside to "fix" the cap holes, since they were tightly connected to the lower SiC layer (see snapshot b of Figure 9.6, t=50.4 ps). At this stage we can no longer ascribe a certain tube chirality, and therefore chirality preference due to the multitude of defects created.

During the third (see snapshot c of Figure 9.6, t=75.6 ps) and fourth (see snapshot d of Figure 9.6, t=100.8 ps) cycle, the trajectory followed similar patterns as during the first two cycles described above. Only the carbon atoms immediately linked to the cap were found to contribute to the growth of the nanotube, while the carbon atoms at other positions could not insert into the CNT sidewall due to their low mobility, which is an indirect consequence of the gradual removal of Si atoms. We find that such C atoms are typically caught by the longer growing polyyne chains, and as their number increases, they become entangled and start forming small rings and more complicated sp^2-carbon structures, often leading to smaller-diameter cap creation inside the original cap. Attachment of polyyne chains to the inside of intact tube sidewalls was not seen, similar as in the case of magic carpet removal. We also found that there were some structures with a high ratio of sp^3 carbon atoms inside

and protruding outside of the tube wall. From an esthetic point of view these are rather "ugly" structures, and in chemical terms we found that the outer defective CNT and inner carbon structures merge and prevent further growth of ordered sp^2 carbon species. Amorphous carbon seems to develop at this stage. We therefore stopped our simulations after 4 removal cycles.

Similar tube growth are also observed in some of the other trajectories, such as **C_3000_R_0.024** at 3000 K temperature and with Si removal interval Δt_g of 0.024 ps (see snapshot a in Figure 9.7). However, there were also other trajectories that failed to maintain the tube structure after the fourth cycle of Si removal. For example, in **C_2000_R_0.12** at 2000 K with Δt_g of 0.12 ps, we observed some growth in the direction perpendicular to the surface, but only half of the tube was connected to the surface (see snapshot b in Figure 9.7), which indicates insufficient annealing time during growth to eliminate the large defects, and similar structural failure patterns were found in the trajectories obtained in **C_2000_R_0.024**, **C_3000_R_0.06**, **C_3000_R_0.06**, and **C_3000_R_0.24**. We note that common to these trajectories is the very short annealing time, or higher temperature. Despite these failures, noticeable perpendicular growth of carbon cluster was observed in all cases, although fast removal rates seem to introduce a greater number of defects and therefore can severely interfere with perpendicular tube growth. Understanding how and on what time scale the Si atoms leave would be crucial for understanding the growth of more regular CNTs, but this is computationally extremely difficult, and on the other hand even in experiment the tubes created exhibit a high degree of defects as visible in very high Raman D/G band intensity ratios.[28]

D. Random Si atom removal on the Si-face

To compare the random removal between C face and Si face, we also ran several trajectories with different time intervals of Si removal Δt_g on the Si-face. The initial structures were obtained in a similar way as the C-face trajectories, using the same

size of SiC slab and types and size of the graphene sheet, but this time on the Si-face. The target temperatures T_t were also set to 2000 K and 3000 K, and the time intervals for the Si removal Δt_g were also chosen to be 0.024, 0.060, 0.120 and 0.240 ps to achieve comparability with the corresponding simulations on the C-face. We found that the random Si atom removal from the Si-face is very different from the one on the C-face described above, as can be seen in Figure 9.8, where we show initial structure (a) and the final structures obtained after random removal of the top Si layer at the end of the first cycle under three different conditions as (b) to (d). Structure (b) for instance depicts a structure obtained in **Si_2000_R_0.24** at 2000 K with Δt_g=0.240 ps time interval at elapsed time t=25.2 ps, and we will describe typical events occurring during random Si removal in more detail in the following paragraph.

Before removal, the graphene sheet hovering above the Si face is rather planar. When a Si atom is removed, the three C atoms, which were linked to it in the same SiC layer, obviously lose their neighboring binding partner (see Figure 9.3). However, in this case each affected carbon atom is left with only one dangling bond rather than two in the case of the C face Si-removal, and of course no dangling bond is created in the bulk layer below. We find that the three-valent carbon atoms of the Si face remain more or less at the same positions shortly after the removal and can create new bonds with each other in the same layer. If one more Si atom is removed in the vicinity of the destabilized carbon atoms, the affected C atoms become more mobile, connecting with each other rather than with the upper graphene sheet, which is still kept at distance by longer Si-C bonds in other positions. Consequently, any potential bond formation between graphene sheet and gradually exposed carbon surface was very slow. When all the Si atoms were removed, there were only few polyyne chains formed on the SiC surface, as most carbons of that layer were already connected by an sp^2-carbon graphene network. Moreover, these newly formed graphene sheets do

not contact well with the SiC surface underneath, as was the case with the original graphene sheet. Thus, a double-graphene-layer is typically established, "sitting" on top of a new Si-face surface. We therefore decided not to continue these Si-face trajectories after the removal of the first layer of Si atoms.

Similar feature of the final structures can be observed under simulations with a 0.12 ps time interval (structure (c)) or at 3000 K target temperature (d), which indicates that the Si face is intrinsically difficult for nanotube growth. This result is consistent with experimental observation that there is no perpendicular tube growth on the Si face but the accumulation of planar graphitic layers.20 In our case, the sheets have almost no curvature, but exhibit several wobbling C chains pointing upward. In general, removing only one Si atom in a relatively Si rich region does not effect the surface very much. In particular, the upper graphene sheet cannot effectively make contact with the lower C atoms to form bonds because the remaining Si atoms prevent this from happening by blocking the connection pathway. As more and more Si atoms are removed, the C atoms in the SiC layer become more mobile and form readily polyyne chains directly on the SiC surface underneath, forming a second graphite layer below the top graphene sheet and the gradually evaporating Si layer.

E. CNT ring and length statistics of individual trajectories

We have analyzed the time evolution of the number of 5-, 6-, and 7-membered rings and tube length for two trajectories we have discussed above, namely a) the trajectory with "magic carpet" Si removal, and b) for the trajectory with random Si removal on c face at temperature of 2000K and Δt_g of 0.024 ps. Figures 9.9(a) and 9.9(b) show numbers of 5-, 6-, and 7-membered rings, while Figures 9.10(a) and 9.10(b) show the tube lengths as defined by the largest distance from the upper carbon structure to the bulk-side lowest SiC layer.

As for the number of rings (Figure 9.9(a)) for the "magic carpet" model, we can see that all types of rings increase as the simulation time increases, which indicates

that the tube does grow according to this Si removal scheme. The 6-membered rings are always most abundant during simulation, while the 5-membered rings are less and the 7-membered rings are the least abundant. The existence of the 5-membered rings and 7-membered rings suggests the irregularity of the tube as their numbers should remain steady as cap features (5-membered rings) or 0 (7-membered rings) if perfect CNTs were grown. As the tube grows longer, the ratio of the 6-membered rings to the 5, and 7-membered rings becomes smaller, which means that the tube becomes even more irregular. This phenomenon was qualitatively described above and reflects the fact that large defects appear over time, which grow larger. The tube length statistics for "magic carpet" removal (Figure 9.10(a)) also indicates that there is a substantial tube growth as it grows from about 6 Å to about 16 Å. The final tube structure has an average diameter of approximately 1.0 nm, and length/diameter ratio of 1.6, and consists of roughly 200 carbon atoms. Because one layer of SiC is added at the beginning of each cycle, there is a sudden jump of the tube length at this time. After the removal of the top Si layer in each cycle, the tube attempts to attach back to the surface by connecting to the free carbon atoms and the freshly exposed surface below. However, not all the free C atoms are incorporated and the tube moves therefore down a little bit, which leads to a small contraction of the tube length each time after the removal. For the random Si removal model, Figure 9.9(b) shows the time evolution of the 5-, 6-, and 7-membered rings. Similar to the sudden removal, the increase in the number of all types of rings indicates growth of tube under this scheme, although the rate of increase is visibly slower here. Of course, the number of bulk-addition and Si-layer removal cycles is smaller with 4 instead of 6 in the case of the "magic carpet" cycle, due to the time spent for individual Si atom removal and annealing Δt_g of 0.024 ps. Unsurprisingly, the 6-membered rings are also most abundant all the time during this simulation. However, the 5-, and 7-membered rings have a much larger ratio to 6-membered rings compared to the

sudden removal scheme, which indicates that the tube grown under this scheme is even more irregular than grown under the sudden removal scheme. Figure 9.10(b) shows the time evolution of tube length. It has similar features to the one from the sudden removal scheme, namely the sudden jump of the tube length at the beginning of each cycle when one layer of SiC is added, followed by subsequent contraction due to the removal of Si atoms. Since the Si atoms are removed one by one randomly, the C atoms left by the Si atoms are not as mobile as in the case of the sudden removal scheme, and therefore cannot become incorporated into the tube so efficiently. In this case, the tube length contraction is larger than in the sudden removal case, and the tube is not grown as well, as was discussed qualitatively above. However, it still grows substantially from about 6 Å to about 11 Å after 4 cycles, at which stage the "magic carpet" tube had grown already to a length of 13 Å. The carbon obviously missing from the tube was used for the construction of the inner half-tube and an amorphous carbon layer around the tube base.

9.4 Summary and Conclusions

In summary, we have studied the time evolution of SiC (000-1) surfaces under sublimation decomposition on both C- and Si-face types of surfaces. As we already had reported before, small nanocaps can nucleate on the C-face while planar graphene layers are observed on the Si-face, due to the differences in the energy of the C-C and Si-C bonds.46 Following nanocap formation, substantial perpendicular nanotube growth was observed on the C-face, both during sudden removal ("magic carpet" removal) and random removal schemes for the modeling of the Si evaporation process. On the contrary, the Si-face was demonstrated to be incapable for nanocap nucleation and subsequent perpendicular nanotube growth. If "magic carpet" removal is applied to the Si-face, the surface is de facto converted into a C-face, and cap nucleation becomes possible. If "random removal" of Si atoms is applied to the Si-face, we observe

the formation of a graphitic sheet underneath the gradually evaporating Si layer due to the absence of reactive centers below the C-layer. The difference in both removal approaches merely reflects the difference in annealing time in between disappearance of Si atoms. The factors influencing the perpendicular CNT growth on the C-face and multi-layer graphite formation on the Si-face can be summarized as follows:

1.) CNT caps only nucleate on the C-face due to the two antagonistic forces attempting to form a balance: formation of strong C-C bonds between top-layer graphene and dangling C surface valences on one hand, and the resistance of the planar sp^2 graphene sheet under vacuum conditions to form sp^3 bonds throughout to form a nanodiamond, leading to a bent sp^2 cap structure instead as discussed previously.46

2.) The presence of surfaces with dangling bonds prevents the formation of giant fullerenes after cap formation on the C-face, a mechanism which is probably similar to root- or tip-growth in case of metal-catalyzed SWCNTs, only here the surface is mostly solid and therefore allows the chirality specific synthesis of zigzag tubes. The chirality preference is lost due to increased sidewall defect formation at the high Si removal ("evaporation") rates we were forced to adopt due to our inability to simulate on nanosecond or microsecond time scales.

3.) For rather obvious geometric reasons, Si atom removal on the C-face leads to more unstable carbon species than on the Si-face: four versus three carbon atoms with dangling bonds are left after Si atom removal, and three of these carbon atoms are only two- versus three-coordinated. Moreover, Si removal on the C-face creates a reactive center in the layer below, thereby enabling linkage between different layers of carbon (see Figure 9.3) and perpendicular growth of carbon structures. On the other hand, the dangling bonds of the C atoms created in the case of the Si-face are protected by the Si atoms above them against attack by the graphite sheet hovering above the surface. They are all located in the same carbon layer and in this case start

to form a new graphite sheet parallel to the surface.

4.) Layer-wise Si removal ("evaporation") facilitates the formation of SWCNT formation as the freed carbon atoms can readily move to the relatively stable tube sidewalls, while slower random removal of Si surface atoms leads to MWCNT formation due to the reduced mobility of the "liberated" C atoms. Amorphous carbon built-up can also be observed which may be related to termination of tube growth at the end of the Si evaporation process.

The tubes grown according to both Si removal schemes on the C-face are not perfect at all, containing many 5-, 7-, and even 8-membered rings, as well as several large hole defects. In experiment, it is found that the CNT crystallinity and alignment suffers with increasing decomposition rate, which is consistent with our simulations producing very defective tubes with very fast removal rates due to computational requirements. Indeed, the tubes were found to grow to slightly better sidewall quality with longer annealing times.

In conclusion, our QM/MD simulations using Si atom removal as means to model Si evaporation provide clear explanation for the different carbon growth modes on C- and Si-faces of SiC at the atomic level, namely graphene sheet formation on the Si-face and perpendicular nanotube growth on the C-face.

References

1. IIJIMA, S. *NATURE* **1991**, *354*, 56–58.

2. IIJIMA, S.; ICHIHASHI, T. *NATURE* **1993**, *363*, 603–605.

3. BETHUNE, D.; KIANG, C.; DEVRIES, M.; GORMAN, G.; SAVOY, R.; VAZQUEZ, J.; BEYERS, R. *NATURE* **1993**, *363*, 605–607.

4. Thess, A.; Lee, R.; Nikolaev, P.; Dai, H.; Petit, P.; Robert, J.; Xu, C.; Lee, Y.; Kim, S.; Rinzler, A.; Colbert, D.; Scuseria, G.; Tomanek, D.; Fischer, J.; Smalley, R. *SCIENCE* **1996**, *273*, 483–487.

5. Terrones, M.; Grobert, N.; Olivares, J.; Zhang, J.; Terrones, H.; Kordatos, K.; Hsu, W.; Hare, J.; Townsend, P.; Prassides, K.; Cheetham, A.; Kroto, H.; Walton, D. *NATURE* **1997**, *388*, 52–55.

6. Li, W.; Xie, S.; Qian, L.; Chang, B.; Zou, B.; Zhou, W.; Zhao, R.; Wang, G. *SCIENCE* **1996**, *274*, 1701–1703.

7. Ren, Z.; Huang, Z.; Xu, J.; Wang, J.; Bush, P.; Siegal, M.; Provencio, P. *SCIENCE* **1998**, *282*, 1105–1107.

8. Fan, S.; Chapline, M.; Franklin, N.; Tombler, T.; Cassell, A.; Dai, H. *SCIENCE* **1999**, *283*, 512–514.

9. Harris, P. J. F. *CARBON* **2007**, *45*, 229–239.

10. Journet, C.; Bernier, P. *APPLIED PHYSICS A-MATERIALS SCIENCE & PROCESSING* **1998**, *67*, 1–9.

11. Jost, O.; Gorbunov, A.; Moller, J.; Pompe, W.; Liu, X.; Georgi, P.; Dunsch, L.; Golden, M.; Fink, J. *JOURNAL OF PHYSICAL CHEMISTRY B* **2002**, *106*, 2875–2883.

12. Delpeux, S.; Szostak, K.; Frackowiak, E.; Bonnamy, S.; Beguin, F. *JOURNAL OF NANOSCIENCE AND NANOTECHNOLOGY* **2002**, *2*, 481–484.

13. Nagatsu, M.; Yoshida, T.; Mesko, M.; Ogino, A.; Matsuda, T.; Tanaka, T.; Tatsuoka, H.; Murakami, K. *CARBON* **2006**, *44*, 3336–3341.

14. Rinzler, A.; Liu, J.; Dai, H.; Nikolaev, P.; Huffman, C.; Rodriguez-Macias, F.; Boul, P.; Lu, A.; Heymann, D.; Colbert, D.; Lee, R.; Fischer, J.; Rao, A.; Eklund, P.; Smalley, R. *APPLIED PHYSICS A-MATERIALS SCIENCE & PROCESSING* **1998**, *67*, 29–37.

15. Itkis, M.; Perea, D.; Jung, R.; Niyogi, S.; Haddon, R. *JOURNAL OF THE AMERICAN CHEMICAL SOCIETY* **2005**, *127*, 3439–3448.

16. SAITO, R.; FUJITA, M.; DRESSELHAUS, G.; DRESSELHAUS, M. *APPLIED PHYSICS LETTERS* **1992**, *60*, 2204–2206.

17. WHITE, C.; ROBERTSON, D.; MINTMIRE, J. *PHYSICAL REVIEW B* **1993**, *47*, 5485–5488.

18. Kusunoki, M.; Rokkaku, M.; Suzuki, T. *APPLIED PHYSICS LETTERS* **1997**, *71*, 2620–2622.

19. Kusunoki, M.; Suzuki, T.; Kaneko, K.; Ito, M. *PHILOSOPHICAL MAGAZINE LETTERS* **1999**, *79*, 153–161.

20. Kusunoki, M.; Suzuki, T.; Hirayama, T.; Shibata, N.; Kaneko, K. *APPLIED PHYSICS LETTERS* **2000**, *77*, 531–533.

21. Kusunoki, M.; Suzuki, T.; Honjo, C.; Hirayama, T.; Shibata, N. *CHEMICAL PHYSICS LETTERS* **2002**, *366*, 458–462.

22. Kusunoki, M.; Honjo, C.; Suzuki, T.; Hirayama, T. *APPLIED PHYSICS LETTERS* **2005**, *87*, 103105.

23. Derycke, V.; Martel, R.; Radosvljevic, M.; Ross, F.; Avouris, P. *NANO LETTERS* **2002**, *2*, 1043–1046.

24. Nagano, T.; Ishikawa, Y.; Shibata, N. *JAPANESE JOURNAL OF APPLIED PHYSICS PART 1-REGULAR PAPERS SHORT NOTES & REVIEW PAPERS* **2003**, *42*, 1380–1385.

25. Maruyama, T.; Bang, H.; Kawamura, Y.; Fujita, N.; Tanioku, K.; Shiraiwa, T.; Hozumi, Y.; Naritsuka, S.; Kusunoki, M. *CHEMICAL PHYSICS LETTERS* **2006**, *423*, 317–320.

26. Bang, H.; Ito, Y.; Kawamura, Y.; Hosoda, E.; Yoshida, C.; Maruyama, T.; Naritsuka, S.; Kusunoki, M. *JAPANESE JOURNAL OF APPLIED PHYSICS PART 1-REGULAR PAPERS BRIEF COMMUNICATIONS & REVIEW PAPERS* **2006**, *45*, 372–374.

27. Botti, S.; Asilyan, L.; Ciardi, R.; Fabbri, F.; Loreti, S.; Santoni, A.; Orlanducci, S. *CHEMICAL PHYSICS LETTERS* **2004**, *396*, 1–5.

28. Botti, S.; Ciardi, R.; Asilyan, L.; De Dominicis, L.; Fabbri, F.; Orlanducci, S.; Fiori, A. *CHEMICAL PHYSICS LETTERS* **2004**, *400*, 264–267.

29. Konishi, H.; Matsuoka, H.; Toyama, N.; Naitoh, M.; Nishigaki, S.; Kusunoki, M. *THIN SOLID FILMS* **2004**, *464-65*, 295–298.

30. VANBOMMEL, A.; CROMBEEN, J.; VANTOOREN, A. *SURFACE SCIENCE* **1975**, *48*, 463–472.

31. Hass, J.; Feng, R.; Li, T.; Li, X.; Zong, Z.; de Heer, W. A.; First, P. N.; Conrad, E. H.; Jeffrey, C. A.; Berger, C. *APPLIED PHYSICS LETTERS* **2006**, *89*, 143106.

32. Gogotsi, V., Y. Kamyshenko; Shevchenko, V.; Welz, S.; Ersoy, D.; McNallan, M. **2001**, , 239–255.

33. Irle, S.; Zheng, G.; Elstner, M.; Morokuma, K. *NANO LETTERS* **2003**, *3*, 1657–1664.

34. Irle, S.; Zheng, G.; Elstner, M.; Morokuma, K. *Theory-experiment relationship of the "shrinking hot giant" road of dynamic fullerene self-assembly in hot carbon vapor*; Elsevier: New York, 2005.

35. Zheng, G.; Irle, S.; Morokuma, K. *JOURNAL OF CHEMICAL PHYSICS* **2005**, *122*, 014708.

36. Irle, S.; Zheng, G.; Wang, Z.; Morokuma, K. *JOURNAL OF PHYSICAL CHEMISTRY B* **2006**, *110*, 14531–14545.

37. Irle, S.; Zheng, G.; Wang, Z.; Morokuma, K. *NANO* **2007**, *2*, 21–30.

38. BRENNER, D. *PHYSICAL REVIEW B* **1990**, *42*, 9458–9471.

39. BRENNER, D. *PHYSICAL REVIEW B* **1992**, *46*, 1948.

40. POREZAG, D.; FRAUENHEIM, T.; KOHLER, T.; SEIFERT, G.; KASCHNER, R. *PHYSICAL REVIEW B* **1995**, *51*, 12947–12957.

41. Elstner, M.; Porezag, D.; Jungnickel, G.; Elsner, J.; Haugk, M.; Frauenheim, T.; Suhai, S.; Seifert, G. *PHYSICAL REVIEW B* **1998**, *58*, 7260–7268.

42. Frauenheim, T.; Seifert, G.; Elstner, M.; Hajnal, Z.; Jungnickel, G.; Porezag, D.; Suhai, S.; Scholz, R. *PHYSICA STATUS SOLIDI B-BASIC SOLID STATE PHYSICS* **2000**, *217*, 41–62.

43. Frauenheim, T.; Seifert, G.; Elstner, M.; Niehaus, T.; Kohler, C.; Amkreutz, M.; Sternberg, M.; Hajnal, Z.; Di Carlo, A.; Suhai, S. *JOURNAL OF PHYSICS-CONDENSED MATTER* **2002**, *14*, 3015–3047.

44. Zheng, G.; Irle, S.; Elstner, M.; Morokuma, K. *JOURNAL OF PHYSICAL CHEMISTRY A* **2004**, *108*, 3182–3194.

45. Irle, S.; Wang, Z.; Zheng, G.; Morokuma, K.; Kusunoki, M. *JOURNAL OF CHEMICAL PHYSICS* **2006**, *125*, 044702.

46. FRAUENHEIM, T.; WEICH, F.; KOHLER, T.; UHLMANN, S.; POREZAG, D.; SEIFERT, G. *PHYSICAL REVIEW B* **1995**, *52*, 11492–11501.

47. Gutierrez, R.; Frauenheim, T.; Kohler, T.; Seifert, G. *JOURNAL OF MATERIALS CHEMISTRY* **1996**, *6*, 1657–1663.

48. Zheng, G.; Irle, S.; Morokuma, K. *CHEMICAL PHYSICS LETTERS* **2005**, *412*, 210–216.

49. Forbeaux, I.; Themlin, J.; Charrier, A.; Thibaudau, F.; Debever, J. *APPLIED SURFACE SCIENCE* **2000**, *162*, 406–412.

50. Charrier, A.; Coati, A.; Argunova, T.; Thibaudau, F.; Garreau, Y.; Pinchaux, R.; Forbeaux, I.; Debever, J.; Sauvage-Simkin, M.; Themlin, J. *JOURNAL OF APPLIED PHYSICS* **2002**, *92*, 2479–2484.

51. Irle, S.; Zheng, G.; Elstner, M.; Morokuma, K. *NANO LETTERS* **2003**, *3*, 465–470.

52. WHITTAKER, A. *SCIENCE* **1978**, *200*, 763–764.

53. Li, S.; Zhou, H.; Gu, J.; Zhu, J. *CARBON* **2000**, *38*, 934–937.

54. Lamperti, A.; Ossi, P. *CHEMICAL PHYSICS LETTERS* **2003**, *376*, 662–665.

55. Zhao, X.; Ando, Y.; Liu, Y.; Jinno, M.; Suzuki, T. *PHYSICAL REVIEW LETTERS* **2003**, *90*, 187401.

56. Ravagnan, L.; Bongiorno, G.; Bandiera, D.; Salis, E.; Piseri, P.; Milani, P.; Lenardi, C.; Coreno, M.; de Simone, M.; Prince, K. C. *CARBON* **2006**, *44*, 1518–1524.

Table 9.1: Overview of Trajectories in This Study[a].

name	face	temperature	removal scheme	Δt_R[ps]	# cycles	initial coordinates
C_2000_C	C	2000	magic carpet	0.000	6	C face model
C_2000_R_0.024	C	2000	random removal	0.024	4	C face model
C_2000_R_0.06	C	2000	random removal	0.060	4	C face model
C_2000_R_0.12	C	2000	random removal	0.120	4	C face model
C_2000_R_0.24	C	2000	random removal	0.240	4	C face model
C_3000_R_0.024	C	3000	random removal	0.024	4	C face model
C_3000_R_0.06	C	3000	random removal	0.060	4	C face model
C_3000_R_0.12	C	3000	random removal	0.120	4	C face model
C_3000_R_0.24	C	3000	random removal	0.240	4	C face model
Si_2000_R_0.024	Si	2000	random removal	0.024	1	Si face model
Si_2000_R_0.06	Si	2000	random removal	0.060	1	Si face model
Si_2000_R_0.12	Si	2000	random removal	0.120	1	Si face model
Si_2000_R_0.24	Si	2000	random removal	0.240	1	Si face model
Si_3000_R_0.024	Si	3000	random removal	0.024	1	Si face model
Si_3000_R_0.06	Si	3000	random removal	0.060	1	Si face model
Si_3000_R_0.12	Si	3000	random removal	0.120	1	Si face model
Si_3000_R_0.24	Si	3000	random removal	0.240	1	Si face model

[a] Δt_g is the time for individual Si atom removal as explained in text. The column "# cycles" indicates the number of cycles according to Figure 9.2. Initial coordinates correspond to the C and Si face models with Cartesian coordinates listed in Supporting Information.

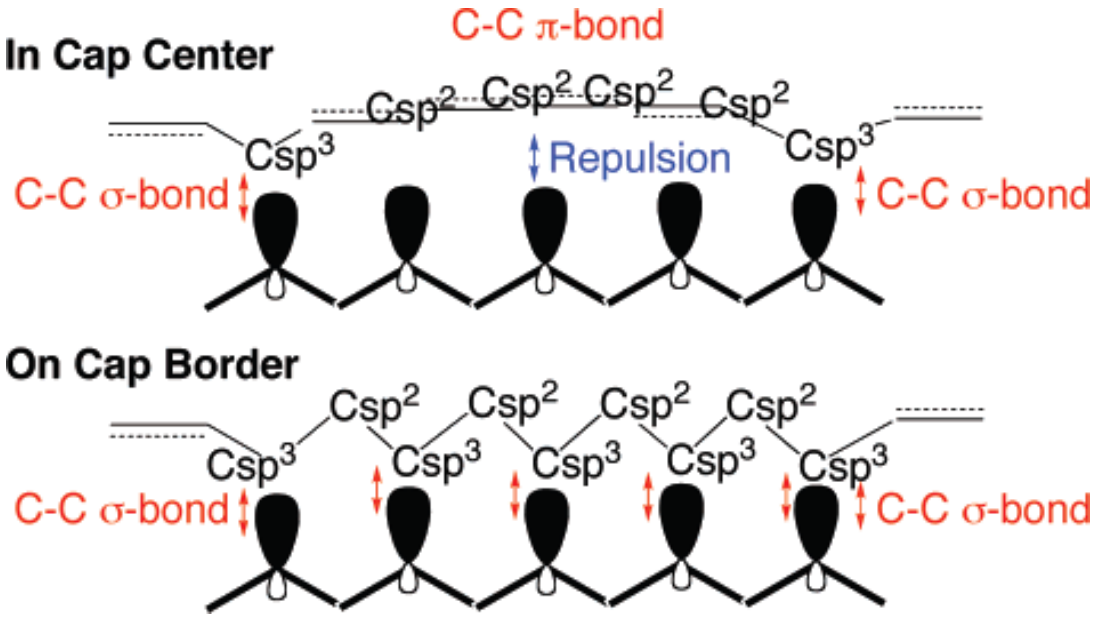

Figure 9.1: In Schematic Cuttings through the Cap Center (top) and along the Cap Border (below), Interactions Are Shown Leading to Nanocap Formation on the C Face of SiC during Vacuum Decomposition[a].

[a] Antagonist forces due to C-C σ-bond formation and persistence of C-C π-bonds, resulting in repulsion in the cap center that is responsible for the cap formation.

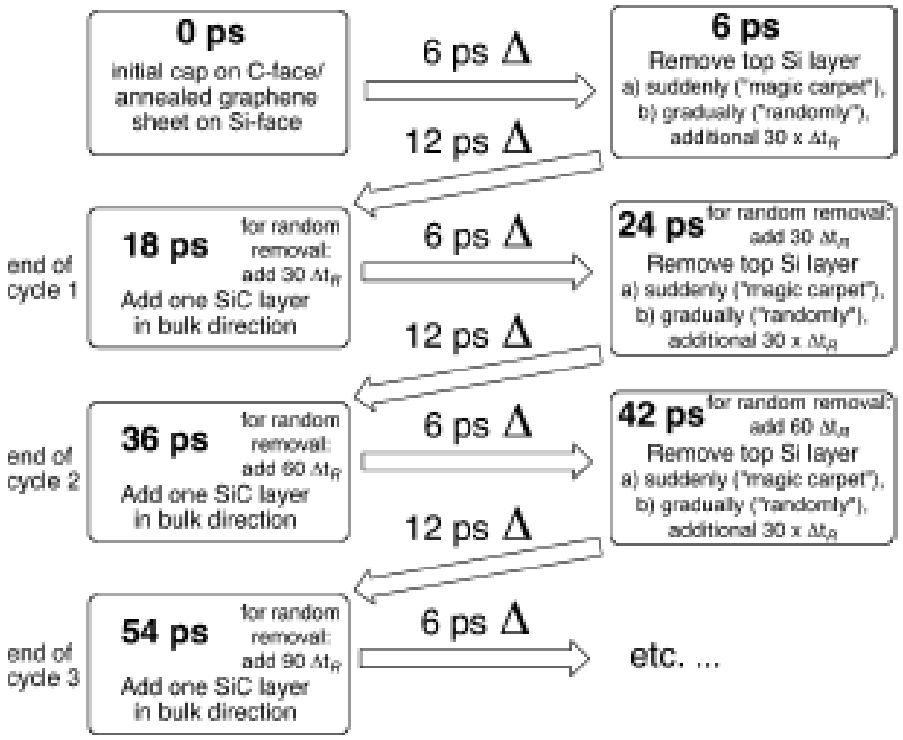

Figure 9.2: Steps during Si Atom Removal with Simulation "Time Clock" for Both "Magic Carpet" and "Random Removal" Approaches.

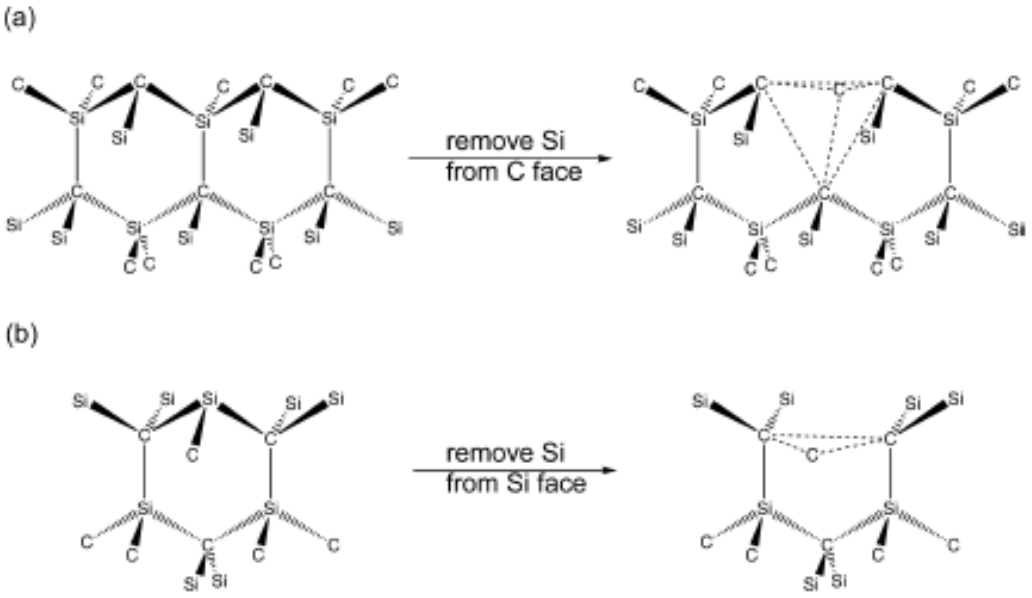

Figure 9.3: Si Removal from SiC Slab on the (a) C face Leads to Three Two-Coordinated Surface Carbon Atoms and a Total of Four Carbon Atoms with Dangling Bonds Including One Bulk Layer Carbon Atom, while Si from the SiC Slab on the (b) Si Face Leads to Three Carbon Atoms with Dangling Bonds Located in the Same Subsurface Layer.

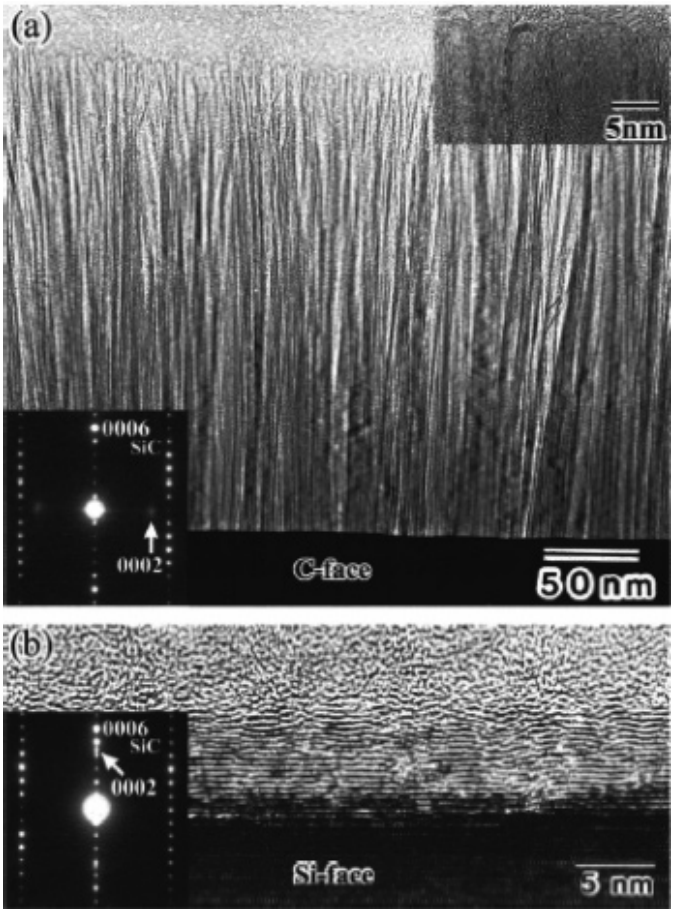

Figure 9.4: Cross-sectional HREM images and the diffraction patterns of the surface of SiC single-crystal wafers heated to 1700 °C for half an hour, on (a) the C and (b) the Si faces from ref.[20]

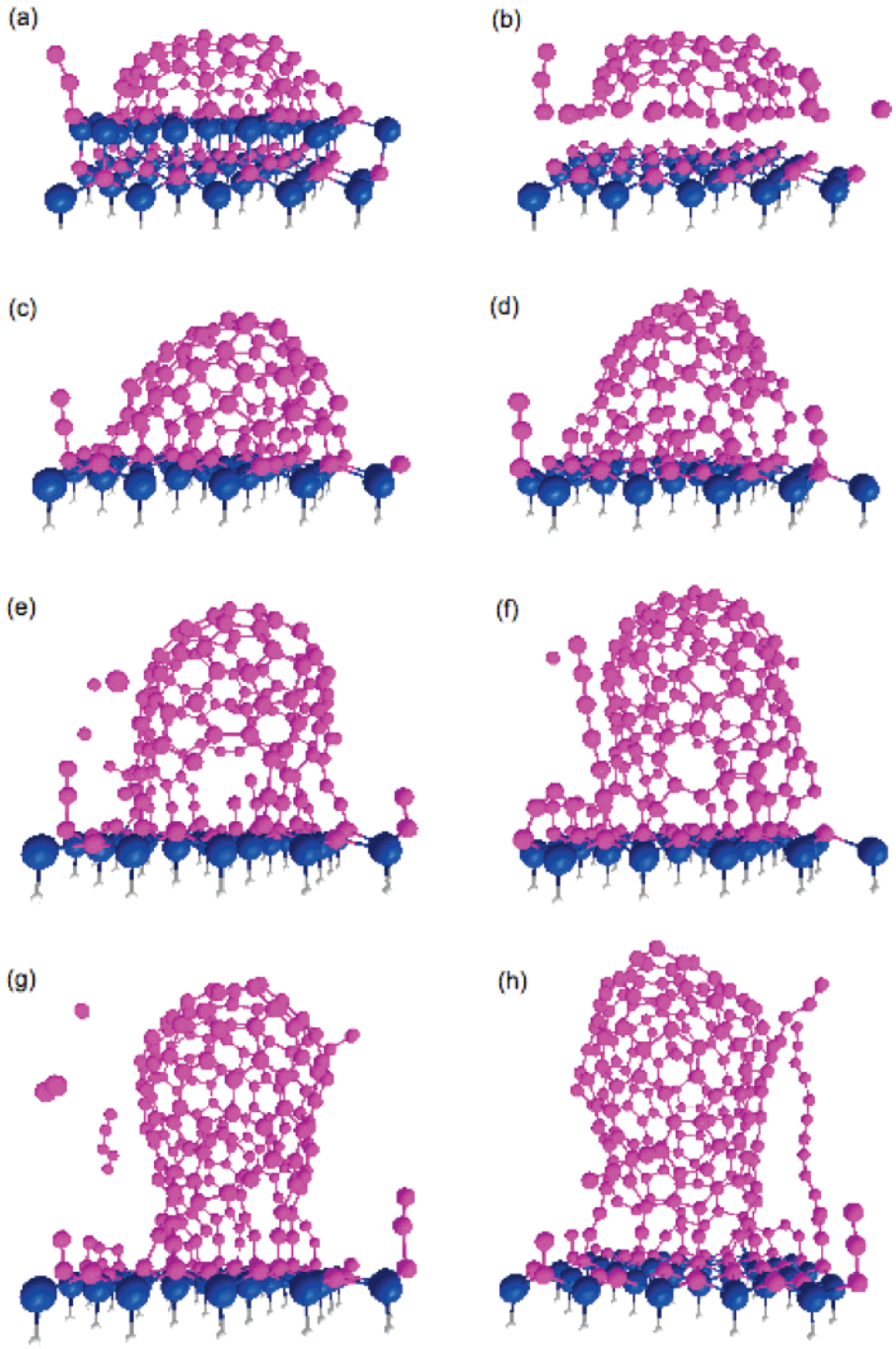

Figure 9.5: Removal of top Si surface layers suddenly ("magic carpet" Si removal) at T_t = 2000 K. Blue color represents Si atoms, purple color represents C atoms. (a) Initial structure; (b) suddenly remove top layer of Si atoms at 6 ps; (c) the structure after 12 ps annealing at the end of first removal cycle (18 ps); (d-h) the end structures after the second (36 ps), third (54 ps), fourth (72 ps), fifth (90 ps), and sixth (108 ps) removal cycles.

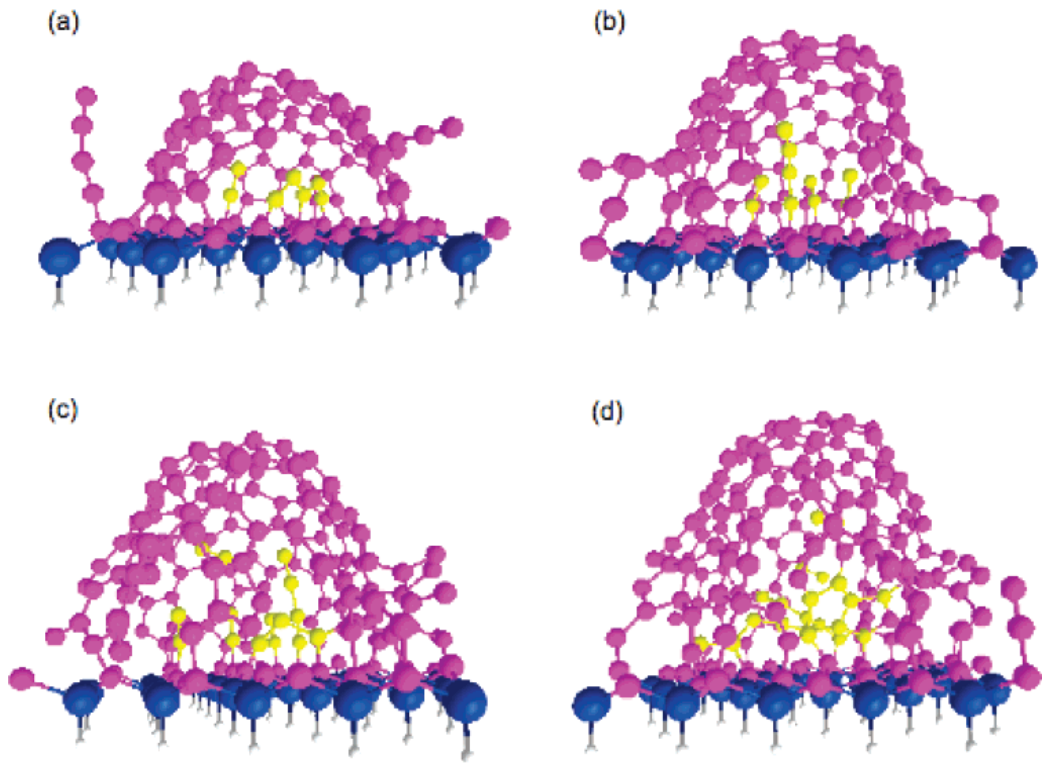

Figure 9.6: Random removal of Si atoms with $\Delta t_g = 0.24$ ps at $T_t = 2000$ K, here in case of the C face. Blue color represents Si atoms, purple color represents C atoms, yellow color represents inside C atoms. See text for details of the random removal procedure. (a), (b), (c), and (d) are snapshots of the end structures after the first (25.2 ps), second (50.4 ps), third (75.6 ps) and fourth (100.8 ps) cycle.

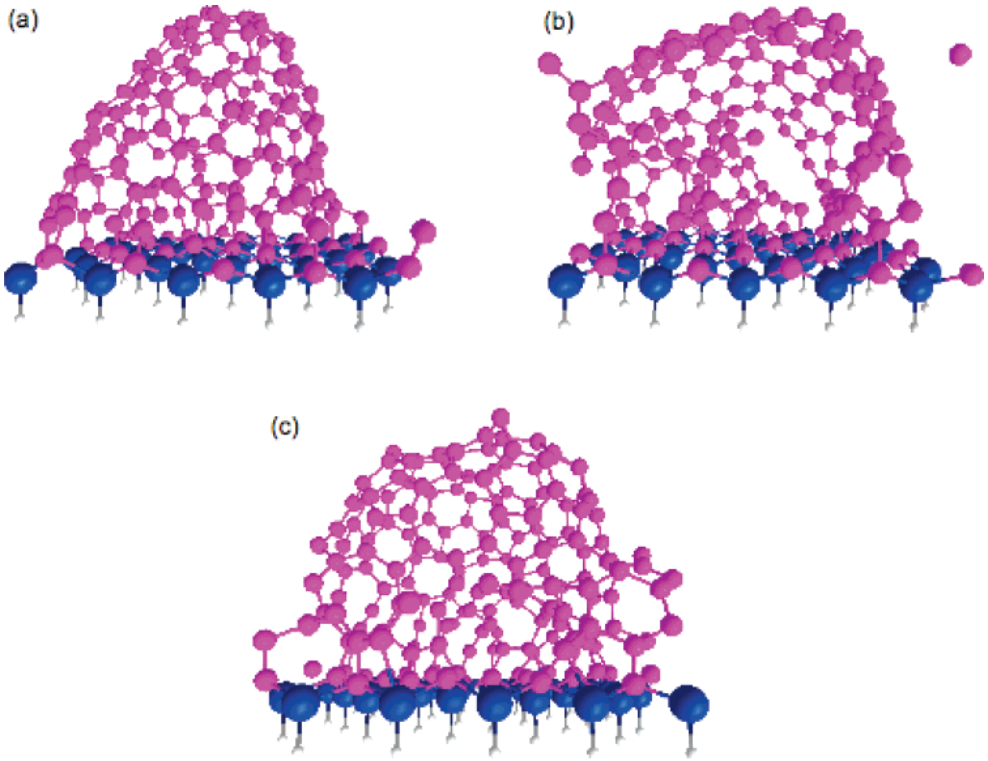

Figure 9.7: End snapshots obtained at the end of the fourth removal cycle of selected trajectories with random removal of Si atoms using different time intervals and temperatures, here in case of the C face. Blue color represents Si atoms, purple color represents C atoms. (a) $\Delta t_g = 0.024$ ps, elapsed time is $t = 74.9$ ps, $T_t = 3000$ K; (b) $\Delta t_g = 0.12$ ps, elapsed time is $t = 86.4$ ps, $T_t = 2000$ K; (c) $\Delta t_g = 0.06$ ps, elapsed time is $t = 79.2$ ps, $T_t = 2000$ K.

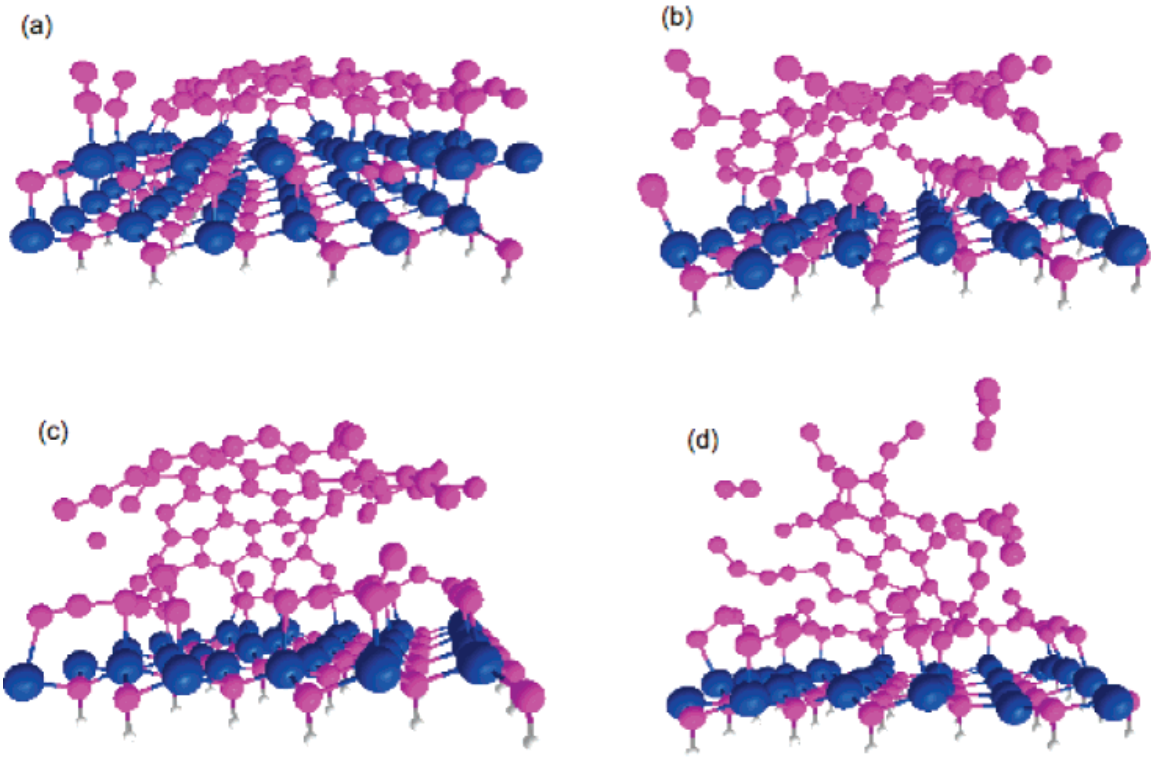

Figure 9.8: End snapshots obtained at the end of the first removal cycle of selected trajectories with random removal of Si atoms using different time intervals and temperatures, here in case of the Si face. Blue color represents Si atoms, purple color represents C atoms. (a) initial structure at $t = 0$ ps; (b-d): stuctures obtained after removal of the surface Si layer: (b) $\Delta t_g = 0.24$ ps, elapsed time $t = 25.2$ ps, $T_t = 2000$ K; (c) $\Delta t_g = 0.12$ ps, elapsed time $t = 21.6$ ps, $T_t = 2000$ K; (d) $\Delta t_g = 0.24$ ps, elapsed time $t = 25.2$ ps, $T_t = 3000$ K.

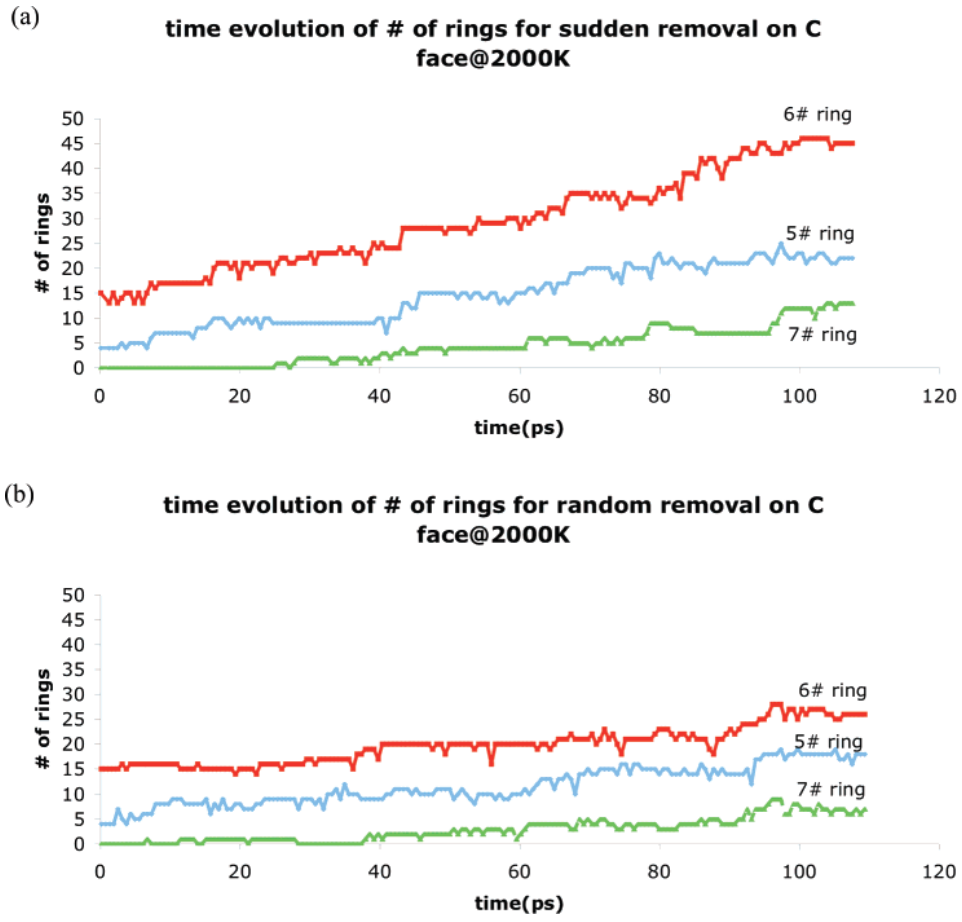

Figure 9.9: Time evolution of the number of 5-, 6-, and 7-membered rings as the CNT growth on C face at T_t = 2000 K. (a) sudden removal ("magic carpet"); (b) random removal, trajectory **C_2000_R_0.24**.

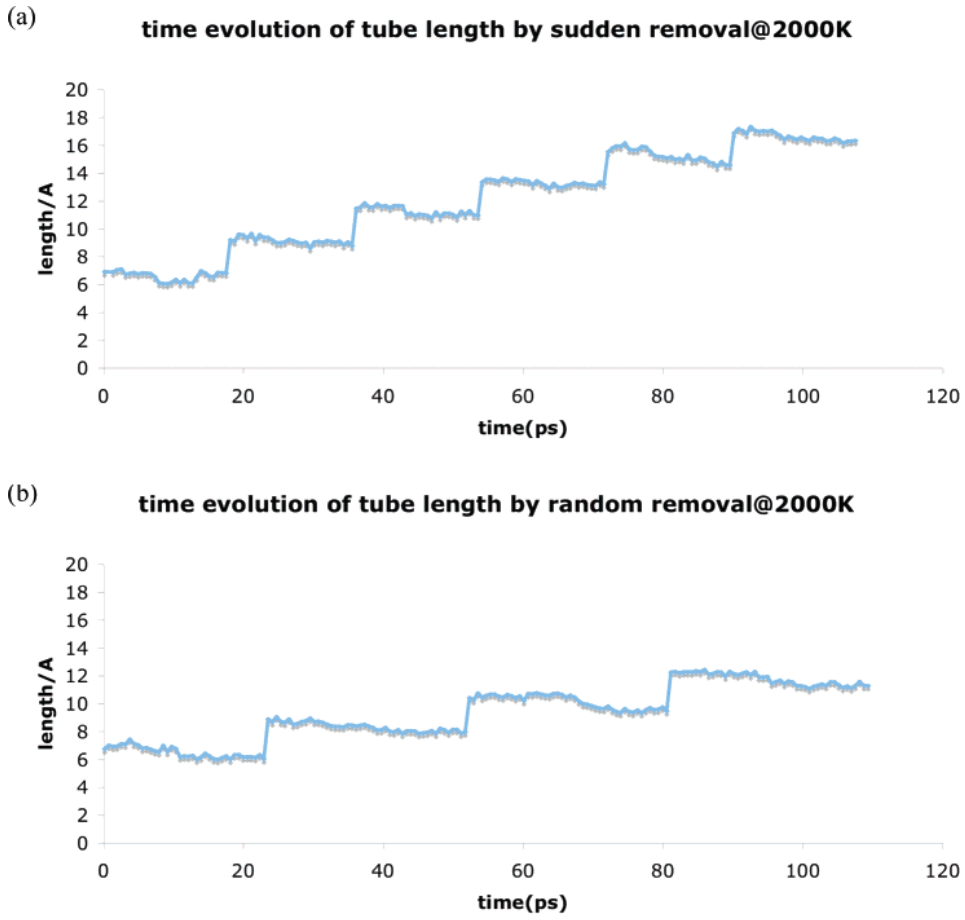

Figure 9.10: Time evolution of the tube length as measure for CNT growth on the C face at T_t = 2000 K. (a) sudden removal ("magic carpet"); (b) random removal, trajectory **C_2000_R_0.24**.

Chapter 10. Graphene growth during sublimation decomposition of SiC: A Quantum Chemical Molecular Dynamics Investigation

10.1 Introduction

Among many allotropes of carbon, graphites and carbon nanotubes (CNTs) are the two which are related in the sense that CNTs could be viewed as the warp up of grephene sheets. Both of them are made of carbon hexagonal network but graphite is planar while CNTs experience a curvature due to the warp up. In these two decades, CNTs are undoubted the most famous allotrope that arise great interests among researchers due to their superior electronic and mechanic properties. These unique properties have potential applications at nanoscale device designs and could change the current techniques dramatically. However, as a well-known carbon allotrope for long time, graphite, could also obtain these superior properties at the nanoscale dimension.[1]

It is interesting that under certain conditions, both nanotubes and graphite could be produced from SiC. Forbeaux and Charrier showed that graphite films can be grown on Si face by sublimating Si from SiC during heating above 1200 °C in ultrahigh vacuum UHV.[2,3,4] Conrad and coworkers reported that graphene could also grow on C face from the Si sublimation, with better quality than the one grown on Si face.[5] Kuzunoki et al found that CNTs are preferentially grown on C face perpendicular to the (0001) surface, while graphite layers are grown on Si face. In addition, they claimed that at the initial stage of CNTs growth, nanocaps are formed on C face.[6,7,8,9,10,11,12] In contrast, Derycke et al observed parallel CNTs growth on Si face, and they found graphite layers formed as well.[13] All these experimental groups

assume that Si atoms leave the surface in the ultrahigh vacuum condition during heating, although so far no one have given the satisfactory explanation of how Si leaves. As for theoretical investigations, Gogotsi *et al.* used an empirical reactive molecular mechanics force field for the study of diamond growth on the Si-face of the 6H-SiC (1000) surface.[14] They found that a single diamond layer of sp^3-carbon C atoms would rearrange and form a graphene sheet consisting of mostly sp^2-carbon atoms, in agreement with their experiments.[15]

We have recently performed high temperature QM/MD simulation on model system of SiC surface with graphene sheets on top of either C or Si face.[16] In agreement with experiment, we found that (a) the C face attached graphene layer warps readily to form small diameter and stable nanocaps, (b) the Si face attached graphene sheet keeps flat and forms more volatile Si-graphene bonds, and (c) C face nanocaps appear to anneal to dome-shape short nanotube structures with tube-surface connectivity consistent with zigzag nanotube chirality. Based on these initially formed nano structures, we continued the simulation by subsequent removal of Si atoms to mimic the Si sublimation at high temperature ultrahigh vacuum condition.[17] Substantial perpendicular nanotube growth is observed on the C face, while on the contrary, the Si face appears not capable of such growth. One concern of our simulation is that the model system is relatively small, it would be interesting to perform simulations on larger systems and see whether several small nanocaps will be formed or a bigger nanocap. The other thing which is not clear to us is that how graphene sheets are formed on SiC surface, although we borrow it from nowhere for the previous simulation. Therefore, we are trying to answer these questions in this study. In the first part of present investigation, we increased the size of our SiC model system and re-performed our QM/MD simulation in a slightly different scheme, which is called "press and bake". Then we tried to study the graphene nucleation process by either shooting C_2 molecules to the SiC surfaces or removing top layer Si atoms of

SiC slabs. Both these two approaches are intended to provide C sources on SiC surface, simulating the experimental Si sublimation decomposition which occurs on the order of minutes and too slow to be modeled straightforwardly. We will elaborate our simulations in details and conclude by comparing our results with experimental observations.

10.2 Computational Method

Throughout our simulations, the quantum chemical Density Functional Tight Binding (DFTB) method[18,19,20,21] is employed to provide energies and gradient direct on the fly, with the parameters adopted from references.[18,22,23] As have been shown by us[24] in the comparison for energies and geometries of different fullerene isomers C_{28}-C_{86} obtained by different methods, DFTB produces comparable results to ab-initio B3LYP/6-31G(d) and performs significantly better than semiempricial AM1 and PM3 methods. Regarding the application of DFTB to SiC system, we have verified[16] for the small model compounds that geometry parameters predicted by DFTB are in great agreement with B3LYP/6-31G(d) calculations, whereas the binding energies produced by DFTB are systematically overestimated compared to B3LYP results while preserving the correct order C-C > Si-C > Si-Si. As usual, a velocity Verlet integrator is used to propagate the trajectories with a time step of 1.209 fs (50 atomic units), and scaling of velocities with an overall probability of 20% is taken to maintain the constant target temperature.

To simulate the nucleation process, we choose the 2-dimensional periodic SiC slab with different sizes and layers as model systems. The dangling bonds of SiC layer farthest away from the surface are passivated with hydrogen atoms and their positions are kept frozen to mimic the bulk effect. The very first simulation we did here is to study the nanocap formation for a larger system, with 400 atoms and 26.665 Å × 26.432 Å × 1000 Å as the three periodic dimension. In order to reduce the

calculation cost, as opposed of putting two graphene sheets on SiC surfaces in our previous simulation, we placed only one layer of graphene sheet on top of SiC surfaces with close contact to the SiC surface, to avoid the flying away of graphene layer. The temperature we chose in this simulation is 2000 K, thus we call this scheme "press and bake". To study the graphene nucleation, we took several different approaches. The largest difficulty in our simulation is the Si sublimation, which is a long-term process typically around 20 minutes in experiment, hence inaccessible to our short time simulation on the order of 10 ps to 100 ps. Therefore, by assuming Si atoms having already left the system, we provided the system with C sources in the form of C_2 molecules on top of a single layer of SiC surface. To avoid the leaving of C sources from the surface, C_2 molecules are shot toward the surface and the length of unit cell in Z dimension is set to be 20 Å. The other approaches that we took to better mimic the Si sublimation process were to start the simulation with three layers of SiC slabs but artificially remove the Si atoms during the subsequent heating to simulate their sublimation. As the Si atoms in the top two layers are removed with certain time intervals, free C atoms are released to provide the C sources on SiC surface for the graphene nucleation. However, as observed for our small three-layer model, removing all the Si atoms left insufficient amount of C sources on the SiC surfaces. To improve our model, we decided to take off only half of the Si atoms in the top two layers, and change the other half of Si atoms directly to C atoms. Whether the Si atoms are removed or changed to C atoms are purely random, but the removal and change occurs one after another in a regular pattern. In addition, since the top layer of SiC is more exposed to vacuum compared to the second layer, the rate for the top layer Si removal or change to C atoms are set to be twice as for the second layer Si atoms. When looking at the movies of the simulations, the change of Si atom to C atom corresponds to a color change of a sphere at a randomly chosen site, therefore the approach involved with changing Si to C is named as "change color removal".

10.3 Results and Discussions

10.3.1 "Press-and-Bake" simulations

Due to the high computational cost, we ran only 4 trajectories in total, with 2 on C face and 2 on Si face. As in our previous paper,[16] two different type of graphene sheet were used as the starting structure for the simulations, one with 56 hexagon and 16 C_2 units (trajectory a) and the other with 63 hexagon and 2 C_2 units (trajectory b). Only one graphene layer is placed on top of the surface with initial interlayer distance between graphene sheet and SiC surface to be 2.0 Å. Although this short distance is very unphysical as the initial condition, the following continued heating would make the system to achieve the thermodynamic equilibrium. Also, with this choice of initial distance, a second layer of graphene sheet that keeps the lower layer graphene sheet from flying away is not necessary any more, in this sense we push the system for the purpose of saving computational cost. The snapshots of the initial geometry of C face and Si face are shown in Figure 10.3 (a) and (b).

Unlike our previous trajectories in which the initial distance is van der vaals radius and graphene sheet attaches to the surface with one side of its borders first, the whole border of graphene sheet makes bonds with SiC surface immediately since the simulation starts. Because random velocities are assigned to C atoms in the graphene sheet at the beginning of trajectories, some atoms moves upward and some downward, which makes the graphene sheet no longer flat at 0.12 ps. This feature is observed in all those trajectories. For the C face trajectory a, several C atoms from the borders of the graphene sheet make C-C bonds to the SiC surface, introducing some curvature at the edges of graphene sheet. However, some C-C bonds are also made between the central C atoms of the graphene sheet and the surface, therefore, the whole graphene sheet does not look like a big cap but four small caps with the center sucked onto the SiC surface at the beginning of the trajectory. Although the C-C

bond is strong, there are only a few of them in the central area of the graphene sheet, which cannot resist the whole graphene sheet from being a big smooth cap and gaining conjugation energy. After the continued heating, the volatile C-C bonds at the central area disappear, and the center of graphene sheet budges up to make a homogenous big cap on the SiC surface. (see snapshot (c) in Figure 10.3) For the C face trajectory b, the initial observation is quite similar to trajectory a, that many C-C bonds are made between the garphene sheet and C face, both at the border and in the central area. Some of the bonds formed in the central area then disppear during the following continued heating and the graphene layer experience less curvature. However, unlike trajectory a, at the end of our 12 ps simulation, there are still substantial number of C-C bonds between the central line of graphene sheet and surface, so the central area did not bulge up at the end of simulation. Instead of forming a big cap, two parallel vault are formed by the graphene sheet in this trajectory b. (see snapshot (e) in Figure 10.3) The result is not conclusive, and may largely depend on the initial random numbers, but in general, relatively large caps should be favored over many small nanocaps. It could be possible that the two parallel nanovault merge together and form a homogeneous big nanocap if the simulation time is extended longer.

The Si face trajectories are similar to C face trajectories at the initial stage. C-Si bonds are made both at the graphene borders and the central area when simulation starts. However, because of the weaker C-Si bonds, they are more volatile and cannot make the graphene sheet curved up at the edge of graphene sheet. Since the whole grephene sheet is in favor of keeping flat for better conjugation, the bulged parts of the graphene sheet are actually pulled down during the heating. Consequently, even more C-Si bonds are formed at the central area of graphene sheet during the simulation. At the end, the graphene sheet keeps rather flat as a whole, despite some bulging up atoms in small local regions. Similar structures for Si face trajectory a and b are observed as one can see in snapshot (d) and (f) of Figure 10.3.

10.3.2 Shooting C_2 molecules on SiC surfaces

As of yet, it is not clear at all how Si atoms leave C atoms behind in high-temperature vacuum decomposition of SiC,[25] although it is known that the higher vapor pressure of Si compared to C is somehow related to the selective Si sublimation.[2,3,4] It is certainly that the leaving of Si atoms is essential for the graphene nucleation on SiC surfaces. However, we found no evidence that Si atoms leave the surfaces by themselves or as Si_2 particles in simulations lasting hundreds of picoseconds at 2000 K and 3000 K. We even performed preliminary simulations with oxygen atoms or O_2 molecules added above SiC surfaces but we still could observe significant Si removal in the form of SiO_x. Since experiments are performed at the timescale of minutes, we have to get around this Si sublimation process and provided C sources to the system. Without losing generosity, we decided to add on the SiC surfaces with the smallest stable C units, C_2 molecules, which we have used to successfully make fullerenes.[26] We have run 24 trajectories, with 12 on C face and the other 12 on Si face. In each of these trajectories, 50 C_2 molecules are added into the system. In order to make efficient nucleation of C source on the SiC surface, C_2 molecules are shot toward the surface when added to the system. The direction of initial velocities of the C_2 molecules are random, but with negative component on the z axis which make sure the molecules are moving toward the surface. The region from which C_2 molecules are shot from is between 6 and 10 angstroms above the surface. 3 different schemes are chosen for the feeding of C_2 molecules, with 1, 5, and 10 C_2 molecules added to the system at a time. For each feeding scheme, 2 feeding speed are chosen, which are 0.24/0.48 ps interval for 1 C_2, 1.2/2.4 ps interval for 5 C_2, and 2.4/4.8 ps intervals for 10 C_2. Trajectories are running both in 2000 K and 3000 K, making the total number of trajectories being $2 \times 3 \times 2 \times 2 = 24$. To avoid the leaving of C_2 molecules from the surface, the periodic box size in Z dimension is reduced to 20 Å.

Let's take the C face trajectory with 1 C_2 shooting each time and 0.48 ps shooting

interval at 2000 K as an example. The initial single layer SiC structure with C face is shown in snapshot (a) of Figure 10.4. At the beginning of the shooting, C_2 molecules come down and attached to the surface, but a few of them may also bounce back. When C_2 is attached to the surface, the linking C atom adopts *sp* hybridization so that a short C_2 chain is formed perpendicular to the surface. At first there were not many C_2 molecules so they are well distributed on the C face without affecting each other. As a result, we observe many short perpendicular C chains at the initial stage of the shooting. As the shooting goes on, more C_2 molecules come down to the surface, they either attach to the surface or linked to other C_2 molecules that are already on the surface and make longer chains. As the surface C density becomes larger and larger, the neighboring C chains wobble and connect to each other, which makes the linking atoms to adopt sp^2 hybridization. Consequently some of the C chains become parallel to the surface with small angles to the surface instead of perpendicular. At the end of shooting, so many C atoms are there on surface that they all connect to each other, forming rather complicated structures. (see snapshot (c) of Figure 10.4) Most of them adopt sp^2 hybridization, and some curved ring structures are observed. Few of them adopt sp^3 hybridization, which make the structure entangled and complicated in topology. Still, some of them are at terminals with *sp* hybridization, and perpendicular to the surface. During the following 12 ps heating time, not much change occurs, except some flying C_2 molecules come down and incorporated to this C cluster, while some of the wobbling chains were also caught by the cluster and integrated together. In this complex structure, we observe many curved C rings curved on the surface. (see snapshot (c) of Figure 10.4) The other trajectories on C face with different feeding scheme lead to more or less the same results. The final structures obtained are always entangled and complicated, many chains are left perpendicular to the surface, rings are formed but are entangled and we never see a complete cap nucleation. In reality, the cap nucleation could take

substantially longer time than our simulation, and how Si atoms leave might actually important in this process. However, we still see some hint from our current simplified simulations.

The simulations on Si face lead to very different results compared to C face. We will take the Si face trajectory with 1 C_2 shooting each time and 0.24 ps shooting interval at 2000 K as an example. The initial single layer SiC structure with Si face is shown in snapshot (d) of Figure 10.4. The initial stage of the trajectory is similar to the one on C face. When the C density is low on Si face, we observe many perpendicular short C_2 chains attached to the surface, due to the *sp* hybridization. Since the Si-C bonds are weaker, we also observe large wobbling of these C chains. When more and more C_2 molecules come to surface, the wobbling chains connect to each other and form parallel chains on top of the surface. Most of them are still in *sp* hybridization and looks like floating, with ends attached to the surface. As surface C density gets even higher, C atoms with sp^2 hybridization appear. It seems that C atoms prefer to make sp^2 bonds among themselves, and we observe many C rings on top of the surface. At the edge of the conjugated ring structure, C atoms may connected to Si face with sp^2 or even sp^3 hybridization, however, due to the weak Si-C interactions, these bonds are very volatile so the ring plane is still parallel to the surface. At the end of shooting, a partial graphene sheet has already been formed on the surface (see snapshot (c) of Figure 10.4). Then during the subsequent 12 ps heating time, some C_2 molecules flying over the surface are merged into the surface C cluster, and the whole C surface are fully covered by a grephene sheet like structure. This structure is made up of 5, 6 and 7 membered rings, very flat as a whole, with a small bulge, under which stays a knocked out Si atom (see snapshot (c) of Figure 10.4). Again, other trajectories on Si face are quite similar, graphene sheet or partial grephene sheet like structures with attached perpendicular C chains are formed on the surface at the end of the simulation. Out of 12 Si face trajectories,

6 lead to fully covered graphene sheet, while the other 6 end up with partial grephene sheet with C chains protruding up. In general, all those structures are very flat compared to the structures on C face. We noticed that for all those trajectories with 10 C_2 molecules feeded each time, the final structures are only partial graphene sheet with long C chains protruding up or flying in the air. This is because feeding 10 C_2 molecules each time cause too high C density above surface so that chain formation occurs before the actual graphene nucleation on Si face. In addition, we observed that many Si atoms are knocked out at 3000 K simulations, which indicates that this temperature is too high for such kind of simulation.

10.3.3 Random Si removal from C- and Si-face

To further simulate the Si sublimation and graphene nucleation process, we took the approach in our previous paper for nanotube growth from the cap.[17] We use a three-layer SiC slab, saturated with H atoms at the bottom, as our model system (see Figure 10.5 snapshot (a) for C face and snapshot (d) for Si face). Si atoms from the top two layers of SiC are removed one by one from the system artificially, thus providing C sources for graphene nucleation. The Si atoms from top layer are removed 2 times faster than those from middle layer, with the removal interval 0.24 ps and 0.48 ps respectively, while the position from which Si atom is removed each time is purely random. The whole removal procedure is shown in Figure 10.1. At the first 1.2 ps, no removal occurs, all the atoms are vibrating around their equilibrium position. Then 2 Si atoms, one from the top layer, the other from the middle layer SiC slab, are removed at the same time. Each removal breaks four Si-C bonds, making the adjacent C atoms very unstable, especially for the top layer C atoms, which only have 2 neighbors after the removal. With the first removal of top layer Si atom, the 4 C adjacent C atoms make two pair of C-C bonds, one between the 2 C atoms in the top layer, the other between the left C atoms in top layer and the C atom in middle layer. While for the second layer, after the first Si atom is removed, the closest 4 C

atoms still have 3 neighbors, so they are not so unstable as the case in top layer. 3 of them do not make new bonds, but adjust their positions to better bonding their neighbors; however, the other one makes a new bond with a top layer C atom, drags it down, making its neighbor Si atom to be at the top. Then 0.24 ps later, another Si atom is removed, but this time no Si is removed from the middle layer, since we assume that top layer Si atoms are removed faster. This removal again causes the formation of new bonds between the surrounding C atoms. As a result of continuous Si removal, many C-C bonds form, which makes a few embedded C_2 units in the slab. Since the top layer Si atoms are removed faster, the top layer surface soon loses its regularity while the middle layer keeps relatively intact. As more and more Si atoms are removed, some C_2 units lose contact to the slab and fly away to the vacuum, while others make bond between each other and form C chains. When all the Si atoms are removed, there leaves some entangled C chains parallel to the SiC surface in a zigzag shape, as well as some small C_2 units perpendicular to the surface due to *sp* hybridization (see snapshot (b) of Figure 10.5). Then we continue with 12 ps annealing of the system. Some of the flying C_2 molecules come back and are caught by dangling surface C chains. Meanwhile, the dangling chains may catch each other, which forms longer chains or a few C rings. However, the overall C face are only partially covered by some perpendicular C chains (see snapshot (c) of Figure 10.5), as well as a few parallel C rings, and we feel that C source is not sufficiently provided.

The situation on Si face is a little bit different. The first 1.2 ps is for equilibrium and nothing occurs. When Si atoms are first removed from the top layer and middle SiC layer, their 4 immediate neighbor C atoms still have 3 companies, which help these C atoms to be not very unstable but keep in more or less the same position as before the Si removal. Then a third Si atom is removed from top layer, but still not much occurs. As more Si atoms are removed, some C atoms may have only 2 partners and become unstable, starting making bonds with nearest C atoms. However, since

middle layer Si atoms are removed slower, the rest Si atoms impede the bonding between C atoms between layers. Therefore, C atoms are more likely to make bonds or rings parallel to the surface, which is the major difference with the trajectories on Si face. After substantial amount of Si atoms are removed, some of the parallel structures are destroyed, resulting in the leaving of C_2 molecules and standing up of short C chains. When all Si atoms are gone, there are both parallel and perpendicular C chains on top of the surface (see snapshot (e) of Figure 10.5). At the following 12 ps annealing time, again some C_2 molecules come back to the surface, some dangling chains are caught by other chains, and the overall effect is that a few C chains and rings are made parallel to the surface (see snapshot (f) of Figure 10.5). Nevertheless, the C atoms on top of the surface are not enough to cover up the whole surface, thus only partial structure are formed. It is desired to provide more C sources to the surface for the complete graphene nucleation.

10.3.4 Si Change Color removal

One solution to provide more C sources is to increase the number of SiC layers; however, this will make the calculation very expensive and significantly increase simulation time. Therefore another approach named "change color removal" is adopted (see Figure 10.2). In this scheme, instead of removing all Si atoms, only half of them are removed, while the other half are changed to C atoms artificially, and everything else is otherwise the same as in the random removal approach. Because of the change of Si atom to C atom, more C sources are feed to the system. We run trajectories on both C face and Si face, with the same 3-layer model system (see Figure 10.6 snapshot (a) and (d) for initial C and Si face structure). Two different events, Si removal and direct change from Si to C, occurs one after another repeatly during the simulation. Similar to the Si removal scheme, the event happening rate for the top layer is twice as fast as for the middle layer. After all the Si atoms are removed, the system is annealed at 2000 K for 12 ps.

We will use c_face_1 trajectory as the example to demonstrate the C face simulations. Again, we let the first 1.2 ps to be the equilibrium time and basically nothing occurs except vibrations. The first two Si atoms removed from top and middle layer are very close, thus introducing huge disturbance to the system. C-C bonds form at this area both between layers and in the top layer, which make large deformation at the local region. The third event happening is a color change from Si to C, which also occurs around this site, causing even larger local deformation. Then the following removal on the top layer and the color change on the middle layer occur at the same time. The removal caused the instability of its neighboring C atoms, which move away from their original position and make bonds either between layers or among the top layer. The color change on the middle layer does not induce large changes since the local structure is still quite stable, but due to the shorter C-C distance, the neighboring C atoms are dragged closer to the C atom at the color change site. As more and more removal and color change occurred, the system loses its regularity gradually. It is observed that C chains and rings formed at the top two layers. Because half of the Si atoms are changed to C atoms directly, more C atoms stay on the surface after the removal compared to the pure removal case, consequently some entangled ring structure is formed on the surface. These rings are either curved or perpendicular to the surface, with short C chains protruding up at the terminals. As some of the Si atoms are directly changed to C atoms, many of them keep sp^3 hybridization after the removal (see snapshot (b) of Figure 10.6). During the subsequent 12 ps heating time, this entangled structure is quite stable, not many flying C_2 molecules are merged to it. The entangled rings look like a partial cap (see snapshot (c) of Figure 10.6), curved and ugly, and seem hard to be repaired or form a complete cap at the current simulation scale. We calculated the curvatures based on two different definitions for the maximum C block of the final structure. The first curvature is calculated as the average curvature of all the sp^2 C atoms in the blocks, while the second curvature is

calculated by least square fitting the whole block to a sphere. These two definition of curvature both give the value of 0.173 $Å^{-1}$ for the particular final structure. We noticed that all the 10 C face trajectories are quite similar in the sense of partial cap formation or the entangled ring structure, as well as the perpendicular C chains, and the average value of the two curvatures for the 10 C face trajectories are 0.159 $Å^{-1}$ and 0.194 $Å^{-1}$ respectively.

The Si face trajectories are different from C face trajectories, and we will take si_face_1 as the example. The first 1.2 ps is the same as before. The first removal from the top layer and second layer occur at the same time. As demonstrated before, at the initial stage of removal, not too much local deformation are observed at the removal site. When a Si atom is removed, its neighboring C atoms still have 3 partners, which keep them relative stable. Meanwhile, the existence of middle layer Si atoms prevents the bond formation between C atoms among different layers. When the next event happens, which is a color change from Si to C in the top layer, 3 Si-C bonds are changed to 3 C-C bonds, leading this center C atom to be sp^2 hybridization. As the removal goes on, C atoms are more flexible and likely to make parallel bonds among layers. Even when the color change occurs at the middle layer, the changed C atom tend to make only 3 C-C bonds with the same layer neighboring C atoms but not form the fourth bond with the upper layer C atoms. Therefore these two C atoms are in sp^2 hybridization and the local structures are planar. During the color change removal process, not many C-C bonds are formed between layers. Consequently, many C_2 molecules or short C chains fly away from the system when important Si linker atoms are removed. When the color change removal process finished, the so formed C cluster on surface are layer- wised instead of totally entangled as on the C face. As you can see in the snapshot (e) of Figure 10.6, we observe parallel C chains from the middle SiC layer on surface, and short perpendicular C chains standing up on this parallel chains, as well as many flying C chains above the surface. At the following

12 ps annealing time, it is observed that a few flying C_2 molecules move back and are merged to the surface C cluster. In addition, the wobbling C chains came down and are merged to the C cluster as well. Due to the mergence of C_2 molecules and these C chains, rings are formed inside this C cluster and it looks like a partial flat graphene sheet with only 2 protruding up C_2 molecules, although the surface is still not fully covered (see in the snapshot (e) of Figure 10.6). This flat structure on Si face is very much different from the curved entangled ring structure on the C face, which again indicates the different nature of these two faces. Also, the two curvatures are calculated to be 0.141 $Å^{-1}$ and 0.154 $Å^{-1}$ for this particular structure, smaller than the one obtained from C face. The other Si face trajectories are also very similar; in most cases, we observe the formation of the flat graphene sheet or partial graphene sheet. While in two of them, partial graphene sheet is formed with perpendicular ring structure on the surface, but this mixed feature should not change the distinguished nature of Si face with respect to C face. The curvatures for all those trajectories are summarized in Table 10.1. The two average curvatures of these 10 Si face trajectories are 0.130 $Å^{-1}$ and 0.124 $Å^{-1}$, smaller than the average curvatures obtained from C face trajectories.

10.4 Conclusions

In summary, we have performed high temperature QM/MD simulations to study the graphene nucleation on both C face and Si face of SiC surfaces. As have been reported before, nanocaps can nucleate on the C face while graphene sheet remains planar on Si face in a small size model. We increased the size of the model and similar behaviors were observed: bigger nanocaps forms on C face while the larger grephene layers still tend to be planar. This difference between C face and Si face nature should come from the difference in energy between the C-C and Si-C bonds. We continued our investigation on the graphene nucleation by simulating the Si decomposition process

with several approaches. Under both "shooting C_2" and "random color change" approaches, incomplete nanocaps and entangled ring structure, as well as C chains perpendicular to the surface, tend to be formed on C face; whereas graphene layer or partial graphene layer like structure, with 5,6 and 7 rings, are preferable to be formed on Si face. These observations are in good agreement with Kuzunoki's experiment.

References

1. Nakada, K.; Fujita, M.; Dresselhaus, G.; Dresselhaus, M. *PHYSICAL REVIEW B* **1996**, *54*, 17954–17961.

2. Forbeaux, I.; Themlin, J.; Debever, J. *PHYSICAL REVIEW B* **1998**, *58*, 16396–16406.

3. Forbeaux, I.; Themlin, J.; Charrier, A.; Thibaudau, F.; Debever, J. *APPLIED SURFACE SCIENCE* **2000**, *162*, 406–412.

4. Charrier, A.; Coati, A.; Argunova, T.; Thibaudau, F.; Garreau, Y.; Pinchaux, R.; Forbeaux, I.; Debever, J.; Sauvage-Simkin, M.; Themlin, J. *JOURNAL OF APPLIED PHYSICS* **2002**, *92*, 2479–2484.

5. Hass, J.; Feng, R.; Li, T.; Li, X.; Zong, Z.; de Heer, W. A.; First, P. N.; Conrad, E. H.; Jeffrey, C. A.; Berger, C. *APPLIED PHYSICS LETTERS* **2006**, *89*, 143106.

6. Kusunoki, M.; Rokkaku, M.; Suzuki, T. *APPLIED PHYSICS LETTERS* **1997**, *71*, 2620–2622.

7. Kusunoki, M.; Suzuki, T.; Kaneko, K.; Ito, M. *PHILOSOPHICAL MAGAZINE LETTERS* **1999**, *79*, 153–161.

8. Kusunoki, M.; Suzuki, T.; Hirayama, T.; Shibata, N.; Kaneko, K. *APPLIED PHYSICS LETTERS* **2000**, *77*, 531–533.

9. Kusunoki, M.; Suzuki, T.; Honjo, C.; Hirayama, T.; Shibata, N. *CHEMICAL PHYSICS LETTERS* **2002**, *366*, 458–462.

10. Kusunoki, M.; Honjo, C.; Suzuki, T.; Hirayama, T. *APPLIED PHYSICS LETTERS* **2005**, *87*, 103105.

11. Maruyama, T.; Bang, H.; Kawamura, Y.; Fujita, N.; Tanioku, K.; Shiraiwa, T.; Hozumi, Y.; Naritsuka, S.; Kusunoki, M. *CHEMICAL PHYSICS LETTERS* **2006**, *423*, 317–320.

12. Bang, H.; Ito, Y.; Kawamura, Y.; Hosoda, E.; Yoshida, C.; Maruyama, T.; Naritsuka, S.; Kusunoki, M. *JAPANESE JOURNAL OF APPLIED PHYSICS PART 1-REGULAR PAPERS BRIEF COMMUNICATIONS & REVIEW PAPERS* **2006**, *45*, 372–374.

13. Derycke, V.; Martel, R.; Radosvljevic, M.; Ross, F.; Avouris, P. *NANO LETTERS* **2002**, *2*, 1043–1046.

14. Gogotsi, V., Y. Kamyshenko; Shevchenko, V.; Welz, S.; Ersoy, D.; McNallan, M. **2001**, , 239–255.

15. Gogotsi, Y.; Welz, S.; Ersoy, D.; McNallan, M. *NATURE* **2001**, *411*, 283–287.

16. Irle, S.; Wang, Z.; Zheng, G.; Morokuma, K.; Kusunoki, M. *JOURNAL OF CHEMICAL PHYSICS* **2006**, *125*, 044702.

17. Wang, Z.; Irle, S.; Zheng, G.; Kusunoki, M.; Morokuma, K. *JOURNAL OF PHYSICAL CHEMISTRY C* **2007**, *111*, 12960–12972.

18. POREZAG, D.; FRAUENHEIM, T.; KOHLER, T.; SEIFERT, G.; KASCHNER, R. *PHYSICAL REVIEW B* **1995**, *51*, 12947–12957.

19. Elstner, M.; Porezag, D.; Jungnickel, G.; Elsner, J.; Haugk, M.; Frauenheim, T.; Suhai, S.; Seifert, G. *PHYSICAL REVIEW B* **1998**, *58*, 7260–7268.

20. Frauenheim, T.; Seifert, G.; Elstner, M.; Hajnal, Z.; Jungnickel, G.; Porezag, D.; Suhai, S.; Scholz, R. *PHYSICA STATUS SOLIDI B-BASIC SOLID STATE PHYSICS* **2000**, *217*, 41–62.

21. Frauenheim, T.; Seifert, G.; Elstner, M.; Niehaus, T.; Kohler, C.; Amkreutz, M.; Sternberg, M.; Hajnal, Z.; Di Carlo, A.; Suhai, S. *JOURNAL OF PHYSICS-CONDENSED MATTER* **2002**, *14*, 3015–3047.

22. FRAUENHEIM, T.; WEICH, F.; KOHLER, T.; UHLMANN, S.; POREZAG, D.; SEIFERT, G. *PHYSICAL REVIEW B* **1995**, *52*, 11492–11501.

23. Gutierrez, R.; Frauenheim, T.; Kohler, T.; Seifert, G. *JOURNAL OF MATERIALS CHEMISTRY* **1996**, *6*, 1657–1663.

24. Zheng, G.; Irle, S.; Morokuma, K. *CHEMICAL PHYSICS LETTERS* **2005**, *412*, 210–216.

25. Nagano, T.; Ishikawa, Y.; Shibata, N. *JAPANESE JOURNAL OF APPLIED PHYSICS PART 1-REGULAR PAPERS SHORT NOTES & REVIEW PAPERS* **2003**, *42*, 1380–1385.

26. Irle, S.; Zheng, G.; Elstner, M.; Morokuma, K. *NANO LETTERS* **2003**, *3*, 1657–1664.

Table 10.1: Curvature of the maximum C block on surface at the end of Si "change color" removal simulation.

Tracjectory	C face		Si face	
	curv1($1/A^{-1}$)	curv2($1/A^{-1}$)	curv1($1/A^{-1}$)	curv2($1/A^{-1}$)
1	0.173	0.173	0.141	0.154
2	0.170	0.202	0.145	0.147
3	0.141	0.185	0.106	0.074
4	0.155	0.160	0.140	0.111
5	0.164	0.296	0.172	0.161
6	0.160	0.211	0.122	0.158
7	0.095	0.215	0.099	0.165
8	0.195	0.164	0.140	0.135
9	0.196	0.187	0.105	0.071
10	0.138	0.147	0.132	0.067
AVG	0.159	0.194	0.130	0.124

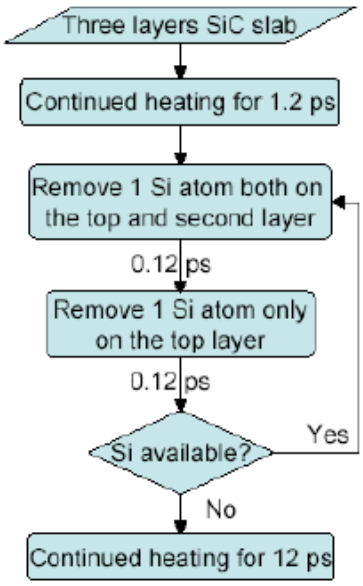

Figure 10.1: Flow chart for Si random removal simulation.

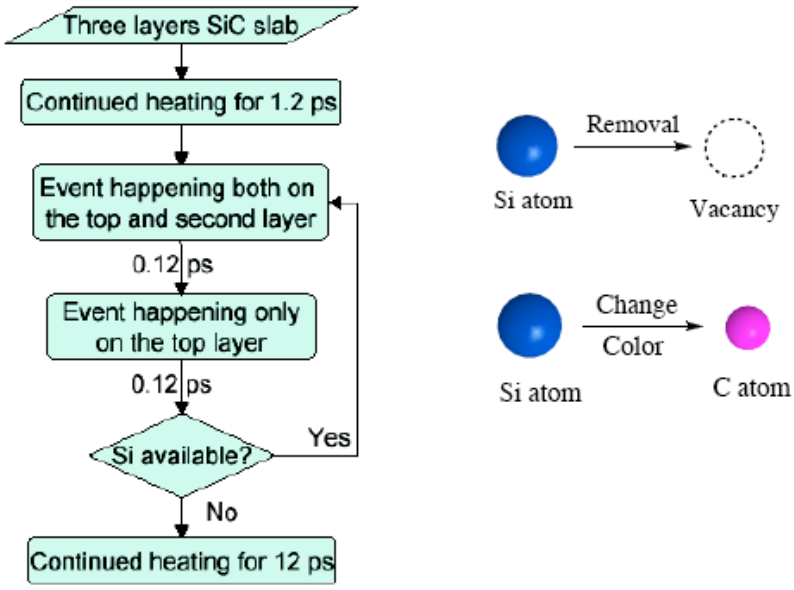

Figure 10.2: Flow chart for Si "change color" removal simulation

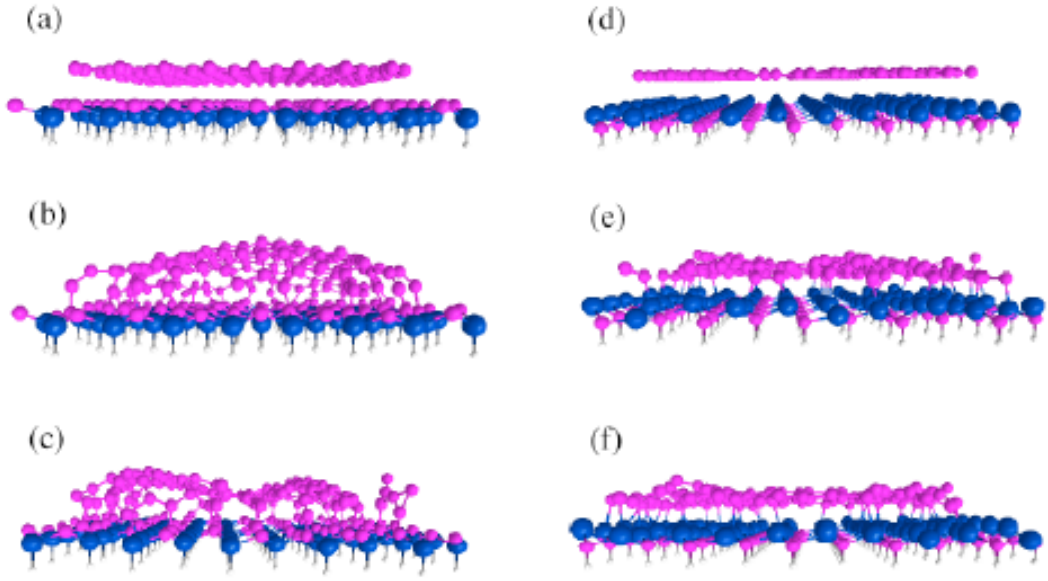

Figure 10.3: Large nano cap nucleation from "Press-and-Bake" simulations at $T = 2000K$. (a) Initial structure with large graphene sheet on C face; (b) end snapshot on C face with "type a" graphene; (c) end snapshot on C face with "type b" graphene; (d) Initial structure with large graphene sheet on Si face; (e) end snapshot on Si face with "type a" graphene; (f) end snapshot on Si face with "type b" graphene.

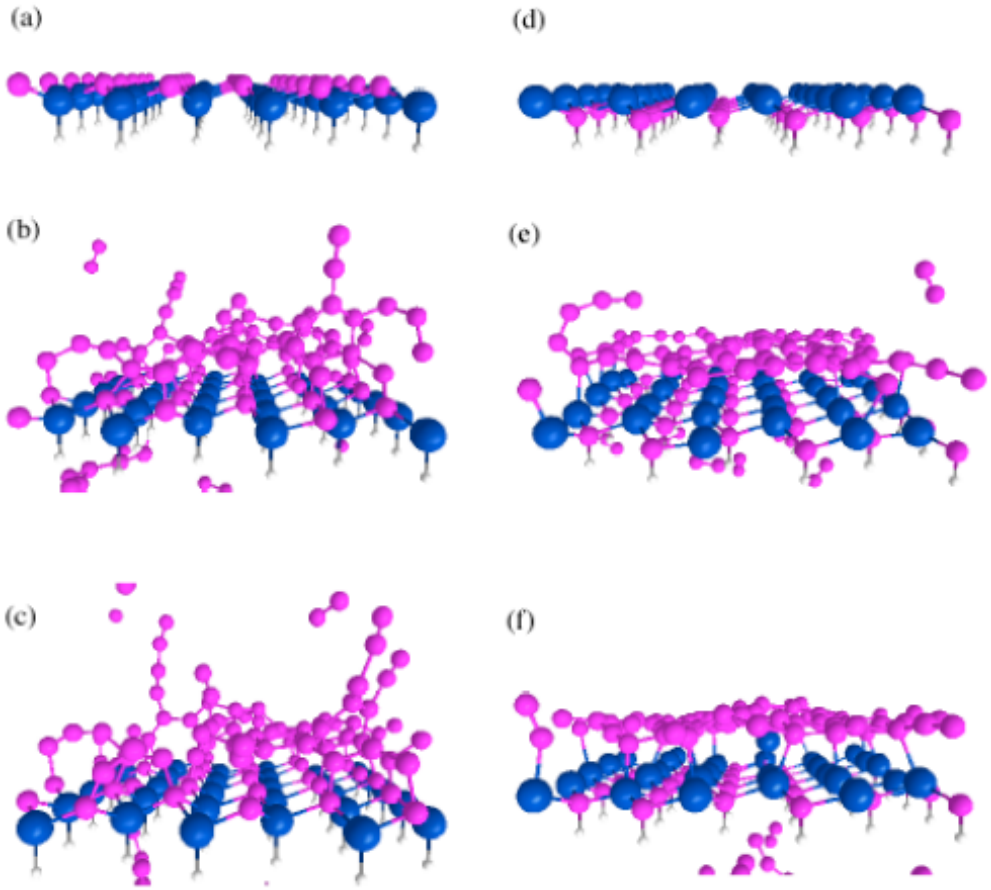

Figure 10.4: Snapshots with C_2 shooting on SiC surfaces at $T = 2000K$. (a) Inital C face sturcture; (b) snapshot at the end of shooting with 1 C_2 each time at $\Delta t = 0.48$ ps, elapsed time $t = 25.2$ ps; (c) snapshot for the same C face trajectory at the end of continued heating, elapsed time $t = 37.2$ ps; (d) inital Si face sturcture; (e) snapshot at the end of shooting with 1 C_2 each time at $\Delta t = 0.24$ ps, elapsed time $t = 13.2$ ps; (f) snapshot for the same Si face trajectory at the end of continued heating, elapsed time $t = 25.2$ ps.

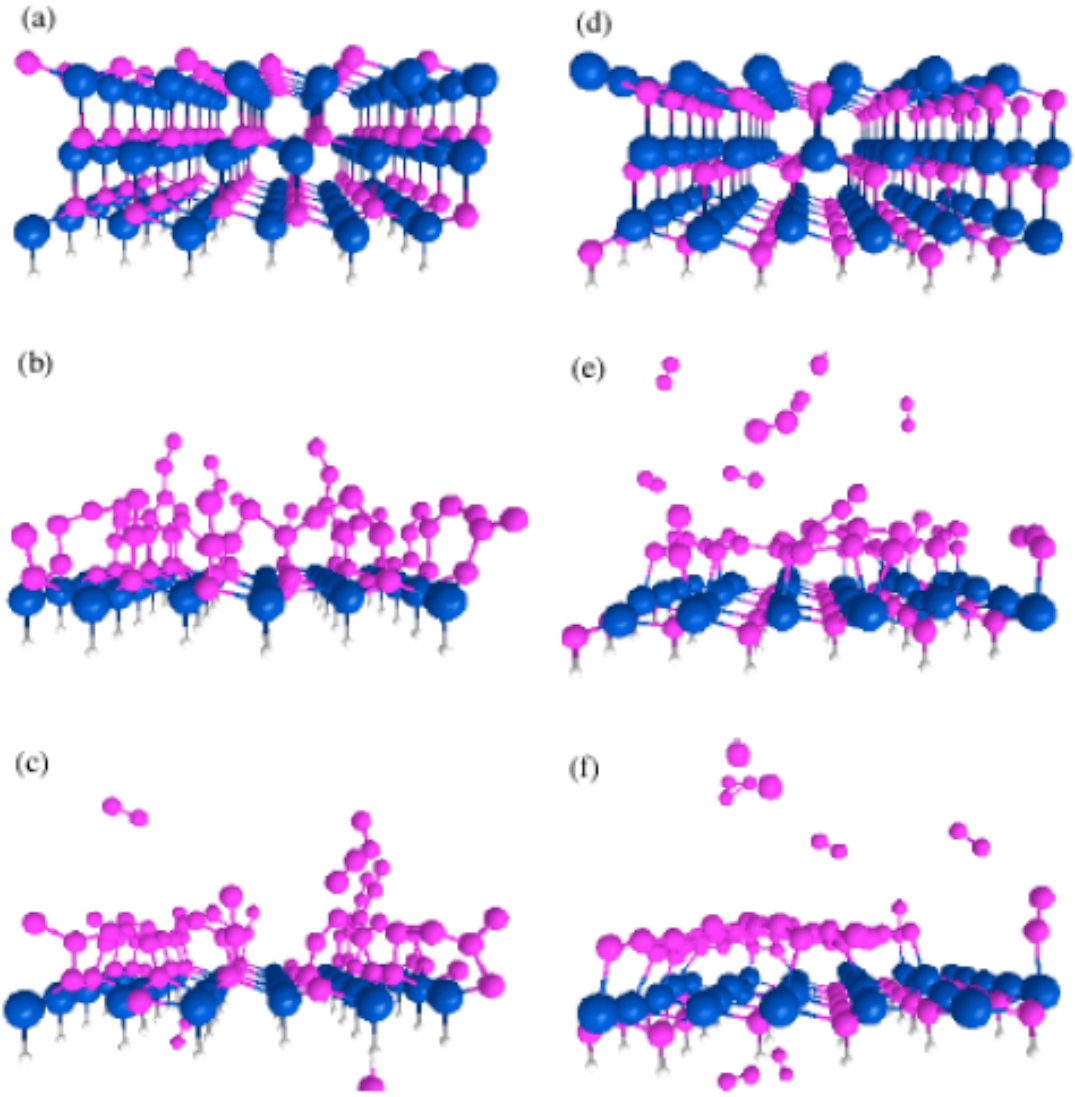

Figure 10.5: Snapshots with Si random removal simulations at $T = 2000K$. (a) Inital 3 layer SiC slab with C face; (b) snapshot at the end of Si removal for C face trajectory, elapsed time $t = 15.6$ ps; (c) snapshot for the same C face trajectory at the end of continued heating, elapsed time $t = 27.6$ ps; (d) inital 3 layer SiC slab with Si face; (e) snapshot at the end of Si removal for C face trajectory, elapsed time $t = 15.6$ ps; (f) snapshot for the same Si face trajectory at the end of continued heating, elapsed time $t = 27.6$ ps.

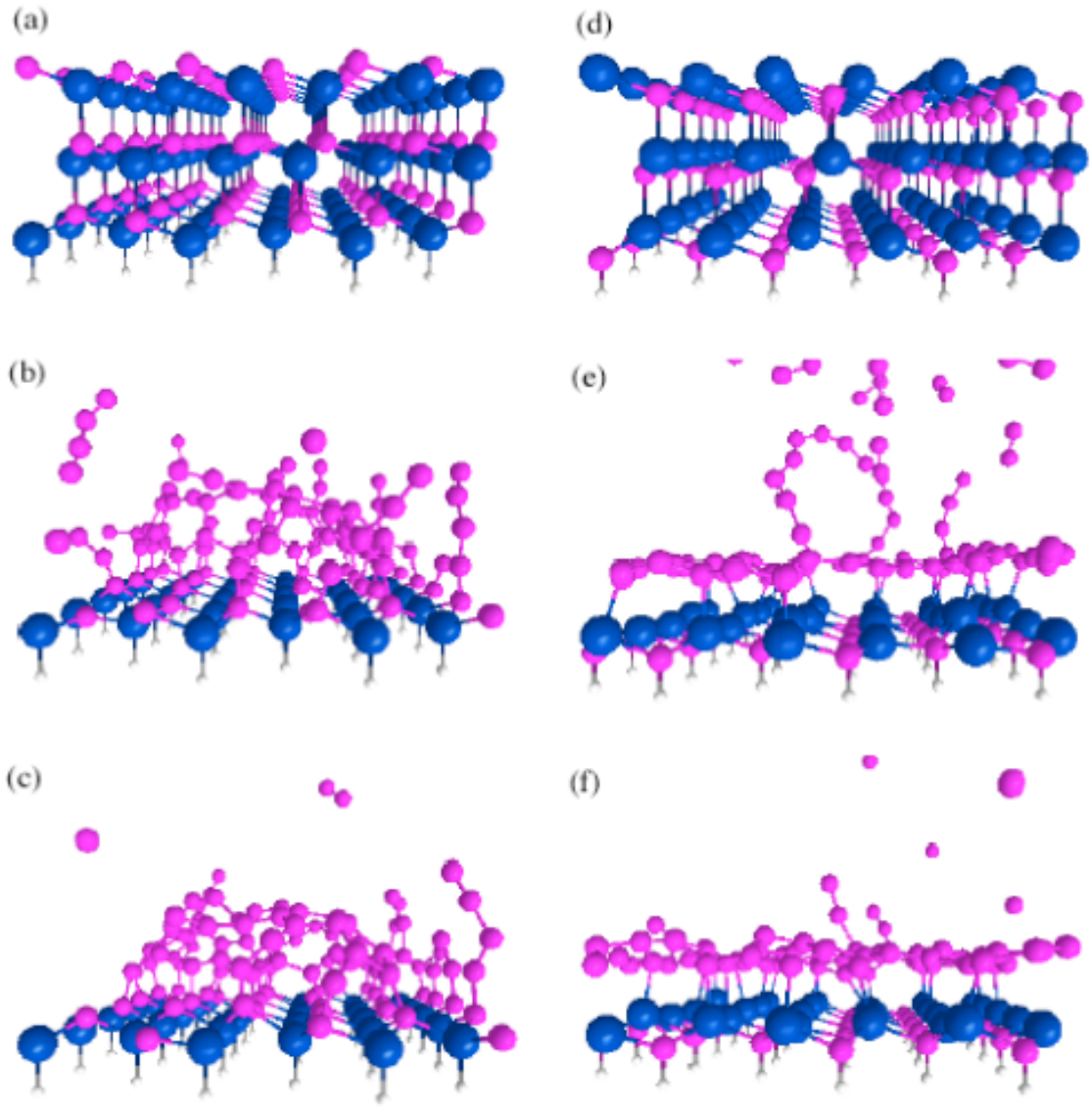

Figure 10.6: Snapshots with Si "change color" removal simulations at $T = 2000K$. (a) Inital 3 layer SiC slab with C face; (b) snapshot at the end of Si removal for C face trajectory, elapsed time $t = 15.6$ ps; (c) snapshot for the same C face trajectory at the end of continued heating, elapsed time $t = 27.6$ ps; (d) inital 3 layer SiC slab with Si face; (e) snapshot at the end of Si removal for C face trajectory, elapsed time $t = 15.6$ ps; (f) snapshot for the same Si face trajectory at the end of continued heating, elapsed time $t = 27.6$ ps.